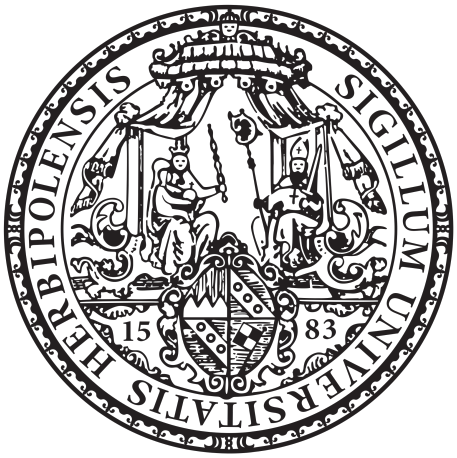

Two-Dimensional Electron Systems at Surfaces

—

Spin-Orbit Interaction and Electronic Correlations

Dissertation zur Erlangung des
naturwissenschaftlichen Doktorgrades
der Julius-Maximilians-Universität Würzburg

vorgelegt von
Philipp Alexander Höpfner
aus Münster

Würzburg 2012

Eingereicht am: 06.12.2012

bei der Fakultät für Physik und Astronomie

Gutachter der Dissertation:

1. Gutachter: Prof. Dr. Ralph Claessen

2. Gutachter: Prof. Dr. Jean Geurts

3. Gutachter: —

Vorsitzende(r) im Promotionskolloquium:

Prof. Dr. Matthias Bode

Prüfer im Promotionskolloquium:

1. Prüfer: Prof. Dr. Ralph Claessen

2. Prüfer: Prof. Dr. Jean Geurts

3. Prüfer: Prof. Dr. Werner Hanke

Tag des Promotionskolloquiums: 27.06.2013

Doktorurkunde ausgehändigt am:

"The most beautiful experience we can have is the mysterious."

Albert Einstein

Abstract

This thesis addresses three different realizations of a truly two-dimensional electron system (2DES), established at the surface of elemental semiconductors, i.e., Pt/Si(111), Au/Ge(111), and Sn/Si(111).

Characteristic features of atomic structures at surfaces have been studied using scanning tunneling microscopy and low energy electron diffraction with special emphasis on Pt deposition onto Si(111). Topographic inspection reveals that Pt atoms agglomerate as trimers, which represent the structural building block of phase-slip domains. Surprisingly, each trimer is rotated by 30 ° with respect to the substrate, which results in an unexpected symmetry breaking. In turn, this represents a unique example of a chiral structure at a semiconductor surface, and marks Pt/Si(111) as a promising candidate for catalytic processes at the atomic scale.

Spin-orbit interactions (SOIs) play a significant role at surfaces involving heavy adatoms. As a result, a lift of the spin degeneracy in the electronic states, termed as "Rashba effect", may be observed. A candidate system to exhibit such physics is Au/Ge(111). Its large hexagonal Fermi sheet is suggested to be spin-split by calculations within the density functional theory. Experimental clarification is obtained by exploiting the unique capabilities of three-dimensional spin detection in spin- and angle-resolved photoelectron spectroscopy. Besides verification of the spin splitting, the in-plane components of the spin are shown to possess helical character, while also a prominent rotation out of this plane is observed along straight sections of the Fermi surface. Surprisingly and for the first time in a 2DES, additional in-plane rotations of the spin are revealed close to high symmetry directions. This complex spin pattern must originate from crystalline anisotropies, and it is best described by augmenting the original Rashba model with higher order Dresselhaus-like SOI terms.

The alternative use of group-IV adatoms at a significantly reduced coverage drastically changes the basic properties of a 2DES. Electron localization is strongly enhanced, and the ground state characteristics will be dominated by correlation effects then. Sn/Si(111) is scrutinized with this regard. It serves as an ideal realization of a triangular lattice, that inherently suffers from spin frustration. Consequently, long-range magnetic order is prohibited, and the ground state is assumed to be either a spiral antiferromagnetic (AFM) insulator or a spin liquid. Here, the single-particle spectral function is utilized as a fundamental quantity to address the complex interplay of geometric frustration and electronic correlations. In particular, this is achieved by combining the complementary strengths of *ab initio* local density approximation (LDA) calculations, state-of-the-art angle-resolved photoelectron spectroscopy, and the sophisticated many-body LDA+DCA. In this way, the evolution of a "shadow band" and a band backfolding incompatible with a spiral AFM order are unveiled. Moreover, beyond nearest-neighbor hopping processes are crucial here, and the spectral features must be attributed to a collinear AFM ground state, contrary to common expectation for a frustrated spin lattice.

Zusammenfassung

In der vorliegenden Arbeit werden drei unterschiedliche Beispiele für ein zwei-dimensionales Elektronensystem (2DES) auf der Oberfläche von Elementhalbleitern behandelt: Pt/Si(111), Au/Ge(111) und Sn/Si(111).

Atomare Strukturen und deren spezielle Merkmale wurden mit Rastertunnelmikroskopie (STM) und Elektronenbeugung (LEED) untersucht, wobei ein Schwerpunkt die Abscheidung von Pt auf Si(111) war. Hervorzuheben ist hier die Anordnung von Pt Atomen als Trimere, die das Grundgerüst phasenverschobener Domänen bilden. Interessanterweise sind die Trimere um 30 ° gegenüber dem Substrat verdreht, was einen unerwarteten Symmetriebruch bedeutet. Daher stellt Pt/Si(111) ein einzigartiges Beispiel einer chiralen Struktur auf Halbleitern dar und könnte außerdem für katalytische Prozesse im atomaren Bereich interessant sein.

Die Spin-Bahn Wechselwirkung ist auf Oberflächen, die schwere Elemente enthalten, von großer Bedeutung. Hier kann die Spin-Entartung in den elektronischen Zuständen aufgehoben sein, was als *Rashba-Effekt* bekannt ist. Rechnungen mittels Dichtefunktionaltheorie (DFT) zeigen, dass eine solche Aufspaltung in der hexagonalen Fermi-Fläche von Au/Ge(111) existiert. Experimentell wurde dies mit dreidimensionaler spin- und winkelaufgelöster Photoelektronenspektroskopie bestätigt. Dabei folgt die planare Spin-Komponente einem kreisförmigen Umlaufsinn, während zudem eine starke Aufrichtung des Spins aus der Ebene hinaus entlang gerader Abschnitte der Fermi-Fläche auftritt. Hierbei wurden zum ersten Mal in einem 2DES zusätzliche Rotationen des planaren Spinanteils in der Oberflächenebene nahe von Hochsymmetrierichtungen nachgewiesen. Dieses komplexe Spin-Muster resultiert aus den kristallinen Anisotropien und kann exzellent modelliert werden, indem das Rashba-Modell um Dresselhaus-artige Spin-Bahn Terme höherer Ordnung erweitert wird.

Die alternative Verwendung von Gruppe-IV Adatomen bei einer geringeren Bedeckung ändert die Eigenschaften eines 2DES deutlich. Kennzeichnend sind eine verstärkte Ladungsträger-Lokalisierung und ein von Korrelationen bestimmter Grundzustand. Dabei stellt Sn/Si(111) ein Modell-System dar, das zudem ein spin-frustriertes Dreiecksgitter bildet. In einem solchen fehlt üblicherweise die langreichweitige magnetische Ordnung und der Grundzustand ist entweder ein isolierender spiralförmiger Antiferromagnet (AF) oder eine Spin-Flüssigkeit. Zur Analyse des Wechselspiels von geometrischer Frustration und elektronischen Korrelationen dient die Ein-Teilchen Spektralfunktion als Basisgröße. Dazu wurden die sich ergänzenden Stärken von Bandstruktur-Rechnungen in der lokalen Dichtenäherung (LDA), winkelaufgelöster Photoelektronenspektroskopie und Viel-Teilchen Modellen (hier LDA+DCA) kombiniert. Dabei wurde die Existenz eines Schattenbandes und einer Bandrückfaltung nachgewiesen, wobei letztere einen spiralförmigen AF als Grundzustand ausschließt. Vielmehr sind Hüpfprozesse über den nächsten Nachbarn im Gitter hinaus relevant und die spektralen Merkmale sind, trotz der Spin-Frustration, durch einen langreichweitigen *kollinearen* AF als Grundzustand erklärbar.

Contents

List of Figures

List of Tables

List of acronyms

1D	one-dimensional
1U2D	"one up two down"
2D	two-dimensional
2DES	two-dimensional electron system
3D	three-dimensional
AES	Auger electron spectroscopy
AF	antiferromagnet
AFM	antiferromagnetic
ALS	Advanced Light Source
ARPES	angle-resolved photoelectron spectroscopy
BIA	bulk inversion asymmetry
BZ	Brillouin zone
CAF	collinear antiferromagnetic
CDW	charge density wave
CHCT	conjugate honeycomb-chained trimer
COPHEE	COmplete PHotoEmission Experiment
DAS	dimer adatom stacking fault
DB	dangling bond
DCA	dynamical cluster approximation
DF	dual fermion
DFT	density functional theory

DMFT dynamical mean field theory

DOS density of states

EDC energy distribution curve

EELS electron energy loss spectroscopy

ESF electronic structure factory

FAT fixed analyzer transmission

fcc face-centered cubic

FRR fixed retarding ratio

FS Fermi surface

FWHM full width at half maximum

HCT honeycomb-chained trimer

HDA hemispherical deflection analyzer

HRPES High Resolution Photoemission Spectroscopy

IET inequivalent triangle

IPES inverse photoelectron spectroscopy

KRIPES k-resolved inverse photoelectron spectroscopy

LDA local density approximation

LDOS local density of states

LEED low energy electron diffraction

LHB lower Hubbard band

LINAC linear accelerator

LT low temperature

MCP multi channel plate

MDC momentum distribution curve

MIT metal-to-insulator transition

ML monolayer

MLWF maximally localized Wannier functions

MTL missing top layer

PED photoelectron diffraction

PES photoelectron spectroscopy

QP quasi-particle

QSL quantum spin liquid

QW quantum well

RF radio frequency

RHEED reflection high energy electron diffraction

RT room temperature

RVB resonant valence bond

RW row-wise

SARPES spin- and angle-resolved photoelectron spectroscopy

SBZ surface Brillouin zone

SDW spin density wave

SIA structure inversion asymmetry

SIC self-interaction correction

SLS Swiss Light Source

SOC spin-orbit coupling

SOI spin-orbit interaction

SP scan position

STM scanning tunneling microscopy

STS scanning tunneling spectroscopy

SXRD surface x-ray diffraction

UHB upper Hubbard band

UHV ultra high vacuum

UPS ultraviolet photoelectron spectroscopy

UV ultraviolet

VBM valence band maximum

VCA variational cluster approach

VT-SPM variable temperature scanning probe microscope

XPS x-ray photoelectron spectroscopy

XSW x-ray standing waves

1 Introduction

Condensed matter physics is one of the most important and most lively fields in modern physics, since it covers a huge variety of topics ranging from strictly fundamental research to technologically relevant applied subjects. In particular, explicit many-body effects, such as the electron-electron interaction, govern the physical properties in most solids. Here, the competing interactions of charge, spin, and the crystal lattice can lead to oftentimes rich phase diagrams. By tuning the dimensionality of such a crystalline system, and thus reducing the translational degrees of freedom, intriguing quantum phenomena may occur, which are not observable in isotropic bulk materials as, e.g., the high-temperature superconductivity [10].

While the stacked crystal structure in some solids already provides a two-dimensional (2D) confinement at the interface of adjacent layers, a different access to generate low-dimensional quantum systems exists in depositing adatoms in the sub-monolayer to monolayer (ML) coverage regime at the surface of an elemental semiconductor. Today, advanced semiconductor treatment and preparation techniques allow to build quantum systems of truly two-dimensional (surfaces and interfaces), one-dimensional (atomic wires), or even zero-dimensional (quantum dots) character. Self-organized growth is utilized to fabricate such systems with large lateral extent. Depending on the respective choice of adatom-substrate composition, in many cases adatom-induced surface states are formed, which are located in the bulk band gap of the semiconductor. In this way, a strict electron confinement is established. A variety of particularly surface sensitive probes is then utilized to access the dominating physics therein. These include scanning tunneling microscopy (STM), which allows for detailed analysis of geometric and electronic features at the atomic scale, and angle-resolved photoelectron spectroscopy (ARPES) with its direct access to the spectral function and the fundamental electronic characteristics.

As one of the most important implications in a low-dimensional system, *electronic correlations* gain relevance, since screening between charges is strongly reduced. Consequently, each electron is noticeably affected by the Coulomb repulsion force related to its adjacent charges. In a correlated system, it is "dressed" with a cloud of interacting electrons, and its properties are described as those of an electron ensemble, the so-called quasi-particle (QP). For even larger Coulomb repulsions, electron localization is often notably enhanced, which may evoke a Mott-Hubbard insulating ground state [11]. In this regard, two prime examples must be mentioned, i.e., the 2D system generated by a sub-monolayer coverage of potassium on top of boron enriched Si(111) and the surface of the $6H$ polytype of SiC(0001) [12, 13].

Besides its charge, the electron *spin* is a second important quantity, that gains rele-

vance in reduced dimensions. Exchange between neighboring electrons should intuitively lead to some kind of magnetic order. However, 2D systems are oftentimes arranged in terms of a *triangular lattice*, where any long-range magnetic ordering is prohibited as a consequence of *spin frustration*. The interplay of the electron spin and electronic correlations provokes competing ground states as, e.g., a spiral spin density wave (SDW) antiferromagnet (AF) and a gapless quantum spin liquid (QSL) [14, 15]. It would thus be interesting to study, whether a magnetically ordered state can be established despite the spin frustration. In this context, the $(\sqrt{3} \times \sqrt{3})$ reconstructed two-dimensional electron system (2DES), generated by 1/3 ML of Sn adatoms on Si(111), has been discussed as a model system in the literature [16–18].

The electron spin is also origin of spin-orbit coupling (SOC) effects at surfaces. Here, the structure inversion asymmetry (SIA) leads to a perpendicular potential gradient, which can lift the spin degeneracy and result in a specific splitting of the surface states, known as "Rashba splitting" [19]. Single crystal metal surfaces, such as Au(111) and Bi(111) and their surface alloys, characterized by a high atomic number Z, are well studied representatives [20–22]. Yet, realizing *metallic* spin-split Rashba states in semiconductors and their interfaces could pave the way towards the emerging field of *semiconductor-based spintronics* [23]. So far, experimental reports are rare and mostly restricted to insulating surfaces, such as Bi/Si(111) and Tl/Si(111) [24, 25], while a spin-splitting in conducting states has only been observed in the dense phase of Pb/Ge(111) [26]. Recently, it turned out that the isotropic spin arrangement, as described in the Rashba model, must be regarded as an exceptional case. While it still captures the spin topology in the surface states of single crystals, drastic deviations with rather complex spin patterns exist in many other heavy adatom induced 2DESs due to the presence of anisotropic and non-perpendicular field gradients at the surface [24, 25]. Notably, this is predicted to affect the spin texture of the three-dimensional (3D) topological insulator Bi_2Te_3 [27–29].

From a technological point of view, the possibility to control the spin electronically [23, 30] in a 2D system has been reviewed just recently [31]. Here, the prominent concept of a spin-field-effect transistor, theoretically proposed by S. Datta and B. Das, yet not technically realized, gives a glimpse of possible spintronic devices [32]. It is basically composed of source, drain, gate, and transport channel (see Fig. 1.1) as in a conventional field-effect transistor, where the electric current from source to drain is switched on and off by applying a voltage U_{gate} to the gate. In addition, the channel needs to provide Rashba-split states for spin-selective charge transport. Electrons from the source are injected with a predefined spin orientation into this channel, where a spin precession is induced by the gate voltage. Only those charges that fit through the spin filter (drain) finally contribute to the detected signal. The spin-field-effect transistor would represent a challenging, but at the same time fascinating stage in developing the electronics of tomorrow. Yet, as basic requirements on the path towards experimental realization, a transport channel, where spin separation is maintained over the full gate length, and an effective spin filter (drain) for spin selective detection are still to be developed. Feasible

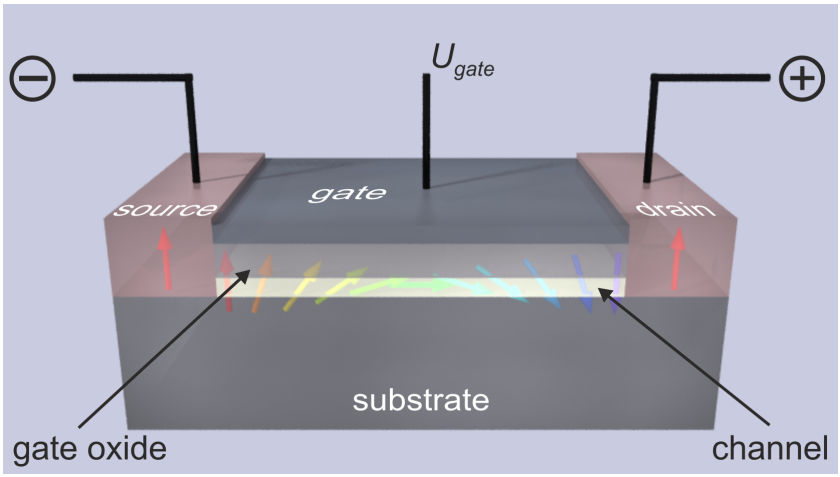

Figure 1.1: *Illustration of the spin-field-effect transistor, as proposed by S. Datta and B. Das [32]. Charges with a predefined spin orientation (arrows) are injected from the source into the channel. During their passage to the drain (spin filter) a spin precession is induced by the gate voltage* U_{gate}*, which modifies the detectable spin current.*

concepts for spin filtering in Rashba systems have been proposed in terms of a resonant tunneling setup [33], or by utilizing spin-polarized electrodes of a ferromagnetic material [34]. In addition, the Rashba coupling strength within the transport channel should be tunable by a gate field, as already shown for heterostructures [35]. Here, it would be interesting to explore, whether a surface 2DES with metallic spin-split states could be utilized for charge transport between source and drain.

Besides correlations and SOC at surfaces, the list of phenomena observed in 2DESs can still be extended by, e.g., charge density wave (CDW) phase transitions [36], massless Dirac particles in graphene [37], and metallic edge states in topological insulators [38]. Moreover, even a superconducting state has established in the very 2D limit of the dense phases of Pb/Si(111) and In/Si(111) [39]. Quite generally, the delicate choice of materials and the amount of deposited adatoms for preparing such systems are the basic parameters to precisely tune the degree of interaction. In all, the large variety of possible compositions represents a versatile *atomic construction kit*, that allows to access many of the most fascinating phenomena in low-dimensional solid state physics.

In turn, for the three 2DESs studied in this thesis, i.e., Pt/Si(111), Au/Ge(111), and Sn/Si(111) in triangular reconstructions, there exist a couple of key issues to be addressed:

- Development or validation of the structural models describing the local atomic arrangement at the surface.
- The topology of the Fermi surface (FS).
- The spin arrangement at the FS in systems with strong SOC.

- The electronic band structure with a particular focus on the degree of correlation and the ground state properties, i.e., metallic vs. insulating character.
- The influence of external (e.g., temperature T) and internal (e.g., interaction strength U) parameters on the phase diagram, i.e., possibility of phase transitions.
- The particular size of electronic correlations (Hubbard U) and their origin.
- Existence, and if present, type of a magnetically ordered ground state in a frustrated triangular lattice.
- Signatures of geometric and/or magnetic superstructures in the band structure, i.e., existence of a related band backfolding.

The particular choice of Sn/Si(111)-($\sqrt{3} \times \sqrt{3}$) as a model system to investigate correlation effects is encouraged by several studies that have reported phase transitions to distorted and/or insulating ground states in related surfaces as, e.g., in Pb/Ge(111)-($\sqrt{3}\times\sqrt{3}$) [40]. Specifically, correlations were claimed to be responsible for the formation of a Mott insulating ground state in Sn/Si(111)-($\sqrt{3} \times \sqrt{3}$) [16, 17]. However, it seems questionable, how to connect the abrupt transition from metallic to insulating behavior to a Mott-Hubbard type metal-to-insulator transition (MIT), where one would expect a rather gradual loss of spectral weight at the Fermi level for decreasing temperatures. Moreover, it remains unclear, whether the potential Mott-Hubbard ground state also involves a magnetic order, since spin frustration is a fundamental complication here. Besides such a group-IV adatom system, noble metals can be used alternatively, which involve a different electronic configuration, characterized by d and s orbitals. A key issue here is the local atomic structure, which can be notably different for related surfaces, as evidenced for the noble metal induced 2DES Pt/Si(111)-($\sqrt{3} \times \sqrt{3}$). But also the possibility of spin-separated metallic states in heavy noble metal 2D adatom systems requires further scrutiny. With this in mind, the rarely studied Au/Ge(111)-($\sqrt{3} \times \sqrt{3}$) surface is being chosen here.

The present thesis is organized as follows. Ch. 2 presents the fundamental concepts of the spin-orbit interaction (SOI) at surfaces and introduces the Hubbard model for electronic correlations. Subsequently, Ch. 3 addresses the most relevant experimental techniques utilized in the thesis, i.e., low energy electron diffraction (LEED), STM, ARPES, as well as spin- and angle-resolved photoelectron spectroscopy (SARPES). The presentation of the results starts in Ch. 4, where the preparation of high quality Si(111) and Ge(111) substrates is described. Hereafter, the characteristic atomic structure induced by deposition of Pt atoms onto Si(111) is in the focus of Ch. 5. Ch. 6 addresses the complex spin texture in Au/Ge(111)-($\sqrt{3} \times \sqrt{3}$) as a result of SOIs, while Ch. 7 is concerned with magnetic ordering and electron correlation effects in Sn/Si(111)-($\sqrt{3}\times\sqrt{3}$). Finally, a short summary and a prospect of future research goals and challenges will be given in Ch. 8.

2 Theoretical concepts

2.1 Spin-orbit interaction in crystalline solids

Of particular interest in the study of a crystalline surface, which represents a confined quantum system, are states that evolve in the bulk-projected band gap due to the lack of translational symmetry in direction perpendicular to the surface. These "surface states" exhibit a strong 2D character, since they are strictly confined within only a few atomic layers, while their wave functions quickly decay into the bulk. Accordingly, the confined layer is described as a 2DES. Here, the prime example is the L-gap state at the Au(111) surface [41]. Importantly, ARPES experiments revealed this state to be split into two subbands as a result of SOIs at the surface [20]. The prerequisite for such a splitting is a breaking of inversion symmetry, which is not given in the bulk, but at the surface, as will be discussed in detail in the following paragraphs. The realization of spin-split surface states on top of semiconducting substrates would be of high relevance for the development of spintronic applications, aiming at the manipulation of the electron spin, e.g., in the spin field-effect transistor [32, 35].

The SOI in solids is a relativistic effect, and it bears some similarities to its counterpart in the atomic potential of the nuclei. It can be understood as follows [42]. Imagine an electron traveling at the velocity $\mathbf{v}$ in an electric field $\mathbf{E}$. A Lorentz transformation turns this field into the magnetic field

$$\mathbf{B} = \frac{\gamma}{c^2}\left(\mathbf{v} \times \mathbf{E}\right) \tag{2.1}$$

within the rest frame of the electron. Here, c denotes the speed of light, and $\gamma = (1 - v^2/c^2)^{-1/2}$ accounts for the relativistic motion (typically $\gamma = 1$). This field couples to the electron spin $\boldsymbol{\sigma}$ ($\boldsymbol{\sigma}$ is a vector containing the Pauli-matrices σ_x, σ_y, and σ_z as components), which yields a Zeeman type contribution

$$\mathcal{H}_{\mathrm{SOC}} = \frac{\mu_B}{2}\mathbf{B} \cdot \boldsymbol{\sigma} = \frac{\mu_B}{2c^2}\left(\mathbf{v} \times \mathbf{E}\right) \cdot \boldsymbol{\sigma} \tag{2.2}$$

to the respective Hamiltonian (μ_B is the Bohr magneton). It becomes evident that the spin dependency in the Hamiltonian produces a splitting into two distinct spin-polarized states, as a result of the SOC.

The considerations above lead us to the question, how such a field is generated inside a solid, presupposing the absence of any external field. The answer is related to the prevailing symmetries in the crystal and their effect on the eigenvalues of a certain state.

In quantum mechanical band structure calculations each band is doubly-degenerate with respect to its spin.[1] A centrosymmetric crystal, as it is the case for the *face-centered cubic (fcc)* lattice in Au, exhibits time-reversal invariance, i.e.,

$$E(\mathbf{k},\uparrow) = E(-\mathbf{k},\downarrow), \tag{2.3}$$

which means that both momentum and spin are flipped under a time-reversal operation. Moreover, the lattice is invariant under a space inversion operation. In other words, the band structure obeys the condition

$$E(\mathbf{k},\uparrow) = E(-\mathbf{k},\uparrow). \tag{2.4}$$

Taking both equations for granted, which is indeed the case for the Au *fcc* lattice, one easily derives

$$E(\mathbf{k},\uparrow) = E(\mathbf{k},\downarrow). \tag{2.5}$$

Apparently, in centrosymmetric crystals bulk bands are Kramers degenerate, and a spin splitting is ruled out, as long as the two symmetries are intact [42]. The splitting can only be lifted, if either time-reversal symmetry is broken by an external magnetic field, or spatial inversion symmetry is no longer given. The latter applies to the class of non-centrosymmetric bulk crystals like III-V semiconductors of the zincblende type. The possibility of this bulk inversion asymmetry (BIA)-induced spin-orbit splitting was first described by Dresselhaus in 1955 [43]. It accounts for the missing symmetry for an inversion in the bulk material. The corresponding *Dresselhaus Hamiltonian* for the technical relevant case of a narrow quantum well (QW) ([001] growth direction) in a non-centrosymmetric crystal of $C_{2\nu}$ symmetry is given by

$$\mathcal{H}_D = \alpha_D \left(k_x\sigma_x - k_y\sigma_y\right). \tag{2.6}$$

The Dresselhaus parameter α_D, which determines the size of the splitting, essentially depends on the width of the QW. In addition, there exists a second contribution, caused by a structure inversion asymmetry (SIA) in the QW [19, 44], the *Rashba Hamiltonian*

$$\mathcal{H}_R = \alpha_R \left(k_x\sigma_y - k_y\sigma_x\right), \tag{2.7}$$

whose strength is defined by the Rashba parameter α_R. In other words, the asymmetry along the [001] growth direction in the QW cancels spatial inversion in the QW [31, 45]. The total SOC Hamiltonian is thus

$$\mathcal{H}_{\mathrm{SOC}} = \mathcal{H}_D + \mathcal{H}_R, \tag{2.8}$$

[1] Band structure calculations are usually based on the non-relativistic Schrödinger equation, which represents a good approximation to the problem. For an even more precise theoretical description the relativistic Dirac equation should be used instead, leading to the exact Hamiltonian.

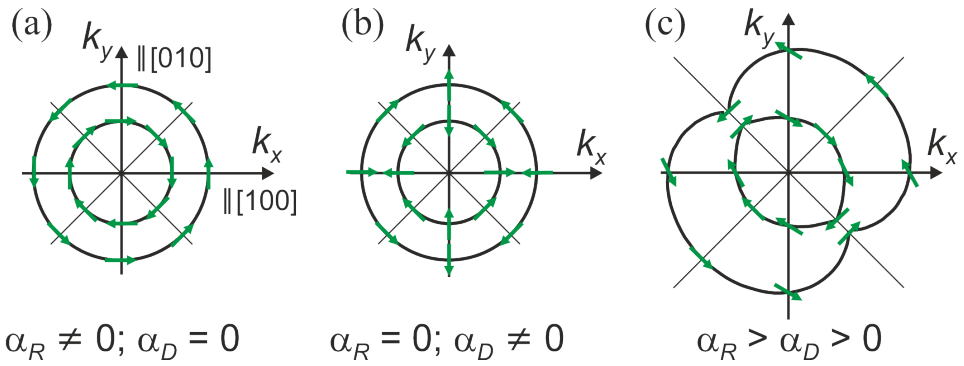

Figure 2.1: *Calculated spin orientations (green arrows) at the FS of a QW in a III-V-semiconductor with $C_{2\nu}$ symmetry, following Eq. 2.8; figure according to [46]. (a) In the case of Rashba SOI only, the spin polarization vector is always perpendicularly aligned with respect to $\mathbf{k}_\parallel$ and the potential gradient $(\partial V/\partial z)\,\hat{\mathbf{e}}_z$. (b) For Dresselhaus SOI only, this still holds for the mirror planes (diagonal lines), but strong radial in-plane rotations are found elsewhere, and the circularly revolving character is lost. (c) For both Rashba and Dresselhaus SOI at the same time, an anisotropic band splitting and a more complex spin pattern are present.*

which results in a zero-field splitting.[1] Both terms are inseparable, and their interplay is visualized in Fig. 2.1, where the eigenvalues of $\mathcal{H}_{\mathrm{SOC}}$ at the Fermi energy are plotted (calculations by S. D. Ganichev *et al.* [46]). In case of Rashba SOI only [Fig. 2.1(a)], the FS consists of two free-electron-like parabolas, equally shifted in the $\mathbf{k}_\parallel$-plane against one another. The spin is aligned in plane and is always oriented orthogonal to the momentum vector $\mathbf{k}_\parallel$, which leads to a circularly revolving spin pattern. The FS contours do not differ in the Dresselhaus-only case [Fig. 2.1(b)]. However, dramatic deviations are found concerning the spin orientation, which is now highly $\mathbf{k}_\parallel$-dependent. The spin remains in plane and perpendicular to $\mathbf{k}_\parallel$ along high symmetry directions (diagonal lines) only, while strong in-plane rotations apart from there prevail, and the circularly revolving spin pattern is lost. In the relevant case of the QW with $C_{2\nu}$ symmetric substrate [Fig. 2.1(c)] the FS is highly anisotropic. The spins remain orthogonal to $\mathbf{k}_\parallel$ in the high symmetry directions (diagonal lines) only. Away from these directions strong radial in-plane rotations are observed again, yet, with the circularly revolving character preserved. These three scenarios point at the delicate interaction of both BIA- and SIA-induced spin splittings and offer a first view on the rather complex spin geometries resulting from crystalline anisotropies. In particular, this will become relevant in the correct description of the spin texture in Au/Ge(111)-($\sqrt{3} \times \sqrt{3}$), which will be in the focus of Sec. 6.3.

The SIA-induced spin splitting also bears some technical relevance that needs to be emphasized. The Rashba parameter α_R, and in consequence the size of the splitting, can be adjusted by a gate field applied across the QW [35, 47], which points at the

[1] Linear terms in $\mathcal{H}_{\mathrm{SOC}}$ are sufficient in the case of the zincblende QW structure of $C_{2\nu}$ symmetry [46]. Higher order contributions may become necessary, if other internal fields are present. These can result from a more complex potential landscape in solids deviating from the $C_{2\nu}$ symmetry.

importance of the Rashba spin splitting for spintronic devices as the Datta-Das spin-field-effect transistor [32]. It should also be noted that the realization of a non-ballistic spin-field-effect transistor has been proposed for the limiting case of $\alpha_R = \alpha_D$ [48].

Spin-orbit interaction at surfaces

Following this introduction to the SOI in non-centrosymmetric bulk crystals, we will now return to crystalline surfaces as object of investigation in this thesis. Here, the abrupt transition from the ordered crystal into the vacuum breaks the spatial inversion symmetry (Eq. 2.4), which thus should lead to a SIA related SOC. Recalling the spin splitting of the Au(111) L-gap surface state, which is observed in absence of an external field, the SIA type SOC is the only plausible mechanism to lift the spin-degeneracy here.

An easy and convincing free-electron model that describes the effect of SOI at the surface is the "Rashba model" [19], which bases on the assumption of a free-electron-like surface state with parabolic dispersion. The corresponding kinetic energy part of the Hamiltonian

$$\mathcal{H}_{\mathrm{kin}} = \sigma_0 \left(E_0 - \frac{\hbar^2}{2m_e^*} \nabla^2 \right) \tag{2.9}$$

includes the unity spin matrix σ_0, which still leaves the band spin-degenerate up to here [49]. E_0 refers to the band minimum, as shown in Fig. 2.2, and m_e^* is the effective electron mass. The electrons are only free to move within the surface plane, yet being confined in their motion along the surface normal by the potential $V = V_\perp$ in this model, i.e., $\mathbf{k} = \mathbf{k}_\parallel = \mathbf{k}_x + \mathbf{k}_y$. Thus, the relevant potential gradient is oriented perpendicular

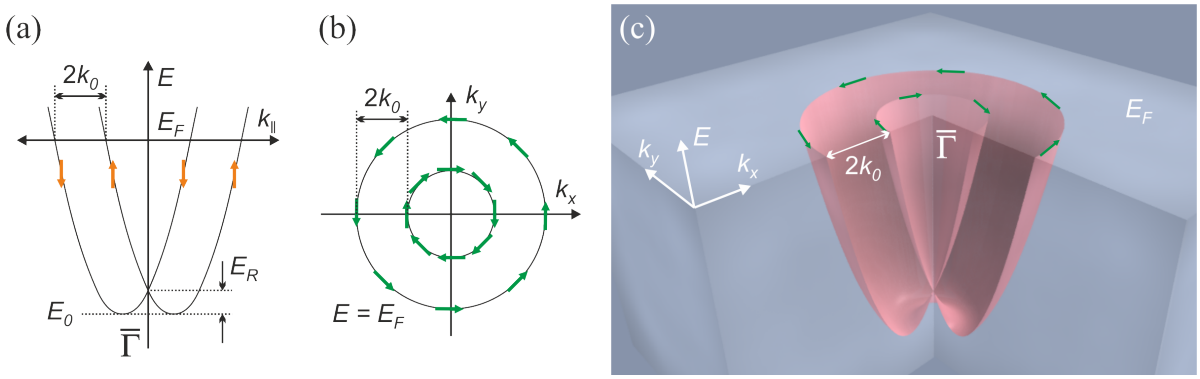

Figure 2.2: *(a) Spin-orbit band splitting in the Rashba model for a free-electron-like parabolic dispersion $E(k_\parallel)$ in the 2D surface plane. The spin-degeneracy of the initial parabola is lifted due to SOIs, and two spin-polarized bands divided by a splitting of $2k_0$ are observable. The Rashba energy E_R is defined as energy offset between the band crossing at the $\bar{\Gamma}$ symmetry line and the band minimum E_0. The orange arrows do only indicate opposite spin orientations, but are not to be confused with their geometrical orientation. (b) FS for the same band structure as in (a). The spin polarization vector (green arrows) is always perpendicularly aligned with $\mathbf{k}_\parallel = \mathbf{k}_x + \mathbf{k}_y$ and $(\partial V/\partial z)\hat{\mathbf{e}}_z$. (c) 3D visualization of the the Rashba effect for a free-electron-like dispersion.*

to the plane: $\nabla V = \partial V/\partial z\, \hat{\mathbf{e}}_z$ (unit vector $\hat{\mathbf{e}}_z$ along surface normal). Besides providing electron confinement, ∇V effectively controls the strength of the SOI, which is described by the *Rashba parameter*

$$\alpha_R = \frac{\hbar^2 k_0}{m_e^*}, \tag{2.10}$$

with k_0 representing the magnitude of the spin splitting in momentum. In particular, this involves the atomic contribution

$$\alpha_R \propto \int \mathrm{d}\mathbf{r}\, \frac{\partial V}{\partial z}\, |\Psi(\mathbf{r})|^2 \tag{2.11}$$

within each layer of the crystal lattice to which the surface state wave function $\Psi(\mathbf{r})$ is extended [50, 51]. The antisymmetric Coulomb gradient $\partial V/\partial z$ is given by the average field of nucleus and electrons, and thus, it is largest close to the atomic cores. Additionally, a notable asymmetry close to the core along z in the distribution of the wave function $\Psi(\mathbf{r})$ is necessary to induce the splitting. The total band shift observed in the experiment, is then obtained by summing over all contributing layers [51]. The relevant Hamiltonian including the SOI in this model has already been introduced in Eq. 2.7. After a simple transformation the complete Hamiltonian is derived together with Eq. 2.9 as

$$\mathcal{H} = \mathcal{H}_{\mathrm{kin}} + \mathcal{H}_R = \sigma_0 \left(E_0 - \frac{\hbar^2}{2m_e^*} \nabla^2 \right) - \alpha_R \left(i\sigma_y \frac{\partial}{\partial x} - i\sigma_x \frac{\partial}{\partial y} \right). \tag{2.12}$$

It can be solved analytically, and one gains the eigenstates

$$E_{\pm}(\mathbf{k}_\parallel) = E_0 + \frac{\hbar \mathbf{k}_\parallel^2}{2m_e^*} \pm \alpha_R \left| \mathbf{k}_\parallel \right|, \tag{2.13}$$

which describe the spin-split solution of the parabolic free-electron-like dispersion, see Fig. 2.2. The size of the splitting $\Delta k = 2k_0$ in momentum and $\Delta E = 2\alpha_R \left| \mathbf{k}_\parallel \right|$ in energy is reflected in the Rashba parameter (Eq. 2.10) and in the Rashba energy defined as $E_R = \hbar^2 k_0^2/(2m_e^*)$. It contains two contributions: **i)** the intra-atomic SOI, which is large in heavy element surfaces as, e.g., Au [20, 52], W [53], and Bi [21, 54], and **ii)** the strength of the potential gradient $\partial V/\partial z$. In the Datta-Das spin-field effect transistor Δk corresponds to the induced phase shift between source and drain, and thus may be tuned by either adjusting i) or ii) [32]. The two non-degenerate branches are fully spin-polarized with opposite orientation of the spin polarization vector, i.e., $\mathbf{P}(\mathbf{k}_\parallel) = -\mathbf{P}(-\mathbf{k}_\parallel)$ and have an in-plane spin alignment with circularly revolving character (see also Sec. 3.3.2, p. 53 ff.).

The "Rashba model" is capable to grasp and reproduce the experimental dispersion relation in Au(111) quite well. However, it underestimates the size of the splitting, which is most likely ascribed to a much larger potential gradient in the real system, and should be more exactly discussed within a tight-binding approach [42]. Moreover, several recent publications, basing on spin-resolved photoemission and *ab initio* band

structure calculations, have pointed out that a pure Rashba scenario must be regarded as an exceptional case [22, 24, 25], which is a good approximation to the surface states of single crystals like Au(111) only. More generally, non-perpendicular and non-isotropic electric field gradients, as well as in-plane asymmetries in the wavefunction distribution contribute to the spin pattern of heavy adatom spin-split surface states. Here, strong deviations from the "Rashba" type in-plane and orthogonal to $\mathbf{k}_{\parallel}$ spin alignment do occur. This may favor, e.g., momentum-dependent out-of-plane undulations of the spin polarization vector at the FS [22, 28]. It has thus been suggested to extend the Rashba Hamiltonian (contained in Eq. 2.12) by Dresselhaus SOC terms of higher order in k to achieve a more adequate theoretical description of the complex spin patterns in "real-world" surface systems [27, 55]. This idea will be seized again in Sec. 6.3, where the SOC in Au/Ge(111)-($\sqrt{3} \times \sqrt{3}$) is scrutinized.

2.2 The Mott-Hubbard insulator

The fact that some crystalline materials show metallic (conducting) behavior, while others are insulating, represents a fascinating and fundamental issue in solid state physics. The development of band theories then provided insight into the electronic properties of many materials with various elemental compositions. The basic prerequisite of an insulator is the existence of a band gap, which separates unoccupied from occupied states (conduction band from valence band), with the Fermi energy ϵ_F situated in between. Metallic materials on the other hand are characterized by a partly filled band. In this frame the *nearly-free electron approximation* has proved to classify many solid state materials with respect to their conductivity quite successfully. In particular, this applies to the electronic structure of metals in the vicinity of ϵ_F, where the electrons are well screened from one another (screening length $\sim k_F^{-1} \approx$ Å). This behavior is well described within Landau's Fermi liquid theory (see also Sec. 3.3.1) [56].

Yet, the band theory fails to describe non-crystalline solids or those with defects. In addition, it turned out that for some materials, in particular those with strongly localized and partly filled outer d- and f-shells, band theory predicts metallic behavior in contrast to experimental observation. In this regard, it was pointed out that the insulator NiO would be metallic according to band theories, in contrast to experimental observation [57]. Today, other intriguing examples, where band theory actually fails, are high-temperature superconductors [15] and doped fullerenes [58]. N. F. Mott argued that electrons in transition metal oxides are subject to strong local Coulomb repulsions and may no longer be considered free, as assumed in the nearly-free electron model [59]. This postulation has prevailed in solid state physics [60–62] and has led to a robust many-body description in the *Hubbard model* [63–65]. This is the most widely studied lattice fermion model in the solid state physical community today. At the same time it includes the simplest many-body Hamiltonian which is capable of a profound description of the interplay between kinetic energy and Coulomb repulsions.

The Hubbard model

The Hubbard model, which will be introduced in the following on the basis of Refs. 66 and 67, relies on two fundamental assumptions: **i)** interactions are local, i.e., restricted to a single lattice site, and **ii)** there exists only one band at half filling.[1] Although for "real-world" materials this might seem too much simplified at first glance, its accurate description of transition-metal insulators, in particular regarding their low energy and low temperature (LT) properties, strongly supports its potential. Actually, in many cases a one band situation is found at the Fermi level. An illustrative way to visualize the Hubbard model is given by the hypothetical case of a one-dimensional (1D) chain of hydrogen atoms with L lattice sites and an interatomic spacing a, as it is shown in Fig. 2.3(a). Each atom hosts one electron with a certain orbital overlap to its nearest-neighbors. According to the *tight-binding model* of band theory, we deal with a half-filled band in a D-dimensional cubic lattice ($D = 1$ here) with the tight-binding energy

$$\epsilon(\mathbf{k}) = -2t \sum_{j=1}^{D} \cos \mathbf{k}_j a, \tag{2.14}$$

which is typically centered at the zero energy line. Therein, t denotes the tight-binding matrix element, which is related to the probability of an electron to hop from its initial lattice site to the nearest-neighbor site. According to Eq. 2.14, the bandwidth is given by $W = 4Dt$. By increasing a, the orbital overlap, and hence, also the bandwidth become smaller. However, even for a large spacing, where the chain may be more suitably regarded as an array of isolated atoms, the half-filled band situation survives, which is against common sense. It becomes evident that such a metallic situation is no longer valid, and the tight-binding model is no more applicable.

This insufficiency is overcome in the Hubbard model, according to which an electron has to "pay" the Coulomb energy U (the so-called "Hubbard U") after hopping to its singly occupied nearest-neighbor site. For a critical spacing a, and thus a critical bandwidth W, the energy gain by hopping will be smaller than the energy consumption by overcoming the on-site Coulomb repulsion U on a neighboring atom. These considerations are reflected in the main formula within this model, the Hubbard Hamiltonian

$$\mathcal{H} = \mathcal{H}_{\text{band}} + \mathcal{H}_U = -t \sum_{\langle \mathbf{j},\mathbf{l} \rangle} \sum_{\sigma} \left(c^{\dagger}_{\mathbf{j}\sigma} c_{\mathbf{l}\sigma} + c^{\dagger}_{\mathbf{l}\sigma} c_{\mathbf{j}\sigma} \right) + U \sum_{\mathbf{j}} \hat{n}_{\mathbf{j}\uparrow} \hat{n}_{\mathbf{j}\downarrow}. \tag{2.15}$$

It describes the interplay between the kinetic energy band term $\mathcal{H}_{\text{band}}$ and the Coulomb term $\mathcal{H}_U$ in second quantization [68], which is a suitable and convenient approach for quantum many-particle problems. The first term deals with the electron hopping between the neighboring lattice sites $\mathbf{j}$ and $\mathbf{l}$ in both directions along the chain, counting each pair once. Therein, the operators $c^{\dagger}_{\mathbf{j}\sigma}$ and $c^{\dagger}_{\mathbf{l}\sigma}$ ($c_{\mathbf{j}\sigma}$ and $c_{\mathbf{l}\sigma}$) create (annihilate) an

[1] With respect to the second assumption, the model is often specified as *one-band Hubbard model* in the literature.

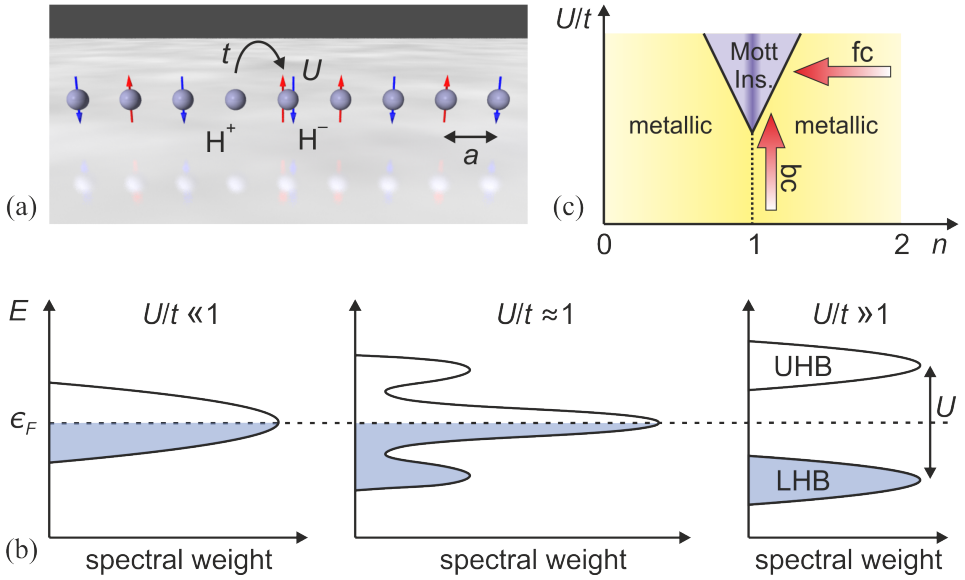

Figure 2.3: *(a) Illustration of the Hubbard model in 1D on the basis of an atomic chain of hydrogen atoms with spacing a and single occupancy. Charge transport requires an electron to hop from its initial atom to a neighboring one (energy gain t), leading to double occupancy with an energy cost of U. (b) Spectral weight distribution for the three cases $U \ll t$ (left), $U \approx t$ (middle), and $U \gg t$ (right), showing the transition from the metallic to the Mott insulating phase. For further details, refer to text. (c) Phase diagram of the Mott MIT (band filling $0 \leq n \leq 2$ with half filling at $n = 1$); according to [11]. In the non-correlated case at half filling the system is stabilized in its metallic phase. With increasing U/t the system exhibits a bandwidth-controlled (bc) MIT into the Mott insulating phase at $n = 1$. By changing the band filling n a filling-controlled (fc) MIT is induced. The purple area besides the $n = 1$ line indicates the unstable fluctuation regime.*

electron in the Wannier states $\phi(\mathbf{r} - \mathbf{R}_j)$ and $\phi(\mathbf{r} - \mathbf{R}_l)$, which are the Fourier transforms of the Bloch states at the lattice sites $\mathbf{j}$ and $\mathbf{l}$, respectively. The Wannier states represent the local orbitals needed to correctly incorporate the postulation of purely local interactions. The second term $\mathcal{H}_U$ with the number operator for double occupancy $\sum_{\mathbf{j}} \hat{n}_{\mathbf{j}\uparrow}\hat{n}_{\mathbf{j}\downarrow}$ ($\hat{n}_{\mathbf{j}\sigma} = c^{\dagger}_{\mathbf{j}\sigma}c_{\mathbf{j}\sigma}$) accounts for the local interaction U at each site. Eq. 2.15 shall now be discussed for the limiting cases of absent and strong correlations, as well as the intermediate regime.

$U \ll t$**:** In this non-correlated case there is an equal probability of 25 % to find a lattice site either occupied by a ↑- or a ↓-electron, whereas neutral lattice sites will be found at 50 % probability.[1] This is a consequence of the free electron motion in the absense of any on-site repulsion, making the model system metallic. This results in the highly delocalized scenario of a half-filled band with equal spectral weight distribution in the density of states (DOS) around the Fermi level ϵ_F,

[1]The Hubbard model totally disregards the exchange interaction. Thus, no kind of magnetic order is in favor.

as shown in Fig. 2.3(b) on the left.[1]

$U \gg t$**:** The strongly correlated case is characterized by a high degree of localization, i.e., by single electrons on every lattice site. Doubly occupied lattice sites are prohibited due to the strong Coulomb repulsion. Therefore, electron transport is not possible, and the system exhibits insulating behavior, as shown in the right of Fig. 2.3(b). The spectral weight is redistributed to lower and higher energies, forming the lower Hubbard band (LHB) and the upper Hubbard band (UHB), respectively. These bands are separated by the Hubbard U, which thus corresponds to the energy difference in removing an electron from a single occupied site and adding it to a single occupied neighboring site. It has to be noted that the very existence of the UHB is a pure consequence of the electrons in the LHB. In contrast to a band in a conventional insulator, which is completely filled for $N = 2L$ electrons, the LHB and the UHB can carry only $N = L$ electrons each.

$U \approx t$**:** In the intermediate regime spectral weight is already redistributed from ϵ_F into the incoherent parts on both sides of the energy scale, forming the precursors of the Hubbard bands. These exhibit a finite width due to scattering processes which are not accounted for in the Hubbard model. Yet, a sharp QP peak (coherent part of the spectral function) still remains at the Fermi level (see also Sec. 3.3.1). This applies to the case of a correlated metal, as described within Landau's Fermi liquid theory [56].

We will now leave this simple 1D scenario and turn to a more generalized interpretation of both terms in Eq. 2.15. At first, the $\mathcal{H}_U$ term shall be disregarded. $\mathcal{H}_{\text{band}}$ describes the gain in energy associated with the hopping of an electron from its initial site to the nearest-neighbor site. So far, this term is not diagonal in the basis of the Wannier orbitals. This is achieved by a Fourier transform, leading to its diagonalized k-space representation

$$\mathcal{H}_{\text{band}} = \sum_{\mathbf{k}\sigma} \epsilon_{\mathbf{k}} \hat{n}_{\mathbf{k}\sigma}, \tag{2.16}$$

with the energy of the Bloch wave defined in Eq. 2.14. As has already been pointed out above, this ($U \ll t$) scenario involves a half-filled metallic band, and the corresponding metallic ground state

$$|\Psi_{\text{met}}\rangle = \prod_{\mathbf{k}}^{\epsilon_{\mathbf{k}}<\epsilon_F} c^\dagger_{\mathbf{k},\uparrow} c^\dagger_{\mathbf{k},\downarrow} |0\rangle \tag{2.17}$$

describes a *Fermi sea*, filled with electrons up to the Fermi level ϵ_F. Now $\mathcal{H}_{\text{band}}$ will be disregarded, and on-site Coulomb interactions of the electrons at $\mathbf{r}_1$ and $\mathbf{r}_2$ with respect

[1] For interacting electron systems the DOS should be replaced by the spectral function $A(\mathbf{k}, \omega)$. For futher details see Sec. 3.3.1.

to the the lattice site $\mathbf{R}_j$ are considered by

$$U = \int \mathrm{d}\mathbf{r}_1 \int \mathrm{d}\mathbf{r}_2 \left|\phi\left(\mathbf{r}_1 - \mathbf{R}_j\right)\right|^2 \frac{e^2}{\left|\mathbf{r}_1 - \mathbf{r}_2\right|} \left|\phi\left(\mathbf{r}_2 - \mathbf{R}_j\right)\right|^2 . \tag{2.18}$$

Interactions with neighboring lattice site electrons are neglected, which represents a valid approximation, since the long-range part of the Coulomb interaction is effectively screened at the distance of the neighboring sites. The corresponding ground state $|\Psi_{\mathrm{ins}}\rangle$ describes the single occupancy situation in the ($U \gg t$) case. Applying the Hamiltonian in Eq. 2.15 to $|\Psi_{\mathrm{met}}\rangle$ and $|\Psi_{\mathrm{ins}}\rangle$ returns the respective band energies $\epsilon_{\mathrm{met}} = -16t/\pi^2 + U/4$ and $\epsilon_{\mathrm{ins}} = 0$. As both states correspond to the limiting cases $U \ll t$ and $U \gg t$, there must exist a critical value of the U/t-ratio for a transition between metal and insulator.

As described before, the insulating phase in the Hubbard model is only formed above the critical U/t-ratio and at half filling, i.e., with one electron per lattice site. This can be plotted as a phase diagram of the electron density $n = N/L$ (N as total number of electrons) in dependence of U/t, shown in Fig. 2.3(c) [11]. Deviations from half filling ($n = 1$), i.e., by either adding or removing an electron from the system, lead to a metallic situation. For sufficiently high correlations one would end up in the fluctuation regime then (blue shaded area), which is generally assumed metallic, but shows a strong coupling to the insulating phase. The arrows indicate that there are in principle two different possibilities to induce a Mott MIT. The first is the bandwidth-controlled (bc) MIT, which relates to the U/t-ratio. It is triggered by adjusting the bandwidth W ($\propto t$), which may experimentally be achieved by a change of the lattice constant under high pressure. The second option is the filling-controlled (fc) MIT, where the transition is actuated upon a change in the band filling. Experimentally, this may be realized by electron or hole doping or by temperature (T) adjustments in the case of semiconductor-based systems. In particular, for Sn/Si(111)-($\sqrt{3} \times \sqrt{3}$) the influence of U and T on the reversible transition from metal to insulator is scrutinized in detail in Sec. 7.2.4.

With respect to symmetries, the Hubbard model is spin-rotational and time-reversal invariant [66]. Electron-hole invariance is generally not given with exception of bipartite lattices. Importantly, in the case of magnetic ordering the spin-rotational invariance is spontaneously broken, which is relevant for the magnetism in 2D surfaces as, e.g., the Sn/Si(111)-($\sqrt{3} \times \sqrt{3}$) system, being addressed in detail in Ch. 7.

Spin frustration in the triangular lattice

Going beyond the Hubbard model with the inclusion of exchange interactions, an antiferromagnetic (AFM) ordering of the spins will be favored. This follows the general tendency of the system to lower its inner energy, and it is thus the most likely magnetic order in 1D chain and 2D square lattices. However, in triangular lattices this leads to *spin frustration*, which means an *"inability to satisfy the competing exchange interactions"* between neighboring atomic sites in a magnetic system [69]. To illustrate this, Fig. 2.4(a) shows a triangular lattice with electrons on each site having their spins

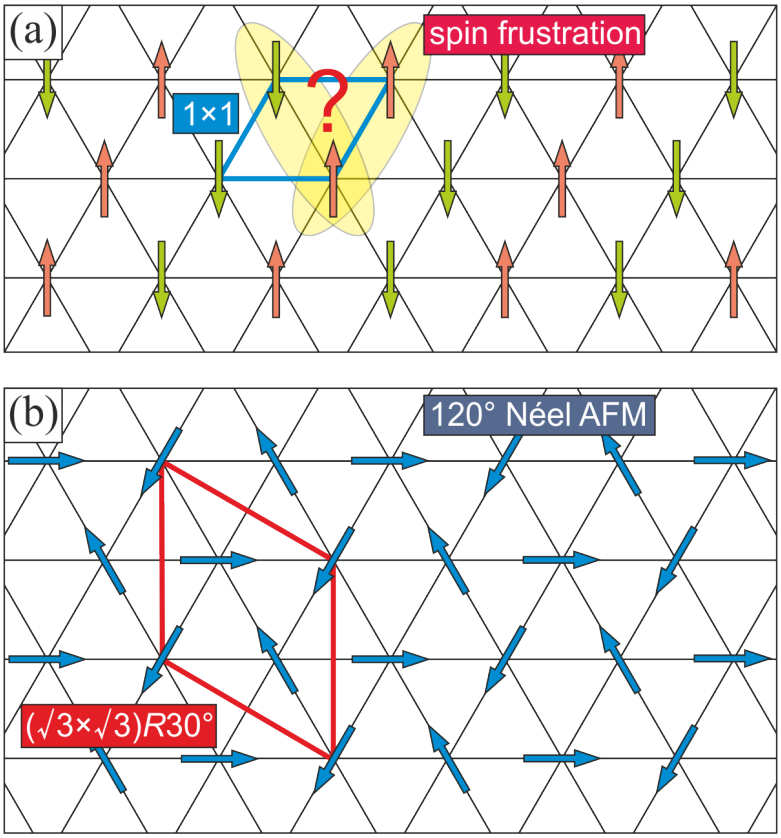

Figure 2.4: *Visualization of spin frustration in a triangular lattice. (a) An AFM ordering, as the favorable alignment of the electron spins in 2D lattices, is only realized within each single row here. For the two nearest-neighbors in adjacent rows this does not work any more, and the spins become "frustrated". Thus, long-range AFM ordering is suppressed. (b) 120° Néel AFM order. The electron spins are rotated by 120° against one another. This type of 2D AF represents a possible ordered ground state despite spin frustration. Unit cells are given as blue and red parallelograms in (a) and (b), respectively.*

aligned antiparallel to its nearest-neighbor in the same row. This works as long as one regards only a single row, but each electron has also two additional nearest-neighbors in the adjacent row. Thus, the spins become "frustrated", since they cannot take an orientation antiparallel to all neighbors at the same time. A possible way out is the *120° Néel AFM order* depicted in Fig. 2.4(b), where the energy is minimized in rotating the spins by 120° against one another with a resulting zero net spin per unit cell [70]. This new magnetic unit cell is enlarged by a factor of $\sqrt{3}$ and rotated by 30°. Spin frustration plays a crucial role in the magnetic and electronic properties of a variety of 2D surface systems. In particular, these include the $(\sqrt{3} \times \sqrt{3})$ surface reconstructions of dilute group-IV adlayers on top of Si(111) and Ge(111), as will be addressed later in Ch. 7.

Finally, it shall be noted that one has to distinguish between the Mott-Hubbard insulator and the Mott-Heisenberg insulator. In the latter an exchange-related spin excitation gap occurs below the Néel-temperature T_N. Its size is typically much smaller than the Hubbard gap ($k_B T_N \ll U$). Both phases may coexist, yet due to its small size, the spin excitation gap is superimposed by the Hubbard gap.

From an experimental point of view, multiple examples of Mott insulators are known in the literature today. These include a couple of transition metal oxides as, e.g., Ti_2O_3, V_2O_3, Cr_2O_3, and their most prominent representative NiO [11, 60, 71]. Importantly, also the 2D surface systems K/Si(111)-B-($\sqrt{3} \times \sqrt{3}$) and 6H-SiC(0001)-($\sqrt{3} \times \sqrt{3}$) are experimentally verified Mott insulators at room temperature (RT) with $U_{\text{eff}} = 1.3\,\text{eV}$ and $U_{\text{eff}} = 2.3\,\text{eV}$, respectively [12, 13, 72]. Theoretically, 2D Mott-Hubbard insulators have been treated by several different approaches. Among these, the LDA+U introduces an extra intra-atomic interaction, that acts on the localized d and f electrons as a local replacement of the local density approximation (LDA) [73]. Alternatively, combinations of the *ab initio* LDA and dedicated many-body techniques, such as the dynamical mean field theory (DMFT) and the dynamical cluster approximation (DCA), have been utilized [74, H7]. The respective reliability of these methods in approximating the correlated ground state physics will be discussed later in Sec. 7.2.4 for the model system Sn/Si(111)-($\sqrt{3} \times \sqrt{3}$).

3 Experimental techniques

3.1 Low energy electron diffraction

Among the diverse diffraction techniques, low energy electron diffraction (LEED) has developed to an instrument of choice for a quick analysis of lattice periodicities on crystalline surfaces. Moreover, it provides information on surface disorder and on the atomic arrangement in the unit cell (I/V-LEED).

The LEED technique bases on the wave nature of electrons [75], where the momentum p of a particle is related to its wavelength λ by $\lambda = h/p$, with h as Planck's constant. The general prerequisites for electron diffraction experiments in high quality comprise an ultra high vacuum (UHV) host system, providing a sufficiently low pressure ($\sim 10^{-10}$ mbar), but also preparation techniques for clean and well-ordered surfaces. Here, the requirement of an UHV environment is mainly due to two reasons. First, a large mean free path of the probe electrons is necessary for an undisturbed experiment. Second, a low adsorption rate for rest gas atoms and molecules is needed in order to maintain clean surfaces, at least on the timescale of the measurement.

Usually, LEED is performed at energies from $E_{\text{kin}} = 20\,\text{eV}$ to $E_{\text{kin}} = 500\,\text{eV}$ (*LEED working range*) [76]. According to L. de Broglie, this relates to a particle wave length in the order of atomic distances ($\sim$ Å). The wave length is further easily tunable by adjusting the electron kinetic energy, a possibility missing in conventional x-ray diffraction experiments. However, the main difference between particle waves and x-ray waves lies in their different way of interaction with matter. Electrons, as charged particles, are strongly affected by the crystalline potentials at the surface, thus, penetration depths are rather small. In particular, for very low energies ($< 20\,\text{eV}$) the interaction with phonons and the generation of electron-hole pairs are the main contributions to inelastic electron scattering [77]. Yet, plasmon excitations represent the most disruptive factor for escaping electrons at the relevant energies in LEED. The corresponding cross section has a maximum above the typical plasmon energies (20 eV), and consequently, one observes a minimum in the electron's mean free path here. For energies larger than 200 eV, plasmon excitations are less probable, which results in an enhanced escape depth again. Such inelastically scattered electrons give rise to a disturbing continuous background in LEED and also in photoelectron spectroscopy (PES) experiments. Interestingly, the mean free path of electrons inside a solid is largely independent of the elemental composition of the crystal. This relies on the fact that the valence electrons in solids are often well described as a nearly-free electron gas. Then, the plasma frequency, which primarily

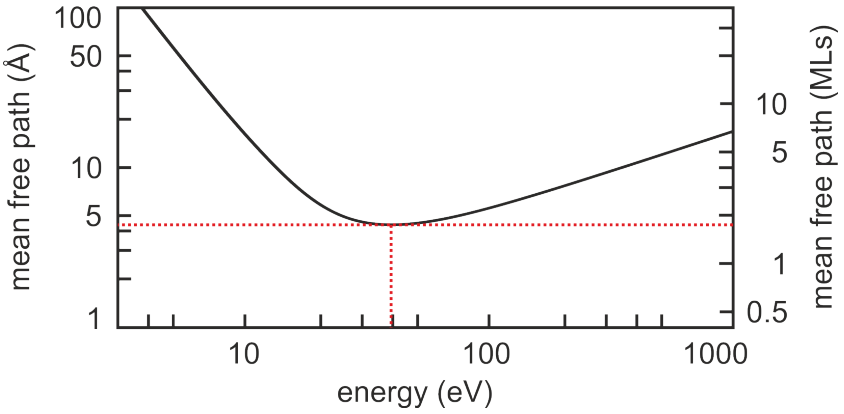

Figure 3.1: *Universal curve. Inelastic electron mean free path inside a crystal in dependence of the kinetic energy; according to Ref. 78. The general trend of the graph is valid for all elemental compositions of a crystal with only slight variations.*

determines the electron's mean free path, does rely on the electron density only. This in turn is roughly equal for all materials. Therefore, the dependency of the mean free path on the electron energy is known as *universal curve* [78], being depicted in Fig. 3.1. It exhibits a minimum for electrons at $E_{\mathrm{kin}} \approx 40\,\mathrm{eV}$ with a penetration depth of about 4–5 Å. For the working range of LEED, one deals with a mean free path between ≈ 5 and $\approx 10\,\text{Å}$, which relates to $\approx 2-5$ monolayers and reflects the surface sensitivity of this method.

3.1.1 Theoretical description of low energy electron diffraction

With the increased utilization of LEED first theories were developed to explain experimentally obtained LEED patterns. An elemental approach is given by the *geometric theory*, simply relying on Laue's conditions of diffraction at a crystal. Yet, intensity modulations in the LEED pattern are not explained therein. These are included in the *kinematic theory*, which is adopted from x-ray diffraction and relies on a plane wave approach, however, with the neglection of multiple scattering events. The kinematic theory is suitable for most cases. Nevertheless, a more differentiated analysis, e.g., for the determination of atomic arrangements, requires a more comprehensive approach, which is finally provided by the *dynamic theory*.

Geometric theory

The geometric theory of LEED is the simplest approach towards the interpretation of LEED data. It relies on Laue's condition of diffraction and is a reliable source for the prediction of LEED spot positions. However, it neglects differences in spot intensities, as well as inelastic and multiple scattering processes.

Here, elastic scattering at a 2D surface lattice with *in-plane* basis vectors $\mathbf{a}_1$ and $\mathbf{a}_2$

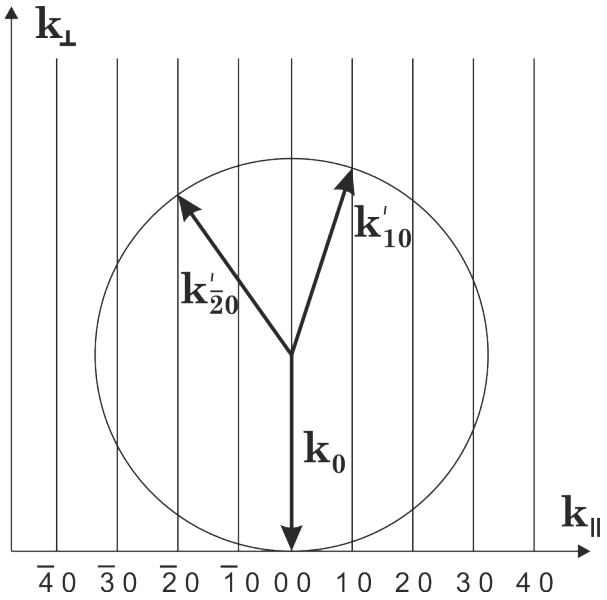

Figure 3.2: *Ewald sphere construction for the determination of diffraction peaks on a 2D lattice. Laue's conditions (Eq. 3.1) are fulfilled for all diffracted wave vectors* $\mathbf{k}'$*, pointing at intersection points of sphere and reciprocal lattice rods.*

is considered. The perpendicular vector $\mathbf{a}_3$ is infinitely large due to the constriction to only one diffraction layer. The reciprocal lattice is then defined by the basis vectors $\mathbf{a}_1^*$ and $\mathbf{a}_2^*$ parallel to the surface plane and the perpendicular vector $\mathbf{a}_3^*$, which is infinitely small. Thus, in vertical direction the reciprocal lattice consists of rods rather than single points. Now let us consider a plane wave with momentum $\mathbf{k}_0$ in normal incidence which is elastically scattered at each single point of the lattice. The resulting waves with momentum $\mathbf{k}'$ interfere in dependence of their path difference following Laue's condition. In the 2D case these are

$$(\mathbf{k}_0 - \mathbf{k}') \cdot \mathbf{a}_1 = 2\pi m \quad \text{and} \quad (\mathbf{k}_0 - \mathbf{k}') \cdot \mathbf{a}_2 = 2\pi n, \tag{3.1}$$

with m and n being integer numbers. The solution of Laue's equations is easily obtained with the *Ewald sphere construction*, which is shown in Fig. 3.2 as a 2D representation along one in-plane axis $\mathbf{k}_\parallel$ and the vertical axis $\mathbf{k}_\perp$. The wave vector $\mathbf{k}_0$ is oriented perpendicular to the surface, with its length defined by the kinetic energy of the electrons. In drawing a sphere around the origin of $\mathbf{k}_0$, all possible diffracted waves are defined by $\mathbf{k}'$ pointing on locations at the skin of the sphere. According to Eq. 3.1, only those at intersection points with the k-space rods lead to constructive interference and thus, to intensity spots in the LEED pattern. For small energies only a few rods lie within the sphere. With an increase in energy, the radius of the sphere becomes larger, and Laue's conditions are fulfilled for more diffracted beams, giving rise to higher order spots observable in experiment. All intensity maxima gravitate towards the static direct reflection (0 0) spot for increasing kinetic energies [79].

Kinematic theory

The kinematic theory of LEED relies on the assumption of a weak interaction between electrons and matter, as it is also the case for x-rays. Therefore, only single scattering events are taken into account, with full neglection of multiple scattering. In general, a good approximation to experimental LEED patterns is given, including the position and intensity of single spots.

The incident electron is described by a plane wave

$$\Psi^0 = \Psi_0 \cdot e^{i\mathbf{k}_0 \cdot \mathbf{r}} \tag{3.2}$$

with the electron momentum $\mathbf{k}_0$ [79]. After a single scattering event one may observe, at a fixed position $\mathbf{R}$ in space, the scattered wave

$$\Psi = \left(\Psi_0 \cdot \frac{e^{i\mathbf{k}' \cdot \mathbf{R}}}{\mathbf{R}} \right) \cdot f_j(\mathbf{k}_0, \mathbf{k}') e^{i(\mathbf{k}' - \mathbf{k}_0) \cdot \mathbf{R}_j}, \tag{3.3}$$

originating from a point scatterer j located at $\mathbf{R}_j$ in the crystal. Herein, $\mathbf{k}'$ is the momentum of the scattered wave, and f_j is the atomic scattering factor. The argument of the exponential function on the right accounts for a phase shift between incident and scattered wave. In an augmented view, scattering occurs at all points of a 2D periodic lattice, and the total scattered wave is a superposition of the waves from all single scatterers. Therefore, f_j may be replaced by the *structure factor* F, which sums over the atomic scattering factors within a unit cell. In addition, the phase shift in Eq. 3.3 may be included in the *lattice factor* G, which is a quantity that depends on the lattice periodicity and the momentum vectors $\mathbf{k}_0$ and $\mathbf{k}'$. In summary, the scattered wave function

$$\Psi \propto F \cdot G \tag{3.4}$$

simply depends on these two factors. In LEED, where the intensity

$$I \propto |\Psi|^2 \propto |F|^2 \cdot |G|^2 \tag{3.5}$$

of the diffracted electron beam is detected, the phase information is lost [79]. Thus, the wave function is not directly accessible in the experiment.

In this way, the kinematic theory is able to predict LEED spot positions and intensities at an adequate level. Nevertheless, it fails at the important task of atomic structure determination by the analysis of LEED spot intensities as a function of the kinetic energy of the incident electrons (i.e., the interpretation of LEED I/V-curves).

Dynamic theory

The dynamic theory of LEED has been introduced in order to exclude the shortcomings of the kinematic theory. In contrast to x-ray diffraction, electrons exhibit a largely

enhanced interaction with matter, thus leading to a high probability of inelastic and multiple scattering. The inclusion of both effects allows determining the atomic structure and not only the periodicity of a crystal. Here, one may not simply evaluate the Fourier transform of the obtained reciprocal lattice, since the phase information is missing in the intensity signal. Instead, the dependency of the spot intensities (I) on the kinetic energy (V) of the incident electrons is recorded as an I/V-curve. Structural information is then obtained by postulation of a suitable structural model and calculating theoretical LEED I/V-curves, which are compared with the measured curves. The more accurately the experimental findings are reproduced, the more probable is the validity of the underlying structural model. Such calculations are repeated until a reliable agreement is achieved. Dynamical LEED has successfully been used, e.g., in the determination of the structural model of Au/Ge(111)-($\sqrt{3} \times \sqrt{3}$) [80], which is in the focus of Sec. 6.1.1.

In general, the dynamic theory includes four basic parameters which have not been accounted for in the kinematic theory [79]:

- The scattering potential of the individual atoms is considered as a local approximation in form of atomic core orbitals.
- The inner potential of the crystal is included to account for the reduced potential energy of electrons inside a crystal.
- Inelastic scattering, which is primarily due to plasmonic excitations.
- The temperature dependence of the LEED spot intensities is considered by introducing a Debye-Waller factor, similarly as in x-ray diffraction.

For a detailed description of the dynamical theory, which is beyond the scope of this section, the reader is referred to Refs. 76 and 79.

3.1.2 Low energy electron diffraction: Instrumentation

Today, most commercially available LEED optics share a common concept in design, which is schematically shown in Fig. 3.3. It consists of an electron gun, a detection system for the scattered electrons, and it also requires a goniometer holding the sample, which allows changing the angle of incidence of the electron beam. The gun includes the filament, typically made of LaB_6, a Wehnelt cylinder for beam profile control, and a lens system for beam focusing. By this means, thermally emitted electrons from the filament are shaped to an intense and monochromatized (energy spread $\Delta E \approx 0.5\,\mathrm{eV}$) electron beam of $\approx 1\,\mathrm{mm}$ in diameter [76]. The coherence width of electron waves typically ranges from 20 to 50 nm [76]. Therefore, on an ideal sample an area of uniform periodicity should exceed this order of size. Otherwise, a spot profile broadening will be indicative of a lack of long-range order. Moreover, defect-disturbed or disordered regions become visible as an increased background noise due to diffuse scattering. In order to maintain the trajectories of electrons undisturbed, the charge carriers pass a field-free

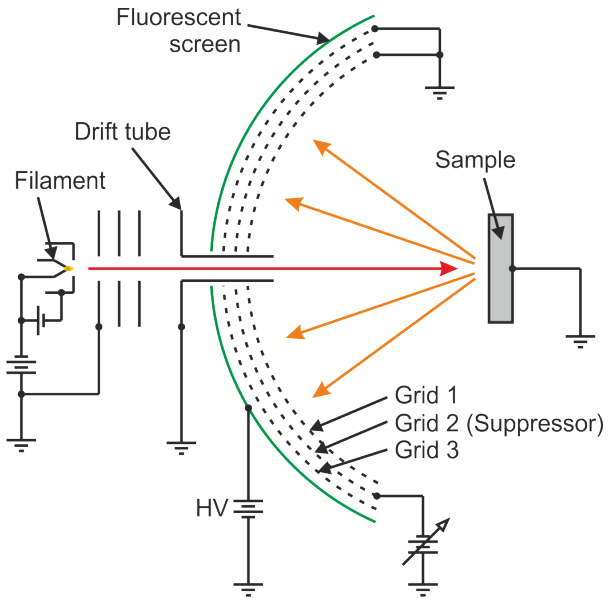

Figure 3.3: *Schematic design of a prevalent LEED optics. A sharp electron beam is generated in the electron gun, consisting of filament, Wehnelt cylinder, and a lens system. Diffracted electrons from the surface of a sample pass the field free space between sample and the grids and produce interference maxima on a fluorescent screen at locations according to Laue's conditions of diffraction. "Grid 2" acts as repeller for inelastically scattered electrons to reduce the noise level.*

space between gun and sample and towards "Grid 1" after diffraction. Most electrons (95 – 98 %) are inelastically scattered [76] and hindered from reaching the screen by a small negative voltage applied to "Grid 2", however, allowing the elastically diffracted electrons to pass. Constructively interfering electron waves are vizualized on a fluorescent screen, after being accelerated by a high voltage in the order of a few kV. In rear-view LEED optics the fluorescent screen is transparent so that observation through a viewport behind the electron gun is feasible. The LEED pattern can easily be recorded by a digital- or video-camera. In combination with a suitable software for spot-profile tracking I/V-LEED curves can be recorded [79].

For most parts of the LEED data presented in this thesis a "SPECS ErLEED 150 - Reverse View LEED Optics" was used [81]. It provides primary electron spot sizes smaller than 1 mm in diameter with optimized settings.

3.2 Scanning tunneling microscopy

With the invention of scanning tunneling microscopy (STM) by G. Binnig and H. Rohrer in 1982 [82–84] surface science has been given a fascinating tool for the exploration of structures at the atomic scale. The importance of this invention has been appreciated with the promotion of the Nobel Prize in Physics in 1986. So far, real-space atomic surface analysis was restricted to field emission techniques with some inherent limitations

as, e.g., the need for vacuum conditions and tip shaped surfaces. These deficiencies are overcome in STM. In addition, some further arguments make STM a tool of first choice in surface analysis:

- Diffraction techniques as, e.g., LEED, are limited to measurements on extended periodic structures and only give a view of the reciprocal space. Due to the rather large electron beam diameter, sizable areas of a sample surface are mapped at the same time. This demands a homogeneous surface quality and does not give a probe of local properties as, e.g., defects and disordered adsorbates.

- As in photoemission, STM is suitable of mapping the DOS of a specimen. However, the information is locally confined so that a detailed map of the local density of states (LDOS) is achieved.

- In contrast to most other surface analysis techniques, UHV conditions are not mandatory. This means an important advantage, especially in the case of biological specimens, which need to be analyzed under atmospheric pressure.

- Surface manipulation is another intriguing feature of STM. The microscope tip is capable of manipulating the arrangement of single atoms on a surface. Thus, one may consider STM as *building block kit* on the atomic level.

Before turning to the basics of tunneling theory and its application to the tunneling process in STM, the fundamental concept of STM is shortly introduced here on the basis of Fig. 3.4. An atomically sharp metallic tip is brought into close vicinity (<1 nm) of a flat conducting surface. By applying a bias voltage to the sample, a quantum mechanical tunneling current through the potential barrier between sample and tip is established, as will be discussed in detail later (see Sec. 3.2.1). The size of the tunneling current exponentially depends on the distance between tip and surface. The signal is then amplified and fed to a feedback loop (controls) to readjust the tip-surface distance. The required precision is achieved by utilizing ceramic piezo drives, allowing for smallest movements in the Å regime along the vertical (z) and lateral directions (x,y). Therefore, even a surface buckling in atomic dimensions is resolvable. The tip is scanned line-by-line over the surface with the x-, and y-piezos. In this manner a landscape of the charge distribution is obtained and presented as a false-color plot on a computer screen [85–87].

3.2.1 Theoretical discussion of the tunneling current

The experimental feasibility of STM relies on the quantum mechanical effect of tunneling. Imagine an electron of energy E approaching a 1D potential barrier of height ϕ ($E \leq \phi$). In classical physics the particle would be reflected at this boundary. Yet, in quantum mechanics there exists a finite probability for tunneling to the other side of the barrier. This fundamental property represents the basis of STM. The following theoretical description of the tunneling process is primarily based on Ref. 85.

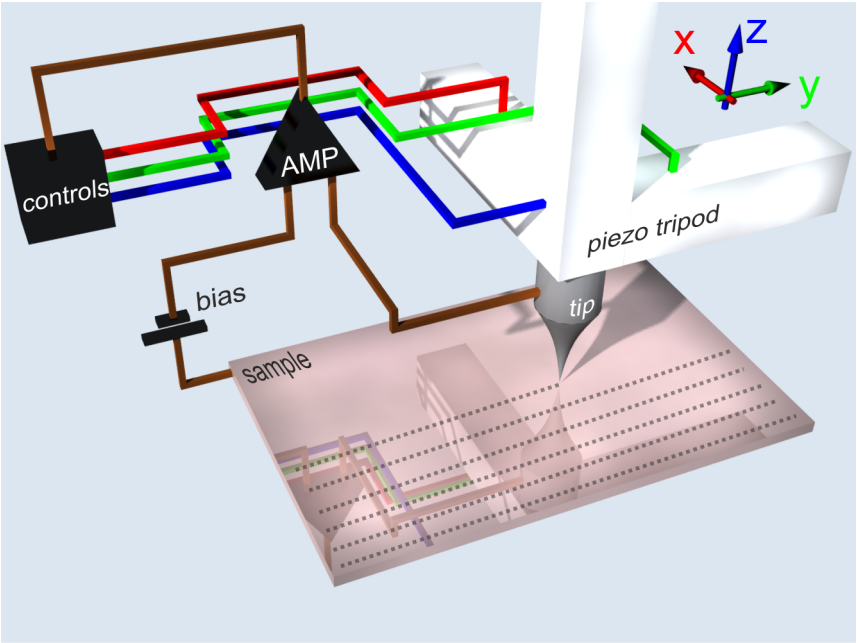

Figure 3.4: *Basic setup of an STM experiment. An atomically sharp tip is brought into close vicinity (< 1 nm) of a conducting sample surface. By applying a bias voltage to the sample, a tunneling current evolves. The current signal is amplified and fed to a control loop, which in turn regulates the vertical (z) piezo drive. In a line-by-line scan over the surface, the tip height (z) is plotted as function of lateral (x,y) tip position. This results in a "topographic" image of the surface.*

Early in advance of the breakthrough development by G. Binnig and H. Rohrer, J. Bardeen has proposed a *transfer Hamiltonian approach* based on time-dependent perturbation theory for describing the tunneling process [88]. Its main advantage is the suitability for a wide range of tunneling scenarios. Among these, the case of tunneling through a 3D barrier has been used by J. Tersoff and D. R. Hamann to calculate the tunneling current in STM [84, 89]. Following the formalism of J. Bardeen, the tunneling current is obtained as

$$\begin{aligned} I &= \tfrac{2\pi e}{\hbar} \textstyle\sum_{\mu,\nu} \{ f(E_\mu) [1 - f(E_\nu + eU)] - f(E_\nu + eU) [1 - f(E_\mu)] \} \\ &\quad \cdot |M_{\mu\nu}|^2 \, \delta(E_\nu - E_\mu) \end{aligned} \tag{3.6}$$

with the Fermi function $f(E)$ and the bias U applied to the sample [85]. $M_{\mu\nu}$ denotes the tunneling matrix element of the perturbation operator, which describes the transition among the unperturbed electronic states of tip Ψ_μ and surface Ψ_ν. E_μ and E_ν are the energies of the related states in case of equilibrium between the two electrodes, i.e., in absence of tunneling. The conservation of energy is considered by adding the delta-function δ. From the equation above it becomes clear that tunneling will occur only from unoccupied states of the surface into occupied states of the sample and vice-versa. The exact size of the tunneling current essentially depends on the evaluation of the matrix

element

$$M_{\mu\nu} = -\frac{\hbar^2}{2m_e} \int \mathrm{d}\mathbf{S} \cdot \left(\Psi_\mu^* \nabla \Psi_\nu - \Psi_\nu \nabla \Psi_\mu^* \right) . \tag{3.7}$$

This formalism represents the quantum mechanical current density integrated over the surface element d$\mathbf{S}$ between the two tunneling electrodes. Within this equation one has to make assumptions on the wave functions, which are generally not known. J. Tersoff and D. R. Hamann first considered an *ideal* tip and then turned to modeling of a more *realistic* tip.

Idealized tip

As a first assumption the evaluation is restricted to low bias (meV regime) and LTs. This simplifies Eq. 3.6 to

$$I = \frac{2\pi e^2}{\hbar} U \sum_{\mu,\nu} |M_{\mu\nu}|^2 \, \delta \left(E_\nu - E_F \right) \delta \left(E_\mu - E_F \right) \tag{3.8}$$

with the Fermi energy E_F[1]. Before turning to a more realistic situation, the tip is modeled as a locally spherical point probe centered at $\mathbf{r}_0$ without any spatial extension. For arbitrarily localized wave functions Eq. 3.8 reduces to

$$I \propto \sum_{\nu} |\Psi_\nu(\mathbf{r}_0)|^2 \, \delta(E_\nu - E_F) \, . \tag{3.9}$$

One can easily identify the quantity on the right side as the LDOS of the sample at the Fermi energy, "seen" at the position of the tip center $\mathbf{r}_0$. This means that the tunneling current, mapped in a line-by-line scan, reflects the sample LDOS in a 2D image of the surface.

Real tip

So far, the considerations above give a useful interpretation of the tunneling current. However, in a more realistic scenario the calculation of the tunneling matrix element requires a reasonable assumption on the wave functions. Therefore, J. Tersoff and D. R. Hamann introduced a spherical tip of radius R with an s type atomic orbital (see Fig. 3.5). In this way one derives

$$I \propto U \cdot n_t \left(E_F \right) \cdot \exp \left(2\kappa R \right) \cdot \sum_{\nu} \left| \Psi_\nu \left(\mathbf{r}_0 \right) \right|^2 \delta \left(E_\nu - E_F \right) \tag{3.10}$$

as relation for the tunneling current [85]. $\kappa = (2m_e\phi)/\hbar$, with ϕ as the barrier height, denotes the inverse decay length of the wave function in direction normal to the surface.

[1]The expression Fermi energy E_F will be used throughout this thesis instead of the more general chemical potential μ. In a strict sense, this convention is only valid for zero temperature with the system in equilibrium.

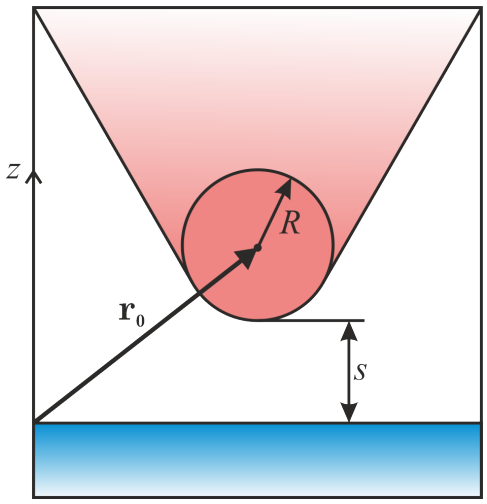

Figure 3.5: *Tunneling geometry according to J. Tersoff and D. R. Hamann [84]. The center of a locally spherical tip with radius R is positioned at* $\mathbf{r}_0$*. The length s represents the distance between the sample surface (shaded area) and the tip.*

$n_t(E_F)$ is the DOS of the tip at the Fermi energy, and $\mathbf{r}_0$ denotes the location of the tip center. As in the case of an ideal tip, the sum relates again to the LDOS in the surface ("seen" at the center of the tip $\mathbf{r}_0$)

$$n_s\left(E_F, \mathbf{r}_0\right) = \sum_{\nu} \left|\Psi_\nu\left(\mathbf{r}_0\right)\right|^2 \delta\left(E_\nu - E_F\right). \tag{3.11}$$

This leads to a first important finding. Taking the simplifications above as valid assumptions, the tunneling current in STM is a direct measure of the LDOS of the sample surface, which is independent of the exact character of the wave function. In addition, one has to take into account that s type wave functions, as assumed for our spherical tip, decay exponentially with distance from their origin. Therefore, one finds

$$\left|\Psi_\nu\left(\mathbf{r}_0\right)\right|^2 \propto \exp\left[-2\kappa\left(s + R\right)\right], \tag{3.12}$$

which in consequence means that the tunneling current depends exponentially on the distance s between tip and sample surface:

$$I \propto \exp\left(-2\kappa s\right). \tag{3.13}$$

In other words, a small change in distance, e.g., $\Delta s = 1\,\text{Å}$, leads to a shift in the tunneling current with an order of magnitude. This also means that the atom with the minimal distance to the surface will be automatically selected as main contributor to the overall tunneling current, which is the same as an atomically sharp tip. Eventually, the derivation of the tunneling current in Eq. 3.13 gives a conclusive explanation for the high vertical resolution in STM.

Finite bias approximation

The approximations above basically reproduce the main characteristics of the tunneling current in STM. However, in a real experimental situation the scenario of low bias is often no longer valid. Thus, one has to extend this constricted view to the case of finite bias. This becomes plausible, when imagining samples without conducting states at the Fermi level. A tunneling current will only be realized for voltages that are high enough to shift the energy levels so that occupied (unoccupied) states of the sample overlap with unoccupied (occupied) states of the tip. Neglecting the influence of bias on the wave functions and energy eigenvalues in both sample and tip, one may generalize Eq. 3.6 to

$$I \propto \int_0^{eU} n_t \left(\pm eU \pm E\right) \cdot n_s \left(E, \mathbf{r}_0\right) \mathrm{d}E \,, \tag{3.14}$$

which now covers the whole energy range. The LDOS of the sample is then further approximated by using Eqs. 3.11 and 3.12 at the center of the tip $\mathbf{r}_0$:

$$n_s \left(E, \mathbf{r}_0\right) \propto n_s \left(E\right) \cdot \exp\left\{-2 \left(s + R\right) \left[\frac{2m_e}{\hbar^2} \left(\frac{\phi_t + \phi_s}{2} + \frac{eU}{2} - E\right)\right]^{1/2}\right\} . \tag{3.15}$$

The matrix element is included in the modified inverse decay length κ in the sample LDOS. It now depends on the energy E and applied bias, and it is composed of a mean potential of tip (ϕ_t) and sample (ϕ_s). The tunneling current is finally obtained as

$$I \propto \int_0^{eU} n_t \left(\pm eU \mp E\right) \cdot n_s \left(E\right) \cdot T \left(E, eU\right) \mathrm{d}E \tag{3.16}$$

with the transmission coefficient

$$T \left(E, eU\right) = \exp\left\{-2 \left(s + R\right) \left[\frac{2m_e}{\hbar^2} \left(\frac{\phi_t + \phi_s}{2} + \frac{eU}{2} - E\right)\right]^{1/2}\right\} . \tag{3.17}$$

Here, it is obvious that states at the Fermi level will contribute mostly to the tunneling current, since these "see" the lowest barrier height (cf. Fig. 3.6).

The findings for finite bias reveal that the tunneling current does not show ohmic behavior as in the low bias regime (compare to Eq. 3.10). It rather unveils the spectroscopic character of STM. To illustrate this, Fig. 3.6 displays the three cases of (a) zero, (b) positive, and (c) negative sample bias for a 1D potential barrier at zero temperature. Without bias, tunneling is prohibited, since there are no overlapping occupied/unoccupied states on both sides of the barrier. When a positive sample bias is applied (b), electrons from the tip may tunnel through the barrier into unoccupied states of the sample. According to Eq. 3.17, this mainly happens for sample states at $E_{F,t}$ (tunneling probability is indicated by arrow lengths). If electrons from the tip at $E_{F,t}$ tunnel into a high sample LDOS, the current I will be enhanced. Yet, according

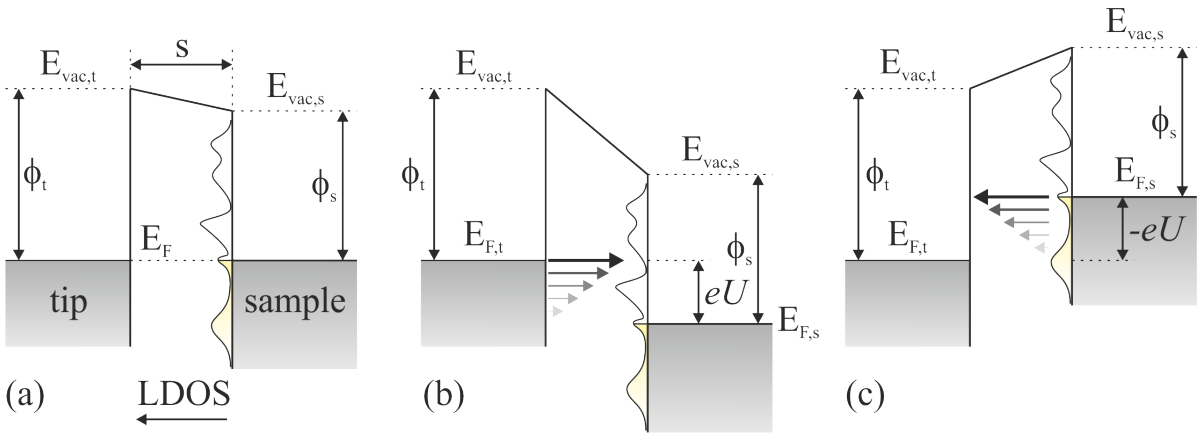

Figure 3.6: *Energy level diagram for tunneling at finite sample bias and at zero temperature. (a) Zero sample bias. Tip and sample in equilibrium ($E_{F,t} = E_{F,s}$) are separated by the potential barrier of width s. ϕ_t and ϕ_s are the work functions, and $E_{\mathrm{vac,t}}$ and $E_{\mathrm{vac,s}}$ are the corresponding vacuum energies of tip and sample, respectively. (b) Positive sample bias (eU): Tunneling from occupied tip states into unoccupied sample states (LDOS). (c) Negative sample bias ($-eU$): Tunneling from occupied sample states into unoccupied tip states. The arrow lengths correspond to the tunneling probability of the relevant states.*

to Eq. 3.14 the tunneling current is basically a convolution of the DOS from tip and sample. This becomes even more relevant for negative sample bias (c), where the situation is reversed, and one probes occupied states of the sample. Here, the tunneling current is much larger affected by the DOS of the tip. A convenient solution to reduce this influence is to use tips with rather uniform DOS, i.e., with negligible dependence on the bias voltage. Typical tip materials, such as W and PtIr, are dominated by more than 85 % of d-like orbitals at E_F [85]. The much faster decay of d-like wave functions with distance from their origin leads to a notably reduced transmission probability then. Thus, these states should not contribute significantly to the tunneling current, contrary to the s-states of the surface, as assumed above. Therefore, at least for probing unoccupied states of the sample, the contribution from the tip DOS is negligible, and the size of the tunneling current approximately reflects the the magnitude of the sample LDOS for a given bias. This has to be considered, when inspecting and comparing the lateral charge distribution in STM images captured at different bias voltages. Notable differences depending on the bias may occur, as will be shown later in Secs. 5.2.1, 6.1.3, and 7.2.1.

3.2.2 Experimental aspects and instrumentation in scanning tunneling microscopy

Since the early stages of STM much progress in optimizing the stability and precision of the instrument has been made. This includes advanced scanner designs, noise-reduced electronics, improved vibration damping systems, good thermal isolation, and flexible

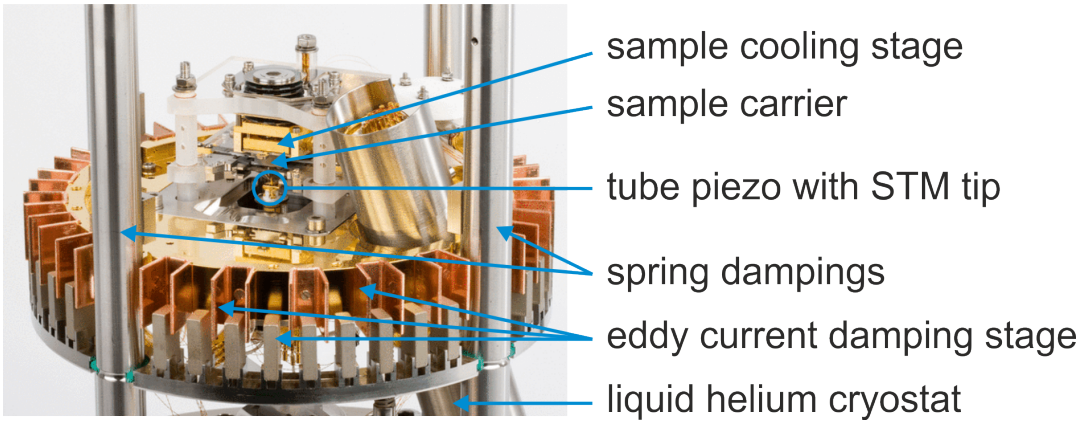

Figure 3.7: *Image of the Omicron VT-SPM without UHV housing, taken from Ref. 90, Copyright (2011) by Omicron NanoTechnology GmbH. The microscope stage is suspended by four springs enclosed in steel cylinders and receives further damping by an eddy current brake. The tip on top of a tube piezo is located in the center of the microscope stage, facing a sample carrier turned upside down. Sample cooling is achieved through a liquid helium flow cryostat, which connects by a copper braid to the sample carrier.*

software solutions. Commercial STM designs include multi-purpose microscopes, but also specialized versions, e.g., for LT applications.

The measurements in this thesis have been carried out with a variable temperature scanning probe microscope (VT-SPM), manufactured by *Omicron NanoTechnology* [90]. The microscope is part of an UHV system, operating at a base pressure of 1×10^{-10} mbar. Besides STM capabilities, it features atomic force microscopy, which has not been used here. Adjustable temperatures range from 45 K to 1500 K with a vertical resolution better than 0.1 Å at the same time [90]. The design of the VT-SPM is shown in Fig. 3.7. It contains effective vibration isolation by both spring suspension and eddy current damping. Sample temperatures may be controlled by a combination of direct current heating and a liquid helium flow cryostat. Atomic resolution in both lateral (x,y) and vertical (z) direction is provided by a tube piezo scanner. In order to avoid thermal drift due to distinct temperatures of piezo and specimen, the scanner is fitted with a radiation shielding. Effective noise reduction of the measurement signal is provided by an integrated preamplifier.

The sample is mounted onto a sample carrier, as shown in Fig. 3.8, which is mostly made of molybdenum. Electrical contacts are provided by tantalum sheets. These also keep the sample fixed directly below a ceramics plate on top. This design is quite suitable for high-temperature sample preparation, since the contact region between sample carrier and sample is small, and the thermal conductivity of Mo is only $\lambda = 143\,\mathrm{W/mK}$ at $T = 273\,\mathrm{K}$ [91]. Compared to the good thermal conductor copper ($\lambda = 403.5\,\mathrm{W/mK}$ at $T = 275\,\mathrm{K}$ [91]), this is a rather low value. Thus, heating is mainly reduced to the sample itself with marginal warming of the surroundings. Concomitantly, Mo sustains rather high temperatures with its melting point at $T = 2885\,\mathrm{K}$ [92]. This is essential for

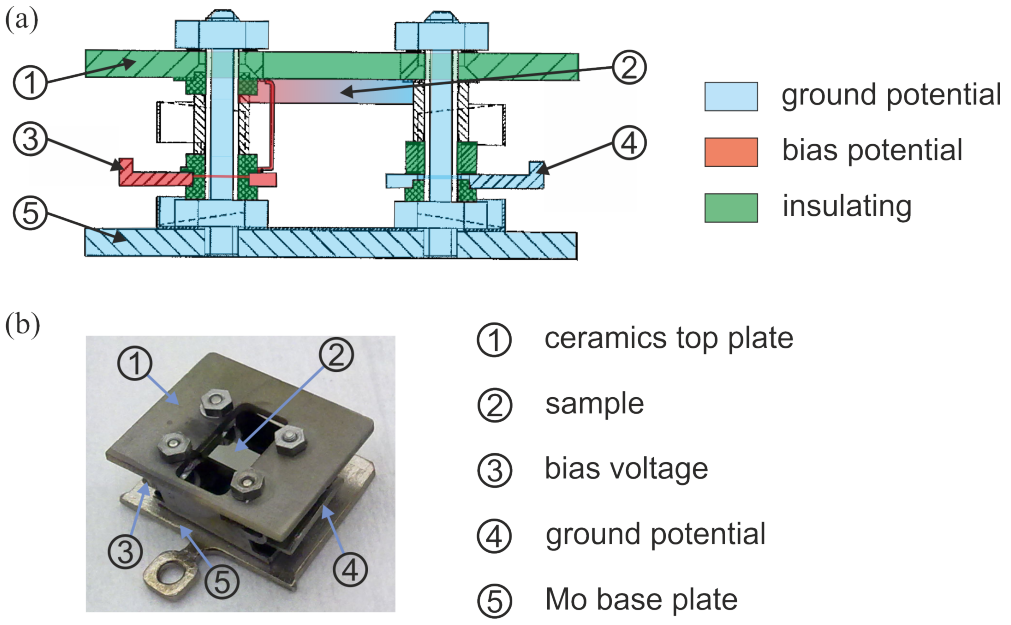

Figure 3.8: *Sample carrier design. (a) Technical drawing from side view, showing the main components and illustrating voltage potentials in direct current heating; derived from Ref. 94. (b) Photograph of the sample carrier with semiconductor sample mounted.*

the preparation of semiconductors as, e.g., Si. On the other hand, in experiments at LT this leads to an increase in time for cooling down, and the lowest achievable temperature is slightly above $T = 60\,\mathrm{K}$ [93], which is higher than the specified minimum value [90]. The sample carrier is positioned with face down orientation into the microscope stage, while the tunneling tip is approached from below.

In the following, focus is put on the basic modes of operation. A presentation of more sophisticated applications of STM may be found in Refs. 85 and 86.

Modes of operation

In STM the most prominent modes of operation are topographic and spectroscopic imaging. Topographic imaging may either be done with a *constant current* during the scan or with the tip at a *constant height*. However, topographic images always include spectroscopic information at the same time and may only be regarded as an approximation to the real topography of a surface. In contrast, it is possible to focus on spectroscopy only. This can be performed either locally on interesting spots or as a kind of spectroscopic grid in a wider scan range. The following paragraphs are dedicated to the different details and capabilities, but also drawbacks of these modes.

Constant current mode

In *constant current imaging* the tip is brought into close vicinity ($<1\,\mathrm{nm}$) of a sample

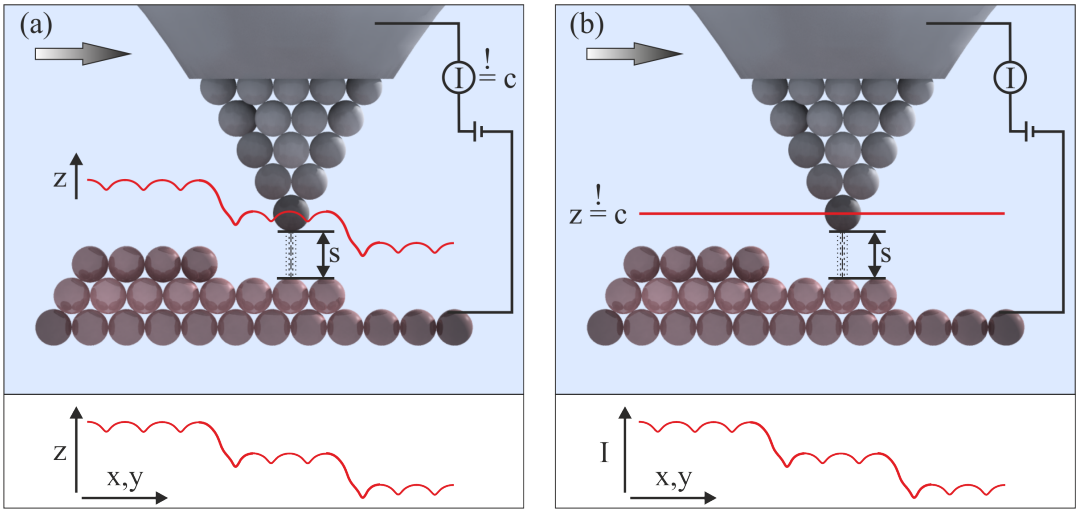

Figure 3.9: *(a) Constant current imaging. An atomically sharp tip is scanned over a sample surface with the tunneling current I held constant. The tip follows the sample's height profile with unchanged distance s. The necessary height adjustment is realized by a piezo drive, with the z-piezo voltage proportional to the dilatation Δz. Therefore, the sample corrugation is represented by a $z(x, y)$ profile (bottom). (b) Constant height imaging. The same setup as in (a), but with the tip held at constant height z. The distance between tip and sample s is no more fixed. The resulting change in I during a line scan is plotted as an $I(x, y)$ profile (bottom), which reflects the change in sample corrugation.*

surface, and a bias voltage is applied to the sample, see Fig. 3.9(a). This mode requires a constant tunneling current throughout the scan. This also implies that the distance s between tip and sample is kept fixed (neglecting any electronic contribution to the tunneling current here). The tip is then scanned along a lateral direction (x,y). Any change in surface height while scanning would result in a change of the tunneling current, according to Eq. 3.13. Therefore, the current signal is fed into a feedback loop, which adjusts the voltage U_z, applied to the vertical piezo drive, to keep the current at its setpoint value. This voltage naturally corresponds to a linear shift in piezo dilatation, and is therefore a direct measure of the surface corrugation [86]. The z-piezo voltage may thus be plotted as a height profile in dependence of the lateral position, i.e.,

$$z(x, y) \propto \beta U_z(x, y), \tag{3.18}$$

as shown in the bottom of Fig. 3.9(a). The calibration constant β depends on the experimental setup and needs to be obtained on a reference specimen.

The major drawback of this mode is the rather long duration for image capturing due to the finite frequency of the feedback loop for level adjustments. On the other hand, the danger of damaging or even destroying a tip by crashing into the surface, especially on samples with larger height contrast, is rather small. Eventually, one has to keep in mind that constant current imaging always includes electronic information and may not be seen as a topographic view on the sample alone.

Nevertheless, constant current imaging is the ideal mode to map the local atomic arrangement at the metal coated semiconductor surfaces studied in this thesis. All measurement shown hereafter were performed in constant current mode at RT. Bright contrast in the STM figures corresponds to elevations in the constant current scan. Image processing afterwards includes subtraction of a linear background, drift correction, and elimination of horizontal scars. Deviations from these general settings and procedures are stated for the corresponding images.

Since *constant height imaging* has not been used in the STM experiments presented in this thesis, the following lines do only briefly outline the fundamental concept. The experimental setup is basically the same as in the constant current mode. Here, the z-piezo is decoupled from the feedback loop. Therefore, no height adjustment to the tip occurs (z = const), which is scanned along the in-plane directions x and y, see Fig. 3.9(b). The varying signal of the tunneling current is plotted in dependence of the tip position $I(x, y)$ and reflects the surface corrugation.

Spectroscopic imaging

The mechanism of scanning tunneling spectroscopy (STS) bases on probing the LDOS in dependence of the applied bias, as has already been introduced in Sec. 3.2.1. In general, an $I(U)$ curve is obtained at a fixed lateral position on the surface. The sample LDOS is then approximately described by the first derivative of the tunneling current [95]

$$\frac{\mathrm{d}\,I}{\mathrm{d}\,U} \propto e n_s(eU) T(eU, eU) + e \int_0^{eU} n_s(E) \frac{\mathrm{d}}{\mathrm{d}\,(eU)} [T(E, eU)] \mathrm{d}E\,. \tag{3.19}$$

Basically, Eq. 3.19 reflects the LDOS in the sample $n_s(eU)$, however, with a superimposed background due to the transmission probability, which depends on the bias voltage U and the distance s, according to Eq. 3.17. While the first dependency represents a monotonic background, the second leads to difficulties in interpreting LDOS features at different sample locations, with topographic and spectroscopic information being mixed. For a better resolution of pure spectroscopic features in the $\mathrm{d}I/\mathrm{d}U$ curve, one usually needs to compensate for the dependence on the conductance I/U by normalizing the differential conductance as $(\mathrm{d}I/\mathrm{d}U)/(I/U)$. Tunneling spectroscopy has only once been used to compare spectral features from ARPES and many-body LDA+DCA calculations in Sec. 7.2.3, hence, further details on the method shall be omitted here.

3.3 Photoelectron spectroscopy

Photoelectron spectroscopy (PES) has developed to a standard technique in materials science today [77, 96, 97]. Its most convincing capability is the precise determination of the stoichiometric elemental composition in solid samples, which is therefore also known as *electron spectroscopy for chemical analysis* (ESCA) [98]. The basic principle of photoemission relies on the famous interpretation of the photo effect by A. Einstein

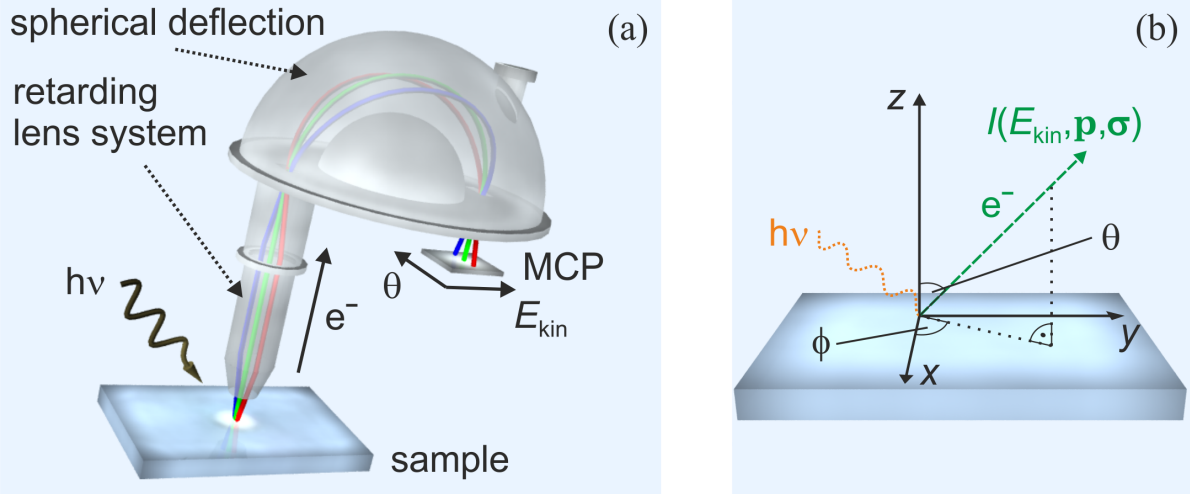

Figure 3.10: *(a) Principle of PES. Photons with energy $h\nu$ excite electrons in a sample, which pass through a retarding lens system and a spherical deflection analyzer, before being analyzed on a MCP with regard to their energy and angular distribution. (b) Close-up to the sample surface. The photoemission intensity I is a function of electron kinetic energy E_{kin}, momentum $\mathbf{p}$, and spin $\boldsymbol{\sigma}$.*

in 1905 [99]. He explained earlier observations of photoemitted electrons from a solid by H. Hertz [100], in assuming the light to consist of photons as quanta of light with discrete energies $h\nu$ (h as Planck's constant and ν as the photon frequency). According to this description, photons with sufficiently high energy excite electrons with respective binding energy E_B in a solid. These *photoelectrons* can then be detected with a kinetic energy

$$E_{\mathrm{kin}} = h\nu - E_B - \phi_A \tag{3.20}$$

outside the solid ($\phi_A \approx 4-6\,\mathrm{eV}$ as material-specific work function). In describing light as a current of particles with discrete energy, it was proved that the kinetic energy of the emitted photoelectrons simply depends on the wavelength of the incident photons and not on the intensity of the light source.

This fundamental principle is illustrated in Fig. 3.10. Monochromatized radiation $h\nu$ impinges on a sample and excites electrons within, which then pass a spherical deflecting analyzer to be subsequently detected at a multi channel plate (MCP) with regard to their angular (θ, ϕ) and kinetic energy distribution. The resulting signal of a photoemission experiment is thus the intensity I depending on E_{kin} and momentum $\mathbf{p}$, which is related to the angular distribution. It is further possible to detect the spin polarization $\boldsymbol{\sigma}$ with an appropriate experimental setup, as described in Sec. 3.3.2.

Electrons in a solid may either occupy discrete core level states with high binding energy or valance states close to the Fermi energy E_F, see Fig. 3.11. In order to excite an electron from a given binding energy into the vacuum, an incident photon energy high enough to overcome the binding strength $E_B + \phi_A$ is required, according to Eq. 3.20. The photoexcited electrons are then detected outside the solid with respect to their kinetic

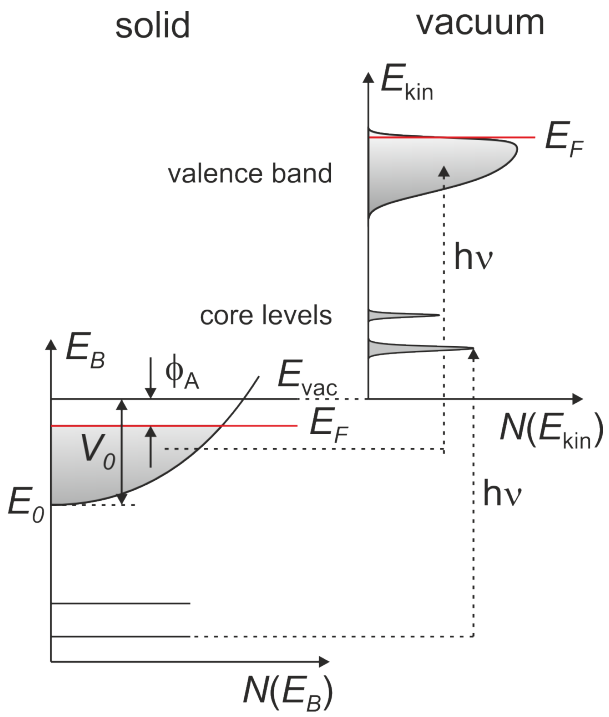

Figure 3.11: *General scheme of the electron energy distribution $N(E_B)$ in the photoemission process after [77]. Electrons inside a solid with binding energy E_B are excited by a photon of energy $h\nu$ into free electron states in the vacuum. The binding energy is referred to the Fermi level E_F, whereas the kinetic energy refers to the vacuum energy E_{vac}. The potential V_0 and the energy E_0 relate to the position of the valence band minimum. E_F and E_{vac} are separated by a material-specific work function ϕ_A.*

energies. All states are dressed with a certain energy broadening due to the finite lifetime of the excited state and the limited experimental resolution. The resulting electron distribution $N(E_{\mathrm{kin}})$ may be regarded as a replica of the DOS within the solid [77].

Three-step model of photoemission

In contrast to the rather straightforward introduction to the photoemission process given above, there exist a couple of factors which complicate the interpretation of PES data. Therefore, the description of photoemission is often reduced to the non-interacting case with neglect of many-body effects. In addition, the *sudden approximation* assumes the process to be instant with no time for the system to relax. For a further facilitation, the generally approved *three-step model* has been introduced, which divides the photoemission process into three independent stages [101, 102]:

- Absorption of a photon with energy $h\nu$ by an electron in the initial bulk state and excitation of the photoelectron into the final state.
- Travel of the photoelectron to the surface of the sample.

- Escape of the photoelectron into the vacuum after passing the surface barrier potential.

Although, from an exact theoretical viewpoint, a separation into three discrete steps may seem unphysical, the three-step model reproduces the photoemission process quite accurately.

In addition to the energy-dependent electronic structure in Fig. 3.11, ARPES provides momentum-resolved spectra, derived from the angular distribution of the photoelectrons. Here, the valence and surface band dispersion of a solid in k-space is obtained. The electron wave vector in vacuum $\mathbf{K}$ is related to its momentum by $\mathbf{K} = \mathbf{p}/\hbar$, and its modulus is fully determined from the kinetic energy by $K = \sqrt{2m_e E_{\mathrm{kin}}}/\hbar$. Thus, its three components

$$\mathbf{K} = \begin{pmatrix} K_x \\ K_y \\ K_z \end{pmatrix} = \frac{1}{\hbar}\sqrt{2m_e E_{\mathrm{kin}}} \begin{pmatrix} \sin\theta\cos\phi \\ \sin\theta\sin\phi \\ \cos\theta \end{pmatrix} \tag{3.21}$$

are obtained from the angular electron distribution under consideration of energy and momentum conservation laws [97]. Here, it should be noted that the photon momentum in ARPES is usually small compared to the size of the Brillouin zone (BZ). Therefore, only direct transitions with $\mathbf{k}_i - \mathbf{k}_f = 0$ in the reduced BZ, or $\mathbf{k}_i - \mathbf{k}_f = \mathbf{G}$ in the extended BZ scheme, do occur. $\mathbf{k}_i$ and $\mathbf{k}_f$ are the wave vectors of initial and final states, respectively. $\mathbf{G}$ is a reciprocal lattice vector.

As the interest is to obtain the electronic band structure $E(\mathbf{k})$ inside the solid, one needs to determine the corresponding momentum $\mathbf{k}$ from the in-vacuum momentum $\mathbf{K}$. In the three-step model of PES the transition of the electron from Bloch states inside the sample to free electrons states in the vacuum is achieved by wave matching on either side of the solid-vacuum interface. Due to translational invariance in the surface plane and the small photon momentum, the in-plane momentum is usually conserved at the solid-vacuum transition and one achieves

$$\mathbf{k}_\parallel = (k_x, k_y) = \mathbf{K}_\parallel = \frac{1}{\hbar}\sqrt{2m_e E_{\mathrm{kin}}} \begin{pmatrix} \sin\theta\cos\phi \\ \sin\theta\sin\phi \end{pmatrix}. \tag{3.22}$$

This is visualized in Fig. 3.12, where it also becomes evident that the vertical electron momentum is not conserved at the transition from solid to vacuum ($\mathbf{k}_\perp \neq \mathbf{K}_\perp$) due to the potential change. For the determination of the perpendicular electron momentum in the solid $\mathbf{k}_\perp$ it is necessary to model the final Bloch states as exactly as possible [97]. These may be taken from band structure calculations, if available. Otherwise, one could approximate the final state band dispersion as nearly free electron states with dispersion

$$E_f(\mathbf{k}) = \frac{\hbar^2\left(\mathbf{k}_\parallel^2 + \mathbf{k}_\perp^2\right)}{2m_e} - |E_0|\,. \tag{3.23}$$

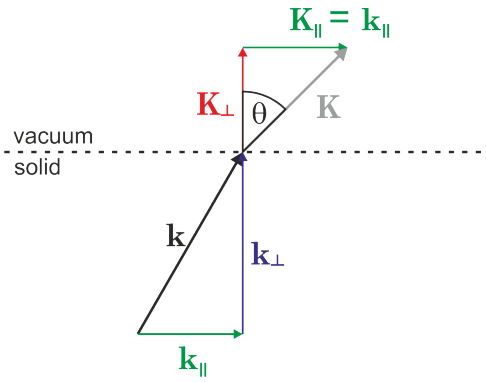

Figure 3.12: *Momentum relations for an electron passing the potential barrier at the solid-vacuum interface. The component perpendicular to the interface is not conserved in contrast to the parallel part of the momentum vector.*

Here, E_0 is the minimum of the valence band, as given in Fig. 3.11. In combination with $E_f = E_{\text{kin}} + \phi_A$ and Eq. 3.22 one finally obtains the perpendicular electron momentum

$$\mathbf{k}_\perp = \frac{1}{\hbar}\sqrt{2m_e\left(E_{\text{kin}}\cos^2\theta + V_0\right)}. \tag{3.24}$$

Therein, $V_0 = |E_0| + \phi_A$ denotes the *inner potential*, which corresponds to the bottom of the valence band with binding energy E_0 (see Fig. 3.11). Unfortunately, V_0 is unknown and has to be either approximated theoretically or to be obtained experimentally. The latter requires a tunable photon source as, e.g., synchrotron radiation (refer to Sec. 3.3.2 for details) to scan the periodicities in the $E(\mathbf{k}_\perp)$ dispersion. However, in some cases it might be sufficient to work with a value of $V_0 = 10\,\text{eV}$, which is often a rather good estimate for the inner potential [103, 104]. In studying 2D systems like surfaces, the dispersion along $\mathbf{k}_\perp$ becomes negligible, and the electronic band structure is completely determined by the $E_{\text{kin}}(\mathbf{k}_\parallel)$ dependency.

Surface sensitivity and energy regimes

It is important to note that PES is a very surface sensitive technique. This is due to the small escape depth of electrons inside a solid, which strongly interact with other electrons and phonons on their way towards the surface. While the latter is mostly relevant for low kinetic energies, the scattering with other electrons has the strongest impact on the mean free path in typical PES energy regimes. As has already been discussed in Sec. 3.1, the escape depth does only slightly depend of the respective kinetic electron energies, and the chemical composition of the sample is negligible. This behavior is well described by the universal curve for the electron mean free path, given in Fig. 3.1 of Sec. 3.1. It should also be noted that UHV conditions are mandatory for high quality PES experiments. On the one hand, this minimizes the probability of electrons colliding with rest gas atoms or molecules on their way to the detector. And on the other hand,

owing to the reduced probing depth, rest gas adsorbants on the surface would otherwise complicate or even hinder probing the desired surface electronic structures.

Photoemission experiments are generally intersected into different regimes depending on the photon energy [77]. In the low energy range ($< 100\,\mathrm{eV}$) ultraviolet photoelectron spectroscopy (UPS) is suitable to obtain the valence band structure in solids. This technique is often used in combination with a hemispherical deflection analyzer (HDA) allowing for ARPES. Due to the small photon momentum one typically deals with direct transitions, which allows to obtain "k-resolved" spectra. On the other hand, in x-ray photoelectron spectroscopy (XPS) photon energies above $1000\,\mathrm{eV}$ are utilized to probe both valence states and core levels of a solid. Yet, the resolution is about one order of magnitude reduced compared to UPS in valence band spectroscopy. Furthermore, the photon momentum is comparable to the BZ size, and thus, indirect transitions lead to "k-averaged" spectra. Depending on the spectroscopic information to be captured, there exist multiple variants of PES nowadays. In this thesis we will focus on ARPES and its variant SARPES in Sec. 3.3.2.

3.3.1 Theory of angle-resolved photoelectron spectroscopy

The most common approach in the interpretation of photoemission data is the three-step model, introduced in the preceding section. Therein, the overall photoemission intensity is given by the product of all single steps. The first step (1) contains the properties of the initial electronic structure. Step (2) deals with the scattering probability of the electron on its way to the surface, defined by an effective mean free path. Inelastic scattering contributes as secondary electron background to the overall intensity. Eventually, in step (3) the transmission probability is included, which is mainly determined by the material-specific work function. The following theoretical discussion is primarily based on Refs. 77, 97, and 105.

The non-correlated case

A realistic description of photoemission from a solid should treat the whole process as a complex many-body problem. A system consisting of N electrons is brought into an excited state with $N-1$ remaining electrons after absorption of the photon, thereby generating a *core hole*. This core hole then interacts with the remaining $N-1$ electrons and mainly affects the less well screened sea of valence electrons. That is the reason, why initial and final states can strongly deviate from each other, resulting in a complex intensity distribution (see discussion on p. 43 ff.). This includes satellites and/or asymmetries in the line shape of a state. Furthermore, it will be necessary to specify different transition probabilities between initial and final electron states.

As a starting point, it is feasible to describe the transition probability $w_{f,i}$ between

an initial state Ψ_i and a final state Ψ_f in the N-particle system by *Fermi's Golden Rule*

$$w_{f,i} = \frac{2\pi}{\hbar} \left| \left\langle \Psi_f^N \mid H_{\text{int}} \mid \Psi_i^N \right\rangle \right|^2 \delta \left(E_f^N - E_i^N - h\nu \right), \tag{3.25}$$

with the δ-function accounting for energy conservation [97]. $E_i^N = E_i^{N-1} - E_B^k$ and $E_f^N = E_f^{N-1} + E_{\text{kin}}$ are initial and final state energies, respectively. The interaction with the electromagnetic field, associated with the photon, is introduced by the small perturbation

$$H_{\text{int}} = \frac{e}{2m_e c} \left(\mathbf{A} \cdot \mathbf{p} + \mathbf{p} \cdot \mathbf{A} \right) \approx \frac{e}{m_e c} \mathbf{A} \cdot \mathbf{p}, \tag{3.26}$$

with $\mathbf{A} = \mathbf{A}(\mathbf{r}, t)$ being the vector potential of the electromagnetic field. Here, a few approximations are made. Two photon processes are excluded, and translational invariance in the solid is assumed. Furthermore, the dipole approximation $\nabla \mathbf{A} = 0$ was employed. This is plausible, since the photon wavelength (e.g., $\lambda = 10^3$ Å for $h\nu = 10\,\text{eV}$) is much larger than atomic distances [77]. Thus, $\mathbf{A}$ may be taken as constant, because PES is restricted to a small region at the crystal surface.

Based on stage (1) in the three-step model, it is convenient to factorize the wave functions in Eq. 3.25 into an electron part and a contribution of the remaining $(N-1)$-electron system. This is applicable, since we do this within the *sudden approximation*, which assumes the photoemission process to occur instantaneously without any relaxation of the electron system left behind [97]. Following this approach, the final state wave function is factorized to

$$\Psi_f^N = \tilde{A} \Phi_f^{\mathbf{k}} \Psi_f^{N-1} \tag{3.27}$$

with the wave function $\Phi_f^{\mathbf{k}}$ of the electron and the final state wave function of the $(N-1)$-electron system Ψ_f^{N-1}. The antisymmetric operator $\tilde{A}$ ensures the compliance of the Pauli principle. At this stage, it is possible to choose an excited state wave function Ψ_m^{N-1} with energy E_m^{N-1} for the final state. Then the total transition probability has to sum over all excited states m. In a similar way, the initial state is given by

$$\Psi_i^N = \tilde{A} \Phi_i^{\mathbf{k}} \Psi_i^{N-1} = \tilde{A} \Phi_i^{\mathbf{k}} c_{\mathbf{k}} \Psi_i^N \tag{3.28}$$

in second quantization with the annihilation operator $c_{\mathbf{k}}$, which describes the removal of an electron from the initial N-particle system. With these ingredients the matrix element term in Fermi's Golden Rule (Eq. 3.25) is rewritten as

$$\left\langle \Psi_f^N \mid H_{\text{int}} \mid \Psi_i^N \right\rangle = \left\langle \Phi_f^{\mathbf{k}} \mid H_{\text{int}} \mid \Phi_i^{\mathbf{k}} \right\rangle \left\langle \Psi_m^{N-1} \mid \Psi_i^{N-1} \right\rangle. \tag{3.29}$$

Therein, $\left\langle \Phi_f^{\mathbf{k}} \mid H_{\text{int}} \mid \Phi_i^{\mathbf{k}} \right\rangle \equiv M_{f,i}^{\mathbf{k}}$ denotes the one-electron dipole matrix element, and the second term is the overlap integral. Based on the derivation so far, it is possible to give an expression for the intensity in the photoemission experiment, including all

possible transitions between initial and final states, as well as all excited states m in the remaining $(N-1)$-particle system:

$$I(\mathbf{k}, E_{\text{kin}}) = \sum_{f,i} w_{f,i} \propto \sum_{f,i} \left| M_{f,i}^{\mathbf{k}} \right|^2 \sum_m |c_{m,i}|^2 \, \delta\left(E_{\text{kin}} + E_m^{N-1} - E_i^N - h\nu\right). \tag{3.30}$$

Here, $|c_{m,i}|^2 = \left| \left\langle \Psi_m^{N-1} \mid \Psi_i^{N-1} \right\rangle \right|^2$ is the probability for an electron released from state i to leave the remaining system in the excited state m. From Eq. 3.30 it becomes evident that the total intensity only consists of single delta shaped peaks at the "Koopman's" binding energy (Hartree-Fock orbital energy) $E_B^{\mathbf{k}} = -\epsilon_{\mathbf{k}}$, if the excited state m_0 is equal to the initial state ($\Psi_i^{N-1} = \Psi_{m_0}^{N-1}$). In this case of absent correlation all $|c_{m,i}|^2$ with $m \neq m_0$ will be zero. Nevertheless, for enhanced electron-electron correlations, there exist multiple $|c_{m,i}|^2 \neq 0$, and thus, a corresponding number of satellite lines, accompanying the main peak, will appear in the total intensity spectrum.

The correlated case – Fermi liquid theory

Electronic correlations in photoemission are best described within the *Green's function formalism* [97]. Therein, the *time-ordered* one-electron Green's function $\tilde{G}(t-t')$ may be interpreted as the probability that an electron added to a state with Bloch vector $\mathbf{k}$ at a time $t = 0$ is still found in this state at the later time $|t - t'|$. The utilization of a Fourier transform then results in $\tilde{G}(\mathbf{k}, \omega) = G^+(\mathbf{k}, \omega) + G^-(\mathbf{k}, \omega)$. Therein,

$$G^{\pm}(\mathbf{k}, \omega) = \sum_m \frac{\left| \left\langle \Psi_m^{N\pm1} | c_{\mathbf{k}}^{\pm} | \Psi_i^N \right\rangle \right|^2}{\omega - E_m^{N\pm1} + E_i^N \pm i\eta} \tag{3.31}$$

is the one electron addition (G^+) and removal (G^-) Green's function at zero temperature. $c_{\mathbf{k}}^+$ ($c_{\mathbf{k}}^-$) is the creation (annihilation) operator, which adds or removes an electron from the initial N-particle system. η is a positive infinitesimal, and the convention $\hbar = 1$ is set in the following. After some additional transformations, one obtains the *one-particle spectral function* $A(\mathbf{k}, \omega) = A^+(\mathbf{k}, \omega) + A^-(\mathbf{k}, \omega)$, which is derived from the *retarded* Green's function $G(\mathbf{k}, \omega) = G^+(\mathbf{k}, \omega) + [G^-(\mathbf{k}, \omega)]^*$ as

$$A(\mathbf{k}, \omega) = -(1/\pi) \operatorname{Im} G(\mathbf{k}, \omega). \tag{3.32}$$

Therein,

$$A^{\pm}(\mathbf{k}, \omega) = \sum_m \left| \left\langle \Psi_m^{N\pm1} | c_{\mathbf{k}}^{\pm} | \Psi_i^N \right\rangle \right|^2 \delta\left(\omega - E_m^{N\pm1} + E_i^N\right) \tag{3.33}$$

describe the one-electron addition (A^+) and removal (A^-) spectra, respectively. These may experimentally be obtained in inverse photoelectron spectroscopy (IPES) and PES.

In a photoemission experiment the spectral function is not directly accessible. But there exists a straightforward relation to the photoemission intensity

$$I(\mathbf{k}, \omega) = I_0(\mathbf{k}, \nu, \mathbf{A}) f(\omega) A(\mathbf{k}, \omega) \tag{3.34}$$

with I_0 being proportional to the squared one-electron transition matrix element $\left|M_{f,i}^{\mathbf{k}}\right|^2$, and therefore also depending on the vector field $\mathbf{A}$. The Fermi distribution $f(\omega) = \left(e^{\omega/k_BT}+1\right)^{-1}$ takes into account that occupied states are probed only. The dependency of the intensity on the matrix elements has a significant impact on a photoemission experiment. It may lead to strongly reduced intensities or even full suppression of specific features in the spectra at different photon energies (see also p. 43 ff.). Similarly, the polarization of the incident radiation influences the experimental spectra. On the one hand, this may be problematic if only a single photon energy is available, as it is the case for inert gas discharge lamps, being used in a typical laboratory environment. Here, one might miss important spectral information. On the other hand, with a tunable photon source (synchrotron radiation) one may selectively attenuate features in the electronic band structure. This gives some kind of orbital preference at hand. And eventually, selection rules can be exploited by utilizing different polarizations.

The description of photoemission within the Green's function formalism so far does not include correlation effects. These are easily taken into account by introducing the *electron proper self-energy*

$$\Sigma(\mathbf{k},\omega) = \Sigma'(\mathbf{k},\omega) + \mathrm{i}\,\Sigma''(\mathbf{k},\omega). \tag{3.35}$$

The real part of the self-energy leads to a mass renormalization in the spectral function, whereas the imaginary part adds a lifetime broadening for an electron with energy $\epsilon_{\mathbf{k}}$ and momentum $\mathbf{k}$. In this way, the Green's function is given by

$$G(\mathbf{k},\omega) = \frac{1}{\omega - \epsilon_{\mathbf{k}} - \Sigma(\mathbf{k},\omega)}. \tag{3.36}$$

The spectral function, which is directly linked to the measurable intensity in an ARPES experiment (Eq. 3.34), is consequently expressed by

$$A(\mathbf{k},\omega) = -\frac{1}{\pi}\,\mathrm{Im}\,G(\mathbf{k},\omega) = -\frac{1}{\pi}\frac{\Sigma''(\mathbf{k},\omega)}{\left[\omega - \epsilon_{\mathbf{k}} - \Sigma'(\mathbf{k},\omega)\right]^2 + \left[\Sigma''(\mathbf{k},\omega)\right]^2}. \tag{3.37}$$

Therefore, and due to the applicability of Kramers-Kronig relations, it is possible to determine the self-energy from high quality ARPES experiments. This sort of evaluation allows then to discuss electron-electron correlation effects, which enter into the electronic band structure. In the following, the two cases of an electron system with interactions switched either "on" or "off" shall be discussed.

Let us first consider the uncorrelated case with zero electron self-energy, i.e., $\Sigma(\mathbf{k},\omega) = 0$. Here, the wave function is a single slater determinant with a distinct eigenstate upon electron addition or removal. Therefore, the one-electron Green's function $G(\mathbf{k},\omega) = 1/\left(\omega - \epsilon_{\mathbf{k}} \pm \mathrm{i}\,\eta\right)$ has a single pole at the energy $\epsilon_{\mathbf{k}}$. This in turn gives a delta-peak shaped spectral function $A(\mathbf{k},\omega) = \delta(\omega - \epsilon_{\mathbf{k}})$ at zero temperature, which is displayed in Fig. 3.13(a). Thus, for each $\mathbf{k}$ there is only one single peak at the band energy $\epsilon_{\mathbf{k}}$,

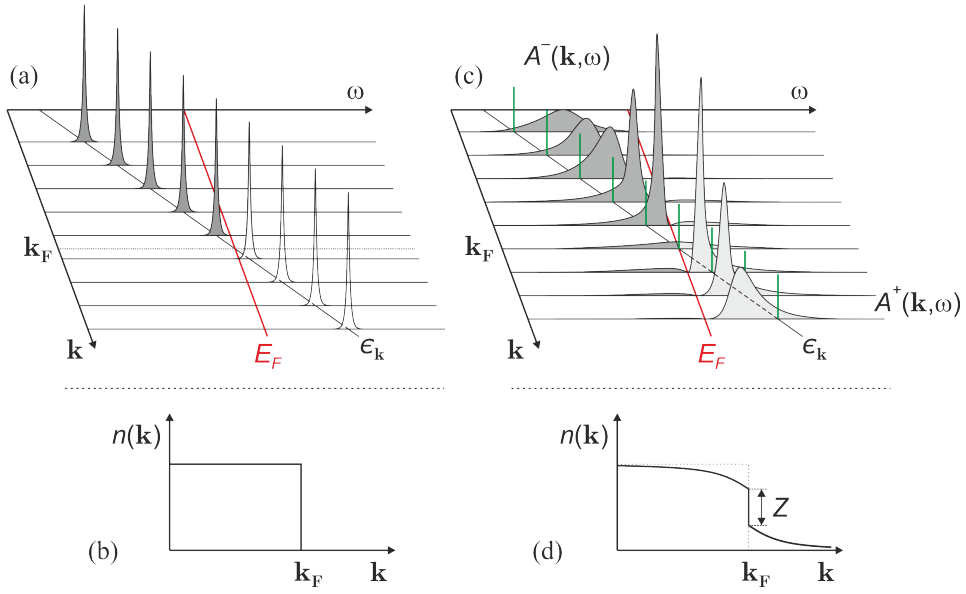

Figure 3.13: *(a) Spectral function for zero electronic correlations. A single line with energy $\epsilon_\mathbf{k}$ displays the band dispersion. Due to the absence of correlations, EDC curves exhibit sharp delta-peaks at the band energy $\epsilon_\mathbf{k}$. (b) The corresponding momentum distribution $n(\mathbf{k})$ is characterized by a sharp drop at the Fermi vector $\mathbf{k_F}$. (c) Spectral function for the interacting case, deviating from the initial band dispersion $\epsilon_\mathbf{k}$ (straight line with green bars at former EDC maxima). Both the one-electron removal (A^-) and addition (A^+) parts of the spectral function show a pronounced lifetime line shape broadening, a mass and energy renormalization (deviation from $\epsilon_\mathbf{k}$ dispersion), and a clear QP peak in close vicinity to $\mathbf{k_F}$. Spectral weight is transferred to momenta above (below) $\mathbf{k_F}$ in A^- (A^+) at zero temperature, which shows up as reduced discontinuity ($Z < 1$) in the momentum distribution at $\mathbf{k_F}$ in (d). Figures are according to [105].*

and the dispersion is given by the solid line crossing the Fermi level at $\mathbf{k_F}$. Here, only states $\mathbf{k} < \mathbf{k_F}$ are occupied according to the Fermi-Dirac distribution $f(\omega, T)$. The corresponding momentum distribution function $n(\mathbf{k})$ in Fig. 3.13(b) shows an instant cut-off from 1 to 0 at $\mathbf{k_F}$, accordingly.

Now, the electron-electron correlations shall be switched on adiabatically to maintain the system in equilibrium. This is described within the *Fermi liquid theory*, which assumes a sea of interacting particles, whose properties are transformed to a system of non-interacting particles. This concept was initially proposed by L. Landau and can be understood as follows [56, 97]. Any electron added to the system has a certain probability of being scattered out of its initial Bloch state with the system remaining in an excited state. In this case an electron-hole pair is created, which shows up as a side band to the main peak in photoemission, and the momentum distribution exhibits a discontinuity $Z_\mathbf{k} < 1$ at $\mathbf{k_F}$, as is shown in Fig. 3.13(c) and (d). Consequently, there is spectral weight below the Fermi energy for $\mathbf{k} > \mathbf{k_F}$ even at zero temperature. The initial electron may now be regarded as a single particle, dressed by all its surrounding excitations, the so-called *quasi-particle* (QP). For a small size of the self-energy, the

spectral function can then be intersected into a coherent pole part (main line) and an incoherent part without poles (excitation spectrum):

$$A(\mathbf{k},\omega) = A_{\mathrm{ch}} + A_{\mathrm{inch}} = Z_{\mathbf{k}} \frac{\Gamma_{\mathbf{k}}/\pi}{\left(\omega - \epsilon^*_{\mathbf{k}}\right)^2 + \Gamma_{\mathbf{k}^2}} + A_{\mathrm{inch}}. \tag{3.38}$$

In this way, the self-energy is contained within the ARPES spectra. The corresponding Green's function, which includes all many-body effects, as electron-electron and electron-phonon interactions, is then:

$$G(\mathbf{k},\omega) = G_{\mathrm{ch}} + G_{\mathrm{inch}} = \frac{Z_{\mathbf{k}}}{\omega - \epsilon^*_{\mathbf{k}} + i\Gamma_{\mathbf{k}}} + G_{\mathrm{inch}}. \tag{3.39}$$

In this formalism, the QP weight, also known as pole strength or coherence factor, $Z_{\mathbf{k}} = (1 - \partial\Sigma'/\partial\omega)^{-1}$ defines the degree of correlation with $\epsilon^*_{\mathbf{k}} = Z_{\mathbf{k}}(\epsilon_{\mathbf{k}} + \Sigma')$ and $\Gamma_{\mathbf{k}} = Z_{\mathbf{k}} |\Sigma''|$, and the self-energy considered at $\omega = \epsilon^*_{\mathbf{k}}$. Thus, this leads to a renormalization of the electron mass ($m_e \longrightarrow m^*_e$), the band energy ($\epsilon_{\mathbf{k}} \longrightarrow \epsilon^*_{\mathbf{k}}$), and the line width $\Gamma_{\mathbf{k}}$, which is related to the finite lifetime $\tau_{\mathbf{k}} = 1/\Gamma_{\mathbf{k}}$. The modified dispersion with its inherent peak-sharpening in approaching $\mathbf{k_F}$ [Fig. 3.13(c)] clearly deviates from the non-interacting case (green bars along the solid $\epsilon_{\mathbf{k}}$ line). In summary, the main hallmarks of a Fermi liquid are [77]:

(i) A renormalization of energy from $\epsilon_{\mathbf{k}}$ in the non-interacting case to $\epsilon^*_{\mathbf{k}}$ as well as the renormalized band mass ($m_e \longrightarrow m^*_e$). The renormalization is expressed in the real-part of the self-energy $\Sigma' \propto \omega$. That implies a smaller renormalized energy ($\epsilon^*_{\mathbf{k}} < \epsilon_{\mathbf{k}}$) and an enhanced electron mass ($m^*_e > m_e$).

(ii) A finite QP lifetime broadening due to electron-electron interactions, given by the imaginary part of the self-energy $\Sigma'' \propto \omega^2$.

(iii) An incoherent background, originating from the excitation of electron-hole pairs.

(iv) Spectral weight outside the FS at zero temperature, which is related to a reduction of the Fermi step from $Z_{\mathbf{k}} = 1$ to $Z_{\mathbf{k}} < 1$.

As $A(\mathbf{k},\omega)$ also describes the probability of adding/removing an electron to/from a many-body system, there exist a few sum rules, which are given below [97]:

$$\int_{-\infty}^{\infty} \mathrm{d}\omega A_{\mathrm{ch}}(\mathbf{k},\omega) + \int_{-\infty}^{\infty} \mathrm{d}\omega A_{\mathrm{inch}}(\mathbf{k},\omega) = \int_{-\infty}^{\infty} \mathrm{d}\omega A(\mathbf{k},\omega) = 1 \tag{3.40}$$

with

$$\int_{-\infty}^{\infty} \mathrm{d}\omega A_{\mathrm{ch}}(\mathbf{k},\omega) = Z_{\mathbf{k}}, \qquad \int_{-\infty}^{\infty} \mathrm{d}\omega A_{\mathrm{inch}}(\mathbf{k},\omega) = 1 - Z_{\mathbf{k}}. \tag{3.41}$$

In ARPES, the electron addition spectra are not accessible, and thus, it may be more appropriate to give the following sum rule in the end

$$\int_{-\infty}^{\infty} \mathrm{d}\omega f(\omega) A(\mathbf{k},\omega) = n(\mathbf{k}). \tag{3.42}$$

It connects the momentum distribution with the one-particle removal spectral function.

A common example of a Fermi liquid system is the 2D metal $1T-TiTe_2$ [106], which shows the behavior described above. Eventually, it should be noted that for the limiting case of $Z_{\mathbf{k}} = 0$ one leaves the Fermi liquid regime and derives at a 1D *Luttinger liquid*, where there is no more sharp Fermi step, but a power law behavior in the photoemission spectrum.

Final state effects

Whenever PES data are evaluated, one has to keep in mind that these reflect the final (electron) states, which can significantly deviate from the original initial (hole) states due to modifications in the photoexcitation and photoemission process. The following discussion is based on the description presented in Ref. 77.

The most relevant final state effect concerns the observable binding energy E_B of a certain state in a photoemission experiment. It may notably differ from the total energy of the initial state E_i^N of the N-electron system. Therefore, Eq. 3.20 must more precisely be written as

$$E_{\text{kin}} = h\nu - (E_f^{N-1} - E_i^N) - \phi_A, \tag{3.43}$$

where E_f^{N-1} is the total energy of the final state in the excited system. Accordingly, the binding energy is just the difference between the total energies, i.e., $E_B = E_f^{N-1} - E_i^N$. The problem arising here is that the total energies cannot be calculated exactly. Therefore, the most common approach is the "Koopmans's approximation", which simply assumes that the binding energy corresponds to the energy $-\epsilon_k$ of the orbital k, from which the photoelectron has been excited. However, this still neglects the influence of the ionized orbital on other orbitals, i.e., the relaxation of the many-electron system is not taken into account so far. In a more accurate way, one thus needs to include both the *intra-atomic* orbital relaxation and the *extra-atomic* flow of electrons towards the ionized orbital. In a many-body picture the relaxation energy can approximately be identified with the self-energy (Eq. 3.35) [77], which is contained in the spectral function.

Line widths in PES spectra are affected from broadening mechanisms in both initial and final states. Therefore, the experimentally observed line width

$$\Gamma_{\text{exp}} = \frac{(\Gamma_h/|v_{h\perp}|) + (\Gamma_e/|v_{e\perp}|)}{\left|(1/v_{h\perp})\left[1 - \left(m_e v_{h\parallel} \sin^2\theta/\hbar k_\parallel\right)\right] - (1/v_{e\perp})\left[1 - \left(m_e v_{e\parallel} \sin^2\theta/\hbar k_\parallel\right)\right]\right|} \tag{3.44}$$

includes both the width of the initial hole state Γ_h and the final electron state Γ_e [77]. Therein, m_e is the free-electron mass, $v_{h\perp}$, $v_{e\perp}$, $v_{h\parallel}$, $v_{e\parallel}$ are the group velocities ($v_{x\alpha} = \hbar^{-1}\partial \mathrm{E}_x/\partial \mathrm{k}_\alpha$) of hole ($x = h$) and electron ($x = e$) states normal ($\alpha = \perp$) and parallel ($\alpha = \parallel$) to the surface, and θ is the angle defined by the surface normal and the direction of detection. In the common experimental situation of normal emission, i.e., $\theta = 0$, Eq. 3.44 is reduced to

$$\Gamma_{\text{exp}} = \frac{\Gamma_h + \Gamma_e\,|v_{h\perp}/v_{e\perp}|}{1 - |v_{h\perp}/v_{e\perp}|}. \tag{3.45}$$

By further assuming a weak dispersion of the initial state compared to the final state, one finally ends up with the even more simplified form

$$\Gamma_{\mathrm{exp}} = \Gamma_h + \Gamma_e \left| v_{h\perp} / v_{e\perp} \right| . \tag{3.46}$$

In 2DESs, as studied in this thesis, the perpendicular group velocity of the hole state ($v_{h\perp}$) becomes zero, since a band dispersion in the surface states along the surface normal is absent. In consequence, the experimentally observed line width in a 2D system equals the one of the hole state, i.e., $\Gamma_{\mathrm{exp}} = \Gamma_h$. Therefore, in PES of surfaces line widths can primarily be related to the initial states.

Furthermore, the dipole matrix element (Eq. 3.29), which couples initial and final states, can induce additional modifications to the spectra [51]. This mainly concerns

- the effectiveness of light absorption in the dipole transition, which is influenced by the polarization and energy of the electromagnetic radiation,
- the availability of a final state at a certain momentum, required for the direct transition in the ultraviolet (UV) radiation regime, and
- intensity modulations due to diffraction of excited electrons in the crystal. These depend on the respective electron wavelength and crystal orientation.

Hence, an enhancement or a damping in the photoemission signal is oftentimes related to matrix element effects, and needs to be disentangled from other possible physical mechanisms. Such modifications again accentuate the importance of final state effects in the evaluation of PES data.

Final states in spin-resolved photoemission

Besides degenerate electron bands, also the spin in a spin-polarized initial state can be altered in the photoemission process under certain circumstances. The following discussion is based on the argumentation, presented in Refs. 51 and 107.

A spin-polarized initial state may arise from the exchange interaction or the SOI, as introduced in Sec. 2.1. Changes to the initial state spin polarization in a solid system can in principle be induced by:

- **Chiral sample effects**: Modifications of the spin polarization relating to the sample crystal symmetries have been reported both theoretically and experimentally for Pt(111) [51]. Here, the photoemitted electrons become spin-polarized along the direction normal to a mirror plane. Likewise, it has been suggested that the Au(111) surface should exhibit similar characteristics in normal emission. Possibly, spin polarization at chiral samples reflects a general trend in the (111) oriented *fcc* crystal surfaces and needs to be disentangled from the initial state spin polarization.

- **Final state interference**: The occurrence of this effect in solids would require the simultaneous occupation of two final states with different orbital angular momentum, following the dipole selection rule $\Delta l = \pm 1$. Resonant interference of these final states in photoemission then gives rise to highly spin-polarized electrons, even if linearly polarized or unpolarized radiation is used. However, such an excitation is not possible, if the initial states stem from s type orbitals, as it is often the case in experimental surface systems with notable SOI. Otherwise, a certain degree of hybridization or contributions from other orbitals would be required in the initial states.

- **Matrix element effects**: These do only become relevant, when circularly polarized radiation is used. Here, the size and degree of polarization in the initial state may be changed significantly. Yet, when using linearly polarized or unpolarized light, the spin polarization induced in the final states does not exceed 10–20 % of the initial state value. Therefore, the SARPES experiments shown in this thesis took use of (horizontal) linearly polarized radiation in the UV regime only. Moreover, also changes in the direction of light polarization and the photon energy are not expected to modify the initial state spin polarization notably.

3.3.2 Experimental aspects and instrumentation in photoelectron spectroscopy

Light sources

Photoemission experiments may be intersected into different categories with regard to their respective excitation energies, e.g., XPS and UPS. This requires suitable light sources for the desired experiment. In general, there exist laboratory light sources, like inert gas discharge lamps and x-ray tubes on the one hand, and large synchrotron radiation facilities on the other hand. While the first only provide distinct excitation energies, synchrotron radiation enables researchers to utilize tunable photon energies and allows to choose the polarization. Recently, UV laser sources have been introduced in low energy ARPES experiments [108].

Since all photoemission experiments shown in this thesis are synchrotron-based, the following paragraph will introduce the basic concept behind and some experimental aspects.

Synchrotron radiation

The largest flexibility and variability in photoemission experiments is provided by synchrotron radiation facilities. Modern third generation storage rings are *dedicated* light sources, which means that their main purpose is to produce radiation, rather than being a source for high kinetic energy particles. The photoemission experiments discussed

Table 3.1: *Typical parameters of third generation synchrotron radiation facilities, given for the two storage rings SLS and ALS. The brilliance is photon energy dependent and refers to the undulators "UE212/424" (SLS; $h\nu = 20\,eV$ [110]) and "U50" (ALS; $h\nu = 100\,eV$ [111]), which were used for the experiments in this thesis. All other data are taken from [109].*

Facility, Country	Storage-ring energy (GeV)	Current (mA)	Circum-ference (m)	Brilliance (photons/s /mrad^2/mm^2/0.1%BW)
SLS, Switzerland	2.4	400	288	3×10^{17}
ALS, USA	1.9	400	198	7×10^{18}

later in this thesis have been conducted at the Swiss Light Source (SLS) and the Advanced Light Source (ALS). A couple of reasons exist to favor synchrotron radiation over laboratory sources. Among these, the photon energy dependent

$$\text{Brilliance} = \frac{photons/s}{(\text{mrad})^2(\text{mm}^2\,\text{source area})(0.1\,\%\,\text{bandwidth})} \tag{3.47}$$

of an insertion device (see discussion below) describes the amount of photons available per second, source area, and angular spread in relation to the bandwidth [109]. It is a measure of the quality of light delivered by the storage ring. A high value leads to enhanced count rates in ARPES experiments, and thus yields short measurement intervals, which are important in spectroscopy of sensitive surfaces, degenerating with time. Modern facilities reach high brilliance values, as listed in Tab. 3.1.

The basic layout of all synchrotron radiation sources is shown in Fig. 3.14(a) [109]. Each synchrotron needs a source for charged particles, which are electrons in most cases. These are generated in the electron gun by thermionic emission, before being accelerated to $\approx 100\,\text{MeV}$ in the linear accelerator (LINAC). The adjacent booster ring is an additional pre-accelerator, which enhances the electron energies to the GeV-range (close to the speed of light), before injection into the main storage ring occurs. Therefore, the motion of the electrons has to be treated relativistically. The main consequence is that radiation, due to the electron's circular motion, is emitted in a small cone tangentially to their path in forward direction.

Modern storage rings are operated in the *top-up mode*, which means that injection happens quasi continuously, and the ring current is maintained at its setpoint value. The storage ring is equipped with bending magnets to keep the electrons on their quasi-circular path, quadrupole magnets for beam focusing, and sextupole magnets for corrections due to chromatic aberration. Radiation from the bending magnets has a wide emission cone and a large energetic spread. In contrast, insertion devices represent an even more flexible alternative to extract radiation from the beam of electrons. After its generation the radiation is shaped, filtered, weakened, and controlled with a front-end

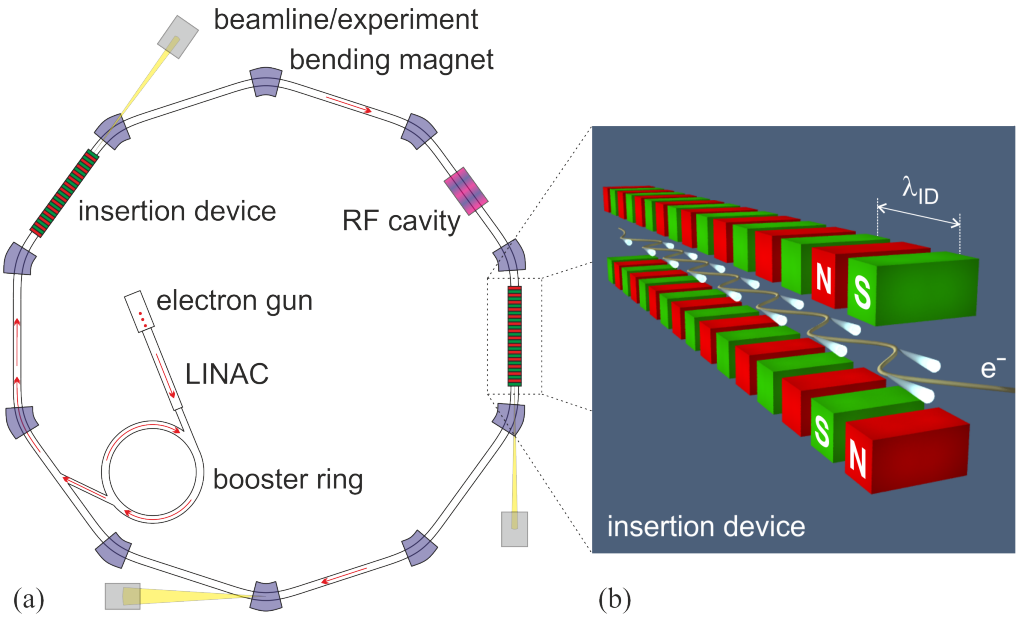

Figure 3.14: *(a) General layout of a synchrotron storage ring. Charged particles (usually electrons) are generated in the electron gun, before gaining kinetic energy in the LINAC. The following booster ring enhances the electron's kinetic energy to the final value, which corresponds to almost the speed of light. After injection into the main storage ring energy losses are balanced in RF cavities. The ring itself consists of bending magnets at the corners, connecting straight sections with insertion devices along these. Radiation for experiments is produced at both the bending magnets, with a wide cone of light and a large spread in energy, and in the insertion devices. (b) The latter consist of linear arrays of magnets with alternating field orientation (period λ_{ID}), which force the electrons to follow an undulated path of flight. At the positions of highest deflection a maximum of radiation is generated, with small cones of light adding up to the total intensity produced by the insertion device. The amplitude of the undulating electron path is highly exaggerated for better visualization.*

aperture, before striking onto a monochromator, which selects a certain wavelength to be used in the adjacent experiment. The radiative loss in kinetic energy is restored in radio frequency (RF) driven cavities, installed along the ring.

Insertion devices consist of a linear array of magnets with alternating magnetic field (period λ_{ID}), as it is shown in Fig. 3.14(b). The electrons traveling along its lateral direction are bent with alternating directions onto an undulating path of motion. Radiation is emitted throughout their passage, being highest at the positions of largest deflection, as indicated by the radiative cones. Insertion devices are intersected into two different subgroups, i.e., *wigglers* and *undulators* [109]. Wigglers consist of fewer but stronger magnets than undulators. The undulation amplitudes in a wiggler are larger, and the single radiation cones do not overlap. Yet, in an undulator, the narrower cones overlap, and in contrast to the broad energy spectrum of a wiggler, constructive interference leads to a distinct spectrum with one main resonance line and a couple of higher harmonics. For a monochromatic beam these higher harmonics are efficiently suppressed, and the full width at half maximum (FWHM) of the main line is additionally sharpened by a

monochromator.

The flexibility of an undulator bases on the possibility to adjust the magnetic field, which allows the experimenter to tune the photon energy of choice. The polarization of light is linear for both wiggler and undulator, as shown in Fig. 3.14(b). By shifting the upper or lower row of magnets by $1/4\,\lambda_{\mathrm{ID}}$, the electrons follow a helical path, and the radiation becomes circular [109]. In combination with a plane grating monochromator, a sharp spot of radiation with narrow bandwidth and high photon flux is available. These are excellent conditions for a variety of photoemission experiments, which are not possible in a standard laboratory environment.

These outstanding capabilities have been utilized for photoemission studies in this thesis. Experiments on Au/Ge(111)-($\sqrt{3}\times\sqrt{3}$) have been performed at the *Surface and Interface Spectroscopy* (SIS) undulator beamline at the SLS, using the *High Resolution Photoemission Spectroscopy* (HRPES) and the *COmplete PHotoEmission Experiment* (COPHEE) for band mapping (total energy resolution of the setup $\Delta E_{\mathrm{tot}} = 20\,\mathrm{meV}$) and spin-resolved photoemission, respectively [110]. The beamline covers a photon energy range from 10 to 800 eV and allows use of linearly (horizontal/vertical) and circularly polarized light, with a spot size of $50 \times 100\,\mu\mathrm{m}^2$ on the sample (at $h\nu = 200\,\mathrm{eV}$). The respective experiments are subject of Ch. 6.

Measurements on Sn/Si(111)-($\sqrt{3}\times\sqrt{3}$) were conducted at beamline 7.0.1 at the ALS, making use of the *electronic structure factory* (ESF) endstation [112]. The available photon energies range from 78 – 1200 eV with linear polarization only and with a spot size of $50 \times 50\,\mu\mathrm{m}^2$ on the sample.

Experimental setup of angle-resolved photoelectron spectroscopy

The theoretical concepts of ARPES have already been discussed in section 3.3.1. Here, some experimental aspects will be illuminated further.

Electron spectrometer

Spectrometers of the HDA type have a common layout, that includes three main sections:

- A lens system, which focuses and retards the electrons.
- The deflector, consisting of two concentric hemispheres at different radii, with the electrons traveling in a radial electric field between them.
- A detector, which amplifies the incoming electrons with position sensitivity and converts them into an electric signal.

The functional principle of such a spectrometer shall now be discussed briefly on the basis of Fig. 3.15. Electrons with kinetic energy E_{kin}, excited by an incident beam of light, enter the retarding lens system (red) under an angular acceptance angle 2α. The lens system consists of a gridless array of electrostatic lenses within a linear tube, serving

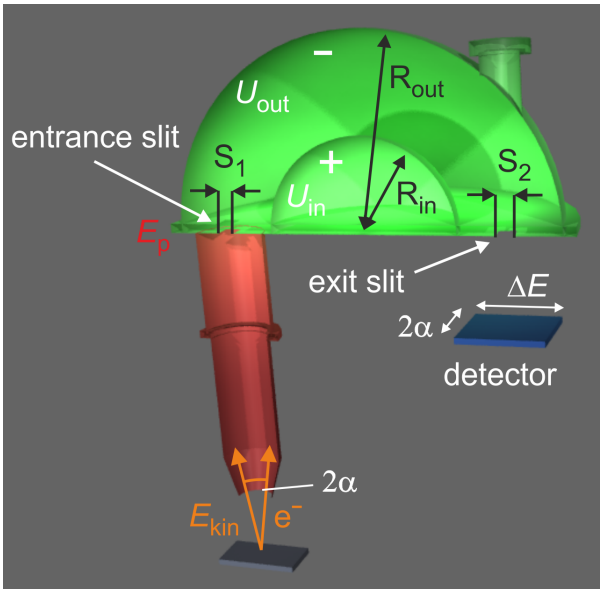

Figure 3.15: *Cut through a HDA. (Red) Photoexcited electrons within the angular acceptance 2α enter the lens system, where they are retarded to the pass energy E_p and focused on the entrance slit. (Green) Electrons between the two HDA spheres are separated with respect to their kinetic energy onto elliptical trajectories by a radial electric field. Only those electrons at $E_p \pm 1/2\,\Delta E$ travel on the mean radius $(R_{\text{out}} + R_{\text{in}})/2$ and traverse the exit slit. (Blue) MCP for angle- and energy-resolved detection of photoelectrons.*

two main functions: i) retarding the electrons to the pass energy E_p, and ii) imaging the electrons from the sample onto the entrance slit. Depending of the desired experiment, the lens system can be operated at a *fixed retarding ratio (FRR)*, or with a *fixed analyzer transmission (FAT)* [113]. In FRR the pass energy of the electrons at the entrance slit is defined by

$$E_p = E_{\text{kin}}/R, \tag{3.48}$$

with R being the retarding ratio. In FAT however, the pass energy is given by

$$E_p = -qk\Delta U \tag{3.49}$$

and is thus only defined by the voltage $\Delta U = U_{\text{out}} - U_{\text{in}}$, applied to the hemispheres (k is a calibration constant). In this thesis it was only made use of the FAT mode, which is most suitable for ARPES.

The retarded electrons (mean kinetic energy E_p) at the entrance slit of width S_1 enter the space between the inner and outer hemispheres (green) with potential difference ΔU. The resulting radial electric field in between forces them to travel on elliptical trajectories to the exit slit (width S_2). Only those electrons with kinetic energy $E_{\text{kin}} = E_p \pm 1/2\,\Delta E$ ($\Delta E \approx 1/5\,E_p$) follow orbits that allow them to exit the analyzer. Electrons with higher (lower) energy hit the outer (inner) hemisphere before reaching the exit slit. In this way, only the small energy window ΔE is detected at the same time. For imaging on a larger

energy scale the retarding voltage is swept in a window of desired range, thus recording intensity from higher or lower kinetic energies additionally. The detector unit (blue) usually consists of a MCP for simultaneous 2D electron amplification and a fluorescence screen, with a charge-coupled device (CCD) behind for detection and conversion into an electrical signal. The whole configuration is effectively shielded by a μ-metal housing against disturbing external fields, yielding values far below the earth's magnetic field.

Depending on the experimental purpose, one out of three different modes of operation can be chosen [113]. These are: **i)** the *spatially resolved mode*, where the image plane of the sample is directly projected onto the entrance slit; **ii)** the *transmission optimized mode*, where electrons from a small spot on the sample are projected with high angular acceptance onto the entrance slit. This is most suitable for XPS studies; **iii)** the *angular resolved modes* image electrons within a small angular range (down to 0.05 °), which is needed for 2D detection in ARPES (band mapping).

The energy resolution of the analyzer is an important quantity especially in angular resolved band mapping, where small spectroscopic features are scrutinized. The resolution of the HDA

$$\Delta E_{\mathrm{an}} = E_p \cdot \frac{S_1 + S_2}{2(R_{\mathrm{out}} + R_{\mathrm{in}})} + \frac{\alpha^2}{4} \tag{3.50}$$

may be tuned by adjusting slit widths, the pass energy, and the angular acceptance. However, any improvement in energy resolution always involves a decreased photoemission signal. Thus, in order to maintain a reasonable signal-to-noise ratio, the analyzer settings should be limited to suitable values, depending on both the material system under observation and the brightness of the photon source. Furthermore, setting the analyzer to a high resolution is only useful, if other broadening mechanisms are smaller. In general, the total resolution in a PES experiment is given by a convolution of the analyzer resolution ΔE_{an} (see Tab. 3.2), the lifetime broadening of the respective electronic state $\Delta E_{\mathrm{lifetime}}$, and the line width of the excitation source $\Delta E_{\mathrm{photon}}$ [113]. Assuming Gaussian profile shapes, the total FWHM is obtained as

$$\Delta E_{\mathrm{tot}} = \left(\Delta E_{\mathrm{an}}^2 + \Delta E_{\mathrm{lifetime}}^2 + \Delta E_{\mathrm{photon}}^2\right)^{1/2}. \tag{3.51}$$

In particular, this becomes relevant for the determination of the Fermi level E_F in photoemission spectra, which is done in this thesis by fitting the function

$$f_{\mathrm{eff}}(E,T) = c_1 + c_2(E - E_F) + \frac{c_3 + c_4(E - E_F)}{e^{\frac{E-E_F}{k_B T_{\mathrm{eff}}}} + 1} \tag{3.52}$$

to a metallic band edge in an energy distribution curve (EDC). Here, the Fermi distribution is multiplied by a linearly increasing density of states (fit parameters c_3 and c_4), while a linear background is also accounted for (c_1 and c_2). The *full broadening* of the Fermi edge $4k_BT_{\mathrm{eff}}$ (k_B is the Boltzmann factor) which one observes in the experiment, is basically a convolution of three independent contributions, i.e., **i)** the *true broadening*

Table 3.2: *Analyzer energy resolution ΔE_{an} in dependence of the pass energy E_p for different entrance slits. All parameters relate to the VG Scienta R4000 HDA, installed at beamline 7.0.1 at the ALS [114].*

slit no.	1	2	3	4	5	6	7	8	9
shape	curved	straight	curved	straight	curved	straight	curved	straight	straight
width (mm)	0.1	0.2	0.2	0.3	0.3	0.5	0.5	1.5	4.0
length (mm)	25	30	25	20	25	30	25	30	30
E_p (eV)	ΔE_{an} (meV)								
2	0.5	1	1	1.5	1.5	2.5	2.5	7.5	20
5	1.25	2.5	2.5	3.75	3.75	6.25	6.25	18.75	50
10	2.5	5	5	7.5	7.5	12.5	12.5	37.5	100
20	5	10	10	15	15	25	25	75	200
50	12.5	25	25	37.5	37.5	62.5	62.5	187.5	500
100	25	50	50	75	75	125	125	375	1000
200	50	80	80	150	150	250	250	750	2000

$4k_BT$ at E_F for the temperature T, given by the Fermi distribution, **ii)** the line width of the light source $\Delta E_{\mathrm{photon}}$, and **iii)** the analyzer resolution ΔE_{an}. $4k_BT_{\mathrm{eff}}$ covers a region from ~ 10 to $\sim 90\,\%$ of the intensity around E_F. The lifetime broadening of the respective state shall be neglected here. For simplicity this convolution is replaced by the pseudo Fermi function $f_{\mathrm{eff}}(E,T)$ with the effective temperature T_{eff} in Eq. 3.52. This approach simplifies the deconvolution of the three components in the energy broadening to

$$4k_BT_{\mathrm{eff}} = \left[(4k_BT)^2 + \Delta E_{\mathrm{an}}^2 + \Delta E_{\mathrm{photon}}^2\right]^{1/2}. \tag{3.53}$$

Since all terms in brackets are known in the experiment, one can derive an estimate of $4k_BT_{\mathrm{eff}}$ in case of a metallic edge at the given temperature T. If the result ranges significantly lower than the $4k_BT_{\mathrm{eff}}$ obtained from fitting with Eq. 3.52, metallicity is only marginal or even absent, and in turn, the respective state is insulating. As an example, typical estimates for measurements at $T = 10\,\mathrm{K}$ and $T = 300\,\mathrm{K}$ are $4k_BT_{\mathrm{eff}} \approx 28\,\mathrm{meV}$ and $4k_BT_{\mathrm{eff}} \approx 107\,\mathrm{meV}$, respectively ($\Delta E_{\mathrm{an}} = 15\,\mathrm{meV}$, $\Delta E_{\mathrm{photon}} = 23\,\mathrm{meV}$; cf. Tab. 3.2).

An additional benefit of an HDA is that the determination of a sample's work function is obsolete, since analyzer and sample are in electrical contact, and the Fermi energies are at the same level. The kinetic energy measured by the spectrometer E'_{kin} and its work function ϕ_{an} are connected to the corresponding values in the electron's frame by

$$E_{\mathrm{kin}} + \phi_A = E'_{\mathrm{kin}} + \phi_{\mathrm{an}}. \tag{3.54}$$

According to Eq. 3.20, with calibrated, and thus known ϕ_{an}, the PES signal can be evaluated without knowledge of ϕ_A.

Endstations at the synchrotron

The ARPES measurements in this thesis were performed using a VG Scienta R4000 HDA, installed at both the HRPES (SLS) and the ESF (ALS) endstations. It has a

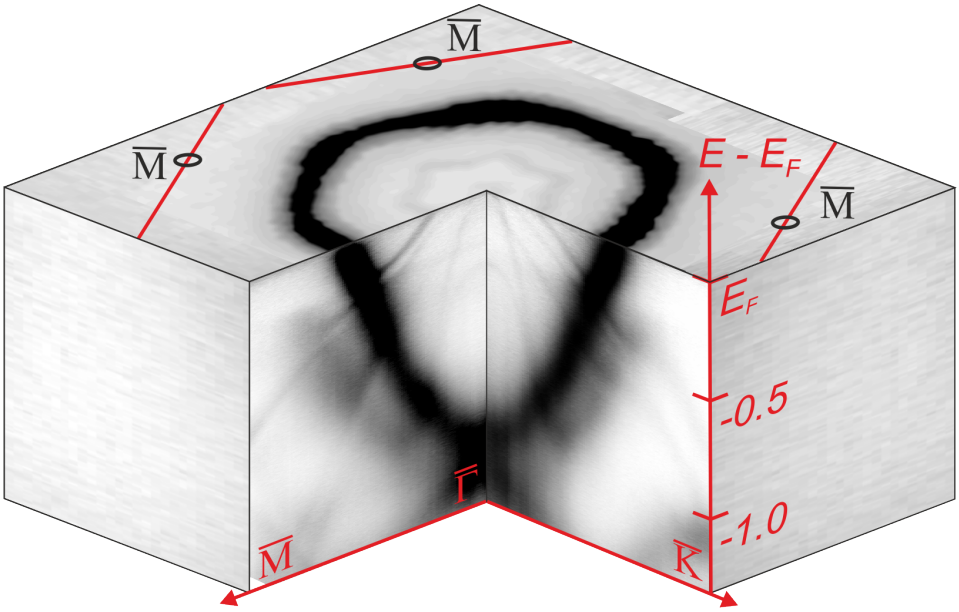

Figure 3.16: *3D visualization of the electronic band structure of Au/Ge(111)-($\sqrt{3} \times \sqrt{3}$), obtained by FS mapping in the second SBZ at $T = 130\,K$ ($h\nu = 35\,eV$). Dark contrast corresponds to high photoemission intensity. The FS map (on top) and the two band maps along the cutting edges have been normalized to maximum intensity and symmetrized, with respect to the $C_{3\nu}$ symmetry of the system. Red lines indicate the zone boundaries. Details on the band structure may be found in Sec. 6.2.1.*

mean radius of 200 mm and an angular acceptance $2\alpha = 38\,^\circ$, with an angular resolved range of $\pm 15\,^\circ$. The angular resolution is $0.1\,^\circ$ at very small beam spot sizes (~ 0.1 mm), and an energy resolution of $\Delta E_{\mathrm{an}} = 1.8$ meV, or even lower than 1 meV under optimal experimental conditions, is achievable [114]. Different entrance slits with either curved or straight shape are positioned on a rotary array. Due to geometrical considerations, curved slits lead to an undistorted energy scale but a trapezoidal distortion on the angular axis. For straight slits the opposite is true. The achievable analyzer resolution ΔE_{an} in dependence of the pass energy is given in Tab. 3.2 for each slit.

Each of the two endstations is further equipped with a 6-axis goniometer, which may be cooled down to ≈ 10 K, utilizing a liquid helium flow cryostat. It further provides full flexibility in sample positioning in front of the analyzer for FS mapping. In this way, single 2D band maps at selectable positions in k-space can be recorded in a slice-by-slice procedure. For this, the goniometer's polar angle is turned in small steps to capture an array of band maps. These are then stacked to a 3D cuboid, that contains the complete electronic valence band structure in the predefined energy and in-plane momentum range. An example is provided in Fig. 3.16, showing the electronic band structure of Au/Ge(111)-($\sqrt{3}\times\sqrt{3}$) in the 2nd surface Brillouin zone (SBZ) at $T = 130$ K. This ARPES cuboid contains multiple band maps along two orthogonal scan directions in reciprocal space. Depending on the respective settings, 3D FS mapping can cover

even larger momentum areas than comprised by a whole SBZ. A part of the cuboid has been cut off in order to visualize the band dispersion in energy direction. Details on the band structure of Au/Ge(111)-($\sqrt{3} \times \sqrt{3}$) may be found in Sec. 6.2.1.

Spin-resolved photoelectron spectroscopy

In PES there are three main observables to be detected. Two of them are already covered in an ARPES experiment, i.e., the kinetic (or binding) energy of an electron and the respective momentum. The electron spin as third quantity is not obtained so far and is subject of investigation in spin-resolved ARPES (SARPES) experiments. This technique has been used to determine the spin texture in Au/Ge(111)-($\sqrt{3} \times \sqrt{3}$) in Sec. 6.3.

The spin polarization is defined as the vector of expectation values of the electron spin operator $\mathbf{S}$ for a certain state or ensemble of states:

$$\mathbf{P} = \frac{2}{\hbar} \left(\langle S_x \rangle , \langle S_y \rangle , \langle S_z \rangle \right) = \left(P_x, P_y, P_z \right) , \tag{3.55}$$

with $P \leq 1$ [115, 116]. For a beam of photoelectrons with total intensity $I = I_\alpha^\uparrow + I_\alpha^\downarrow$ the three spatial components

$$P_\alpha = \frac{I_\alpha^\uparrow - I_\alpha^\downarrow}{I_\alpha^\uparrow + I_\alpha^\downarrow} \tag{3.56}$$

of the polarization vector $\mathbf{P}$ are related to the spin-sensitive intensities $I_\alpha^\uparrow$ and $I_\alpha^\downarrow$ along the respective coordinate axis ($\alpha = x, y, z$), with parallel ($\uparrow$) or antiparallel ($\downarrow$) spin orientation.

In an ideal spin polarimeter a beam of spin-polarized electrons with defined dispersion $E_{\text{kin}}(\mathbf{k})$ enters a spin separator, which divides the total intensity I into the two partial intensities $I_\alpha^\uparrow$ and $I_\alpha^\downarrow$, depending on their respective spin orientation. Thus, a Stern-Gerlach type experiment with a particle beam passing a magnetic field, with a gradient transversal to the direction of motion, would be favorable. However, this kind of experiment does not work for charged and low-mass particles, such as electrons [115]. Today, most experiments designed for the spin-sensitive separation of electrons are based on relativistic scattering at a thin foil target of a heavy element, as originally described by N. F. Mott in 1929 [117]. The mechanism behind can be understood as follows [118]. Imagine an electron traveling at a relativistic speed $\mathbf{v}$ in the electric field

$$\mathbf{E} = \frac{Ze}{r^3}\mathbf{r} \tag{3.57}$$

of a target atom with atomic number Z. The position vector $\mathbf{r}$ denotes the electron's distance from the center of the atomic core here. The electric field then transforms to the magnetic field $\mathbf{B} = c^{-2}(\mathbf{v} \times \mathbf{E})$ in the rest frame of the electron (see also Sec. 2.1). By utilizing the electron's orbital angular momentum $\mathbf{L} = m_e(\mathbf{r} \times \mathbf{v})$, one derives

$$\mathbf{B} = \frac{Ze}{c^2 r^3}(\mathbf{v} \times \mathbf{r}) = -\frac{Ze}{m_e c^2 r^3}\mathbf{L}. \tag{3.58}$$

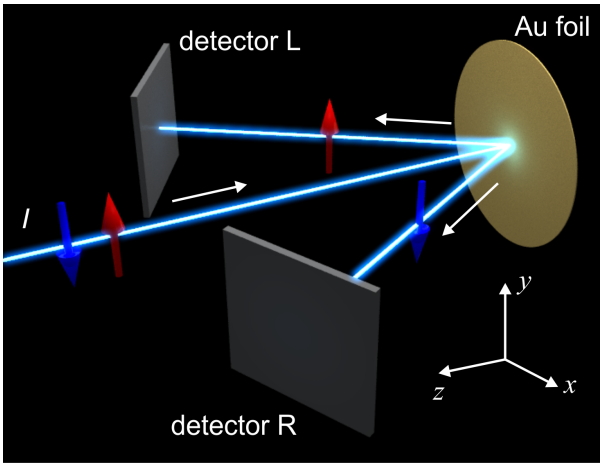

Figure 3.17: *Schematic visualization of a Mott backscattering experiment. A beam of relativistic electrons with intensity I and polarization perpendicular to the scattering plane (x,z) impinges on a thin gold foil. Due to the SOI in the Au atomic core potentials, the backscattering direction is spin-sensitive, which becomes visible in form of an asymmetric number of counts in the respective detectors.*

The electron's spin magnetic moment $\boldsymbol{\mu_s} = -(2\mu_B/\hbar)\mathbf{S} = -\mu_B\boldsymbol{\sigma}$ then interacts with the magnetic field, which thus leads to a SOI-induced contribution

$$V_{\mathrm{SO}} = -\boldsymbol{\mu_s} \cdot \mathbf{B} = -\frac{Ze\mu_B}{2m_e c^2 r^3}\mathbf{L} \cdot \boldsymbol{\sigma} \tag{3.59}$$

to the scattering potential. Note that a factor 1/2 is added to account for the Thomas precession here [118]. As a consequence of the SOI in Eq. 3.59, the angle-dependent scattering cross section is affected by the spin polarization of the incident electrons. Those with a spin component perpendicular to the scattering plane (x,z) possess a larger probability to be scattered to the left or right, respectively, depending on the sign of the vertical spin orientation ($\uparrow$, *up* or $\downarrow$, *down*). Accordingly, a left-right asymmetry

$$A_\alpha = \frac{N_\alpha^L - N_\alpha^R}{N_\alpha^L + N_\alpha^R} \tag{3.60}$$

in the backscattered signal is observed for a beam of spin-polarized electrons. Here, N_α^L (N_α^R) is the count number in the left (right) detector. This basic concept of a *Mott backscattering experiment* is shown schematically in Fig. 3.17 [118].

The typical target of choice is gold, since it offers a good compromise between material inertness and high atomic number ($Z_{\mathrm{Au}} = 79$) [119]. Energy sensitive silicon diodes, which are positioned to the left and right of the target within the scattering plane, serve as detectors. In case of an electron beam which is 100 % spin-polarized, one obtains the maximum scattering asymmetry $A_{\alpha,\mathrm{max}} = S$, with the *Sherman function* S defining the analyzing power of the scattering experiment [118, 120, 121]. Accordingly,

the polarization is connected to the asymmetry by

$$P_\alpha = \frac{A_\alpha}{S}. \tag{3.61}$$

Unfortunately, the polarimeter efficiency in a Mott scattering experiment, defined by the figure of merit

$$\epsilon = \frac{N}{N_0} S^2, \tag{3.62}$$

with N the number of detected electrons and N_0 the number of incoming electrons, is rather bad ($\epsilon \approx 10^{-4} \ldots 10^{-3}$). This disadvantage is partly overcome by utilization of synchrotron radiation with its high photon flux.

For a complete determination of the spin asymmetry transverse to the incoming electron beam, two additional detectors (detector B and detector F) are added to the setup. These must be rotated by 90 ° around the beam axis with respect to detectors L and R. However, such a setup is still not suited to determine the z-component of the spin. This disadvantage is overcome in the *COmplete PHotoEmission Experiment (COPHEE)* apparatus, which provides ARPES in conjunction with a 3D spin polarimeter. All three spin components are obtained by two separate Mott stages, positioned at an angle of 90 ° to each other, with a total number of eight detectors, see Fig. 3.18(a). Electrons with a given spin orientation are first projected onto the entrance slit of an Omicron EA125 HDA for energy separation. Hereafter, the beam of electrons is deflected alternatingly into both Mott detectors at a chopper frequency of 2 Hz, with the spin orientation unaffected by the deflecting fields [119]. Both Mott detectors operate at high voltage ($\sim$ 40 kV), thus providing the required relativistic speed [49]. The special geometry of the Mott detectors (each rotated by 45 ° with respect to the electron beam) guarantees a full 3D spin detection:

- Polarimeter I: Detection of the spin y (detectors I,L and I,R) and z component (detectors I,B and I,F).
- Polarimeter II: Detection of the spin x (detectors II,L and II,R) and (again) z component (detectors II,B and II,F).

In this way, a complete 3D data set, containing **i)** the total measured intensity $I(E_{\mathrm{kin}}, \mathbf{k})$ and **ii)** the spin polarizations $P_x(E_{\mathrm{kin}}, \mathbf{k})$, $P_y(E_{\mathrm{kin}}, \mathbf{k})$, and $P_z(E_{\mathrm{kin}}, \mathbf{k})$, is collected either as a momentum distribution curve (MDC) (line of constant energy E_{kin}) or as an energy distribution curve (EDC) (line of constant momentum $\mathbf{k}$). Based on these data, one can calculate the spin-resolved intensities related with a spin-polarized band. A comprehensive description of COPHEE data evaluation is given in Sec. A.2.

The experiment itself can be performed at various temperatures, since the 5-axis goniometer allows for liquid nitrogen and helium cooling, as well as direct current heating [see Fig. 3.18(b)]. Further installed equipment includes UV and x-ray sources, an Ar^+ ion sputter gun, electron beam evaporators, and a LEED optics for sample characterization

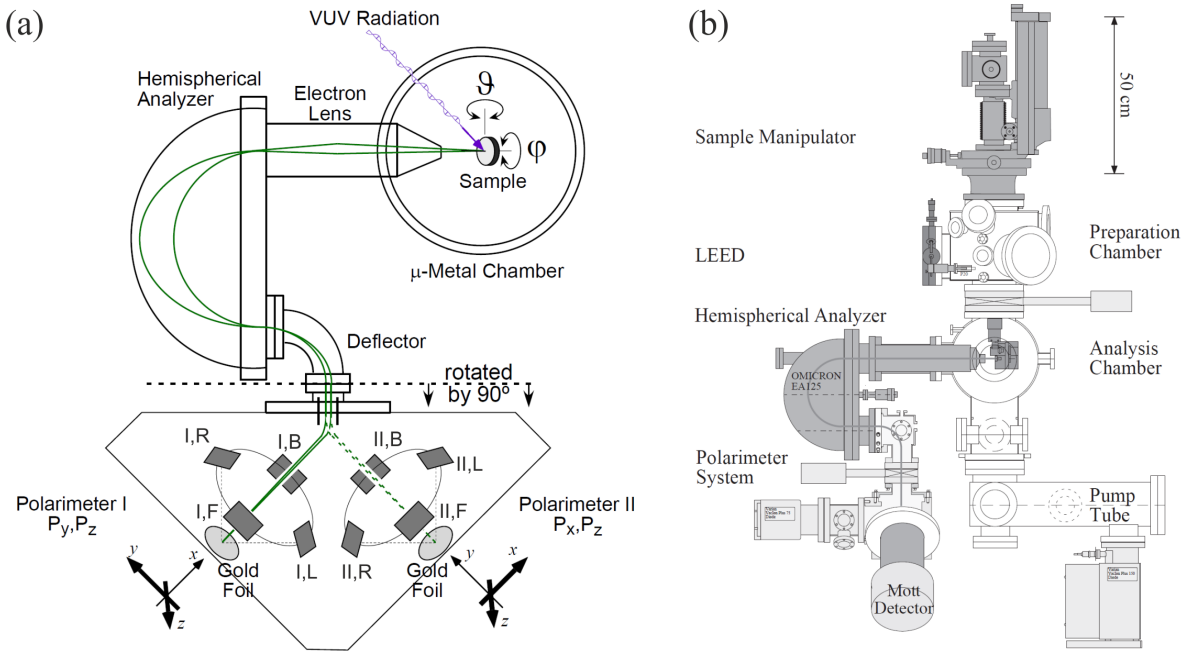

Figure 3.18: *(a) Principle of 3D spin detection at the COPHEE endstation. Spin-polarized photoelectrons from the sample are guided through a lens system to a HDA, where only those with the desired kinetic energy pass. These electrons are further guided and deflected at a frequency of 2 Hz alternatingly into one of the two polarimeter stages, oriented at an angle of 90° to each other. Polarimeter I scans the y and z spin asymmetry, and polarimeter II the x and z spin asymmetry. (b) Drawing of the COPHEE endstation. Sample preparation under UHV conditions is performed in the preparation chamber by utilization of a 5-axis goniometer, with the surface quality controlled by a LEED optics. The adjacent analysis chamber is separated by a gate valve. Both drawings are taken from [122], Copyright (2002) by the University of Zurich.*

prior to the SARPES experiment. The HDA may further be used in a spin-integrated mode with the Mott detectors switched off, while three channeltrons are used for electron detection. The Sherman function of the COPHEE apparatus, which is relevant for the detection efficiency (see Eq. 3.62), was determined as $S = 0.068$ from an earlier calibration. The resolution in energy is 120 meV for spin-sensitive and 100 meV for spin-integrated measurements at $E_p = 5\,\text{eV}$ [122]. The angular resolution has not been tested, but is assumed to be lower than 1° [122].

4 Semiconductor substrates

4.1 Surface reconstructions of Si(111) and Ge(111)

The realization of triangular lattices at crystalline surfaces strongly depends on a suitable substrate, that presets the necessary 120 ° rotational symmetry along the surface normal. Such a situation is given at the (111) surfaces of elements located in group IV of the periodic table. In particular, the elemental semiconductors silicon and germanium belong to this group, and moreover provide advantageous electronic properties, since both have indirect RT band gaps of $E_{\mathrm{gap}} = 1.107\,\mathrm{eV}$ and $E_{\mathrm{gap}} = 0.67\,\mathrm{eV}$ in size, respectively. Si and Ge possess the diamond cubic crystal structure, which basically consists of two *fcc* lattices, being shifted by $(1/4, 1/4, 1/4)\,g$ with respect to the lattice constant g, see Fig. 4.1(a). This common crystal structure does also result in a variety of other similar physical properties, which are summarized in Tab. 4.1. In particular, the lattice constants differ only slightly between both materials, with that of Ge surmounting the Si one by about 4 %. The respective surface lattice constant $a = |\mathbf{a}_1| = |\mathbf{a}_2| = 3/4 \sin(70.5\,^\circ) g$ is then easily obtained from its bulk pendent g by consideration of the tetrahedral coordination of each atom. It marks an important parameter necessary for the description of surface reconstructions.

The (111) surface is obtained by cleaving the crystal along the plane perpendicular to the [111] direction, which ends up with two possible surface terminations. The first option is an intact surface bilayer, which is the natural cleavage plane, whereas the second option is a missing top layer (MTL) situation, where the upper sublattice "A" of the bilayer is missing. These two possibilities exhibit strongly deviating energetics, as the number of unpaired orbitals differs by a factor of three between the bilayer and the MTL cut. The following discussion sets the focus on the intact bilayer configuration, which is depicted in Fig. 4.1(b). It represents a bipartite lattice, consisting of a deeper hexagonal lattice "B" and a higher one "A". One further denotes three different locations on the surface, i.e., T_1, T_4, and H_3, which will become relevant as adsorption sites for the different kinds of adatoms in the following chapters.[1]

So far we have only discussed *ideally truncated* crystals, neglecting the energetics at the surface. In fact, the cleavage disrupts the bonds between the Si (Ge) atoms and leaves half-filled sp^3 hybridized orbitals [dangling bonds (DBs)] behind. This leads to

[1] H_3: hollow site, with the next atom below located in the fourth substrate layer; T_i: atop site, with the next atom below located in the bilayer (first/second substrate layer). The index i corresponds to the symmetry related to the lattice site.

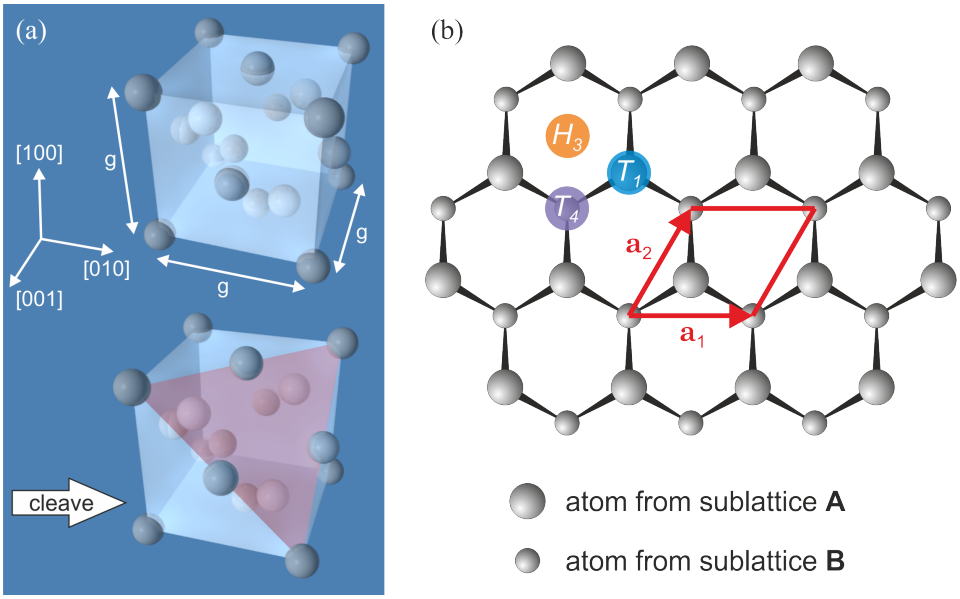

Figure 4.1: *(a) Schematic visualization of the cleavage plane perpendicular to the [111] direction in the diamond cubic lattice (lattice constant g). (b) The topmost bilayer of the unreconstructed (111) surface, built up by atoms from the two hexagonal sublattices "A" and "B". The colored circles represent the different lattice sites relevant for adsorption processes. The surface basis vectors* $\mathbf{a}_1$ *and* $\mathbf{a}_2$ *define the size of the* (1×1) *surface unit cell (area outlined in red).*

an unstable situation, and the system tends to lower the surface energy by minimizing the number of DBs per unit cell. In turn, this includes a lattice distortion at the surface with slight propagation into the bulk due to the bending of the bonds. This second process consumes a certain amount of energy. Thus, the interplay between band structure energy by the saturation of DBs on the one hand, and the elastic energy necessary to distort the lattice on the other hand, determines the energetic stability at the surface. For Si(111) the idealized (1×1) reconstruction after the cleave is unstable, and a (1×2) reconstruction is observed instead [125]. This phase has a surface energy

Table 4.1: *Selection of fundamental physical properties of the bulk semiconductors Si and Ge, the noble metals Ag, Pt, and Au, and the metal Sn under normal conditions. Among these, g denotes the bulk lattice constant, and a is the corresponding (111) surface lattice constant. Cf. Refs. 123 and 124.*

Element	Atomic weight	Covalent radius (Å)	g (Å)	a (Å)	Density (g/cm^3)	Melting point (°C)	Electron configuration	Bulk band gap (eV)
Si	28.0855	1.11	5.4309	3.840	2.330	1414	[Ne] $3s^2\ 3p^2$	1.107
Ge	72.64	1.22	5.6575	4.000	5.323	938.3	[Ar] $3d^{10}\ 4s^2\ 4p^2$	0.67
Ag	107.8682	1.53	4.0853	2.889	10.490	961.78	[Kr] $4d^{10}\ 5s^1$	—
Sn (α-Sn)	118.710	1.41	5.8318	4.123	7.310	231.93	[Kr] $4d^{10}\ 5s^2\ 5p^2$	0.08
Pt	195.084	1.28	3.9242	2.775	21.09	1768.3	[Xe] $4f^{14}\ 5d^9\ 6s^1$	—
Au	196.967	1.44	4.0782	2.884	19.300	1064.18	[Xe] $4f^{14}\ 5d^{10}\ 6s^1$	—

lowered by 0.36 eV with respect to the (1×1) unit cell [126]. If one additionally provides a certain activation energy (thermal anneal), an irreversible transition from the metastable (1×2) phase to the even more stable Si(111)-(7×7) surface reconstruction occurs (energy lowered by 0.403 eV [127]) at elevated temperatures of $T \approx 500 - 700\,^{\circ}\mathrm{C}$ [128].

Si(111)-(7×7)

The Si(111)-(7×7) phase [129], as the most stable reconstruction at RT, is accurately described within the dimer adatom stacking fault (DAS) model, proposed by K. Takayanagi *et al.* in 1985 [130], which is in agreement with STM investigations performed soon after [131]. Fig. 4.2 shows this model in both top view and side view representation. It is clearly visible that strong deviations from the ideally truncated crystal [Fig. 4.1(b)] dominate this phase. The number of DBs per unit cell is lowered by the 12 Si adatoms in the (7×7) unit cell, that reside on top of T_4 lattice sites. An even further decrease in surface energy is supported by the formation of 9 Si dimers, that surround the left triangular half of the unit cell along its boundary. This however, involves a stacking fault in the substrate underneath within this region [dark shaded area in Fig. 4.2(a)]. In sum, the saturation significantly reduces the total energy of the surface, as the number of DBs is decreased from 49 per (7×7) unit cell in the ideally truncated (111) surface to 19 for the reconstructed surface. An additional prominent feature is the *corner hole*, being associated with a DB atom, which marks the origin of the (7×7) unit cell. There are also six restatoms at T_1 sites within the bilayer, whose DBs remain unsaturated.

Ge(111)-(2×8)

Similarly as for Si(111), the cleaved Ge(111) surface exhibits a (1×2) reconstruction, before an irreversible transition to the most stable $c(2 \times 8)$ phase occurs at $\approx 300\,^{\circ}\mathrm{C}$ [132]. The corresponding structural model of the Ge(111)-$c(2 \times 8)$ surface reconstruction

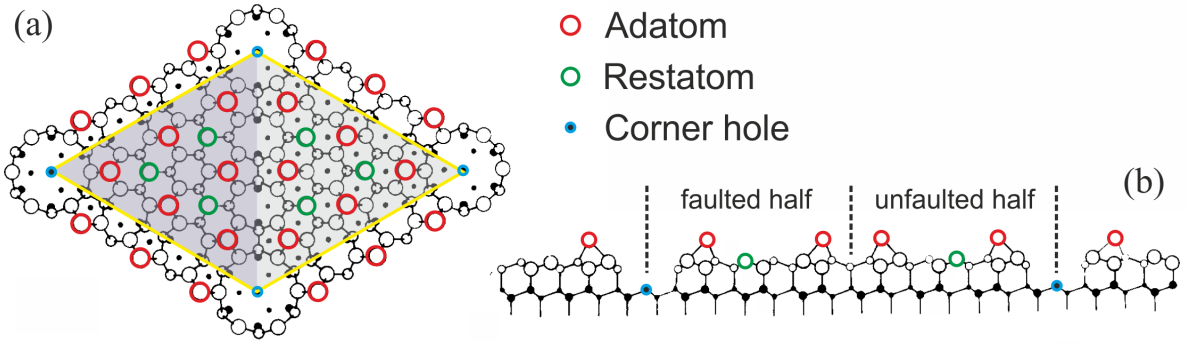

Figure 4.2: *(a) Top view of the (7×7) unit cell at the reconstructed Si(111) surface, as described within the DAS model; according to Ref. 130. The unit cell is subdivided into two halves due to a stacking fault in the left half (dark shaded). Further main characteristics are 1 corner hole, 12 adatoms, and 6 restatoms per (7×7) unit cell. (b) Side view along the longer diagonal in the (7×7) unit cell, illustrating the stacking order.*

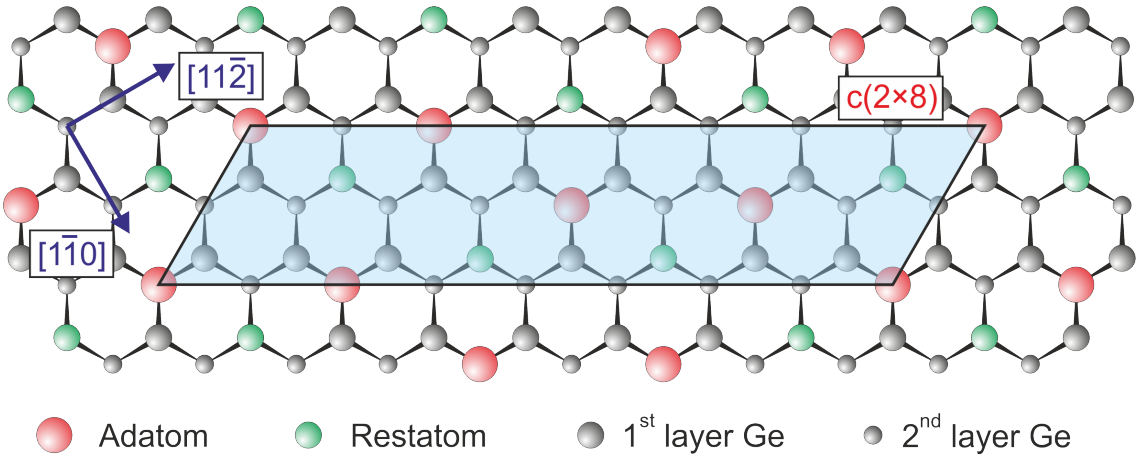

Figure 4.3: *Top view of the structural model for the surface bilayer of the Ge(111)-c(2 × 8) phase. The unit cell (shaded area) comprises four adatoms and four restatoms.*

is shown in Fig. 4.3. The new unit cell includes four adatoms at T_4 lattice sites and four restatoms. The adatoms itself form a (2×2) sublattice, in which one DB atom remains unsaturated (restatom). Here, the reduction of DBs per unit cell again leads to a lowering of band structure energy, that overcompensates the elastic energy necessary to deform the lattice, while the adatoms induce additional strain in the surface. In contrast to Si(111), there exists no dimer formation, and the stacking order remains intact in the whole unit cell.

Both Si(111) and Ge(111) feature reversible transitions to a (1×1) high-temperature phase. Upon cooling to RT the respective (7×7) and $c(2 \times 8)$ phases reoccur again. In comparing the electron charge distribution in the unit cell, one finds differences between Si(111) and Ge(111) in their stable RT reconstructions. For Ge the charge is redistributed such that restatom orbitals are fully occupied, and those of the adatoms become empty. This is in contrast to Si(111), where partly occupied adatom DBs remain. In consequence, the surface band structure of Si(111) exhibits metallic character, whereas that of the Ge(111) is semiconducting [125].

4.2 The $(\sqrt{3} \times \sqrt{3})$ reconstruction on Si(111) and Ge(111)

The well-ordered surfaces of Si and Ge represent an ideal basis for the controlled deposition of thin metallic adlayers. Growth characteristics may differ significantly and lead to thin epitaxial films, islands, or the formation of silicide (germanide) compounds. In reducing the thickness of the metallic adlayer to the atomic limit, a quantization in direction perpendicular to the surface can be achieved. This involves drastic deviations

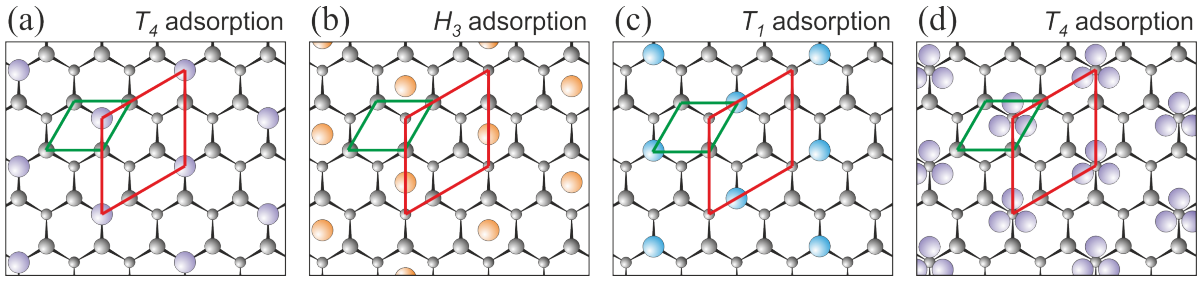

Figure 4.4: *(a)–(c) Adsorption of adatoms with respect to the different lattice sites T_4, H_3, and T_1 in the dilute $(\sqrt{3} \times \sqrt{3})$ phase on Si(111) and Ge(111). The $(\sqrt{3} \times \sqrt{3})$ unit cell (red) exhibits an enlargement by $\sqrt{3}$ and a rotation of 30° with respect to the (1×1) unit cell of the substrate (green). (d) Trimerized adsorption at T_4 sites in the 1 ML dense phase.*

of several physical properties from their behavior in the bulk. Since electrons are strictly confined within the surface, such well-ordered adlayers are considered as pure 2DESs.

Experimentally, the metal deposition is settled in the sub-ML to ML thickness range. 1 ML is defined as the coverage obtained by 1 adatom per (1×1) unit cell of the underlying substrate, and thus amounts to 7.83×10^{14} atoms cm^{-2} for Si(111) and to 7.22×10^{14} atoms cm^{-2} for Ge(111). Suitable elements for deposition are monovalent representatives like alkali atoms, but also noble metals, e.g., Ag, Au, and Pt. Moreover, the tetravalent metals Sn and Pb mark a second class of well suited adsorbate atoms. Importantly, the different electronic configuration (see Tab. 4.1) of monovalent and tetravalent atom species has a strong impact on the bonding characteristics at the substrate surface. Depending on the exact coverage and further growth parameters like the temperature, various surface reconstructions can be realized. Similarly to the bare substrate, the delicate interplay of band structure energy and lattice energy determines the stability of the respective phase. Among the various surface reconstructions, the adatom-induced $(\sqrt{3} \times \sqrt{3})R30°$ phase represents the most prominent and widely studied representative. Its formation is favored by the threefold symmetry of the substrate and leads to an energetic stabilization of the surface by reducing the number of dangling bonds. This new unit cell, enlarged by $\sqrt{3}$ and rotated by 30° with respect to the (1×1) substrate unit cell, is typically established at coverages of 1/3 ML (dilute phase), 1 ML, and 4/3 ML (dense phases). Different adsorption sites may be favored, and even trimerization of adsorbate atoms has been reported [133]. This is visualized in Fig. 4.4(a)–(c), where the three most common bonding configurations in the dilute phase are drawn. These are characterized by adatoms located at the different adsorption sites T_4, H_3, and T_1. In the dense $(\sqrt{3} \times \sqrt{3})$ phases one often observes adsorbate nucleation, such as the trimerization around T_4 lattice sites shown in Fig. 4.4(d) for 1 ML coverage. Oftentimes, metal-metal distances at the surface are found to be close to their respective bulk value, which is indicative of a highly stable surface. Importantly, the monovalent noble metals typically induce $(\sqrt{3} \times \sqrt{3})$ reconstructions at 1 ML metal coverage, whereas the tetravalent group-IV atoms in $(\sqrt{3} \times \sqrt{3})$ configuration exist both as dense and dilute

phases. Essentially, the last-mentioned represent an experimental approach to realize a triangular lattice that suffers from spin frustration, a scenario already pointed out in Sec. 2.2. The details of adsorbate bonding and their relevance for different structural models will be discussed in the respective experimental sections.

In addition to the metals listed above, $(\sqrt{3} \times \sqrt{3})$ reconstructions on Si(111) and Ge(111) have also been realized for Al, In, Tl (group III), and Bi (group V) [134–137]. This leads to a large number of adsorbate-substrate combinations established at various coverages, which involve diverse physical properties. By exchanging or altering one or more of the ingredients that define the final 2DES, i.e., substrate, adsorbate species, temperature, and coverage, the experimenter is given a strong tool to tune the strength of certain properties as, e.g., localization, electronic correlations, electron-phonon interaction, and SOC effects. In this regard, the present thesis scrutinizes the three individual 2DESs Pt/Si(111)-$(\sqrt{3}\times\sqrt{3})$, Au/Ge(111)-$(\sqrt{3}\times\sqrt{3})$, and Sn/Si(111)-$(\sqrt{3}\times\sqrt{3})$ in Chs. 5, 6, and 7, respectively. As will be demonstrated therein, these small changes in the elemental composition lead to three different classes of surface physics explored in a 2DES, i.e., **i)** chiral structures at surfaces, **ii)** complex spin patterns due to the SOI, and **iii)** highly correlated Mott-Hubbard physics in a frustrated triangular lattice. For the adsorbate elements used, a choice of relevant fundamental properties is also listed in Tab. 4.1.

4.3 Preparation of semiconductor substrates

The experimental realization of high quality semiconductor surfaces strongly demands a clean preparation on both the *ex situ* and *in situ* side. Basically, a pure and long-range ordered periodic crystalline surface is advantageous for scattering experiments like LEED, but it is also mandatory for ARPES. However, defects or impurities, which have not been removed prior to the experiment, or even worse, have been incorporated unintentionally during the preparation can strongly degrade the signal and/or alter the physical properties. The following sections describe the efforts necessary to prepare flat and well-ordered surfaces of Si(111) and Ge(111), that are free from impurities and exhibit a low level of defects at the same time.

4.3.1 Si(111)

Crystalline silicon substrates were purchased in two different charges from "CrysTec GmbH Kristalltechnologie". "Charge 1" was delivered as 2" single-side polished wafers, cut perpendicular to the [111] normal. The wafers are highly n-doped (dopant As) to achieve a low specific resistance of $\rho = 0.004$–$0.01\,\Omega\,\mathrm{cm}$, mandatory for direct current heating, STM, and PES even at LT ($\approx 10\,\mathrm{K}$). Prior to preparation, small samples of $10\,\mathrm{mm} \times 2.5\,\mathrm{mm} \times 0.5\,\mathrm{mm}$ (length × width × height) in size were formatted by utilizing a table-top diamond cutter. "Charge 2" contains two 3" wafers, also cut perpendicular

to the [111] normal, which have already been formatted to small samples (10 mm × 2.5 mm × 0.38 mm) by the manufacturer. The substrates are highly n-doped (dopant Sb) with a specific resistance $\rho < 0.01\,\Omega\,\mathrm{cm}$. The single-side polished wafers are covered by a protective photoresist, that minimizes the risk of scratches during transport and storage.

Ex situ

The preparation of silicon substrates outside the vacuum is performed within a flow-box to keep the amount of particles from the environmental air at a low level. The whole procedure consists of five different steps, which are carried out sequentially, as it is shown in Fig. 4.5. In the first step the protective photoresist on top of the polished sample side is removed in acetone (standard analytical grade), with the beaker placed in an ultrasonic bath for 2 min (only necessary for wafer "charge 2"). This step is repeated in unused acetone for the same duration to ensure a complete removal of remnants. While this procedure already guarantees a high degree of cleanliness, surface science experiments require even enhanced purity standards. Therefore, remaining carbon-hydroxides are removed within three independent and sequential steps, that comprise swaying in the purissimo grade organic solvents acetone (purity > 99.5 %), 2-propanol (purity > 99.8 %), and methanol (purity > 99.8 %) for 2 min each. Finally, residual methanol is blown off by dry nitrogen, before the sample is mounted on a sample carrier (for sample carrier design see Fig. 3.8 in Sec. 3.2.2). At this time, the cleaned silicon substrate is still covered by its native and robust oxide SiO_2, that protects the surface against impurities from the surrounding air, like water, rest gas atoms/molecules, and particles. Immediately before introducing the sample carrier into the load-lock entry of the vacuum chamber, dry nitrogen is used again to remove particles that might have been captured unintentionally during transport.

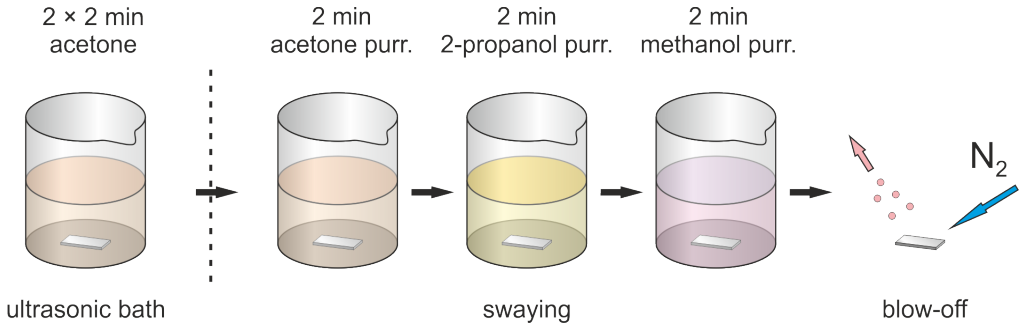

Figure 4.5: *Ex situ preparation cycle for Si(111) substrates. The protective photoresist on top of the polished substrate is effectively removed by two repeated cleaning steps in acetone. Remaining carbon-hydroxide impurities are cleared during three subsequent cleaning stages in purissimo grade organic solvents. Methanol remnants from the last step are removed by dry nitrogen, prior to mounting the substrate on a sample carrier.*

In situ

At an adequate base pressure of $p_b \lesssim 1 \times 10^{-10}$ mbar within the vacuum chamber sample and sample carrier are degassed for at least 12 h at a temperature of $T \approx 600\,^{\circ}\mathrm{C}$. This is achieved by an electric current, that generates thermal heat when flowing through the substrate. By this means, water and other rest gas atoms/molecules, being stuck to the surfaces, are effectively desorbed. During the degassing the pressure is monitored and kept below $p = 1 \times 10^{-9}$ mbar, until it saturates in the p_b-range again. The substrate, now free of adsorbed rest gas layers, is still covered by its native oxide. This is easily decomposed and stripped off without residues at elevated temperatures [125]. This *flash* procedure consists of up to three intense and rather short heating cycles, where the sample is rapidly heated to $T \approx 1250\,^{\circ}\mathrm{C}$ and held at this temperature for 10 s. Afterwards the sample is cooled down to RT at a constant rate of $\mathrm{d}T/\mathrm{d}t = 40\,^{\circ}\mathrm{C}s^{-1}$, which becomes smaller at lower temperatures due to the absence of heat convection in the vacuum. The flashing induces a reaction of the robust SiO_2 with the substrate atoms, i.e.,

$$\mathrm{SiO_2} + \mathrm{Si} \rightarrow 2\,\mathrm{SiO}. \tag{4.1}$$

The remaining loose SiO is easily sublimed at the same elevated temperature. Contrary, the cooling is needed to "heal" the surface and reorder its atoms. The repetition of this process ensures that the oxide removal is complete.

The reordered surface at RT exhibits the well-known (7×7) surface reconstruction, which is easily verified by LEED and STM. These techniques allow to judge the effectiveness of the flash procedure, which manifests itself by a long-range ordering and complete oxide removal. Both are necessary prerequisites for further metallic adlayer deposition in order to create a 2DES. Fig. 4.6(a) shows a LEED image of the (7×7) reconstructed Si(111) surface at RT, that proves the high surface quality obtained in the preparation process. It features sharp (7×7) superstructure spots on a low background, being suggestive of large terraces with long-range ordering and few defects. The LEED image agrees well with the reciprocal surface lattice of a (7×7) reconstruction shown in Fig. 4.6(b). Due to the electron's finite penetration depth of ≈ 5 Å into the crystal (compare to Fig. 3.1 in Sec. 3.1), only the topmost Si substrate layers contribute to the LEED pattern. In this context, the most intense spots relate to (1×1) lattice points of the underlying substrate. Large area STM images [Fig. 4.6(c)] confirm the presence of broad and flat terraces (width $\sim$ 100 nm). A close-up to the atomic level unveils details of the surface reconstruction. In Fig. 4.6(d) unoccupied electronic states (bias: +1.0 V, 0.5 nA) are imaged. Bright protrusions are related to the adatoms in the DAS model, which has been introduced in Sec. 4.1. It should be noted that we deal with maxima in the electron density, which do not necessarily correspond to atom locations, since directional bonds are present. Additional prominent features are the corner holes, that mark the origins of the (7×7) unit cells (blue parallelogram). There are also a few defects visible as missing protrusions or enhanced intensity spots. However, their number is rather low and does not hinder long-range ordering. Adjustments to the

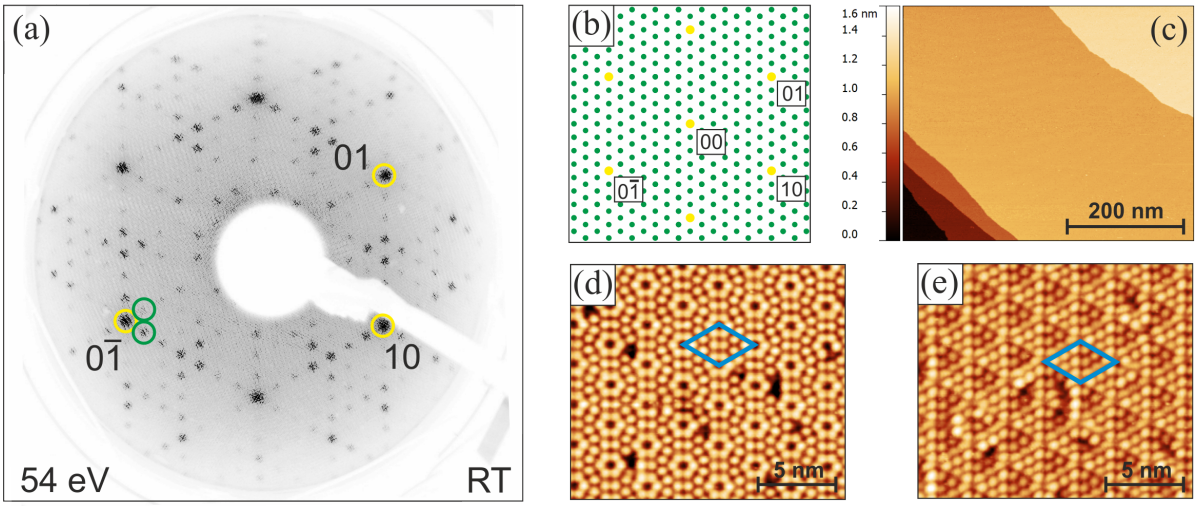

Figure 4.6: *(a) LEED image of (7 × 7) reconstructed Si(111) at RT. Dark contrast corresponds to high intensity. The 1/7-order spots (green) are less pronounced than the intense spots (yellow), related to the substrate. (b) Reciprocal surface lattice of the (7 × 7) reconstruction with 1/7-order spots in between main (1 × 1) points. (c) Large area filled states STM image at RT of the flashed Si(111) surface, exhibiting broad and flat terraces; bias: -1.0 V, 0.5 nA, 500 × 403 nm². (d) Empty states close-up on one of the terraces with the (7 × 7) unit cell indicated; bias: +1.0 V, 0.5 nA, 17.7 × 15.1 nm². The bright intensity maxima are attributed to the adatoms. (e) Filled states close-up on the same terrace; bias: -1.0 V, 0.5 nA, 17.7 × 15.1 nm².*

preparation described above did not prove to enhance the quality obtained, but rather led to worse results in some cases. Turning to the occupied states (bias: -1.0 V, 0.5 nA) in Fig. 4.6(e), a contrasted view at the atomic scale is provided, where the corner holes are less pronounced. Bright protrusions still relate to the adatoms, whose DBs form a partly filled band, and are thus observed at both bias voltage polarities [125]. Notably, one half of the unit cell appears slightly darker than the other. This is attributed to the existence of a stacking fault in one half, as described within the DAS model.

4.3.2 Ge(111)

For germanium-based surface systems, substrates from "CrysTec GmbH Kristalltechnologie" were purchased as a 2" single-side polished wafer with n-type doping (dopant Sb) and the specific resistance $\rho = 0.13$–$0.2\,\Omega\,\mathrm{cm}$. Samples cut from the wafer are 10 mm × 2.5 mm × 0.45 mm (length × width × height) in dimension. A protective photoresist covers the polished surface again.

Ex situ

Like in the Si(111) case sample cleaning includes the removal of the photoresist in acetone prior to elimination of remaining hydrocarbons by the organic solvents acetone,

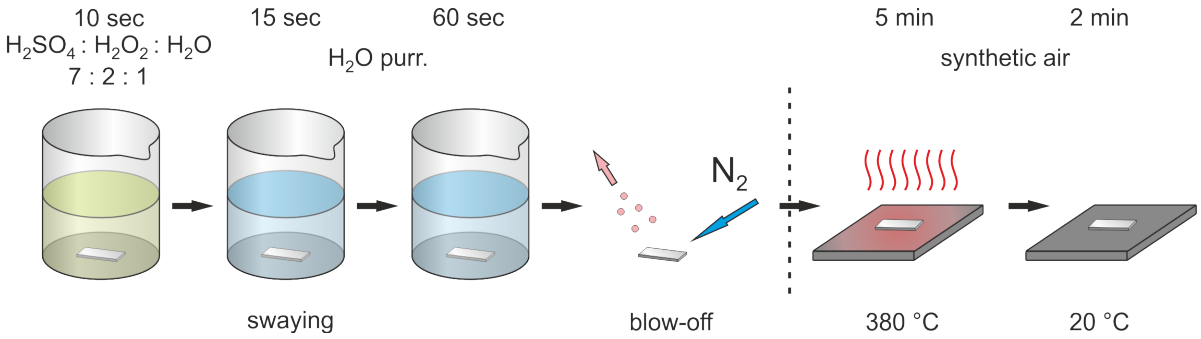

Figure 4.7: *Additional ex situ cleaning of Ge(111) subsequent to the procedure presented in Fig. 4.5. The hydro-carbon freed sample is etched in a Piranha solution (H_2SO_4, H_2O_2, and H_2O) to remove the native Ge oxide and contaminants within. Two rinsing steps in triple distilled water eliminate Piranha solution remnants afterwards. Subsequent to drying by nitrogen, thin artificial GeO_2 layers are grown on top of the substrate in an oven flooded by synthetic air. A final cooling to RT completes the ex situ preparation of Ge(111).*

2-propanol, and methanol during three sequential swaying steps. This procedure has already been illustrated in Fig. 4.5. Unfortunately, the remaining native GeO_2 differs significantly from SiO_2. Basically, it contains cracks due to its large lattice mismatch with Ge, and it has a certain solubility in contact with water [138]. Hence, impurities can permeate towards the Ge substrate. In addition, the Ge oxide layer is robust against *in situ* flashing. Therefore, the native oxide is removed and exchanged by a thin artificially grown oxide layer during the *ex situ* preparation. This extended *ex situ* recipe (Fig. 4.7) is adopted from a detailed study concerning the preparation of Ge(001) surfaces by C. Blumenstein *et al.* [139].

After cleaning by organic solvents, the nitrogen dried sample is etched for 10 s at $T \approx 80\,°C$ (self heating) in a solution of H_2SO_4, H_2O_2, and H_2O, mixed at a ratio of 7:2:1, which is known as *Piranha solution*. This etchant represents an effective oxidizer, capable of removing organics and metal contaminations [139]. The etching rate is assumed to be lower for Ge(111) than for Ge(001) due to its larger surface robustness. Accordingly, etching the (111) surface of Ge for the enhanced period of 10 s [in comparison to 5 s for Ge(001)] is adequate, and does not only remove the oxide but also a couple of substrate layers and detrimental impurities within both. The subsequent swaying in triple distilled H_2O (contaminants $\leq$ ppb) for 15 s abruptly stops the etching process and removes remnants of the Piranha solution, whereas a second rinsing step for 60 s is needed to minimize the concentration of impurities, that may react with the now unprotected surface. To prepare the sample for thermal oxidation, all remaining droplets of water are blown off by dry nitrogen. In the following stage the sample is heated to $T \approx 380\,°C$ for 5 min in an oven flooded by synthetic air (79.5 % N_2 and 20.5 % O_2) to avoid the incorporation of hydrocarbons. The elevated temperature provides the thermal energy, necessary to activate the oxidation process. This results in a homogeneous growth of thin and amorphous, artificial GeO_2 layers, that enclose contaminants and protect the

surface prior to the *in situ* treatment. The resulting GeO_2 layers are much thinner than their native counterpart, as has been shown for the (001) oriented surface [139]. A subsequent cooling, again under a synthetic air athmosphere, precedes mounting of the *ex situ* prepared Ge sample on a sample carrier. Finally, eventual particles, stuck during transport to the vacuum chamber, are blown off by dry nitrogen.

In situ

In situ preparation of Ge(111) starts with sample and sample carrier degassing for at least 12 h at $T \approx 600\,^{\circ}\mathrm{C}$ in an UHV environment ($p_b \lesssim 1 \times 10^{-10}$ mbar). Meanwhile, the pressure is monitored and always kept below $p = 1 \times 10^{-9}$ mbar, until it stabilizes again around $\sim p_b$. Different from the Si(111) and Ge(001) preparation, a thermal flash or anneal does not effectively remove the capping GeO_2 layers, which is most probably due to an enhanced stability of bonds at the Ge(111)/GeO_2 interface. Instead, several cycles of Ar^+-ion bombardment, followed by thermal annealing, are mandatory to effectively remove the grown oxide from the surface, and to initiate the ordering to a $c(2\times8)$ surface reconstruction. Nevertheless, the additional *ex situ* preparation steps represent a useful measure, as they significantly reduce the amount of carbon impurities. Ar-sputtering is performed at an impact energy of $E_{\mathrm{Ar}^+} = 1000\,\mathrm{eV}$ and an argon partial pressure $p_{\mathrm{Ar}} \sim 10^{-4}$ mbar in the discharge region of the sputter gun for 20 min. Subsequent annealing is achieved by direct current heating at $T = 900\,^{\circ}\mathrm{C}$ for $t = 30\,\mathrm{s}$ with the pressure always kept below $p = 1 \times 10^{-9}$ mbar. The anneal is stopped by a soft cooling to RT at a rate of $\mathrm{d}T/\mathrm{d}t = 15\,^{\circ}\mathrm{C}s^{-1}$, which allows for surface "healing" and atom reordering. After 3–5 sputter/anneal cycles LEED and STM images are used to judge the quality of the $c(2 \times 8)$ reconstructed Ge(111) surface. The exact number of cycles depends on the chambers used for preparation, which are equipped with different sputter sources and sample holders/manipulators (distinct heating characteristics).

The LEED image in Fig. 4.8(a) with its well resolved 1/8th- and half-order spots verifies long-range periodic ordering at the Ge(111) surface. Different colors highlight first-order spots (yellow) and superstructure spots (red, green, and blue), which are related to the three domains with 120 ° rotational symmetry, present at the Ge(111) surface. In comparison to the reciprocal surface lattice of the $c(2 \times 8)$ surface reconstruction, which is illustrated in Fig. 4.8(b), the missing of 1/4th-order spots in LEED is apparent. This has been attributed to a small surface structure factor for these peaks [140]. Nevertheless, faint signatures of the 1/4th-order spots have been reported in reflection high energy electron diffraction (RHEED) and also recently in a highly resolved LEED study [141, 142]. STM measurements of Ge(111)-$c(2 \times 8)$ have not been in the focus of this thesis, yet, ordered domain are known to be about five times smaller than for Si(111)-(7×7), i.e., 20 nm compared to 100 nm in width [125]. For completeness, Figs. 4.8(c) and (d) show atomically resolved areas of unoccupied and occupied states, respectively (taken from Ref. 142). In comparison with the structural model introduced in Fig. 4.3, the four bright protrusions per unit cell in (c) are identified as the adatom

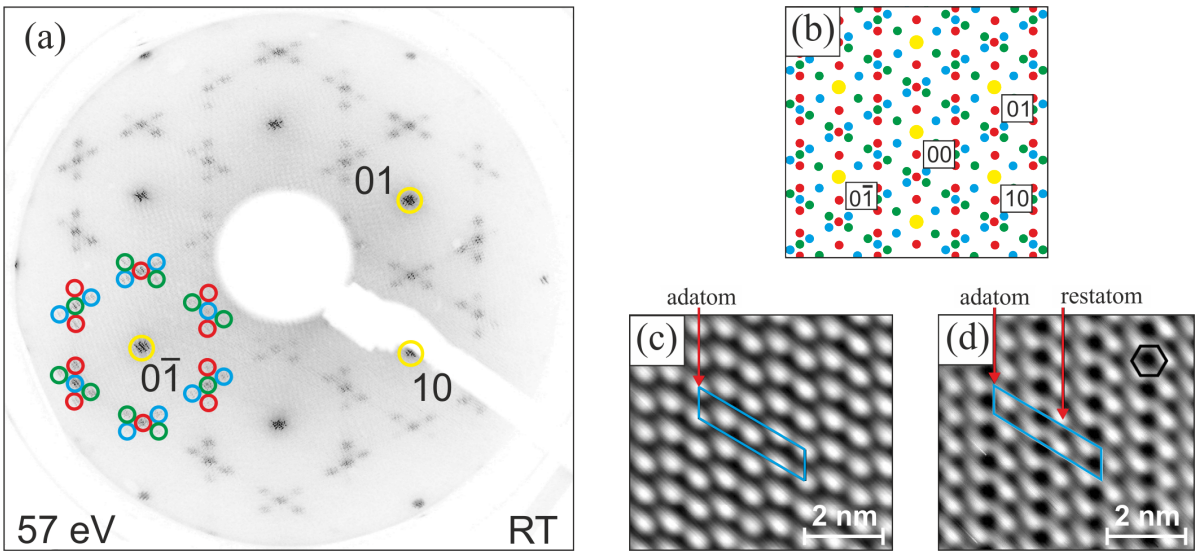

Figure 4.8: *(a) LEED image of $c(2 \times 8)$ reconstructed Ge(111) after four sputter/anneal cycles, according to the preparation procedure described in the text. Dark contrast corresponds to high intensity. The presence of sharp 1/8- and half-order spots, and the low background are suggestive of long-range periodic ordering with only few defects. Yellow circles indicate first-order spots, whereas red, green, and blue circles highlight selected superstructure spots, which relate to the three different domains present at the surface. (b) Reciprocal surface lattice of Ge(111)-$c(2 \times 8)$. Colors are assigned as in (a). (c) Empty states (bias: +1.2 V; 0.1 nA, $6.7 \times 6.1\,\mathrm{nm}^2$) STM image with $c(2 \times 8)$ unit cell (blue). Bright protrusions are due to adatoms. (d) STM image of the same area for filled states (bias: -1.2 V; 0.1 nA, $6.7 \times 6.1\,\mathrm{nm}^2$). Bright protrusions relate to restatoms, and less intense spots correspond to adatoms here. Figures in (c) and (d) are taken from Ref. 142, Copyright (2009) by the American Physical Society.*

DB orbitals. Thus, it becomes evident that adatoms host unoccupied surface states. In contrast, in occupied states four bright and four less intense protrusions per unit cell are observed, which are ascribed to the restatoms and the adatoms, respectively. In conclusion, occupied states are mainly localized at the restatoms, yet, also a small contribution is found at the adatom positions. The latter are located closer to the tunneling tip, yielding an enhanced adatom related signal. The findings above also support the interpretation of a charge transfer from the adatoms to the restatoms. The positions of the protrusions agree well with the atomic locations in the structural model, and do thus indicate a small lateral bending of the DBs.

5 Adsorption of a chiral structure on a semiconductor surface

2DESs, established by a metal coating of 1 ML on a (111) oriented semiconductor surface, often result in a stable $(\sqrt{3} \times \sqrt{3})$ reconstruction [143]. Such systems have been studied for several atom species. Among these, the noble metal adatoms gold and silver on Si(111) and Ge(111) have been extensively analyzed by STM and theoretical modeling in the past [133, 143–147]. In particular, for noble metal atom species the electronic configuration is dominated by d and s orbitals, which differ significantly from the sp^3 hybridized orbitals of the semiconducting substrate (see Tab. 4.1). In this way, the variety of 2DESs with different properties is extended beyond the group-IV adatom induced $(\sqrt{3} \times \sqrt{3})$ systems, which will be discussed in Ch. 7.

5.1 Noble metal induced $(\sqrt{3} \times \sqrt{3})$ reconstructions at (111) semiconductor surfaces

Structural models

A crucial point in the analysis of the noble metal based $(\sqrt{3} \times \sqrt{3})$ surface reconstruction is the atomic configuration, which determines the specific electronic properties. These systems develop at a nominal coverage of 1 ML, and for both Au and Ag on the surfaces of Si(111) and Ge(111) the local atomic geometry is well understood today [133, 144, 146, 148, 149]. In spite of the closely resembling adsorbate and substrate atoms, there exist significant deviations in their respective atomic arrangement. Two different structural models have been discussed in the literature, i.e., on the one hand the conjugate honeycomb-chained trimer (CHCT) model for Au-induced $(\sqrt{3} \times \sqrt{3})$ reconstructions, and on the other hand the honeycomb-chained trimer (HCT) model for Ag-$(\sqrt{3} \times \sqrt{3})$ systems [133, 150, 151]. All models (see Fig. 5.1) feature a metal adsorbate (blue spheres) coverage of 1 ML and a MTL, i.e., there exists an additional half layer of substrate atoms (green spheres) on top of the substrate bilayer (gray spheres). The main difference consists in the atom relaxation within these top layers. In the CHCT model metal atoms move from their initial H_3 sites towards T_4 positions, which leads to one metal trimer per unit cell, as depicted in Fig. 5.1(a). The three substrate adatoms relax away from their T_1 sites in order to increase their distance from the trimer units. All other relaxations, including subsurface and vertical displacements, are disre-

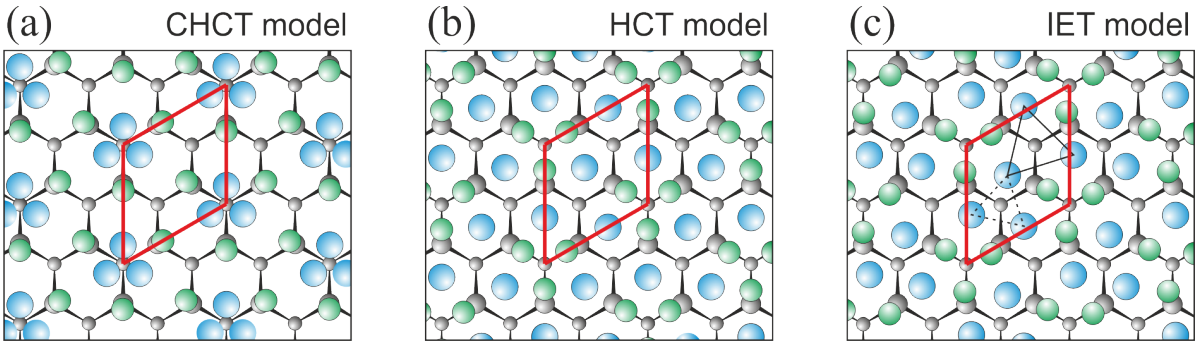

Figure 5.1: *Structural models of noble metal induced* $(\sqrt{3} \times \sqrt{3})$ *reconstructions on Si(111) and Ge(111). (a) CHCT model for the atomic arrangement of a noble metal adsorbate (coverage 1 ML) with respect to the top bilayer of a (111) semiconductor surface (gray spheres). In this MTL configuration semiconductor adatoms (green spheres) are bound to the substrate at* T_1 *lattice sites. The adsorbate metal (blue spheres) trimerizes around* T_4 *lattice sites. The* $(\sqrt{3} \times \sqrt{3})$ *unit cell is indicated in red color. (b) HCT model, with trimers formed by substrate adatoms instead of adsorbate atoms. (c) The IET model in close resemblance to (b), yet, inequivalent and twisted adsorbate atom subunits (marked by triangles) within the* $(\sqrt{3} \times \sqrt{3})$ *unit cell occur. Atom diameters and distances are not to scale in (a)–(c).*

garded at this point for simplicity. The CHCT model is commonly accepted for both Au/Si(111)-$(\sqrt{3}\times\sqrt{3})$ [133, 146] and Au/Ge(111)-$(\sqrt{3}\times\sqrt{3})$ [80, 148, 152]. In contrast, the related Ag/Si(111)-$(\sqrt{3} \times \sqrt{3})$ and Ag/Ge(111)-$(\sqrt{3} \times \sqrt{3})$ surfaces could not be explained within the CHCT model. It turned out that surface relaxations differ significantly, leading to trimers of MTL atoms around T_4 lattice sites instead of trimerized adsorbate atoms [149, 153]. In this HCT model the metal atoms are only slightly shifted from their initial H_3 locations in the opposite direction as in the CHCT model [150], see Fig. 5.1(b). The HCT model was even found to represent a more stable situation than present at the Si(111)-(7×7) surface [150]. Moreover, and in contrast to the other noble metal induced $(\sqrt{3} \times \sqrt{3})$ surface reconstructions, Ag/Si(111)-$(\sqrt{3} \times \sqrt{3})$ exhibits a structural phase transition at $T \approx 150\,\mathrm{K}$ to a LT phase [154]. It has further been revealed experimentally and by means of theoretical modeling to be of an order-disorder type [155, 156]. This reversible transition requires small changes of the HCT model, which are accurately introduced by the inequivalent triangle (IET) model [144, 147], depicted in Fig. 5.1(c). Therein, slight lateral shifts in both adsorbate and MTL atom locations, combined with a small rotation of the Si and Ag triangles by $+6\,^\circ$ and $-6\,^\circ$ with respect to their pristine orientation in the HCT model occur. In consequence, this *symmetry breaking* transition leads to the emergence of two *inequivalent* triangular Ag subunits within the unit cell (indicated by solid and dashed triangles).

Beyond these structural differences, a coarse approach to the electronic nature of the systems can be obtained by simple electron counting. This yields 12 electrons within the $(\sqrt{3} \times \sqrt{3})$ unit cell, stemming from three substrate adatoms, each with three DBs, and three adsorbate atoms, providing one electron each in case of noble metals (refer to

Tab. 4.1). This even number of electrons then ought to lead to fully occupied bands, which means insulating behavior. In fact, this turns out to be a false assumption for all these systems. Obviously, electron counting with integer numbers is not eligible here, since it disregards the possible presence of several overlapping bands with partial filling.

Adsorption of Pt at the Si(111) surface

Besides the noble metal induced surface reconstructions, given in brief review above, a fascinating additional representative is Pt/Si(111)-($\sqrt{3} \times \sqrt{3}$), which unfortunately has not received a comparable attention so far. In contrast to silver and gold, platinum does not possess a filled d shell, see Tab. 4.1. Experimental studies on the Pt-Si interface did mostly focus on thin film deposition, i.e., platinum coverages ranging up to 40 MLs [157–159]. Also, the formation of the platinum silicides Pt_3Si, Pt_2Si, and PtSi has been in the focus of several publications [159–162], since silicides bear some technological importance in the development of Schottky diode interconnects with high barrier potentials [160] and in catalysis applications. At low coverage, i.e., in the ML regime, Pt/Si(111) has been analyzed by electron diffraction and Auger electron spectroscopy (AES) in the 1980s [157, 163–165]. Based on these experiments, it is known that for very small coverages ($\ll$ 1 ML) single atoms and small clusters cover the (7×7) reconstructed Si(111) surface. For depositions above 1 ML, platinum starts to react with the Si surface [160, 165], although there have also been reports that Pt-Si mixing already begins in the sub-ML regime [166]. Other studies suggest that Pt atoms are favorably incorporated at interstitial positions within the topmost Si(111) bilayer, where they induce strain [159]. At increased Pt coverages the strain related elastic energy then initiates further platinum diffusion into the bulk and intermixing with the substrate atoms.

In the low coverage regime two surface reconstructions have been reported, i.e., a ($\sqrt{7} \times \sqrt{7}$) and a ($\sqrt{3} \times \sqrt{3}$) phase. The ($\sqrt{7} \times \sqrt{7}$) reconstruction is observed after annealing (Pt coverage 1 ML and above) at temperatures from T = 450–650 °C, and the ($\sqrt{3} \times \sqrt{3}$) phase evolves after annealing at even higher temperatures (T = 600–1000 °C) [157, 163, 164]. Excess platinum exhibits a strong tendency to diffuse into the Si substrate, if the sample temperature reaches the respective eutectic point ($T \approx 830$ °C) [161, 167]. Hence, the preparation of Pt/Si(111)-($\sqrt{3} \times \sqrt{3}$) does not strictly require exact knowledge of the initially available amount of platinum on the surface. This subsurface diffusion of Pt atoms has also been reported in growth studies of atomic Pt nanowires at the Ge(001) surface, where Pt atoms tend to maximize their coordination with Ge atoms [168]. This is further supported by density functional theory (DFT) calculations, that report an energetically favored subsurface diffusion for Pt atoms on Ge(001) [169].

Knowledge on the exact platinum coverage that induces the ($\sqrt{3} \times \sqrt{3}$) reconstruction on Si(111) is of fundamental importance to correctly describe the atomic arrangement at the surface. P. Morgen *et al.* suggested 1/3 ML in two early AES studies [157, 165]. However, the exact platinum coverage, required to form this reconstruction, remains uncertain. The robustness against excess Pt simplifies the experimental realization of

Pt/Si(111)-($\sqrt{3}\times\sqrt{3}$), yet, it does not seem preferable to work with Pt amounts exceedingly higher than necessary. Diffusion into the bulk might alter the electronic properties at the Pt/Si interface due to an enhanced substitution of subsurface Si atoms. Recently, A. Wawro *et al.* have studied the ($\sqrt{3}\times\sqrt{3}$) phase in between platinum silicide islands with STM in high resolution and reported adatom localization at only one discrete lattice site in agreement with the suggested Pt coverage of 1/3 ML [161, 162]. Yet, the main concern in their analyses was silicide formation. Similarities and differences with the results shown in this thesis will be pointed out in the following sections. Besides these basic studies on the local atomic configuration at the surface, ARPES experiments were not appropriate to draw definite conclusions with regard to the electronic structure so far. This is most probably due to small sizes of reconstructed domains, as will also be discussed later.

5.1.1 Preparation of Pt/Si(111)-($\sqrt{3}\times\sqrt{3}$)

The *in situ* preparation of Pt/Si(111)-($\sqrt{3}\times\sqrt{3}$) resumes at the final stage of Si(111) substrate treatment, as described in Sec. 4.3.1, i.e., a long-range ordered Si(111)-(7 × 7) surface is needed for further processing. All data shown for Pt/Si(111)-($\sqrt{3}\times\sqrt{3}$) base on "charge 1" Si(111) substrates. Platinum is evaporated from a rod (purity 99.99 %) by use of an electron beam evaporator ("Focus EFM 3"), operated at a base pressure lower than 1×10^{-9} mbar during evaporation. A platinum amount of 1–1.5 ML in coverage is deposited onto the Si(111) surface, which is held at RT. In the next step the sample is annealed at $T = 900\,^{\circ}$C for 3 min and cooled down during 30 s subsequently. Several anneal cycles ($\gtrsim$ 3) lead to a stable ($\sqrt{3}\times\sqrt{3}$) pattern in LEED, see Fig. 5.2(a). Further annealing at various temperatures (up to 1000 °C) and durations do not alter the LEED pattern significantly, which is indicative of the high stability of this phase over a broad temperature range in agreement with earlier reports [161, 162]. As a side note, it should be mentioned that a complete platinum removal by thermal flashing up to the Si melting temperature is not possible. Besides reflections related to the Si(111) substrate (marked by yellow circles), additional spots (green circles), rotated by 30 ° and with larger periodicity, are clearly visible. In comparing this pattern to the reciprocal lattice of a ($\sqrt{3}\times\sqrt{3}$) reconstructed surface in Fig. 5.2(b), the realization of the correct surface reconstruction is verified. Nevertheless, the blurred appearance of the 1/3-order spots could indicate the presence of domains with local ($\sqrt{3}\times\sqrt{3}$) periodicity which are smaller than the coherence width in LEED [163]. The mean FWHM of the 1/3-order spots in Fig. 5.2(a) is evaluated as $\Delta k_{\parallel} = 0.127\,\text{Å}^{-1}$, which is about 12 % of the ($\sqrt{3}\times\sqrt{3}$) SBZ size. A simple estimate of regularly ordered real-space domain dimensions is then obtained by application of Heisenberg's uncertainty relation: $\Delta x = 2\pi/\Delta k_{\parallel} = 49.5\,$Å. This is obviously a low value compared to the large Si(111)-(7 × 7) terraces, presented in Sec. 4.3.1.

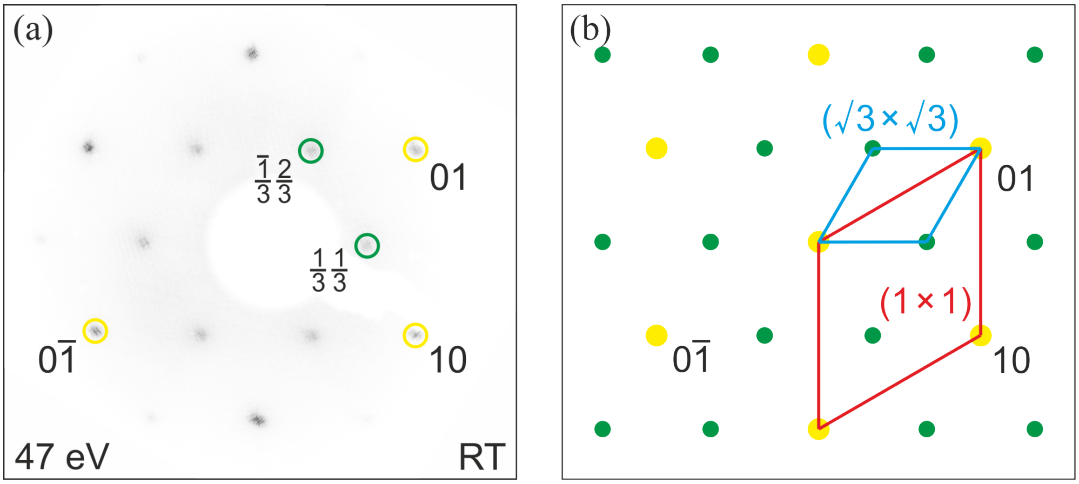

Figure 5.2: *(a) LEED image of Pt/Si(111)-($\sqrt{3} \times \sqrt{3}$) at RT with integer- (yellow) and 1/3-order (green) spots of substrate and reconstruction. (b) Corresponding reciprocal surface lattice with the ($\sqrt{3} \times \sqrt{3}$) and (1×1) unit cells indicated. Colors are used as in (a).*

5.2 The atomic geometry of Pt/Si(111)-($\sqrt{3} \times \sqrt{3}$) inspected by scanning tunneling microscopy

By utilizing STM, the atomic arrangement at the Pt/Si(111)-($\sqrt{3} \times \sqrt{3}$) surface is unveiled in the following [H3]. Parts of the results base on data obtained by F. Sandrock in his diploma thesis [170]. STM imaging and data processing follow the general description given in Sec. 3.2.2, p. 32. To begin, an overview of the global atomic arrangement at the surface is presented, which reveals the presence of a dense network of domain boundaries. In the next section key elements of the atomic structure of domains and their surrounding domain walls are identified and analyzed. On this basis, a refined structural model is proposed in the end.

5.2.1 Domain sizes and distribution

A good impression of the global appearance of Pt/Si(111)-($\sqrt{3} \times \sqrt{3}$) in STM can be obtained by a large area image that captures the basic geometries at the surface. In this regard, Fig. 5.3(a) sheds light on a dense network of domain walls (bright contrast) on a Pt covered single terrace. These domain walls stretch along three different directions with threefold-rotational symmetry and enclose ($\sqrt{3} \times \sqrt{3}$) reconstructed domains (dark contrast). Domain sizes are rather small, as has already been assumed by the LEED spot broadening before. Repeated annealing at various temperatures does not alter the topography or the domain sizes notably. An evaluation of five different empty states STM images yields the domain size distribution, provided in Fig. 5.3(b). Based on this diagram, one may derive an average domain size of 1020 Å^2. In approximat-

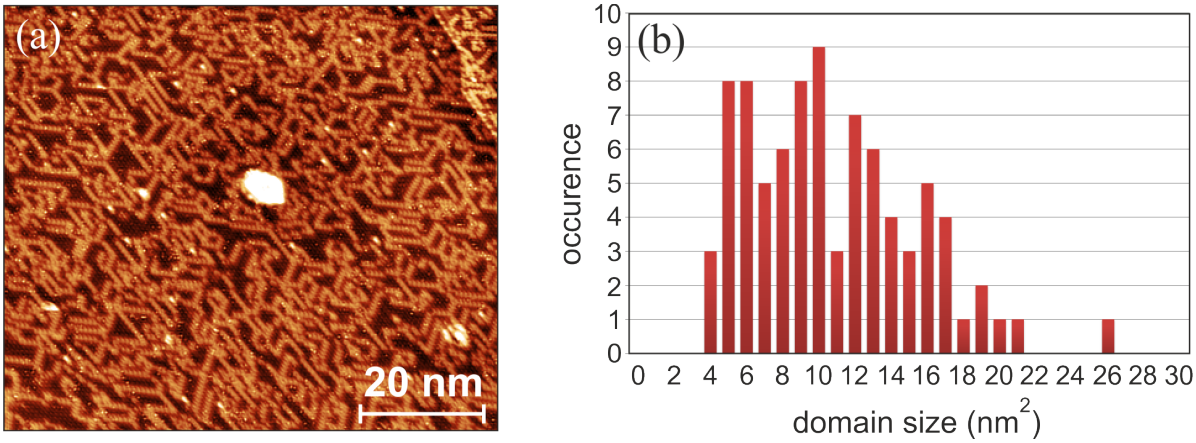

Figure 5.3: *(a) Large-area empty states STM overview image of a single terrace at the Pt/Si(111)-($\sqrt{3} \times \sqrt{3}$) surface; bias: +1.2 V, 0.5 nA, 80.0 × 68.8 nm^2. The bright network of protrusions is related to domain walls, that separate ($\sqrt{3} \times \sqrt{3}$) reconstructed domains (dark contrast). The intense patch in the middle is attributed to a large Pt cluster, while small bright spots are due to tip artifacts. (b) Distribution of domain sizes, evaluated from five different empty states STM images [H3], Copyright (2010) by the American Physical Society.*

ing the typical domain shape as a regular triangle, one obtains a triangle edge length that convincingly agrees with the estimation of 49.5 Å from LEED before. Turning to the related Au/Si(111)-($\sqrt{3} \times \sqrt{3}$) surface, domain sizes are of comparable order, but otherwise do strongly depend on the adsorbate coverage [143, 145, 146]. In contrast, the Ag/Si(111)-($\sqrt{3} \times \sqrt{3}$) surface displays huge domains (extension: 200–300 Å) [153]. Unfortunately, the dense network of domain walls in Pt/Si(111)-($\sqrt{3} \times \sqrt{3}$) means poor long-range ordering, which implies a huge k-space broadening, e.g., in ARPES experiments.

Access to the atomic level in both empty and filled states is provided by Fig. 5.4(a) and (b), respectively. The close-up in (a) reveals that the network of domain walls consists of single *boomerang* shaped sections, that do only align with the threefold-symmetric high symmetry directions $\langle 11\bar{2} \rangle$ of the substrate, as has also been observed in Au/Si(111)-($\sqrt{3} \times \sqrt{3}$) [143, 145]. Interestingly, the apexes of single segments within equivalent domain walls always point towards the same direction, regardless of the exact wall they belong to. This can be understood as a forced registry locking in coupling between Pt and the Si(111) surface. Domain walls running along the three possible high symmetry directions often join in a common *tripoint*, whose optical appearance depends on, whether the boomerang apexes point towards or away from the tripoint. The observations above also hold for similar images, not shown here, and agree with earlier results from the literature by A. Wawro *et al.* [162].

The darker protrusions in between domain walls are arranged in a local ($\sqrt{3} \times \sqrt{3}$) periodicity. A height profile along the indicated direction shows that the domain walls "surmount" the domains by up to 1 Å in vertical direction. However, in turning to the

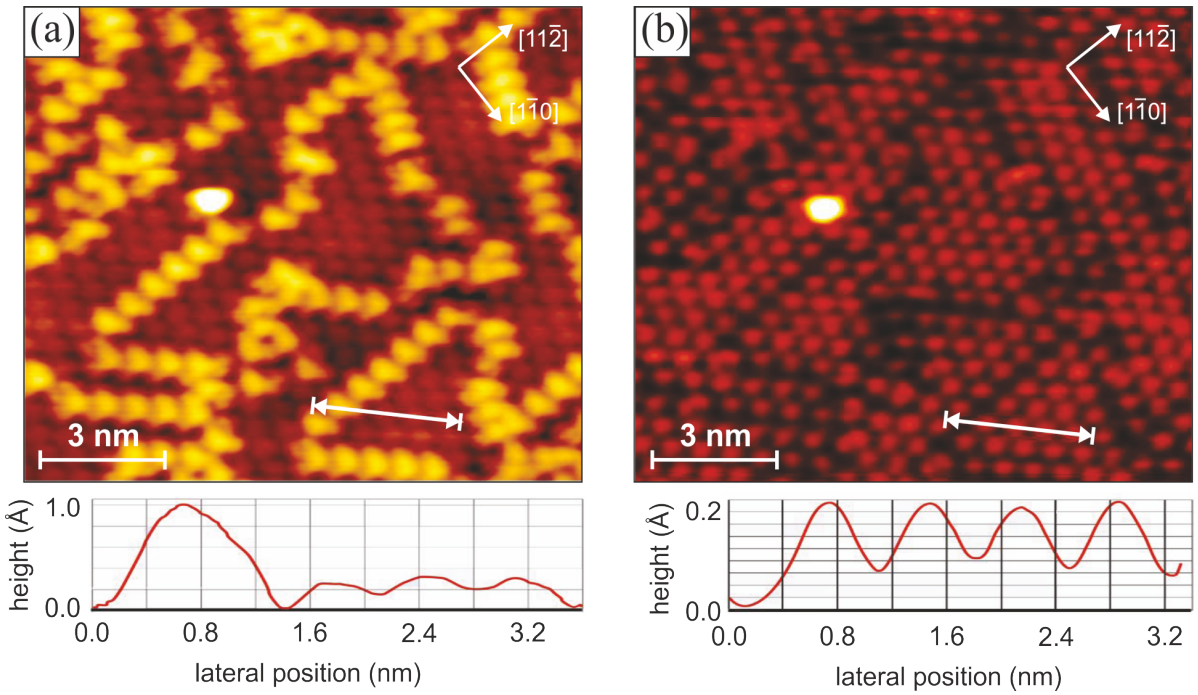

Figure 5.4: *(a) Close-up STM image of the empty states (bias: +1.2 V, 0.5 nA, 13.4 × 11.4 nm^2) in Pt/Si(111)-($\sqrt{3} \times \sqrt{3}$). Boomerang shaped segments of the domain walls "surmount" reconstructed domains in between, as validated by the height profile along the indicated path in the bottom panel. (b) STM image of the same area for filled states (bias: -1.2 V, 0.5 nA, 13.4 × 11.4 nm^2). The height contrast is inverted, and domains seemingly "lie" above the domain walls, as clarified by the height profile (bottom) [H3], Copyright (2010) by the American Physical Society.*

filled states in Fig. 5.4(b), the height contrast is inverted, and the domain walls "lie" about 0.15 Å below the ($\sqrt{3} \times \sqrt{3}$) domains, which is in agreement with earlier results [161, 162, 171]. This reveals that the height contrast represents a strong electronic effect, originating from the LDOS, and that it is not a representation of the true topology. In filled states the dark contrast in between domains corresponds to the domain walls, and the boomerang shape of its segments is barely visible. Such a strong bias dependency is not observed for the protrusions within the ($\sqrt{3} \times \sqrt{3}$) domain. This becomes even more evident in comparing the respective height profiles, displayed in the bottom panels of Fig. 5.4, where the vertical corrugation is almost equal for both polarities. This behavior probably indicates a metallic nature of the ($\sqrt{3} \times \sqrt{3}$) reconstructed domains. As an additional conclusion, unoccupied states orbitals should be highly localized on the domain walls, which is at least valid for the two different bias voltages presented here.

Domain phase shift

An additional result that can be extracted from the STM data is an obvious *phase shift* between neighboring ($\sqrt{3} \times \sqrt{3}$) domains [H3]. The domain walls should then be

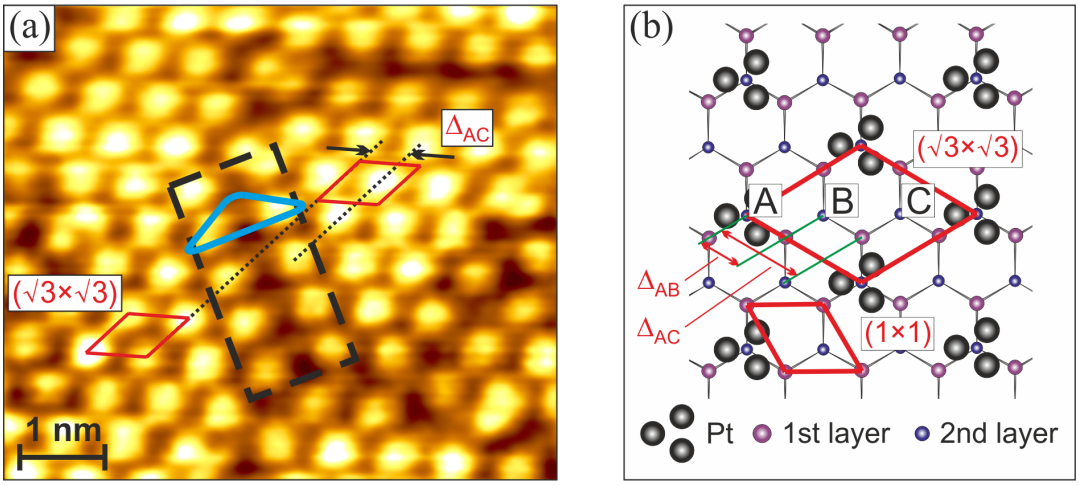

Figure 5.5: *(a) Filled states STM image of a phase-slip domain boundary (dashed rectangle) with two adjacent domains of different phase in Pt/Si(111)-($\sqrt{3} \times \sqrt{3}$); bias: -1.2 V, 0.5 nA, 6.5 × 5.6 nm^2. In-domain protrusions of neighboring domains feature a phase shift of Δ_{AC} with respect to the substrate. ($\sqrt{3} \times \sqrt{3}$) unit cells fixed to the substrate registry are given in red color for both domains. Blue color highlights a boomerang shaped domain wall segment. The contrast has been enhanced for better visibility of domain wall segments. (b) Origin of the phase shifted domains. Pt atoms within the same domain adsorb at only one of the equivalent bonding sites "A", "B", or "C", which allows three shifted ($\sqrt{3} \times \sqrt{3}$) unit cells. Each is anchored at one of these adsorption sites, and thus has a distinct phase relationship to the (1 × 1) substrate unit cell. Accordingly, the domains are phase shifted by Δ_{AB} or Δ_{AC} in dependence of the unit cell anchoring position. Pt atoms are displayed by black spheres (trimers), whereas smaller spheres represent Si atoms of the topmost substrate bilayer (for a detailed discussion refer to text) [H3], Copyright (2010) by the American Physical Society.*

regarded as *phase-slip* domain walls like those in Au/Si(111)-($\sqrt{3} \times \sqrt{3}$) [145]. This becomes even more visible in Fig. 5.5(a), which images the charge density distribution for filled states (bias: -1.2 V, 0.5 nA), centered on a domain wall (dashed rectangle). The ($\sqrt{3} \times \sqrt{3}$) domains to the left and right exhibit a hexagonal array of bright protrusions with one intense spot within the unit cell (red parallelogram). On the basis of the present STM data, the mean distance between adjacent protrusions is evaluated as (6.7 ± 0.1) Å, and the average vertical corrugation is ∼ 0.15 Å. Obviously, this spacing is equal to the surface lattice constant $a_{\sqrt{3},Si}$ of a ($\sqrt{3} \times \sqrt{3}$) reconstruction on Si(111) (refer to Tab. 4.1) [H3]. The domain wall itself exhibits barely visible boomerang shaped segments in filled states (blue color), and it separates the two domains. Evidently, these have a different registry locked to the substrate, resulting in a phase shift between the left and right domain.

The reason for the occurrence of phase-slip domains can be found on the basis of the simple model with threefold-rotational symmetry, depicted in Fig. 5.5(b). It presents the geometric atomic configuration within the two topmost substrate layers and the Pt layer. In close relationship to the CHCT model, platinum trimers are located at T_4 lattice sites, however, with a slight rotation (structural details are presented later in Sec. 5.2.3).

Importantly, there exist three different T_4 sites for Pt trimer localization within one ($\sqrt{3} \times \sqrt{3}$) unit cell, labeled "A", "B", and "C". In consequence, three different domains exist, each characterized by Pt trimers anchored at site "A", "B", or "C", respectively. Hence, phase shifts $\Delta_{\mathrm{AB}} = 1/3\, a_{\sqrt{3},\mathrm{Si}}$ and $\Delta_{\mathrm{AC}} = 2/3\, a_{\sqrt{3},\mathrm{Si}}$, with respect to the surface lattice constant $a_{\sqrt{3},\mathrm{Si}}$, occur between neighboring domains. For the left domain, shown in Fig. 5.5(a) the ($\sqrt{3} \times \sqrt{3}$) unit cell is placed in a way that the protrusion (related to the Pt trimer) is anchored at site "A". Shifting the unit cell by an integer number of its surface lattice vector into the right domain unveils that the locations of the protrusions with respect to the unit cell have changed. This difference agrees well with a phase shift Δ_{AC} in comparison with the model in Fig. 5.5(b). The existence of phase-slip domains at the Pt/Si(111)-($\sqrt{3} \times \sqrt{3}$) surface has also been proposed on the basis of the notable width of the fractional order spots seen in LEED [163].

Comparison and discussion

In comparing these first STM results with those reported for the related Au/Si(111)-($\sqrt{3} \times \sqrt{3}$) surface [146], one remarks unambiguous similarities. Likewise, the most prominent feature in Au/Si(111)-($\sqrt{3} \times \sqrt{3}$) is a network of domain walls, which encloses ($\sqrt{3} \times \sqrt{3}$) reconstructed domains of comparable size [143, 145, 171]. However, the domain wall density, and thus, the domain sizes strongly depend on the initial Au coverage [145]. For Ag/Si(111)-($\sqrt{3} \times \sqrt{3}$), larger deviations are reported. This mainly concerns the domain sizes, which are $\sim$ 4–6 times larger in that surface system [153]. Moreover, the electronic contrast in atomic scale empty states STM images at RT does not feature intensity maxima in a hexagonal arrangement [147]. Instead, a honeycomb pattern is observed here. The electronic properties of Au/Si(111)-($\sqrt{3} \times \sqrt{3}$) are characterized by metallic states, as has been evidenced in photoemission experiments [172, 173]. In turn, it might be possible that Pt/Si(111)-($\sqrt{3} \times \sqrt{3}$) possesses similar electronic properties. ARPES experiments could help clarifying this question in the future.

Lattice mismatch

The differences and similarities, in spite of the close relationship between all three surface 2DESs, provoke the question on their respective origins. In this regard, the formation of domains and their particular sizes represents a major aspect to be scrutinized. In Pt/Si(111)-($\sqrt{3} \times \sqrt{3}$) the notable surface disorder on a short length scale ($\sim$ 10 nm) most likely arises from a lattice mismatch

$$f_{\mathrm{adsorbate-substrate}} = \frac{a_{\mathrm{substrate}} - a_{\mathrm{adsorbate}}}{a_{\mathrm{adsorbate}}} \tag{5.1}$$

between the substrate and the adsorbate [H3, 174]. The lattice repetition period at the surface of bulk Pt(111) ($a_{\mathrm{Pt}} = 2.78$ Å) does strongly deviate from the larger periodicity on Si(111), i.e., $a_{\mathrm{Si}} = 3.84$ Å (see also Tab. 4.1).[1] Utilizing Eq. 5.1 and these values, a

[1] Note that the bulk interatomic distance equals the surface lattice constant for (111) *fcc* crystal surfaces.

lattice mismatch $f_{\mathrm{Pt-Si}} = 38\,\%$ is derived. Hence, it is very likely that strain plays a dominant role in the formation of domain walls here. In Au/Si(111)-($\sqrt{3} \times \sqrt{3}$), where domains of similar size exist, the lattice mismatch between Au ($a_{\mathrm{Au}} = 2.88\,\text{Å}$) and Si is slightly reduced ($f_{\mathrm{Au-Si}} = 33\,\%$). However, in Ag/Si(111)-($\sqrt{3} \times \sqrt{3}$) domains are found to be very large, whereas the surface lattice constant $a_{\mathrm{Ag}} = 2.89\,\text{Å}$ is comparable with the one of Au (a_{Au}), which results in $f_{\mathrm{Ag-Si}} \approx f_{\mathrm{Au-Si}}$. Therefore, a correlation of domain sizes and strain due to a lattice mismatch can only be a part of the whole story.

Orbital character

In addition to a structural origin, also the particular character of the valence electrons needs to be considered. Here, as a common property Au and Ag share a full d shell, while their outermost s orbitals are occupied by a single electron. In contrast, the electronic configuration of Pt is [Xe] $4f^{14}5d^{9}6s^{1}$ (see also Tab. 4.1). Thus, one of the platinum d electrons remains unpaired, while its s shell is half-filled, although partial occupation in terms of $d^{10-\delta}s^{\delta}$ ($0 \leq \delta \leq 1$) is possible likewise [H3]. Despite the different electronic configurations, both Au/Si(111)-($\sqrt{3} \times \sqrt{3}$) and Pt/Si(111)-($\sqrt{3} \times \sqrt{3}$) exhibit domains of similar size, whereas the ordered regions at the Ag/Si(111)-($\sqrt{3} \times \sqrt{3}$) surface are significantly larger. More likely, the directional d orbitals will determine the bonding strength as a consequence of relativistic effects [175]. In this context, the $5d$ metals were reported to exhibit more robust bonds than the $4d$ metals [175]. Thus, it is likely that the long-range character of both the Au and Pt $5d$ orbitals enables the development of robust bonds to the Si substrate, which in consequence might favor the formation of rather small domains.

Energetic stability

A third reason for the observed differences and similarities in these triangular surface systems can be found in their respective cohesion energies, which reflect the energetic stability of an adsorbate [H3]. On the one hand, the cohesion energy of gold is rather large (5.8 eV), whereas the respective value is significantly smaller in the case of silver (2.9 eV) [176]; see also Tab. 5.1. On the other hand, it has been argued that Ag-Ag bonds

Table 5.1: *Surface bond lengths and cohesion energies of bulk noble metal adatoms on Si(111) and Ge(111) in 1 ML ($\sqrt{3} \times \sqrt{3}$) configuration.*

System	surface bond length (Å)	Adatom cohesion energy (eV)
Au/Si(111)	2.83 [133]	5.8 [176]
Au/Ge(111)	2.81 [80, 148]	5.8 [176]
Ag/Si(111)	3.44 [144]	2.9 [176]
Ag/Ge(111)	2.94 [177]	2.9 [176]
Pt/Si(111)	3.1 ± 0.1 [H3]	3.8 [176]

are energetically less stable than Ag-Si bonds [150]. For Ag/Si(111)-($\sqrt{3} \times \sqrt{3}$), both facts can be associated with the huge domains observed experimentally, which evidently are more preferential than accumulation of Ag atoms in form of domain walls. The cohesion energy of platinum (3.8 eV) exceeds the corresponding value of silver, while it is still much smaller than the one of gold. According to the experimental observations, this size of the cohesion energy is obviously sufficient to induce the growth of domain walls in a dense network here.

Furthermore, the energetic differences are also reflected in the two stable, yet distinct, atomic configurations for Au/Si(111)-($\sqrt{3} \times \sqrt{3}$) and Ag/Si(111)-($\sqrt{3} \times \sqrt{3}$), i.e., the CHCT and the HCT model. According to Y. G. Ding *et al.*, the surface energy of Au/Si(111)-($\sqrt{3} \times \sqrt{3}$) is smaller for the CHCT model compared with the related HCT structure [133]. Here, it should be noted that additional stability is gained by the development of strong metal-metal bonds, which represent a typical property of adatom trimers in surface systems described within the CHCT model as, e.g., Au/Si(111)-($\sqrt{3} \times \sqrt{3}$) and Pt/Si(111)-($\sqrt{3} \times \sqrt{3}$). For diatomic molecules of gold and silver the bonding strengths differ significantly, i.e., 2.29 eV (Au-Au) and 1.69 eV (Ag-Ag) [148]. This deviation supports the general observation that in Au-induced ($\sqrt{3} \times \sqrt{3}$) reconstructions trimers are formed, whereas the formation of Ag trimers is less favorable. In contrast, the presence of robust silicon bonds in Ag/Si(111)-($\sqrt{3} \times \sqrt{3}$) favors the HCT surface structure.

In conclusion, it will be a delicate mixture of strain due to lattice mismatch, orbital character of the elements involved, and surface energy, that leads to the formation of rather small domains in Pt/Si(111)-($\sqrt{3} \times \sqrt{3}$).

5.2.2 Sub-structure of protrusions at the atomic level

The lack of knowledge on the exact platinum coverage in the literature cast doubts on the validity of any structural model proposed for Pt/Si(111)-($\sqrt{3} \times \sqrt{3}$). In this view, the one suggested by A. Wawro *et al.*, based on a 1/3 ML Pt coverage within ($\sqrt{3} \times \sqrt{3}$) reconstructed domains, should be regarded critically [162]. According to that study, single Pt atoms reside in the middle of a triangular unit made up by the three general adsorption sites T_4, T_1, and H_3. This seems confusing, since no other related surface system is known, where adsorbate atoms are located at such interstitial sites. Moreover, it lacks any physical reason that would favor this adsorption site for Pt atoms. In addition, the authors of that study claim that the apexes of boomerang shaped domain wall segments should be related to substrate atoms. However, they also admit the impossibility to attribute these spots to either T_4 or H_3 sites by use of STM only. Furthermore, the obvious deviation from the commonly accepted models for noble metal adsorption, i.e., the CHCT, the HCT, or even the IET model, which all assume a coverage of 1 ML, clearly contradicts the proposed model.

In order to unveil the true atomic geometry, it is a logical consequence to scrutinize

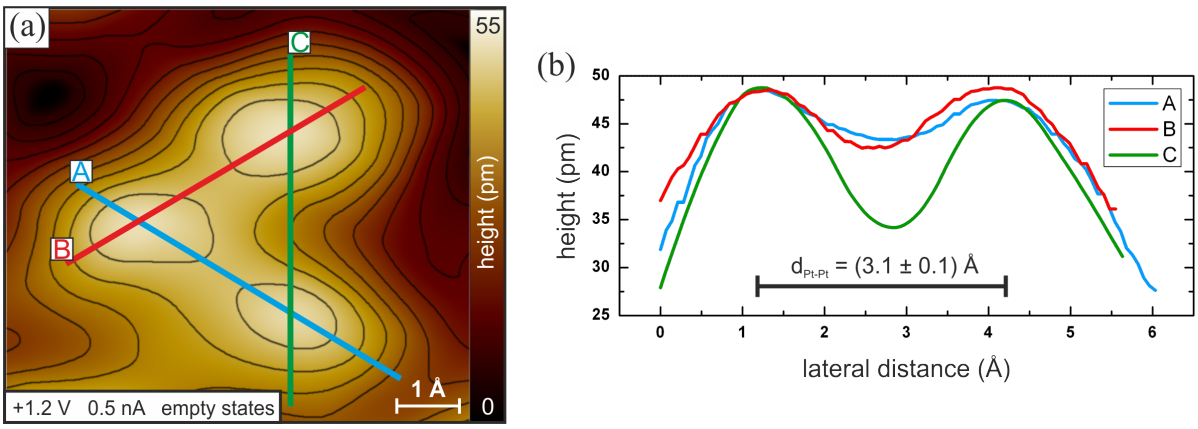

Figure 5.6: *(a) Empty states STM image of a single protrusion within the* $(\sqrt{3} \times \sqrt{3})$ *unit cell in Pt/Si(111) that exhibits a sub-structure of three intensity maxima in a triangular arrangement; bias: +1.2 V, 0.5 nA,* $7.4 \times 6.6\,\text{Å}^2$*. Contour lines serve as a guide to the eye to visualize the height contrast. The straight lines indicate the directions of the height profiles in (b) along two adjacent sub-protrusions. The average sub-protrusion distance* $d_{\text{Pt}-\text{Pt}} = 3.1\,\text{Å}$ *is derived by fitting the profiles with a Gaussian function [H3], Copyright (2010) by the American Physical Society.*

single protrusions at the atomic level, and in particular, their appearance next to the domain walls. In this regard, a closer look to the empty states STM image in Fig. 5.4(a) reveals that single protrusions inside of $(\sqrt{3} \times \sqrt{3})$ domains exhibit a more triangular shape than suggestive of single Pt atoms with their spherical *s* orbitals. A close-up to such a triangular protrusion is given by the empty states STM image in Fig. 5.6(a) in high resolution (bias: +1.2 V, 0.5 nA). Indeed, a sub-structure with triangular arrangement is observed, that consists of three individual protrusions with slight difference in height. The height profiles in Fig. 5.6(b), taken along the directions A, B, and C, support this finding. By fitting their line shapes with a Gaussian function, a spacing of $d_{\text{Pt}-\text{Pt}} = (3.1 \pm 0.1)\,\text{Å}$ between the two peak positions is obtained independently of the individual direction of the height profiles. According to the CHCT model, this distance is interpreted as the length between two Pt atoms within a single *trimer*. The respective spacing for gold atoms in a trimer at the surface of Au/Si(111)-$(\sqrt{3} \times \sqrt{3})$ has been calculated by Y. G. Ding *et al.* as $\sim 2.83\,\text{Å}$ (see also Tab. 5.1) [133]. This value is in good agreement with the distance of nearest-neighbor atoms in a bulk Au crystal ($\sim 2.9\,\text{Å}$). In the same way, it turns out that the deviation of $d_{\text{Pt}-\text{Pt}}$ from the Pt bulk nearest-neighbor distance ($\sim 2.8\,\text{Å}$) is only little larger. Therefore, one may safely conclude that also the experimental *in-trimer* spacing of Pt atoms is well consistent with the corresponding bulk value.

An additional argument for the interpretation above is provided by the bias-dependent protrusion shape analysis in Fig. 5.7. Therein, the protrusion shapes in filled and empty states are compared with calculations of the charge density distribution in the related surface system Au/Si(111)-$(\sqrt{3} \times \sqrt{3})$ by Y. G. Ding *et al.* [133]. As has already been stated, the protrusions visible in (a) filled states STM images (bias: -1.2 V, 0.5 nA) do

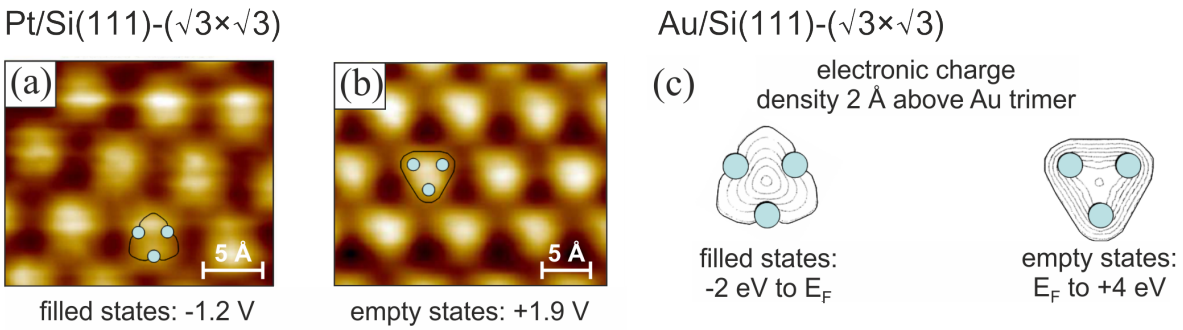

Figure 5.7: *(a) Filled (bias: -1.2 V, 0.5 nA, 2.2 × 1.9 nm²) and (b) empty (bias: +1.9 V, 0.5 nA, 2.8 × 2.3 nm²) states STM images for scrutiny of the protrusion shapes within a ($\sqrt{3} \times \sqrt{3}$) reconstructed domain of Pt/Si(111), overlaid by the outer iso-charge density line from (c). (c) Electronic charge density calculated for filled (-2 eV to E_F) and empty (E_F to +4 eV) states in Au/Si(111)-($\sqrt{3} \times \sqrt{3}$) within the CHCT model [133]. Thin black contours are lines of equal charge at a distance of 2 Å above a single Au trimer (blue color) [H3], Copyright (2010) by the American Physical Society. Calculations are adopted from [133].*

not allow to conclude a triangular arrangement within one single intensity peak. Yet, in the empty states image (b), taken at even larger bias (+1.9 V, 0.5 nA) than in the images shown before, the triangular protrusion shape is equally visible. Thus, there exists no obvious bias dependency of the protrusion shape in the positive voltage regime under investigation. Fig. 5.7(c) shows charge density calculations for Au trimers in the CHCT configuration of Au/Si(111)-($\sqrt{3} \times \sqrt{3}$) in filled (-2 eV to E_F) and empty (E_F to +4 eV) states slightly above (2 Å) the Au trimers (adopted from [133]). The iso-charge lines for both bias polarities exhibit a triangular shape, however, with its apex direction inverted. Importantly, the lateral charge gradient at the triangle edges is much more pronounced for empty states, visible by its high density of iso-charge lines. Based on these calculations, one would expect to observe a Au trimer by its triangular charge density distribution more easily in empty states STM images. Taking this as a valid assumption also in the case of the related Pt atoms, one may attribute the triangular shape in Fig. 5.7(b) to a platinum *trimer* instead of a single platinum atom. This interpretation is indicated by an overlay of the calculated outer iso-charge line. In agreement, the filled states STM graph has no sign of a triangular protrusion shape, as has been presupposed by its smaller lateral charge gradient. Otherwise, one would expect a reversal by 180 ° in the triangle orientation.

In conclusion, the bias-dependent protrusion analysis above provides an additional striking argument for the existence of Pt trimers on the Si(111) surface instead of single atoms. Importantly, this involves a Pt coverage of 1 ML instead of 1/3 ML, as earlier suggested by other groups [157, 162, 165]. A further essential result, derived from the analysis above, concerns the orientation of the trimers. Their apexes are assumed to point in the direction of nearest-neighbor trimers, as described in the original CHCT model [see Fig. 5.1(a)]. Yet, it turns out as a surprise here that they actually point

towards *next-nearest*-neighbor triangles. In consequence, each trimer must be rotated by 30 ° from its orientation defined in the pristine CHCT model. Such an unusual atomic alignment is remarkable, since it involves a *symmetry breaking* of the surface, and hence, the atomic structure of Pt/Si(111)-($\sqrt{3} \times \sqrt{3}$) represents a rare example of *chirality* on a semiconductor surface [H3].

5.2.3 Domain wall structure and refined structural model

The surprising finding of a 1 ML coverage within ($\sqrt{3} \times \sqrt{3}$) reconstructed domains due to the presence of rotated Pt trimers still leaves room for speculation on the atomic structure and Pt density inside the domain walls. It would further be intriguing to ask which local arrangement within the walls induces the phase shift, and how the domain walls couple to the enclosed domains. Answering these questions would contribute to the development of the still unknown structural model for Pt/Si(111)-($\sqrt{3} \times \sqrt{3}$).

In this regard, the detailed in-domain wall protrusion analysis presented in Fig. 5.8 is appropriate to clarify these issues. In Fig. 5.8(a) an empty states STM image (bias: +1.9 V, 0.5 nA) of a few domains, surrounded by domain walls that exhibit a pronounced boomerang shape, is depicted. The domain boundaries are quite reminiscent of the ones seen by STM in Au/Si(111)-($\sqrt{3} \times \sqrt{3}$) [171]. More details of the atomic domain wall structure become visible in the close-up (inset) of the region marked by the red box, which focuses on three adjacent domain wall segments. The main finding of this refined inspection is that the domain wall is constituted of three adjacent rows of protrusions.

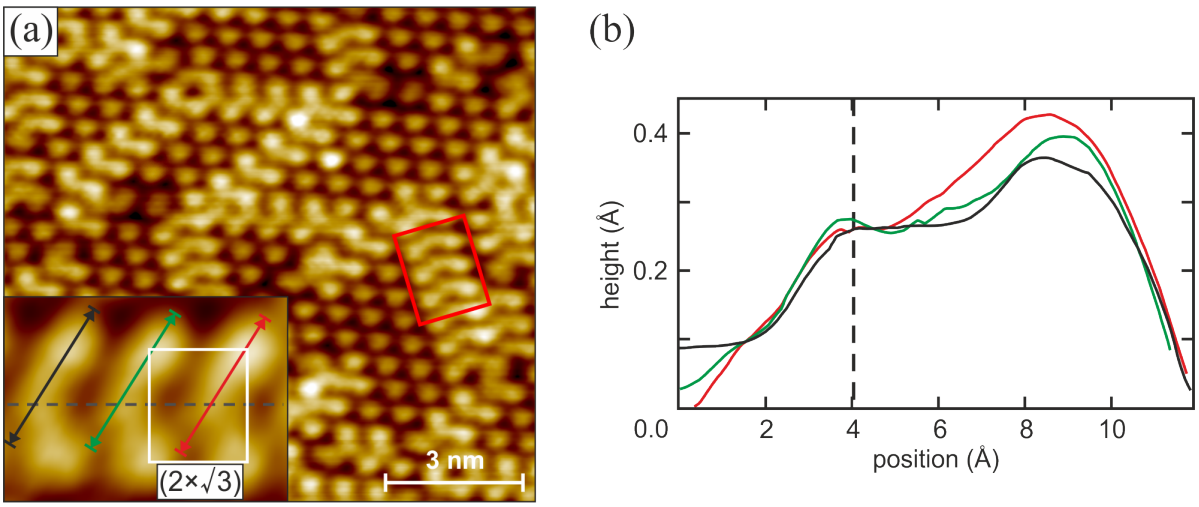

Figure 5.8: *(a) Empty states STM image focusing on the protrusion shape within the domain walls at the Pt/Si(111)-($\sqrt{3} \times \sqrt{3}$) surface; bias: +1.9 V, 0.5 nA, 11.6 × 10.8 nm^2. Inset: close-up (2.0 × 1.6 nm^2) of the region within the red box. A domain wall sub-structure of three protrusion rows with a local ($2 \times \sqrt{3}$) periodic arrangement is unveiled. (b) Height profiles along the three colored lines indicated in (a) validate the existence of a middle protrusion row (dashed line) [H3], Copyright (2010) by the American Physical Society.*

The existence of the less intense middle row is evidenced by three height profiles along the colored lines in Fig. 5.8(b). Its position is indicated by the dashed lines in (a) and (b). The two outer rows, each being part of the two neighboring domains, are spaced by (7.7 ± 0.1) Å, which closely corresponds to $2a_{\mathrm{Si}} = 7.68$ Å. In contrast, the spacing in domain wall direction is the same as within the domains and relates to the $\sqrt{3}$ dilation for all three rows. Yet, the middle row protrusion is shifted by 2.2 Å in domain wall direction with respect to the protrusions in the outer rows. These observations allow to attribute a local $(2 \times \sqrt{3})$ periodicity to the domain walls, as has also been observed for the domain walls in Au/Si(111)-($\sqrt{3} \times \sqrt{3}$) [146, 171]. In the latter system the Au density in the chains is assumed to be higher than in the domains, therefore being called "heavy domain walls" [146].

In the next step the results presented so far shall be merged into a structural model which is capable of describing the Pt trimer rotations, the domain wall geometries, and the phase shifts between the domains. In view of this, the CHCT model is chosen as a robust basis here. The fundamental idea is then to utilize the domain walls as a *landmark* on the surface to detect the trimer orientation and registry with respect to the substrate [H3]. For this purpose, the empty states (bias: +1.9 V, 0.5 nA) STM image in Fig. 5.9(a) represents an excellent basis, as it features both a pronounced domain wall sub-structure and trimer shaped in-domain protrusions. The triangular shaped spots, which are associated with Pt trimers, are overlaid by groups of three spheres arranged in a $(\sqrt{3} \times \sqrt{3})$ periodicity, that represent atomic positions in the left (orange) and right domain (green). Both domains to the left and right of the vertically running domain wall are phase shifted by $\Delta_{\mathrm{AB}} = 2.2$ Å, which conforms to 1/3 of the $\sqrt{3}$-dilated Si surface lattice constant $a_{\sqrt{3},\mathrm{Si}}$. The left (yellow) and right (bright green) outer domain wall protrusion rows also consist of trimers, which exhibit a spacing of $\Delta = 7.7$ Å $\approx 2a_{\mathrm{Si}}$, that interrupts the regular array of trimer rows within the $(\sqrt{3} \times \sqrt{3})$ domains. The protrusions of the shifted middle row do not exhibit a triangular shape and are less intense in STM than the surrounding trimers. Therefore, it is proposed that each middle row intensity spot, enclosed within a $(2 \times \sqrt{3})$ unit cell, represents a *single* Pt adatom (blue spheres).

This approach also results in the following finding. For a domain wall with its boomerang shaped segments pointing downwards (indicated in blue), the apexes of the Pt trimers in the domains always point to the left, regardless to which domain they belong. This seems to be a common property of the Pt/Si(111)-($\sqrt{3} \times \sqrt{3}$) surface, that holds for all empty states STM images. This finding also remains valid for domain walls that point along the two other equivalent $\langle 11\bar{2} \rangle$ high symmetry substrate directions as, e.g., visible in the top right corner of Fig. 5.8(a) for a second, but rotated domain wall, adjacent to the right domain. In comparison with the filled states STM image in Fig. 5.5(a), these empty states data also reveal that, although the contrast is reversed, the same atomic structure of the domain boundary is detected. Thus, it is unlikely that electronic effects obscure the domain wall atomic structure.

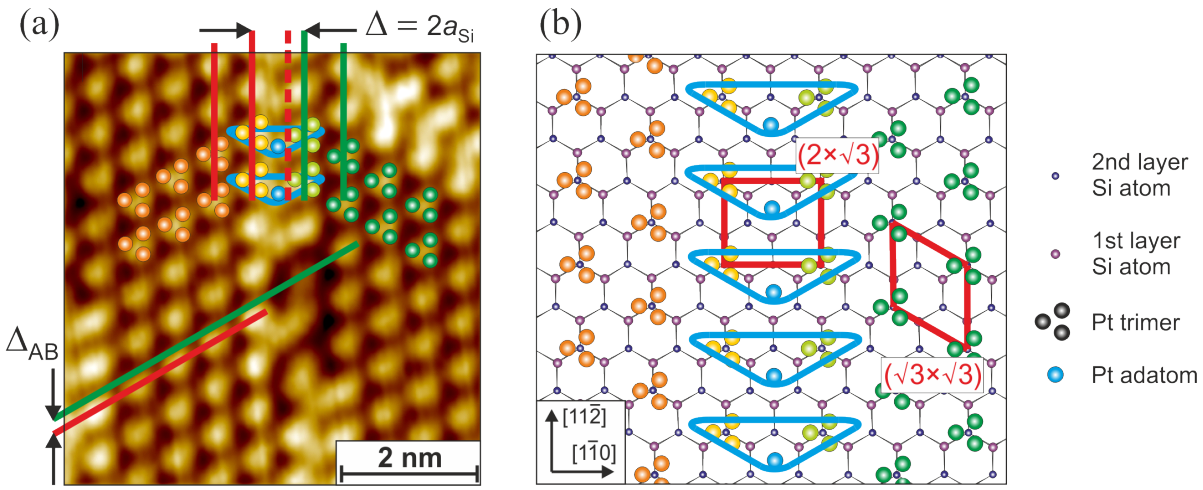

Figure 5.9: *(a) Empty states STM image of two domains, intersected by a vertically running phase-slip domain wall in Pt/Si(111)-($\sqrt{3}\times\sqrt{3}$); bias: +1.9 V, 0.5 nA, 6.1×6.4 nm^2. The lines indicate phase shifts Δ_{AB} and Δ between the domains and outer domain wall protrusion rows, respectively. The colored spheres highlight atomic positions, superimposed on the STM data for left (orange) and right (green) domains, left (yellow) and right (bright green) outer domain wall protrusion rows, as well as middle row protrusions (blue). (b) Domain wall model for Pt/Si(111)-($\sqrt{3}\times\sqrt{3}$) based on the CHCT model. Rotated Pt trimers, arranged in ($\sqrt{3}\times\sqrt{3}$) periodicity on top of the Si(111) surface bilayer, are located at T_4 sites. Color coding agrees with the conventions in (a). Domain wall segments in boomerang shape (outlined in blue) include trimers from the outer domain wall protrusion rows and a single Pt atom at H_3 sites in a local ($2\times\sqrt{3}$) periodicity. For further details refer to text [H3], Copyright (2010) by the American Physical Society.*

Refined structural model

Based on the discussion so far, and by supposing the CHCT model to represent a valid basis also for Pt/Si(111)-($\sqrt{3}\times\sqrt{3}$), which is a reasonable assumption due to the close relationship to Au/Si(111)-($\sqrt{3}\times\sqrt{3}$), one may construct a refined structural model. This is visualized in Fig. 5.9(b), where Pt trimers are locked to T_4 lattice sites of the underlying Si(111) top bilayer, as it is the case in the original CHCT model [compare to Fig. 5.1(a)]. The trimer positions agree with the STM data presented in Fig. 5.9(a). In comparison with Fig. 5.9(a), the construction also uncovers the exact location of the single Pt atoms of the domain wall middle row. These can only reside at H_3 lattice sites, since no other adsorption site, i.e., neither T_1 nor T_4, would be consistent with the middle row shift of 2.2 Å along the domain boundary. As a key signature, this model points out that the Pt trimers need to be rotated by 30 ° around a perpendicular rotational axis with respect to their positions in the original CHCT model. This is mandatory for compliance with the fact that the apexes of the Pt trimers point in between two adjacent trimers, as revealed by STM. Based on the findings above the refined structural model in Fig. 5.9(b) is constructed [H3]. It essentially comprises the following key aspects.

- In-domain protrusions in STM images are due to Pt trimers instead of single atoms.
- Neighboring domains are phase shifted against one another.
- Domain walls possess a local ($2 \times \sqrt{3}$) periodic arrangement.
- The middle domain wall row is composed of single Pt atoms.
- Each Pt trimer is rotated by 30 ° with respect to the substrate.

As a consequence of this symmetry-breaking configuration, the Pt/Si(111)-($\sqrt{3} \times \sqrt{3}$) system represents a rare example of *chirality* at such a semiconductor surface. Intuitively, both left-handed and right-handed chirality should exist alongside each other, i.e., one would assume that enantiomeric domains are formed, where the trimer rotation is either 30 ° clock-wise or 30 ° anti-clockwise. This must not be confused with domains as in Fig. 5.9 which are characterized by a *registry shift* with respect to the substrate [H3]. Interestingly, in the present case there exists only one type of chirality, since the trimer orientation is the same within all domains. These findings are in contrast to the results obtained from Au/Si(111)-($\sqrt{3} \times \sqrt{3}$), where no trimer rotation was observed. In that surface system, and contrary to Pt/Si(111)-($\sqrt{3} \times \sqrt{3}$), the domain wall was suggested to contain Au *trimers* at H_3 sites along the middle row instead of single atoms only [146]. Turning back to Pt/Si(111)-($\sqrt{3} \times \sqrt{3}$), the middle row protrusions were ascribed to Si atoms in the structural model proposed by A. Wawro *et al.* [162]. However, based on their data no definite determination of the according lattice sites was possible. Regardless of the question, whether the middle wall protrusions are identified as Pt or as Si atoms, one may conclude that the atomic configuration of the Pt/Si(111)-($\sqrt{3} \times \sqrt{3}$) surface reconstruction is best described by the refined CHCT model, developed in this thesis. This also implies that both domains and domain walls always possess a platinum adatom coverage of exactly 1 ML. In turn, the domain wall density cannot depend on the deposited amount of Pt, as has been confirmed in STM measurements for different initial adsorbate coverages.

Finally, it is worth discussing possible driving mechanisms behind the surprising Pt trimer rotation. In one probable scenario, the bond distance between the Pt atoms and their nearest Si neighbors is readjusted such that a more stable situation is achieved. More generally expressed, the rotation would result from the local reduction of lattice strain then [H3]. It has further been suggested that a symmetry lowering induced by a 6 ° trimer rotation in Pd/Si(111)-($\sqrt{3} \times \sqrt{3}$) stabilizes that surface [178]. Similarly, the triangle rotation in the Ag/Si(111)-($\sqrt{3} \times \sqrt{3}$) IET phase or the rotation of Pt trimers found here could be understood. In particular, among the known metal-semiconductor surface adsorbate systems, the IET model [see Fig. 5.1(c)] is the only other one which involves a surface chirality, yet being weaker there (only 6 ° rotation). This assignment relies on a profound basis, including STM and DFT modeling [144], while theoretical calculations are still needed to provide further support for the structural model, proposed here for Pt/Si(111)-($\sqrt{3} \times \sqrt{3}$). Besides the class of noble metal induced 2DESs,

other examples of chiral surfaces are known from the literature. This includes, e.g., homochirality triggered by electromigration on Si(110) [179], In clusters with two distinct chiralities on Si(111) [180], high-index metal surfaces [181], and strain-induced chirality on oxygen-adsorbed Cu(110) [182]. As an outlook, it is worth noting that a chiral surface like Pt/Si(111)-($\sqrt{3} \times \sqrt{3}$) could be a promising candidate for enantio-selective adsorption of chiral organic molecules and for catalytic processes [H3]. It would be an intriguing task to study such local effects and reactions with STM or related imaging techniques at the atomic scale.

6 Spin-orbit interaction at a semiconductor surface

The electronic manipulation of spins, and the generation and detection of spin currents in semiconductors and their interfaces are of fundamental importance in the development of semiconductor-based *spintronics*. In particular, the injection of spin-polarized currents can be achieved by use of magnetic coating layers. In this regard, the applicability and potential of the half-metallic ferrimagnet magnetite [183] and thin films of iron on semiconductors [184] have been evaluated. However, major hurdles are the necessity of low-impedance contacts and the quality of the interfaces here. Moreover, control of spin currents in the absence of external magnetic fields will be highly relevant for applications. An intriguing approach to this basic issue is given by the Rashba type SOI at crystalline surfaces [19].

In 1996, S. LaShell *et al.* have reported a splitting in the parabolic L-gap surface state of Au(111) and correctly interpreted this to result from SOIs [20]. Their famous article has set the stage for a series of fascinating studies on the SOI at a variety of solid state surfaces. This includes the (111) orientations of related single crystals, like Bi [21, 185] and Sb [186]. A further important class are the surface alloys, i.e., single crystal surfaces, where usually every third atom is replaced by a heavy substitute atom. Examples comprise binary alloys, such as Bi/Ag(111) [22, 187], Sb/Ag(111) [188], and Pb/Ag(111) [22], but also ternary alloys, e.g., $\mathrm{Bi}_x\mathrm{Pb}_{1-x}$/Ag(111) [189]. All these systems have the (111) surface orientation and the presence of heavy atoms at the surface in common, which represents a main prerequisite for strong SOIs. Thus, the effect of spin separation can be very large in these systems. However, exploitation for spintronic applications demands the absence of bulk conduction, which otherwise dominates the overall signal and hinders the detection of spin separated currents. Therefore, conducting states, located in the bulk band gap of an insulating material, are preferable. In this regard, the Si(111) and Ge(111) surfaces represent a promising basis, and the deposition of Bi and Tl at 1 ML coverage has been shown to cause surface states which are split due to the SOI [24, 25]. Although the band offset in momentum k_0 is comparably large at both surfaces ($2k_0 > 0.2\,\text{Å}^{-1}$, see Tab. 6.1), the spin-split bands are completely filled, and these systems are in fact insulating. Conducting and spin-split surfaces states at the same time have so far only been realized in the dense β-phase of Pb/Ge(111)-($\sqrt{3}\times\sqrt{3}$) [26].

With the increased utilization of SARPES for the study of these systems, it turned out that a conventional spin alignment as in the Rashba effect [19] must be regarded as

an exception and has only been verified experimentally for Au(111) [52]. Importantly, due to the presence of additional potential gradients at the surface that deviate from a strict perpendicular orientation, the spin patterns are rather complex in general. This involves *out-of-plane* spin orientations with threefold symmetry, first observed for the surface alloy Bi/Ag(111) [22, 187], and later also for the metal coated semiconductor system Tl/Si(111)-(1×1) [25]. These findings also extend to the field of 3D topological insulators, where recent theoretical studies for Bi_2Te_3 have predicted an even more complex spin texture due to *Dresselhaus* type contributions to the SOI [27, 28, 55] (cf. discussion in Sec. 2.1).

Tab. 6.1 lists a selection of surface systems that exhibit band splittings due to the SOI at surfaces. Systems that include bismuth as a very heavy element possess the largest splittings in momentum. Importantly, conductive metal induced reconstructions on semiconductors are limited to the cases of Pb/Ge(111)-$(\sqrt{3} \times \sqrt{3})$ and Au/Ge(111)-$(\sqrt{3} \times \sqrt{3})$, as will be elucidated in the following sections for the latter. Finally, it should be noted that the observation of such spin splittings is not only restricted to 2DESs, but can also occur in quantum well films on semiconducting substrates, e.g., Pb films on Si(111) [190], and in quasi-1D surface systems as, e.g., Au/Si(557) [191, 192] and Bi(114) [193].

6.1 Atomic geometries at the Au/Ge(111)-$(\sqrt{3} \times \sqrt{3})$ surface

A novel and promising path towards the realization of strong SOIs at the surface of a semiconductor can be found in noble metal induced reconstructions, which contain particularly heavy elements (high atomic number Z). These involve different electronic and orbital properties (cf. Tab. 4.1) and are candidates to exhibit Rashba physics with conducting spin-split surface states. Here, the adsorption of Au on Si(111) [143, 146, 173] and Pt on Si(111) [H3], but to some extent also the one of Ag [143, 153, 173] on the same surface should be highlighted. Among the huge variety of metal adsorbate induced surface reconstructions which are known to form 2DESs on Si(111), the $(\sqrt{3} \times \sqrt{3})$ phase is the most common one [H5]. Due to its easy preparation and in particular triggered by its potential technological importance, both structural and electronic properties of Au/Si(111)-$(\sqrt{3} \times \sqrt{3})$ are well understood today. Likewise, Au deposition on the related Ge(111) surface generates a corresponding system, albeit the few studies so far were mainly restricted to the structural properties [80, 148, 152]. Details on the valence band structure are essentially unknown, and available angle-resolve photoemission spectra suffer significantly from poor experimental resolution [197]. Thus, the ARPES data in the present study are the first to access the electronic band structure of Au/Ge(111)-$(\sqrt{3} \times \sqrt{3})$ in detail [H5]. In addition, the delicate spin texture at the FS is unveiled for the first time [H6].

Table 6.1: *Selection of spin-orbit coupled low-dimensional electron systems. For comparison the conductive behavior, the maximum size of the splitting $2k_0$, the Rashba parameter α_R, and the respective spin orientations, if procurable, are listed.*

System category	System	Adatom cov.	Conduction	$2k_0$ (Å^{-1})	α_R (eV Å)	Method	Spin orientation reported	Reference
single crystal	Au(111)	—	metallic	0.025	0.33	ARPES, 3D SARPES	in-plane only	52, 187, 194
	Bi(111)	—	metallic	0.10	0.56	SARPES	in-plane	185, 187
surface alloy	Pb/Ag(111)	1/3 ML	metallic	0.05	2.36	3D SARPES	in- & out-of-plane	22
	Bi/Ag(111)	1/3 ML	metallic	0.26	3.05	ARPES, 3D SARPES	in- & out-of-plane	22, 187
	Bi/Cu(111)	1/3 ML	metallic	0.028–0.096	0.62–1.0	ARPES & DFT	in- & out-of-plane	195
thin films	Bi/Si(111)	40 bilayers	metallic	—	—	3D SARPES	in- & out-of-plane	196
	Pb/Si(111)	8 ML	metallic	0.070	0.04	3D SARPES	in-plane only	190
atomic wires	Au/Si(557)	0.2 ML	metallic	0.05	—	3D SARPES	in- & out-of-plane	192
metal on semiconductor 2DES	Bi/Si(111)	1 ML	insulating	0.210	2.3	SARPES	in-plane	24
	Bi/Ge(111)	1 ML	insulating	0.16	1.8	ARPES & DFT	in-plane	50
	Tl/Si(111)	1 ML	insulating	0.4	—	SARPES	in- & out-of-plane	25
	Pb/Ge(111)	4/3 ML	metallic	0.04	0.335	SARPES	in-plane	26
	Au/Ge(111)	1 ML	metallic	0.025	0.10	3D SARPES	in- & out-of-plane	this study, H6

6.1.1 Structural model

Until the 1980s, most studies of $(\sqrt{3} \times \sqrt{3})$ surface reconstructions did not involve a definite clarification of the atomic structure at the surface. However, at least since the proposition of the HCT structural model for Ag/Si(111)-$(\sqrt{3} \times \sqrt{3})$ in 1988 by T. Takahashi *et al.* [151], the focus has turned to scattering techniques, being sensitive to the local coordinates of different atom species at the surface. In this regard, surface x-ray diffraction (SXRD) has prevailed as a highly reliable tool, in particular due to its sensitivity towards in-plane atomic coordinates. Yet, the technique is less reliable with respect to perpendicular distances due to the poor momentum transfer normal to the surface, which results from the grazing incidence experimental setup [80]. This deficiency can be partly resolved by measuring "crystal truncation rods", while the accuracy in determining out-of-plane atomic positions is still limited by the goniometer range. In contrast, IV-LEED allows for a more precise determination of atom coordinates normal to the surface plane, while at the same time the in-plane coordinates are less accurately identified. In addition, these two complementary experimental techniques are usually accompanied by total energy calculations within the DFT. Therein, a probable structural configuration is assumed, with the initial atomic coordinates often taken from the experiment. In allowing the atoms to relax until the desired degree of precision is reached, the total energy of the surface is minimized. In this way, DFT provides a reliable measure for the energetic stability of a particular atomic configuration. In many cases these calculations corroborate the experimental findings, which in turn enhances the general acceptance of the corresponding structural model.

Early experiments on Au/Ge(111)-$(\sqrt{3} \times \sqrt{3})$ were mainly concerned with the growth characteristics, without further characterization of atomic geometries at the surface [198]. Epitaxial growth of Au on Ge(111), i.e., for Au coverages exceeding 1 ML, follows the "Stranski-Krastanov" type, which leads to the formation of islands after completion of a smooth top layer [152]. For 1 ML coverage the SXRD experiments by P. B. Howes *et al.* [148] were then the first to prove the existence of Au *trimers* at the surface, and thus the validity of the CHCT model for this system. The structural model with the atomic coordinates from diffraction is depicted in Fig. 6.1. In the top view representation (a) it can be clearly seen that Au atoms (orange) nucleate as trimers around T_4 adsorption sites, being at the same time embedded in a MTL of Ge adatoms (green). The latter are slightly bent away from their initial T_1 lattice sites in order to increase their distance from the trimer. The close vertical spacing between Au trimers and Ge adatoms becomes more evident in the side view (b). Soon after the SXRD experiments, speculations arose on the basis of STM and XPS measurements, whether the surface should be more precisely described by a slight modification to the original CHCT model [199]. In this refined configuration (M-VI, see Fig. 6.2 and Tab. 6.2) Au trimers are located at T_1 lattice sites, with the Ge adatom density reduced to 1/3 ML at the same time. Nevertheless, this model is energetically unfavorable, as unveiled in the following by total energy DFT calculations. Also an IV-LEED study [80] verifies this view, as it speaks

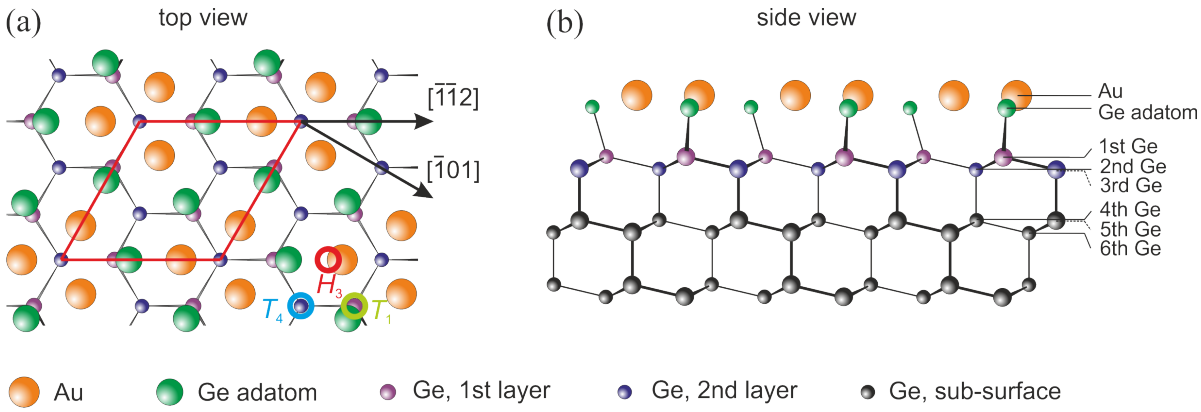

Figure 6.1: *CHCT structural model for Au/Ge(111)-($\sqrt{3} \times \sqrt{3}$) in top view (a) and side view (b) with relative distances, as derived by SXRD [148]. Atom sizes are not to scale, but rather represent the distance from the spectator. Lattice sites H_3, T_4, and T_1 are indicted by colored circles, and the unit cell is outlined in red. Graphics are according to [148].*

again in favor of the originally proposed CHCT structural model, which is also valid for the related Au/Si(111)-($\sqrt{3} \times \sqrt{3}$) surface [133].

DFT total energy calculations of different atomic configurations

Despite the agreement between the SXRD and IV-LEED results for this surface, there is still a lack of DFT total energy calculations. Yet, at least two important reasons for such theoretical modeling should be mentioned at this point. First, these could strengthen the experimental findings or give valuable hints towards necessary modifications of the model. And second, in calculating the total energy of this model in comparison with that of other potential structural models, one obtains a measure of the energetic stability of the surface. This is important, since it is known from the Ag/Si(111)-($\sqrt{3} \times \sqrt{3}$) surface that the IET model describes the most stable configuration at LT, whereas increased temperatures induce the structural phase transition to the RT HCT phase [144, 154].

Thus, besides the so far accepted CHCT model, seven slightly varying models have been scrutinized with regard to their respective total energy per unit cell by A. Fleszar [200]. These include the six modified atomic configurations M-I–M-VI and the well known HCT configuration, which are sketched in Fig. 6.2. The initial atomic coordinates for the CHCT configuration were adopted from the SXRD study by P. B. Howes *et al.* [148]. Details on the calculations will be published elsewhere [200]. All models feature a Au coverage of 1 ML, but differences exist in the Ge adatom density, the Au trimer locations, and their respective orientations with respect to the substrate. From Fig. 6.2 it is clearly visible that

- CHCT, M-III, M-IV, and HCT include 1 ML of Ge adatoms, the so-called MTL configuration.

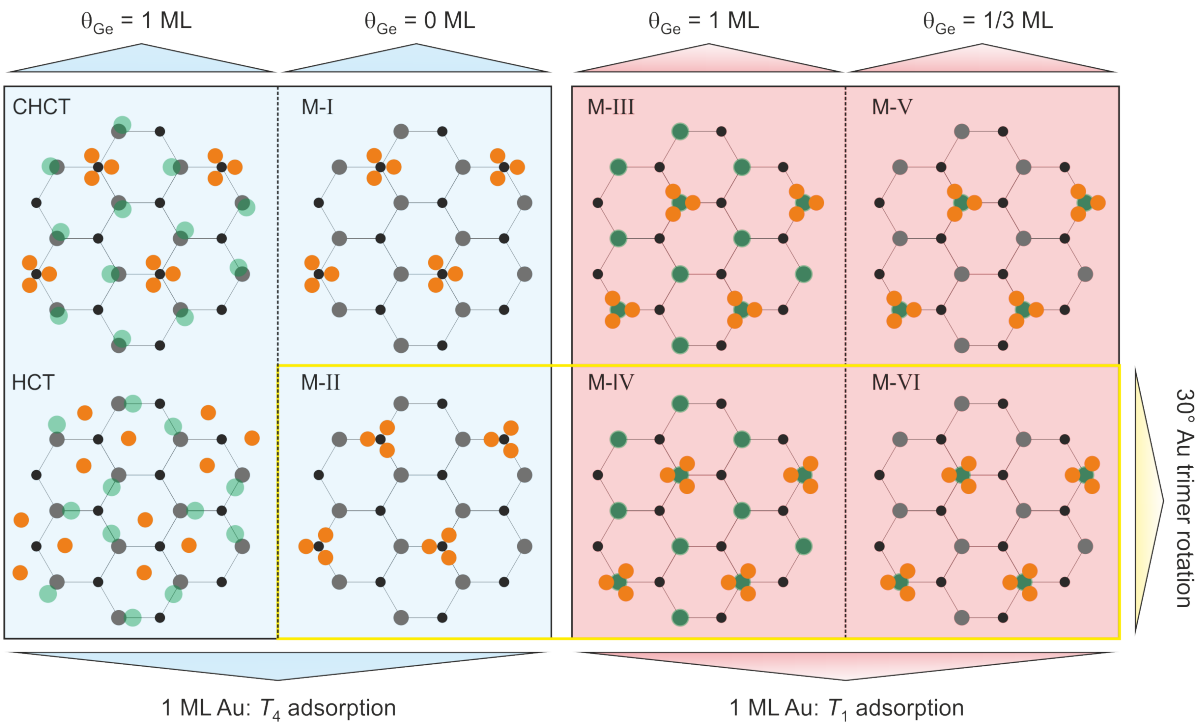

Figure 6.2: *Schematic top view representation of the eight different structural models for Au/Ge(111)-($\sqrt{3} \times \sqrt{3}$), inspected by DFT total energy calculations [200]. The atomic color coding is as follows: Au atoms (orange circles), Ge adatoms (green circles), Ge 1st layer atoms (gray circles), Ge 2nd layer atoms (black circles). The models differ in Ge adatom coverage (θ_{Ge}), Au trimer location (T_4 and T_1 adsorption sites), and orientation (30° rotation), as indicated by the colored boxes. Initial vertical atom distances are the same within all models.*

- M-I and M-II have no germanium adatoms, i.e., they possess a completed Ge bilayer below only.
- an even more exotic configuration exists for M-V and M-VI, which involve a fractional Ge adatom coverage of 1/3 ML.
- the Au trimer adsorption site is T_4 in the four models in the left half of Fig. 6.2 (blue box), whereas it is T_1 in the right half of the figure (red box).
- M-II, M-IV, and M-VI are characterized by a Au trimer rotation of 30 ° with respect to the surface normal (yellow rectangle).

The results of the DFT total energy calculations are summarized in Tab. 6.2. The main finding is that the CHCT structural model, suggested by SXRD and IV-LEED, is indeed the most stable configuration of Au/Ge(111)-($\sqrt{3} \times \sqrt{3}$). Its energy is set to zero for a quantitative comparison with the surface formation energies of the other seven models. One notices that the HCT structure represents the second most stable configuration with a surface formation energy of 0.93 eV per unit cell. This is a rather large value,

Table 6.2: *Surface formation energy of the different structural models for Au/Ge(111)-($\sqrt{3} \times \sqrt{3}$) in Fig. 6.2, calculated by DFT [200]. The Au coverage is always 1 ML.*

Structural model	Ge adatom coverage (ML)	Surface formation energy / unit cell (eV)
CHCT	1	0
HCT	1	0.93
M-I	0	3.09
M-II	0	2.59
M-III	1	4.46
M-IV	1	4.28
M-V	1/3	6.67
M-VI	1/3	6.64

and thus, the HCT model should be excluded as a starting point for band structure modeling. Concerning the surface formation energies of all other models inspected, the calculations return significantly higher values, hence, rendering them even less probable. In particular, the very unfavorable M-VI configuration corresponds to the one proposed by M. Göthelid *et al.* [199], which has been discarded due to its contradiction with the SXRD and IV-LEED studies. In conclusion, all further calculations (including band structure modeling) shown within this thesis are based on the CHCT structural model.

The atomic coordinates in the favored CHCT model have been determined within an extended relaxation scheme, that uses a 63 atom slab [200]. Calculations were conducted as long as the force acting on the atoms has dropped below the threshold of $0.0257\,\mathrm{eV\AA^{-1}}$. In this way, an excellent agreement for the Au-Au bonding length inside the trimer (2.805 Å) with the earlier results from SXRD (2.81 Å) and IV-LEED (2.81 Å) is found [80, 148]. Also good conformity is achieved for the Au-Ge bonding length (DFT: 2.522 Å, SXRD: 2.51 Å, IV-LEED: 2.50 Å), i.e., the distance from a Au atom within the trimer to the nearest Ge adatom in the MTL. Apart from these surface atomic positions, also the perpendicular locations are well comparable with those of the former studies. Even the vertical subsurface buckling (~ 0.2 Å) in the Ge bilayers, not seen in SXRD, but reported in the IV-LEED study, could be verified. The respective perpendicular coordinates are compared in Tab. 6.3.

6.1.2 Experimental realization

The experimental preparation of flat and long-range ordered surfaces with only few defects is essential for mapping the band structure of a 2DES in high resolution. In the case of Au/Ge(111)-($\sqrt{3} \times \sqrt{3}$) this is a rather delicate process due to the rich phase diagram, depicted in Fig. 6.3. Although the desired ($\sqrt{3} \times \sqrt{3}$) phase exists over a wide coverage range from $\theta = 0.1$–1.0 ML independently of the temperature, one strives to

Table 6.3: *Comparison of perpendicular coordinates of atoms in Au/Ge(111)-($\sqrt{3} \times \sqrt{3}$), derived from SXRD, IV-LEED, and DFT. Layer denominations correspond to those given in Fig. 6.1(b).*

Layer	SXRD [148]	IV-LEED [80]	DFT [200]
Au	0.0 Å	0.0 Å	0.0 Å
Ge adatoms	0.42 Å	0.51 Å	0.440 Å
1st Ge	3.022 Å	2.95 Å	2.873 Å
2nd Ge	3.794 Å	3.63 Å	3.542 Å
3rd Ge	3.794 Å	3.87 Å	3.780 Å
4th Ge	6.244 Å	6.10 Å	6.035 Å
5th Ge	6.244 Å	6.32 Å	6.193 Å
6th Ge	7.061 Å	7.06 Å	6.955 Å

exactly achieve completion of a full Au ML (red line). Only in this case, the surface is fully ($\sqrt{3} \times \sqrt{3}$) reconstructed, whereas for lower coverages both ($\sqrt{3} \times \sqrt{3}$) islands and an I(2×2) phase, consisting of Au and Ge atoms, evolve side by side [152]. This additional phase is reminiscent of the high-temperature Ge(111)-I(2×2) reconstruction, though Au atoms are involved here additionally. In LEED, it is easily detected by the presence of half-order spots, split into two peaks. Therefore, LEED represents a very reliable tool to adjust the Au coverage to 1 ML, which is given at full coverage by ($\sqrt{3} \times \sqrt{3}$) areas, i.e., the I(2×2) features must have completely vanished. In any case, less than 1 ML Au means an improper situation for ARPES experiments and urgently needs to be avoided. On the other hand, excess Au, i.e., coverages $\theta > 1$ ML, leads to the formation of 3D islands [148]. Fortunately, these also grow in height and do not significantly cover ($\sqrt{3} \times \sqrt{3}$) reconstructed areas for small amounts of surplus gold. As an example P. B. Howes *et al.* specified the surface area covered by such islands as 0.6 % for 1.25 ML Au coverage [148], which is negligible with respect to the large amount of additional gold atoms. Therefore, excess Au at the surface is much less critical than a Au deficiency.

The precise pretreatment of Ge(111) substrates according to the recipe given in Sec. 4.3.2 establishes the basis in preparing the Au/Ge(111)-($\sqrt{3} \times \sqrt{3}$) surface. In this regard, a sharp $c(2 \times 8)$ pattern in LEED is mandatory for the subsequent deposition of gold. For this purpose, pieces of a high purity Au foil (purity > 99.99 %) are evaporated from a molybdenum crucible within an electron-beam evaporator ("Focus EFM 3"). Deposition occurs with the substrate kept at RT, until an amount of ≥ 1 ML of Au covers the Ge(111) surface. Gold evaporation onto a hot sample represents a possible alternative and should lead to the ($\sqrt{3} \times \sqrt{3}$) phase likewise [202]. This could be verified by LEED, whereas STM measurements indicate an enhanced cluster and impurity density at the surface. Thus, the demand for high quality samples in ARPES

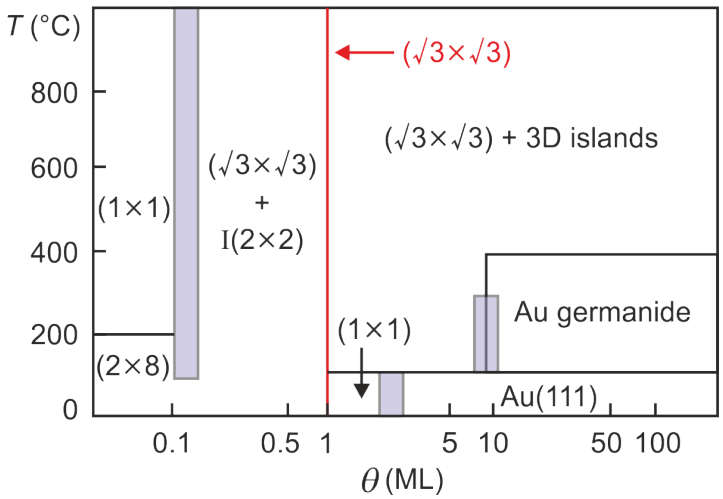

Figure 6.3: *Schematic phase diagram for the deposition of Au onto the Ge(111)-c(2 × 8) surface, according to [201]. In dependence of the deposited amount of gold θ and the temperature T several phases develop. The ($\sqrt{3} \times \sqrt{3}$) reconstruction is established for Au coverages slightly above 0.1 ML, but for a fully ($\sqrt{3} \times \sqrt{3}$) reconstructed surface, completion of one Au ML is mandatory (red line). The shaded areas mark overlapping regions between neighboring phases.*

and SARPES experiments speaks in favor of the RT deposition. Consequently, all data shown in the following are based on the RT deposition type. Subsequent to the gold evaporation, the sample is annealed at $T \approx 700\,^{\circ}\mathrm{C}$ during 3 min by direct current heating within the manipulator stage. The final cooling to RT is induced by cutting off the heating current within 10 s. In this way, the Au-induced ($\sqrt{3} \times \sqrt{3}$) reconstruction on the Ge(111) surface is formed. The bonding of the gold atoms to the substrate is very stable, since a complete adsorbate removal by thermal flashing up to the Ge melting point is not possible [148, 198].

The quality of preparation is checked by STM and LEED, as it is shown in Fig. 6.4(a) and (b), respectively [H5]. STM imaging and data processing follows the general description in Sec. 3.2.2, p. 32. The STM image of unoccupied states reveals that the Au/Ge(111)-($\sqrt{3} \times \sqrt{3}$) surface consists of large terraces (width > 100 nm), that are separated by steps of a single Ge(111) bilayer in height. The close-up to the atomic level in the inset unveils a hexagonal array of protrusions in unoccupied states, that is related to a ($\sqrt{3} \times \sqrt{3}$) periodicity with respect to the distances at the Ge(111) surface. The corresponding unit cell is placed on top to illustrate the surface geometry. According to the CHCT model, each protrusion corresponds to one gold trimer. The Au-Au bonding length inside one trimer has been determined as 2.81 Å by SXRD [148], which is little smaller compared to the Au-Au nearest-neighbor distance in the bulk (2.88 Å). Most likely, this results from the reduced coordination at the surface. The long-range ordered surface is only slightly disturbed by point defects, which cover less than 2 % of the surface area. The bright protrusions seen in STM are probably Au clusters (diameter < 5 nm), since they exhibit a curved appearance in height profiles and have no atomically flat

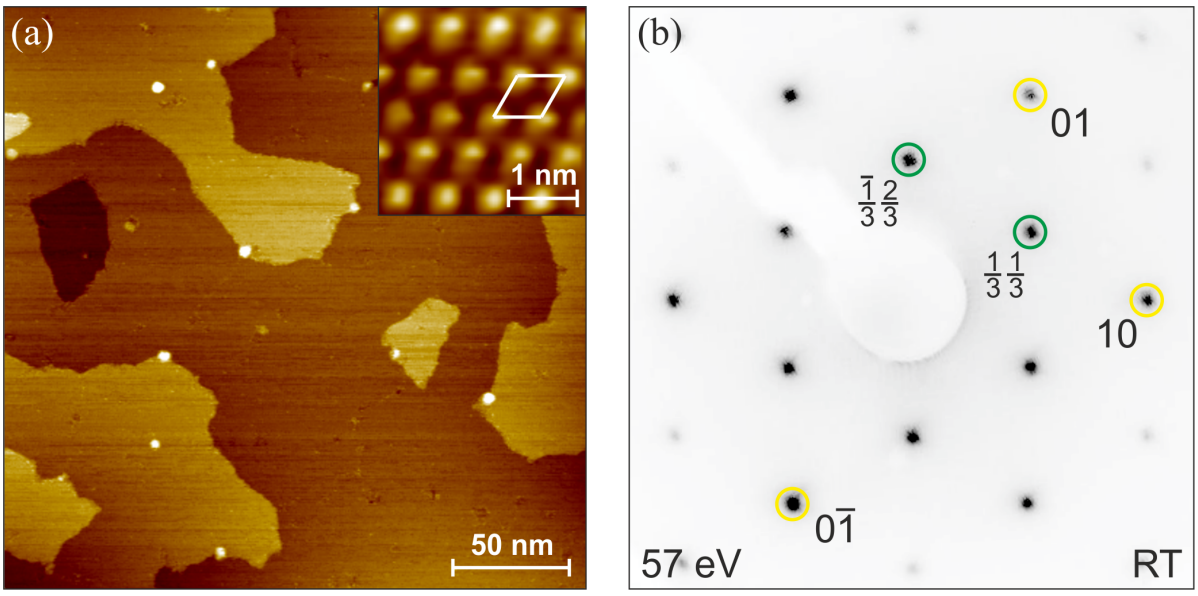

Figure 6.4: *(a) Large area STM image of the empty states at the Au/Ge(111)-($\sqrt{3}\times\sqrt{3}$) surface; bias: +1.6 V, 0.5 nA, 250 × 250 nm². The extended terraces are fully ($\sqrt{3}\times\sqrt{3}$) reconstructed and exhibit a low defect density. The inset presents a slightly smoothed close-up to the atomic level on one of the terraces. It features a hexagonal pattern of protrusions in ($\sqrt{3}\times\sqrt{3}$) periodicity (unit cell given in white) with respect to the Ge(111) substrate; +1.2 V, 1.0 nA, 3.0 × 3.0 nm². (b) Corresponding LEED image with integer (yellow) and fractional order spots (green), that relate to the ($\sqrt{3}\times\sqrt{3}$) surface reconstruction [H5], Copyright (2011) by the American Physical Society.*

plane on top. Their occurence is most likely due to a slight amount of excess Au at the surface, i.e., $\theta \geq 1$ ML. In all, both the cluster and the point defect densities are rather small. Thus, a significant influence of defects, step edges, and clusters on the ARPES spectra should not be expected. This impression is confirmed by the very low background noise in the LEED image in Fig. 6.4(b), taken at RT. Moreover, intense and sharp integer and fractional order spots are observed. The latter relate to a $(\sqrt{3}\times\sqrt{3})R30^\circ$ unit cell with respect to the Ge(111) substrate. Here, a potential broadening of the fractional order spots could be indicative of phase-slip domains, which are not visible in the large area STM image without atomic resolution. Such phase-slip domain boundaries were also observed in Au/Si(111)-($\sqrt{3}\times\sqrt{3}$) [145] and in Pt/Si(111)-($\sqrt{3}\times\sqrt{3}$) in this thesis [H3] (cf. Sec 5.2.1). In this regard, the analysis of the 1/3-order spot profiles returns a mean FWHM of $\Delta k_{\|} = 0.067\,\text{Å}^{-1}$ in reciprocal space. Since optical defocussing can lead to an artificial spot broadening, three alternative LEED images of the same sample at different lens parameters have been evaluated additionally. By utilizing Heisenberg's uncertainty relation, one obtains a length estimate for periodically ordered regions $\Delta x = 2\pi/\Delta k_{\|} = 93.5\,\text{Å}$ in real space. In comparison with the value obtained for the Pt/Si(111)-($\sqrt{3}\times\sqrt{3}$) surface ($\Delta k_{\|} = 0.127\,\text{Å}^{-1}$; $\Delta x = 49.5\,\text{Å}$) one notes that periodically ordered areas, assuming a triangular domain shape, are typically almost

four times larger in dimension here. A similar analysis, applied to the most intense fractional order spot in SXRD, even yields a correlation length of 420 Å [148]. However, the terrace widths still exceed these values significantly, which leads to the conclusion that several phase shifted domains, each being periodically ordered, must exist on the same terrace. In contrast to Au/Si(111)-($\sqrt{3} \times \sqrt{3}$), where the domain sizes strongly depend on the initial gold coverage [145], an influence of the respective preparation conditions on the domain sizes could not be observed for Au/Ge(111)-($\sqrt{3} \times \sqrt{3}$).

6.1.3 Phase-slip domains analyzed by scanning tunneling microscopy

In connecting to the LEED fractional order spot broadening, and due to the relationship with Pt/Si(111)-($\sqrt{3} \times \sqrt{3}$), it appears questionable that phase-slip domains might be absent on the Au/Ge(111)-($\sqrt{3} \times \sqrt{3}$) surface. Again, atomically resolved STM is the tool of first choice to shed light on this issue. Insight is gained by the unoccupied states STM image in Fig. 6.5(a). Therein, to the left and right two different domains exist, that exhibit the hexagonal array of bright protrusions in ($\sqrt{3} \times \sqrt{3}$) periodicity which is already known from the inset in Fig. 6.4(a). Both are separated by a domain wall, which is highlighted by the dashed line. Apparently, it does not display any prominent shape in the empty states image, which is different from the observation for the Pt/Si(111)-($\sqrt{3} \times \sqrt{3}$) and the Au/Si(111)-($\sqrt{3} \times \sqrt{3}$) surfaces [H3, 171]. It has also been reported that these domain walls do only align with $\langle 11\bar{2} \rangle$ high symmetry directions [152], as in Pt/Si(111)-($\sqrt{3} \times \sqrt{3}$). Moreover, it is easily seen that the two domains have a different registry with respect to the substrate. In principle, there must exist three phase shifted domains, depending on the location of the adatom trimers at either site "A", "B", or "C" within a ($\sqrt{3} \times \sqrt{3}$) unit cell. This follows from the model shown in Fig. 5.5(b) of Sec. 5.2.1. Based on this model the present STM images should be further scrutinized.

Following these objectives, the ($\sqrt{3} \times \sqrt{3}$) unit cell (blue) placed on top of the left domain is anchored with its corners to the bright protrusions. This corresponds to trimers that are located at lattices sites "A" in the model introduced for the Pt/Si(111)-($\sqrt{3} \times \sqrt{3}$) surface in Fig. 5.5(b). Shifting this unit cell by an integer number of surface lattice vectors across the domain wall involves a redistribution of the bright protrusions to the lattice site "B" within the ($\sqrt{3} \times \sqrt{3}$) unit cell. This corresponds then to a registry shift Δ_{AB}. Turning to the filled states STM image in Fig. 6.5(b), it is remarkable that the network of bright protrusions is replaced by a honeycomb arrangement of intensities, that encloses a hexagonal array of dark holes in ($\sqrt{3} \times \sqrt{3}$) periodicity. This appearance is similar to STM images obtained at the surfaces of Ag/Si(111)-($\sqrt{3} \times \sqrt{3}$) [203] and Ag/Ge(111)-($\sqrt{3} \times \sqrt{3}$) [204] for certain sample bias settings. Yet, it has to be stated again that the structural model valid for those surfaces is HCT instead of CHCT. Thus, the similarities in STM images do not result from a common structure, but rather represent analogies in the LDOS for certain bias polarities here. Inspection of domain

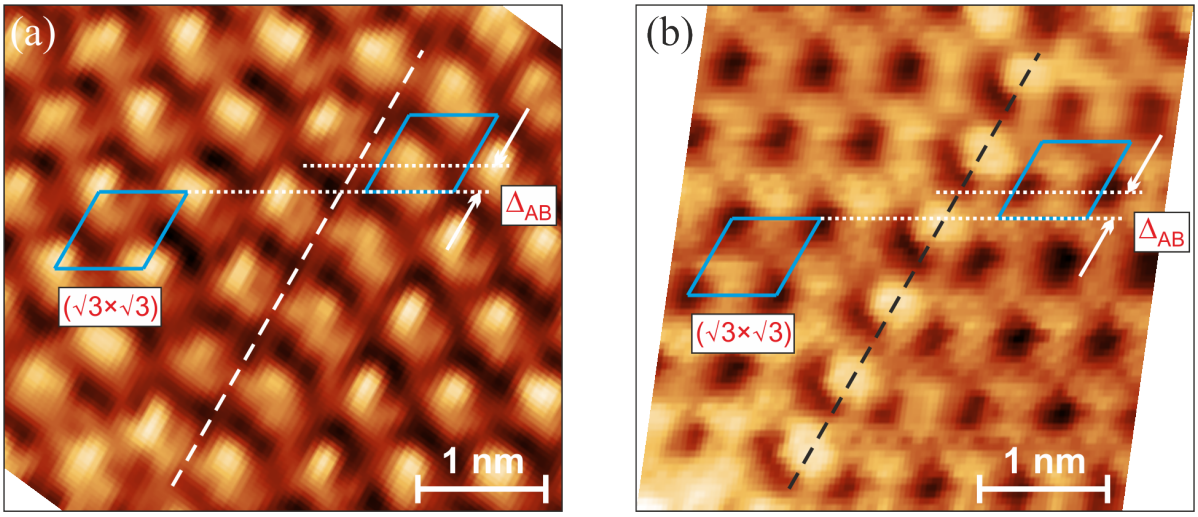

Figure 6.5: *(a) Empty states STM image of Au/Ge(111)-($\sqrt{3} \times \sqrt{3}$) with the focus on a domain wall (dashed line), that separates two adjacent phase shifted domains; bias: +1.2 V, 1.0 nA, 4.4 × 4.0 nm^2. ($\sqrt{3} \times \sqrt{3}$) unit cells (blue), spaced by an integer number of surface lattice vectors, are overlaid on the hexagonal array of bright protrusions. This provides evidence of a phase shift Δ_{AB} between both domains. (b) Filled states STM image with focus on a similar domain wall (dashed line); bias: -1.6 V, 0.2 nA, 4.4 × 4.0 nm^2. In contrast to (a), a hexagonal array of dark holes is observed. The same phase shift is evidenced here likewise.*

registries in Fig. 6.5(b) yields the same phase shift Δ_{AB} between the two domains as obtained from empty states before. Interestingly, in filled states the domain wall becomes visible as a linear array of bright protrusions, spaced by the $\sqrt{3}$ elongated surface lattice constant of Ge(111) $a_{\sqrt{3},Ge}$. These domain wall protrusions "surmount" the adjacent domains by ≈ 4 Å in occupied states (bias: -1.6 V). However, this does not represent the real surface topography here, but rather results from a strong electronic effect, since the protrusions disappear in unoccupied states STM images [see Fig. 6.5(a)]. In contrast, for the related Pt/Si(111)-($\sqrt{3} \times \sqrt{3}$) system the atomic domain wall substructure could be revealed at both bias polarities, although the contrast changes notably between positive and negative tunneling voltages as well (see Sec. 5.2.1). Most likely also in Au/Ge(111)-($\sqrt{3} \times \sqrt{3}$) lattice strain between Au and Ge triggers the formation of domain walls at the surface.

The bias dependency of the protrusion shapes in the domains is mostly comparable with earlier studies [152, 199]. For negative sample bias, a periodic arrangement of one bright protrusion per unit cell was also observed by L. Seehofer and R. L. Johnson [152]. Surprisingly, the authors reported a honeycomb pattern for positive sample bias ranging from +0.03 V to +1.5 V, with the tunneling current set to 1 nA. This is contrary to the STM image in Fig. 6.5(a), which was recorded at the same settings (bias: +1.2 V, 1.0 nA), but shows a hexagonal pattern instead, as has also been found by M. Göthelid *et al.* for positive sample bias. Hence, the observations of L. Seehofer and R. L. Johnson have to

be seen critically. Clarification of this issue would require a more detailed study of the structural appearance in STM, which is obviously highly influenced by the electronic charge distribution. This objective is beyond the scope of this thesis, and thus remains to be scrutinized in future experimental studies.

In comparison with other noble metal induced ($\sqrt{3} \times \sqrt{3}$) surface reconstructions, the most closely related Au/Si(111)-($\sqrt{3} \times \sqrt{3}$), which is also described by the CHCT model, exhibits a hexagonal pattern for all bias polarities [205]. In contrast, Ag/Si(111)-($\sqrt{3} \times \sqrt{3}$) has a protrusion arrangement in filled states (bias: $< -0.8\,\mathrm{V}$) that is highly reminiscent of Au/Ge(111)-($\sqrt{3} \times \sqrt{3}$) filled states images [Fig. 6.5(b)] [206]. However, a honeycomb pattern is observed for less negative bias, i.e., from -0.8 to 0 V and in empty states [206]. Similarly, the Ag/Ge(111)-($\sqrt{3} \times \sqrt{3}$) surface exhibits a change between filled and empty states from a hexagonal arrangement of "holes" to a honeycomb protrusion network [207]. Roughly interpreted, this means that Au/Ge(111)-($\sqrt{3} \times \sqrt{3}$) appears similar to Ag/Si(111)-($\sqrt{3} \times \sqrt{3}$) and Ag/Ge(111)-($\sqrt{3} \times \sqrt{3}$) in filled states, whereas it resembles Au/Si(111)-($\sqrt{3} \times \sqrt{3}$) in empty states.

6.2 The electronic band structure of Au/Ge(111)-($\sqrt{3} \times \sqrt{3}$)

In addition to the basic knowledge on the atomic configuration at the Au/Ge(111)-($\sqrt{3} \times \sqrt{3}$) surface, available from the literature and the experiments described above, this section is dedicated to present the first analysis of the electronic band structure by ARPES at different temperatures [H5]. The capabilities of FS mapping, which are exploited here, have already been introduced in Sec. 3.3.2. The corresponding 3D information on the electronic band structure will be analyzed, evaluated, and discussed in the following.

As a starting point, a coarse attempt to derive an initial guess of the band filling can be obtained by electron counting, i.e., adding up all unpaired electrons within a single surface unit cell. For ($\sqrt{3} \times \sqrt{3}$) reconstructed Au/Ge(111) there are three Au atoms, each providing a $6s$ electron, and three Ge adatoms with nine electrons within the sp^3 hybridized orbitals. Thus, in total an even number of electrons is available. Supposing the correctness of this simple estimate at this point, the electronic properties would be governed by completely filled bands, which in turn means an insulating surface.

Before going into details, the geometries and dimensions in k-space shall be introduced briefly. In real space, the surface unit cell describes the lattice periodicity of the respective surface reconstruction. Typical dimensions for the surface systems under inspection are summarized in Tab. 4.1 of Sec. 4.1. The corresponding equivalent in k-space is the surface Brillouin zone (SBZ), that defines the k-space periodicity. For the ($\sqrt{3} \times \sqrt{3}$) reconstructed surfaces the first and second SBZs are depicted in Fig. 6.6 as solid hexagons. The dashed hexagon, rotated by 30 °, represents the (1×1) SBZ of the substrate, and

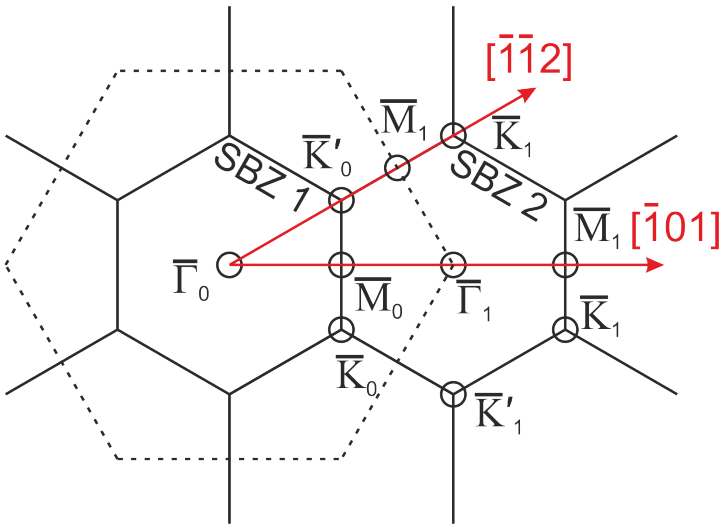

Figure 6.6: *Reciprocal space geometries for the first and the second hexagonal SBZ (solid hexagons) of* $(\sqrt{3} \times \sqrt{3})$ *reconstructed surfaces. The dashed hexagon signifies the* (1×1) *SBZ, related to the substrate. The two high symmetry directions* $[\bar{1}\bar{1}2]$ *and* $[\bar{1}01]$ *stretch from* $\overline{\Gamma}_0$*, the principal center of the first SBZ, across the high symmetry points* $\overline{\Gamma}_i$ $\overline{\mathrm{K}}'_i$, $\overline{\mathrm{K}}_i$, *and* $\overline{\mathrm{M}}_i$*, where the index* i *denotes the respective order of the SBZ, i.e.,* $i = 0$*: first SBZ,* $i = 1$*: second SBZ, etc., [H5], Copyright (2011) by the American Physical Society.*

$\overline{\Gamma}_0$ marks the center of the first $(\sqrt{3}\times\sqrt{3})$ SBZ. Following the high symmetry directions $[\bar{1}\bar{1}2]$ and $[\bar{1}01]$ departing from there, all relevant high symmetry points in k-space are covered. These are $\overline{\Gamma}_i$, $\overline{\mathrm{K}}'_i$, $\overline{\mathrm{K}}_i$, and $\overline{\mathrm{M}}_i$. The index i marks the respective order of the SBZ, i.e., $i = 0$: first SBZ, $i = 1$: second SBZ, etc. In analyzing certain properties in the electronic band structure, e.g., the size of the Fermi vector k_F, it is important to "know where you are", i.e., one needs to specify the k-space dimensions. For $(\sqrt{3} \times \sqrt{3})$ reconstructed surfaces on both Si(111) and Ge(111), Tab. 6.4 provides the respective distances in relation to the $\overline{\Gamma}_0$ principal symmetry point.

So far, the literature provides almost no vital information on the occupied electronic band structure in this system. B. J. Knapp *et al.* have studied the Au/Ge(111)-$(\sqrt{3}\times\sqrt{3})$

Table 6.4: *In-plane reciprocal space distances in the first and second SBZ between selected high symmetry points and the* $\overline{\Gamma}_0$ *point for a* $(\sqrt{3}\times\sqrt{3})$ *reconstruction on Si(111) and Ge(111). For reciprocal space geometries, refer to Fig. 6.6.*

Direction	Substrate	$\overline{\mathrm{K}}'_0$	$\overline{\mathrm{M}}_1$	$\overline{\mathrm{K}}_1$	$\overline{\mathrm{M}}_0$	$\overline{\Gamma}_1$
$[\bar{1}\bar{1}2]$	Si(111)	0.630 Å^{-1}	0.945 Å^{-1}	1.260 Å^{-1}	—	—
$[\bar{1}01]$	Si(111)	—	1.636 Å^{-1}	—	0.545 Å^{-1}	1.091 Å^{-1}
$[\bar{1}\bar{1}2]$	Ge(111)	0.605 Å^{-1}	0.907 Å^{-1}	1.209 Å^{-1}	—	—
$[\bar{1}01]$	Ge(111)	—	1.571 Å^{-1}	—	0.524 Å^{-1}	1.047 Å^{-1}

surface by ARPES already in 1989 [197]. However, these experiments did suffer significantly from poor spectrometer resolutions at that time. Accordingly, the measurements failed to resolve surface states in the vicinity of E_F, apart from a weakly dispersing one at $\approx 2.4\,\mathrm{eV}$ binding energy, but with the surface remaining insulating due to the absence of a Fermi level crossing. A contrasting conclusion was later drawn by G. Le Lay *et al.*, who argued that Au/Ge(111)-($\sqrt{3}\times\sqrt{3}$) should be metallic [205]. This was attributed to a shift in the Ge 3*d* core levels with respect to the Ge(111)-$c(2 \times 8)$ surface, that pushes the Fermi level below the valence band maximum (VBM). Apart from these contrasting and coarse studies, no further information on the occupied electronic band structure is available so far, and the following sections are the first dedicated to this.

6.2.1 The band structure in angle-resolved photoelectron spectroscopy

A general impression of the electronic band structure is best obtained by FS mapping. In this way, a variety of spectral features can be recorded at the same time. Here, the correct determination of the Fermi level is of fundamental importance. Usually, an angle-integrated spectrum, i.e., an EDC without momentum dependence, from a metal surface which is in direct contact to the sample itself is fitted following the procedure in Sec. 3.3.2, p. 50. The Fermi energy should be the same for metal and sample then. Usually, the tantalum clamping strips that keep the sample fixed are used for this purpose. Yet, for the present surface system an unusual potential offset between the metal clips and the surface makes this approach impossible. As a good alternative, angle-integrated EDCs are derived from two band maps captured along both high symmetry directions of the sample. By fitting these curves with Eq. 3.52, it is found that the Au/Ge(111)-($\sqrt{3} \times \sqrt{3}$) surface is indeed metallic, and accordingly E_F is determined precisely. The constant energy contour at E_F, i.e., the FS, is then derived by cutting the ARPES cuboid at exactly this energy.

The Fermi surface topology

Now we shall turn to a closer inspection of the FS topology in Fig. 6.7(a). As a main finding, three metallic states are observed, that cross the Fermi level [H5]. The largest Fermi vector belongs to the band S1, that exhibits a roughly hexagonal shape with six straight segments, connected at corners that are aligned with the $\overline{\Gamma}_0$–$\overline{\mathrm{K}}_0$ and $\overline{\Gamma}_0$–$\overline{\mathrm{K}}_0'$ high symmetry directions. The band is rather weak in intensity in the first SBZ and features a notable broadening in momentum. The more intense and less broadened H1 state is observed closer to the $\overline{\Gamma}_0$ zone center. It has a warped contour, with its corners oriented in the same direction as it is the case for S1. Very close to $\overline{\Gamma}_0$ a third round shaped state H2 is found. This state is partly superimposed by the band B1, which is of bulk origin, since its binding energy depends on $k_\perp$, as verified by changing the photon energy $h\nu$. It

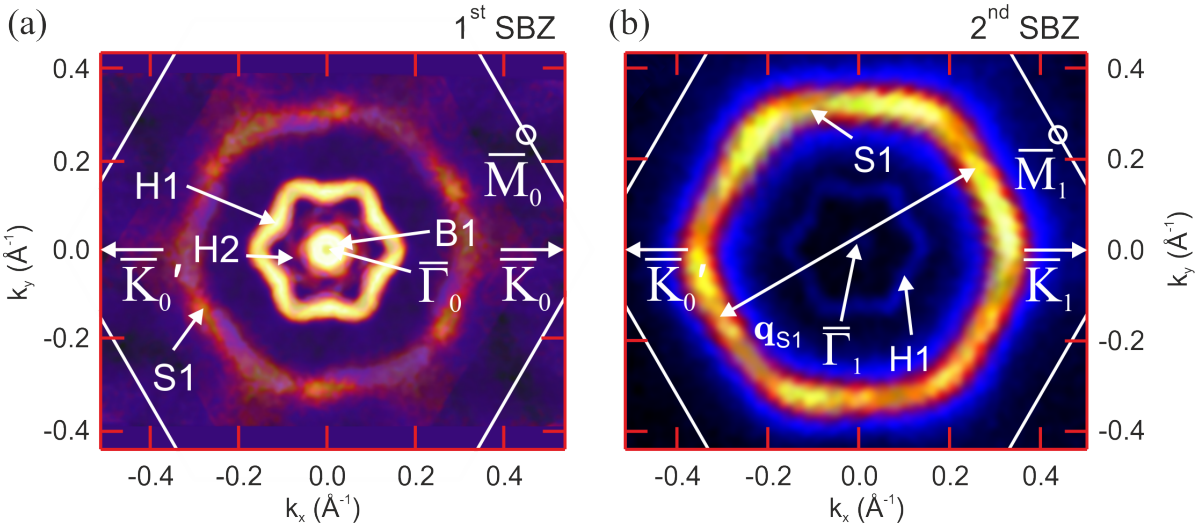

Figure 6.7: *(a) FS of Au/Ge(111)-($\sqrt{3} \times \sqrt{3}$) in the first SBZ at $T = 10\,K$, captured at the photon energy $h\nu = 25\,eV$. The four FS sheets S1, H1, H2, and B1 are tagged with labels. Bright contrast corresponds to enhanced photoemission intensity, and the straight lines indicate the zone boundaries. (b) FS in the second SBZ at $T = 10\,K$, captured at the photon energy $h\nu = 35\,eV$. The nesting vector $\mathbf{q}_{S1}$ interconnects straight parallel sheets within the S1 Fermi contour. The FSs in (a) and (b) represent integrated FS maps in an energy range of $E_F \pm 0.025\,eV$. Further processing includes symmetrization by adding up photoemission intensities with respect to the threefold-symmetry of the substrate to even out momentum-dependent matrix element effects. A moderate Gaussian filter was applied afterwards [H5], Copyright (2011) by the American Physical Society.*

has been suggested that its maximum must be located above E_F due to a surface band bending effect [202].

Repetition of the FS mapping within the second SBZ leads to the FS shown in Fig. 6.7(b). In contrast to the first SBZ, the S1 state is notably enhanced in intensity, whereas the H1 state is barely visible. H2 is also mostly suppressed, and B1 is not observed here. This change in intensity most likely results from photoemission matrix element effects, yet, leaving the band shapes unperturbed. A variation of the photon energy does not influence the intensity ratio between of surface states and bulk states significantly. The photon energy has thus been chosen by optimizing the signal-to-noise ratio in angle-resolved measurements. The energies $h\nu = 25\,eV$ and $h\nu = 35\,eV$ turned out to be best suited to record the band dispersion within all details.

Band structure details

The next and consequential step in the revelation of the electronic band structure of Au/Ge(111)-($\sqrt{3} \times \sqrt{3}$) is capturing high-resolution band maps along $\overline{\Gamma}$–$\overline{\mathrm{M}}$ and $\overline{\Gamma}$–$\overline{\mathrm{K}}$ in both SBZs. In this way, one is able to scrutinize the band dispersion $E(k_\parallel)$ for the metallic states as well as for completely filled states, that do not become visible at the FS. In Fig. 6.8 such band maps are displayed for the first (top panels) and the

second (bottom panels) SBZ along $\overline{\Gamma}$–$\overline{\mathrm{M}}$ (left panels) and $\overline{\Gamma}$–$\overline{\mathrm{K}}$ (right panels). A total number of seven bands is observed, which are classified according to DFT calculations by their respective orbital origin as bulk-like (B), hole-like Ge derived surface states or resonances (H), and electron-like Au derived surface states or resonances (S). As already known from inspection of the FSs in Fig. 6.7 there are three metallic states S1, H1, and H2. In addition, a fourth state H3, which crosses E_F, is observed very close to $\overline{\Gamma}_0$. Here, it is worth noting that bulk bands play a more important role within the first SBZ [Fig. 6.8(a) and (c)] compared to zones of higher order. Accordingly, B1 and B2 are highly pronounced in the first SBZ, but are barely seen in the second SBZ, which agrees well with their bulk-like origin. The hole-like H states are also more pronounced in the first SBZ and become less intense, when turning to the second SBZ, which is most likely due to photoemission matrix element effects. Most strikingly, the intensity of the electron-like band S1 changes dramatically between both zones, yet, retaining its huge k-space broadening. Moreover, it features an almost parabolic curvature. Finally, the fully occupied state S2 has its band maximum at 350 meV binding energy and $k_\parallel = 0.43\,\text{Å}^{-1}$, and it is mostly of weak intensity and significantly broadened.

Concerning the metallic states, Fermi level crossings are derived as $k_{\parallel,F,S1} = 0.33\,\text{Å}^{-1}$, $k_{\parallel,F,H1} = 0.143\,\text{Å}^{-1}$, and $k_{\parallel,F,H2} = 0.072\,\text{Å}^{-1}$ along $\overline{\Gamma}$–$\overline{\mathrm{K}}$. For the $\overline{\Gamma}$–$\overline{\mathrm{M}}$ direction $k_{\parallel,F,S1} = 0.31\,\text{Å}^{-1}$, $k_{\parallel,F,H1} = 0.117\,\text{Å}^{-1}$, and $k_{\parallel,F,H2} = 0.072\,\text{Å}^{-1}$ are obtained (cf. Tab. 6.5). These values correspond to band fillings of 32 %, 95 %, and 98 %, respectively.[1] This finding of fractional order filling for all states is contrary to the attempt to describe the conducting character by simple electron counting within the ($\sqrt{3} \times \sqrt{3}$) unit cell, which resulted in the assumption of an insulating behavior. Yet, here we deal with a partial band filling scenario, that actually leads to conducting behavior. While simple electron counting may be a suitable approach in other systems, the ARPES results reveal that it is not appropriate in case of Au/Ge(111)-($\sqrt{3} \times \sqrt{3}$). Here, the presence of fractionally occupied and overlapping bands does not allow to count with integer electron numbers. In addition, hole-like and electron-like bands exist which stem from various orbitals of different character. The band curvatures of all states are very steep, resulting in very low effective electron masses m_e^*. These have been determined at E_F by $m_e^* = \hbar k_F / v_F$ (v_F: Fermi velocity) and range from $0.05\,m_e$ to $0.09\,m_e$. Such rather small masses lead to the conclusion that electronic correlations are rather insignificant in Au/Ge(111)-($\sqrt{3} \times \sqrt{3}$). This is contrary to strongly correlated surfaces, which are typically characterized by a high band mass, e.g., $m_e^* = 1.2\,m_e$ in Sn/Si(111)-($\sqrt{3} \times \sqrt{3}$), see Sec. 7.2.3. According to the Drude model of charge transport, the electron mobilities are strongly enhanced, i.e., $\mu \propto 1/m_e^*$. This could represent a promising basis for future semiconductor-based electronic applications.

A closer inspection of the faint, but sharp states H1, H2, and H3 reveals that these bands disperse at a fixed distance in momentum to each other. Also a certain comparabil-

[1] The band filling is derived by dividing the $k_\parallel$-area in which the respective band disperses below E_F by the area of the complete ($\sqrt{3} \times \sqrt{3}$) SBZ.

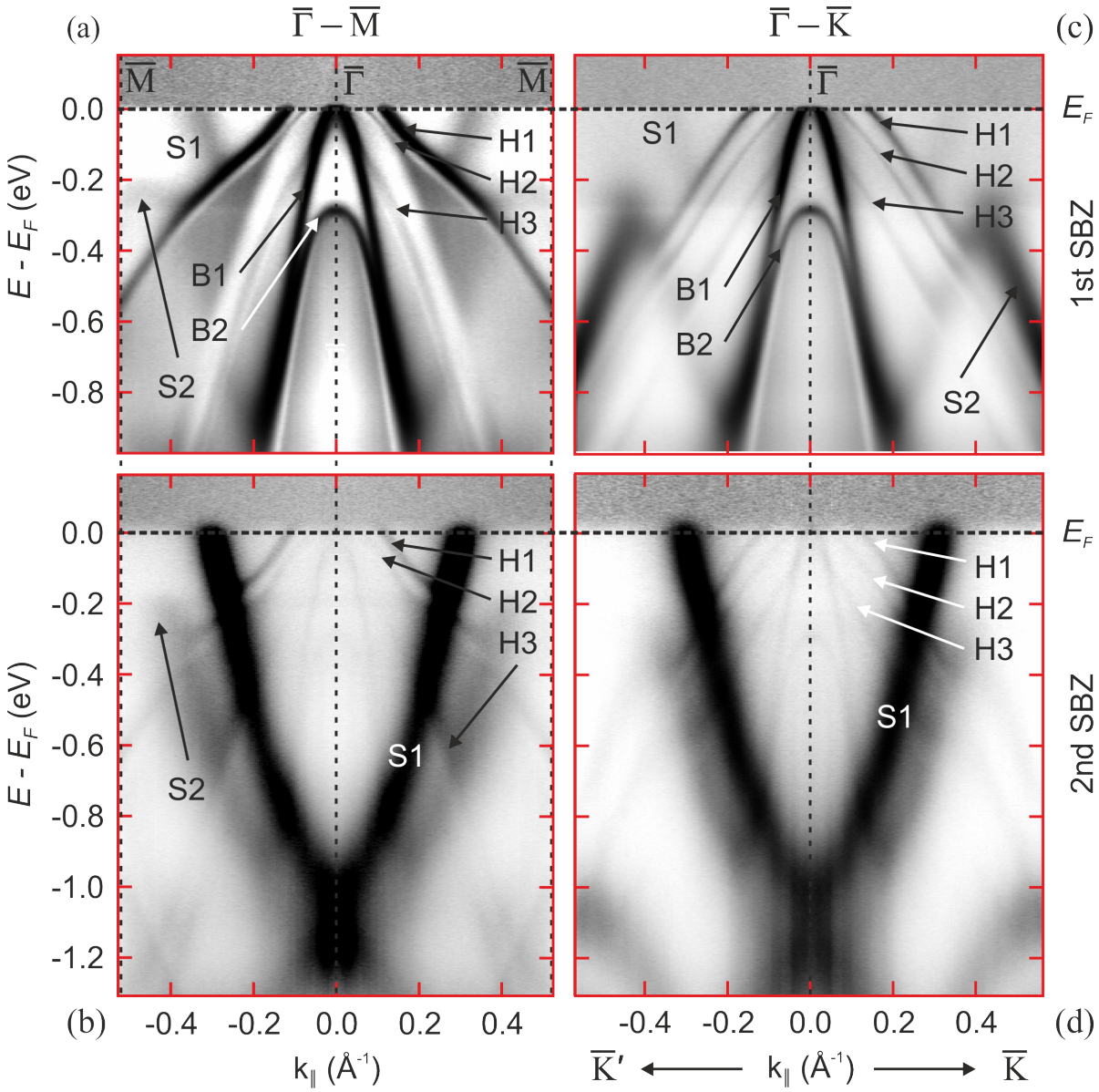

Figure 6.8: *(a) Electronic band structure revealed by ARPES along* $\overline{\Gamma}$–$\overline{M}$ *in the first SBZ of Au/Ge(111)-*$(\sqrt{3}\times\sqrt{3})$*; T* = 10 *K*, $h\nu$ = 25 *eV. Dark contrast corresponds to high photoemission intensity. The metallic states S1, H1, H2, and H3 are observed together with the completely filled state S2. B1 and B2 originate from the bulk. Intensity noise above* E_F *is an artifact due to data normalizing. (b) Band structure along the same direction in the second SBZ for an enlarged binding energy range; T* = 130 *K*, $h\nu$ = 35 *eV. (c), (d) ARPES band maps along the* $\overline{\Gamma}$–$\overline{K}$ *high symmetry direction. The settings agree with those in (a) and (b), respectively. All spectra shown have been normalized for each EDC with respect to the highest intensity, prior to symmetrizing around the* $\overline{\Gamma}$ *point [H5], Copyright (2011) by the American Physical Society.*

Table 6.5: *Parameters obtained from an analysis of the Au/Ge(111)-($\sqrt{3}\times\sqrt{3}$) ARPES band structure of the main surfaces states S1 (subdivision into S1$_\mathrm{A}$ and S1$_\mathrm{B}$ in DFT, see Sec. 6.2.2), H1, and H2, i.e., band type (e: electron-like, h: hole-like), Fermi vector $k_{\parallel,F}$, effective electron mass m_e^*, and band filling. The angular resolution is in the order of 0.005 Å^{-1}. Values in parentheses are derived from the DFT band structure calculations in Sec. 6.2.2.*

Band	type	$k_{\parallel,F}$ ($\overline{\Gamma}_i$ – $\overline{\mathrm{K}}_i$)	$k_{\parallel,F}$ ($\overline{\Gamma}_i$ – $\overline{\mathrm{M}}_i$)	m_e^*	band filling
S1 (S1$_\mathrm{A}$)	e	0.33 (0.288) Å^{-1}	0.31 (0.287) Å^{-1}	0.06 m_e	32 %
S1 (S1$_\mathrm{B}$)	e	0.33 (0.287) Å^{-1}	0.31 (0.247) Å^{-1}	0.06 m_e	32 %
H1	h	0.143 (0.147) Å^{-1}	0.117 (0.113) Å^{-1}	0.09 m_e	95 %
H2	h	0.072 (0.033) Å^{-1}	0.072 (0.035) Å^{-1}	0.05 m_e	98 %

ity with the band structure found by ARPES for the related Pb/Ge(111)-($\sqrt{3}\times\sqrt{3}$) surface, established a 1 ML lead coverage, is obvious [208]. In that study, the relevant states were attributed to germanium orbitals. Another remarkable feature is a change in band curvature for H1 and H2 along the $\overline{\Gamma}$–$\overline{\mathrm{M}}$ direction slightly above ($E - E_F \approx -0.15$ eV) their crossing point with the S1 surface state. A summary of all relevant parameters, extracted for the states S1, H1, and H2 from the ARPES data, is listed in Tab. 6.5.

Spectral broadening of the S1 surface state

Special attention is attracted by the very intense surface state S1 in the second SBZ. Its low effective electron mass ($0.06\,m_e$) is related to the steep dispersion with a minimum at $E - E_F \approx -1.0$ eV. The band also features a significant broadening in momentum, which is evaluated as $\Delta k_\parallel = 0.064$ Å^{-1} (FWHM) at the Fermi energy. Yet, in the ideal case of an infinitely large surface which is free from defects, any intrinsic broadening should be absent in the ARPES spectral function $A(\mathbf{k},\omega)$ at the Fermi energy. Also the experimental resolution of the analyzer (~ 0.005 Å^{-1}) is much smaller than the broadening. A possible reason to explain this observation may be found in impurities and surface defects, which can impose a notable scattering potential. Such irregularities can consist of atomic Au-Ge exchanges and domain walls that induce a registry shift with respect to the substrate. As a consequence of the STM results in Sec. 6.1.2, Au-Ge substitutional defects should not play a crucial role here. On the other hand, phase shifted domains are observed, and the broadening of the 1/3-order LEED spots was determined as $\Delta k_\parallel = 0.067$ Å^{-1}. Thus, small phase-slip domains will notably contribute to the overall S1 band broadening. Nevertheless, in comparison to the sharp H states, which relate to surface and subsurface Ge atoms according to the DFT (see Sec. 6.2.2), the large size of the S1 band broadening cannot fully be explained by domain wall scattering alone.

Alternatively, correlations are not supposed to play a role here. This can be understood in comparison with the dilute phases of group-IV adatoms on Si(111) and

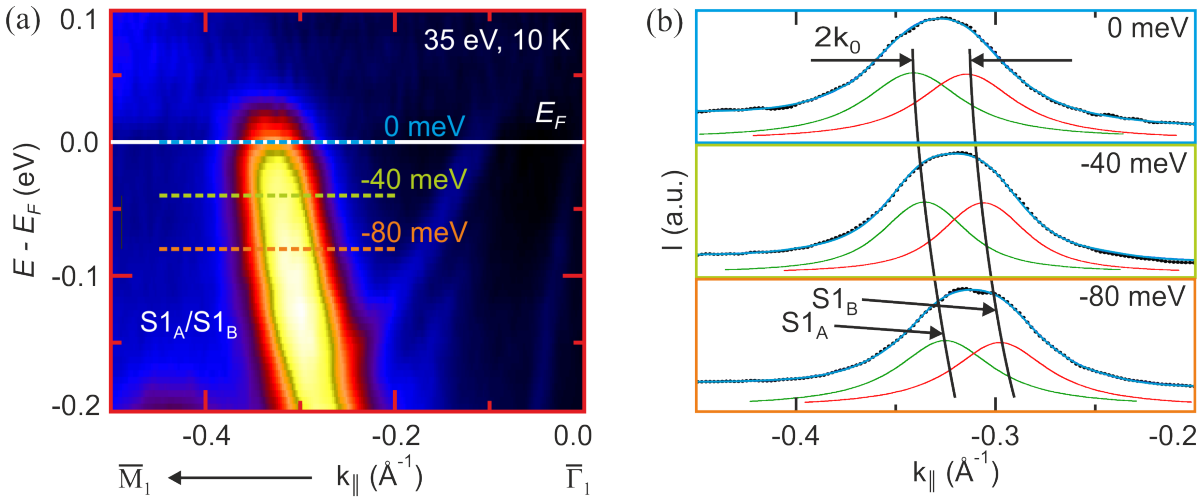

Figure 6.9: *(a) Close-up to the dispersion of the S1 surface state in Au/Ge(111)-($\sqrt{3} \times \sqrt{3}$) along* $\overline{\Gamma}$–$\overline{\mathrm{M}}$ *in the second SBZ in close vicinity to* E_F*;* $T = 10\,K$*,* $h\nu = 35\,eV$*. Bright contrast corresponds to high photoemission intensity. The possibility of two spin-split bands hidden in the broadened S1 band requires the two labels* $S1_\mathrm{A}$ *and* $S1_\mathrm{B}$*. (b) MDC line profiles (black dots) captured along the dashed colored lines in (a). A fit with two Voigt line shapes (green and red curves) results in the overall fit profile (blue). The black curves centered at the single peak maxima suggest the possible curvature of* $S1_\mathrm{A}$ *and* $S1_\mathrm{B}$*, with a distinct splitting* $2k_0 = 0.028\,\text{Å}^{-1}$ *in momentum.*

Ge(111) (see Ch. 7). Au/Ge(111)-($\sqrt{3} \times \sqrt{3}$) is established in the dense 1 ML adsorbate phase, where three Au atoms share approximately the same space as one single Sn or Pb atom has at the Si(111) surface for its own. Even more important is the difference in the atomic orbitals involved. While the Au terminated surface is mainly influenced by widely spread s orbitals, the Sn- and Pb-induced reconstructions exhibit rather localized p_z-like orbitals. Thus, both the lower adsorbate atom density and the difference in atomic orbitals suggest that localization, and hence, electronic correlations should be less important in Au/Ge(111)-($\sqrt{3} \times \sqrt{3}$). Finally, the effective electron masses determined above are an urgent hint to exclude this possibility, too.

Another option would be a band splitting due to SOIs which, in the present material system, is not resolvable in conventional ARPES, but could contribute to the observed k-space broadening. In this regard, the Au/Ge(111)-($\sqrt{3} \times \sqrt{3}$) surface exhibits the necessary ingredients, i.e., a heavy adsorbate element ($Z_\mathrm{Au} = 79$) and a symmetry breaking at the surface (SIA type), which involves a notable potential gradient. To further elucidate this, a MDC profile analysis can serve as a first step towards the identification of a band splitting, while only SARPES is able to provide a definite proof of this assumption. Fig. 6.9(a) presents a close-up of the S1 surface state near the Fermi energy. The possible existence of two spin-split surface states is indicated by renaming the state into its split parts $\mathrm{S1_A}$ and $\mathrm{S1_B}$ ($|k_{\parallel,F,S1_\mathrm{A}}| > |k_{\parallel,F,S1_\mathrm{B}}|$). As in the conventional Rashba effect, and for an idealized parabolic dispersion, one would expect these two states to disperse in parallel in approaching the Fermi level from higher binding

energies. In order to scrutinize the presence of such a band situation hidden within S1, three MDCs at $E - E_F = 0\,\text{eV}$, $E - E_F = -40\,\text{meV}$, and $E - E_F = -80\,\text{meV}$ along the dashed lines in (a) are plotted in dependence of their respective in-plane momentum in Fig. 6.9(b). All three profiles (black dots) exhibit a notable broadening, as already stated above. Moreover, these curves display a plateau-like shape in the region of maximum intensity, possibly indicative of two bands hidden in one single peak. In particular, this is well observable for 80 meV binding energy rather than directly at E_F. The next step is to fit each MDC with two Voigt line profiles (green: $S1_A$, red: $S1_B$). During this procedure the fit curves for each MDC were required to have equal amplitudes, equal Gaussian widths, and equal Lorentzian widths. Finally the peak-to-peak distance was adjusted in such a way that an optimized fit was obtained for all three MDCs. The overall fit curve (blue) is then simply the sum of the two single components (red and green). It accurately reproduces the experimental MDC line shape. Contrary, fitting with only one Voigt profile does not reproduce the data that precisely. The potential dispersion of both split bands is indicated by the black solid lines that are positioned at the maximum amplitude location of each single band fit curve. The splitting between the two bands is derived as $2k_0 = 0.028\,\text{Å}^{-1}$.

Thus, a SOI-induced band splitting in combination with scattering at phase-slip domain walls can account for the intense momentum broadening of S1. It should be emphasized at this point again that a fitting of this type may only be seen as a first and coarse approximation to the exact spin splitting. Moreover, details on the orientation of the spin polarization vector can only be accessed by SARPES.

Nesting in the Au/Ge(111)-($\sqrt{3} \times \sqrt{3}$) Fermi surface

Besides the possibility of a spin-orbit induced band splitting, the remarkable and almost hexagonal shape of the S1 FS [see Fig. 6.7(b)], with its straight segments in between the $\overline{\Gamma}$–$\overline{\text{K}}$ and $\overline{\Gamma}$–$\overline{\text{K}}'$ directions, is suggestive of FS *nesting*. This in turn is a prerequisite for the establishment of a charge density wave (CDW), which was earlier believed to be the mechanism that describes the RT to LT phase transition in Pb/Ge(111)-($\sqrt{3} \times \sqrt{3}$) and Sn/Ge(111)-($\sqrt{3} \times \sqrt{3}$) [40, 209]. This possibility shall now be discussed with regard to the potential nesting at the FS of Au/Ge(111)-($\sqrt{3} \times \sqrt{3}$).

Basically, a CDW is a phase that in particular may develop in 1D crystalline systems below a certain critical temperature T_c [36]. It belongs to the class of electronically driven phase transitions and is a prime example of electron-lattice interactions. Famous representatives of a CDW are the lattice distortions in the quasi-1D transition metal bronzes and the Krogmann's salts [36]. A simple model of a CDW is given by a 1D chain consisting of single atoms, spaced by the distance a, each hosting one electron. As shown in Fig. 6.10(a), this involves a spatially constant charge density $\rho(r)$ and the dispersion of a free electron gas at half filling in reciprocal space. Now, one analyses the reaction of the free electron gas to an external and time-independent perturbation, which is given by the "Lindhard" response function $\chi(\mathbf{q})$, that depends on the "nesting vector" $\mathbf{q}$. For

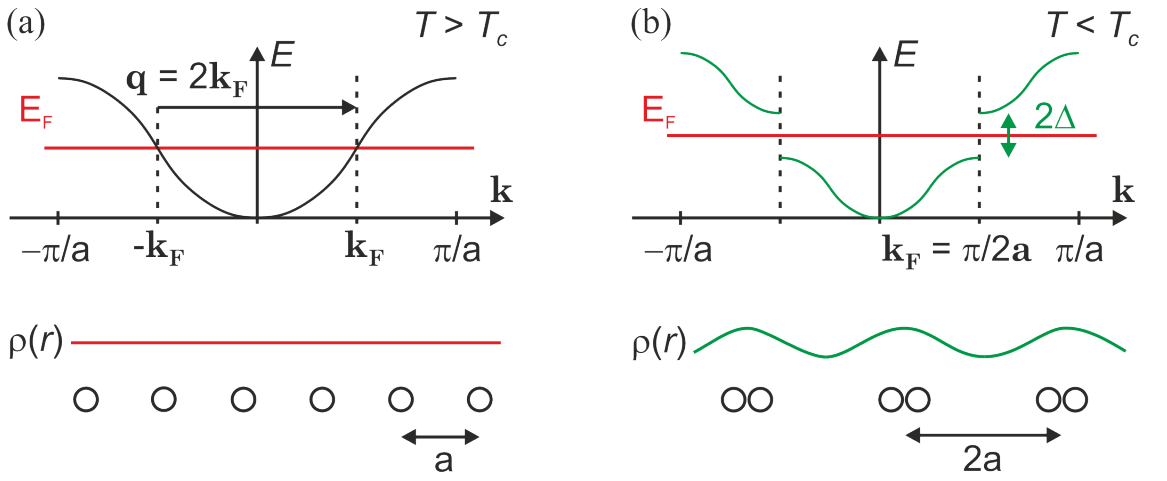

Figure 6.10: *1D model case for the CDW transition in an atomic chain. (a) For $T > T_c$ the atoms, each occupied by one electron, are spaced by a, and an equal charge density $\rho(r)$ in dependence of the location r along the chain is found. In reciprocal space, a half filled band scenario with Fermi vectors $\mathbf{k_F}$, spaced by the nesting vector $\mathbf{q}$, exists. (b) Below T_c the charge density is modulated with a period doubling $2a$ along the chain, followed by a likewise periodic distortion of the lattice. In turn, a band gap 2Δ opens at the new zone boundaries $\pm k_F = \pm\pi/(2a)$.*

our 1D model case this function diverges at $\mathbf{q} = 2\mathbf{k_F}$, i.e., the charges in the chain are redistributed for an external perturbation of that size. Importantly, pairs of occupied and unoccupied states, located at $\pm k_F$ and spaced by $\mathbf{q}$, mainly contribute to the response of the system. Here, it turns out that the dimensionality is an important factor for the instability of a certain system towards a CDW. This is due to the respective shape of the FS, which mainly consists of two straight and equally spaced planes in the 1D case. Hence, there exist multiple pairs of states which are spaced by equivalent vectors $\mathbf{q}$, and thus, the response of the electron gas will be strong. Coupling to higher dimensions reduces the amount of states spaced by equivalent vectors $\mathbf{q}$, and the response becomes weaker. Therefore, nesting is strongest in 1D, whereas systems of higher dimensionality become less unstable towards the development of a CDW. Finally, the situation of our 1D model system below the critical temperature T_c shall be discussed in Fig. 6.10(b). Here, the charge density is periodically modulated, which is followed by a likewise periodic distortion of the lattice. The buckling of the atoms consumes a certain amount of energy, which must be gained in some way to stabilize the CDW. This is achieved by lowering the occupied and raising the unoccupied states at $\pm\mathbf{k_F}$ coupled by $\mathbf{q}$, as shown in the top of Fig. 6.10(b), i.e., a band back folding occurs at the new zone boundaries $k_F = \pm\pi/(2a)$, which reflect the modified lattice periodicity. Concomitantly, an energy gap of 2Δ in size opens, and the system turns its character from metallic to insulating. The resulting new LT lattice constant $a_{\mathrm{LT}} = n \cdot a$ is called commensurate, if n is an integer number, which means a favorable situation for real surface systems that couple to a substrate. In the atomic chain model with half filling we deal with the commensurate

case, thus, the band back folding at $\pm k_F$ involves a real-space period doubling $a_{\mathrm{LT}} = 2a$ [210].

In turning again to the Au/Ge(111)-($\sqrt{3} \times \sqrt{3}$) surface, nesting is roughly achieved for the three pairs of opposite straight sections of the S1 band.[1] Although we do not deal with a 1D system here, there are sufficient states at the FS interconnected by equivalent nesting vectors $\mathbf{q}_{\mathrm{S1}}$. Following this idea, one can derive the size of the nesting vector $|\mathbf{q}_{\mathrm{S1}}| = 0.62\,\text{Å}^{-1}$. With respect to the threefold symmetry of the system, two additional and equivalent nesting vectors can be drawn, rotated by 120 ° and 240 °, respectively. The size of the nesting vector corresponds to a real-space distance of $2.9\,a_{\mathrm{Si}}$. However, this value does not agree with any multiple of the ($\sqrt{3} \times \sqrt{3}$) reconstruction, which would comply to a commensurate nesting condition. In turn, this decreases the likelihood to observe a CDW phase transition. In fact, ARPES experiments performed between 10 K and RT do not show any signature of a CDW phase transition at all. This result agrees with an unchanged LEED pattern within the same temperature range. The absence of a CDW may probably be ascribed to a lack of lock-in energy of a possible CDW triggered lattice distortion with the underlying substrate, as also suggested to suppress the CDW formation in the dense β-phase of Pb/Ge(111)-($\sqrt{3} \times \sqrt{3}$) [211].

Furthermore, an instability towards a CDW is characterized by a singularity in $\chi(\mathbf{q})$ for a specific wave vector $\mathbf{q}$. For the related surfaces of Sn/Ge(111)-($\sqrt{3} \times \sqrt{3}$) and Pb/Ge(111)-($\sqrt{3} \times \sqrt{3}$) the possibility of a CDW formation has been studied theoretically [14]. It was found that the susceptibility is not enhanced at the positions of the relevant (3×3) zone boundaries in k-space, which means an unfavorable situation with respect to a CDW formation. Another property which is involved in the transition probability is the rigidity of the surface lattice. An important parameter to be considered in this context may be the cohesion energy of the adsorbate atoms, which reflects the energetic stability of the surface. Since this value is rather large in case of gold (5.8 eV, [176]), it is likely that interatomic bonds are strong here (see Tab. 5.1). Such a more rigid surface lattice could certainly contribute to suppress the formation of a CDW in Au/Ge(111)-($\sqrt{3} \times \sqrt{3}$).

Band structure of related surface systems

Most closely related to Au/Ge(111)-($\sqrt{3} \times \sqrt{3}$) is the Au/Si(111)-($\sqrt{3} \times \sqrt{3}$) surface, which is also described within the CHCT model. As reported for Au/Ge(111)-($\sqrt{3} \times \sqrt{3}$) and Pt/Si(111)-($\sqrt{3} \times \sqrt{3}$) in this thesis, the existence of phase-shifted domains has been proved there, too [145]. Hence, it is advisable to look for similarities in the electronic band structure in both systems. K. N. Altmann *et al.* have scrutinized Au/Si(111)-($\sqrt{3} \times \sqrt{3}$) along $\overline{\Gamma}$–$\overline{\mathrm{M}}$ by means of ARPES [172]. The respective band structure is shown in Fig. 6.11 along the high symmetry direction $\overline{\Gamma}$–$\overline{\mathrm{M}}$ within the first and second SBZ [172]. In comparison, there are at least three apparent analogies in the electronic

[1] This consideration still assumes a spin degenerate band and neglects the spin splitting evidenced by DFT and SARPES in Secs. 6.2.2 and 6.3.

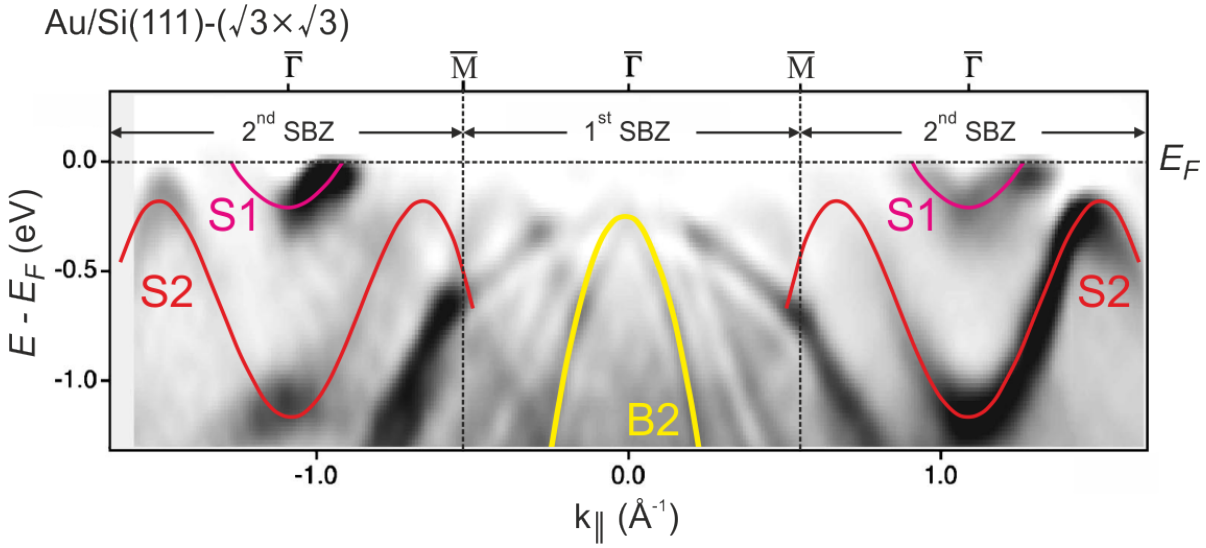

Figure 6.11: *Electronic band structure of the related 2DES Au/Si(111)-($\sqrt{3} \times \sqrt{3}$), inspected by ARPES (RT, $h\nu = 34\,eV$) along the $\overline{\Gamma}$–$\overline{M}$ high symmetry direction in the first and second SBZ [172]. Dark contrast corresponds to high photoemission intensity. The surface states S1, S2, and the bulk band B2 are highlighted by fit curves to the respective ARPES band curvatures. Photoemission data and fit curves are extracted from [172], Copyright (2001) by the American Physical Society.*

band dispersion: **i)** Au/Si(111)-($\sqrt{3}\times\sqrt{3}$) exhibits a small electron pocket (S1), centered around the $\overline{\Gamma}$ point, with a filled bandwidth of 210 meV. This metallic state is only visible in the second SBZ. It has its pendant in the Au/Ge(111)-($\sqrt{3} \times \sqrt{3}$) S1 state, which is barely visible in the first SBZ. The absence of this band in the first SBZ for Au/Si(111)-($\sqrt{3} \times \sqrt{3}$) might be related to a worse experimental resolution, the sample quality, and to the dense network of domain walls, reported for the system. **ii)** There are no H states, as found for Au/Ge(111)-($\sqrt{3} \times \sqrt{3}$) in this thesis, whereas bulk band features could be identified in the first SBZ likewise (e.g., B2). **iii)** A fully occupied surface state (S2), which has approximately the same dispersion as the S2 state in this thesis, is observed. This state should thus be of the same origin, i.e., it must be Au derived, which is indeed verified for Au/Ge(111)-($\sqrt{3} \times \sqrt{3}$) in the following section by means of DFT. The FS has later been examined by J. N. Crain *et al.* [173]. Different from Au/Ge(111)-($\sqrt{3} \times \sqrt{3}$), it appears to be of circular shape and much smaller in diameter. Moreover, it is strongly broadened, most likely due to the small anti-phase domains present at that surface. In all, the striking similarities concerning the electronic band structure are most probably due to their strong structural relationship and the similar orbitals involved in the bonding at the surface. In Ag/Si(111)-($\sqrt{3} \times \sqrt{3}$) a similar electron pocket has been reported [173], although metallicity merely results from doping due to excess silver at the surface there.

6.2.2 Advanced density functional theory modeling of the electronic band structure

The determination of the electronic band structure in many-body systems is a major issue in solid state physics. In this regard, the density functional theory (DFT) serves as a well established tool for clarification [212, 213]. Its concept shall be outlined on the basis of the reviews in Refs. 214–216 in the following. The main idea is to derive the position-dependent density of electrons in the ground state. Further properties as, e.g., the total energy of the system, are functionals of the electron density and may thus be derived from it. This basic concept is known as the "Hohenberg-Kohn theorem" in the literature [214–216].

The determination of the electron density in the ground state of an N-electron system requires to define N single-particle wave functions, the "Kohn-Sham functions", which are solutions to the Schrödinger equation in an effective potential [214, 216]. The corresponding one-electron Schrödinger equations are known as "Kohn-Sham equations". This approach drastically reduces the complexity of the problem, since the Kohn-Sham functions are *independent* solutions to the Kohn-Sham equation. In this way, the electron density for each Kohn-Sham function is calculated, and the overall electron density is then derived by summing over these. A general issue is to determine the exact *effective potential*, which comprises three main contributions [216], i.e., **i)** the external potential, that describes the interaction of the electrons with the atomic nuclei, **ii)** the "Hartree" term, which introduces the electrostatic interaction among the electrons, and **iii)** the exchange-correlation potential for inclusion of many-body effects. The effective potential is part of the Kohn-Sham equations, but also depends on the electron density of the system, and thus also on the solutions of the Kohn-Sham equations. Here, it becomes evident that a self-consistent solution must be found in an iterative way. Thus, after determination of the effective potential, the Kohn-Sham equations are solved again for this corrected potential, which then returns a further refinement of the potential, and so on. Unfortunately, the exact *exchange-correlation energy functional* is not known. However, in dependence of the properties and the respective problem to be scrutinized, several approximations have been proposed to overcome this lack. For many solid state systems, like the ones discussed in this thesis, the *local density approximation* (LDA) has been established as a standard. It locally approximates the exchange-correlation energy by the one of the uniform electron gas (*jellium* model). The exchange-correlation energy is then an explicitly parametrized functional of the electron density. While the LDA is exact for the uniform electron gas, it has also proved to be very useful for describing real-world materials with slightly varying charge density. Although the LDA provides accurate results in many cases here, it features some inherent shortcomings, such as the underestimation of energy band gaps in insulators and semiconductors. Moreover, it does not exclude the electrons' *self-interaction* and is thus error-prone by nature. The latter deficiency can be reduced by introducing a self-interaction correction (SIC) to the LDA in some cases [217].

In a first step, calculations within the LDA shall be used to strengthen the CHCT configuration as the correct structural model for Au/Ge(111)-($\sqrt{3} \times \sqrt{3}$) again. In comparing the results of theoretical band structure modeling with those from ARPES, several adjustments can be applied to the calculations in an iterative way, until a reliable agreement is reached. Second, the LDA allows to allocate different atomic orbitals to the states observed in experiment. In addition, the distribution of the respective wave functions within the slab facilitates to conclude, whether a band should be identified as a surface state, a surface resonance, or a bulk state. And finally, inclusion of the SOI to the calculations will shed light on the spin texture.

The DFT band structure presented in the following has been modeled within the LDA [H5]. A periodic slab array, consisting of 19 layers of germanium, one hydrogen layer at the rear side, and the gold monolayer on top was constructed. The initial atomic coordinates were set to those values derived from the SXRD experiments in Ref. 148. The vacuum separation between neighboring slabs amounts to 7.7 Å in order to exclude an overlap of the wave functions. The calculations have utilized a mixed-basis code, which is distinguished by the fact that in addition to plane waves also localized Gaussian functions of angular momentum $l = 2$ are positioned at the locations of the Au atoms [H5, 218, 219]. While in standard LDA a quite acceptable agreement with the experimental band structure of Au/Ge(111)-($\sqrt{3} \times \sqrt{3}$) is already achieved, the binding energy is notably underestimated. In particular, this becomes obvious with regard to the deviating band minimum position of the mainly Au derived state S1. Since alternative structural models could be excluded (see Sec. 6.1.1), any mismatch between the experimental and the calculated band structure must be related to the inherent limitations of the DFT. Here, the self-interaction error leads to the largest discrepancies. Considering the atom species involved, it mostly affects the localized $5d$ states of gold. These are located close to the Fermi level and are of relevance in the bonding with the germanium atoms. In order to account for this deficiency, a SIC is introduced in a similar way, as has been described for II-VI compounds in Refs. 220 and 221. Accordingly, the d part in the LDA pseudopotentials of Au is altered so that an acceptable agreement between the band structure of bulk Au in experiment and in theory is achieved.

The resulting LDA-SIC band structure, that further includes SOIs, is presented in Fig. 6.12. At first glance the good overall agreement with the ARPES band structure in Fig. 6.8 is quite obvious. All relevant bands reported experimentally are well reproduced, including their respective curvatures [H5]. However, the Fermi level had to be shifted by +110 meV in order to achieve a better agreement between experimental and theoretical k_F-values, which are summarized in Tab. 6.5. In spite of this general agreement, a deviation in the minimum binding energy of the S1 band bottom of ≈ 200 meV in size persists. This is ascribed to a potential self-doping effect in the experiment, where excess Au at the surface is believed to inject additional charge carriers into the surface states, leading to a rigid band shift to higher binding energies. Alternatively, K. Nakatsuji *et al.* suggest that the shift in energy might be due to a surface band bending [202]. In

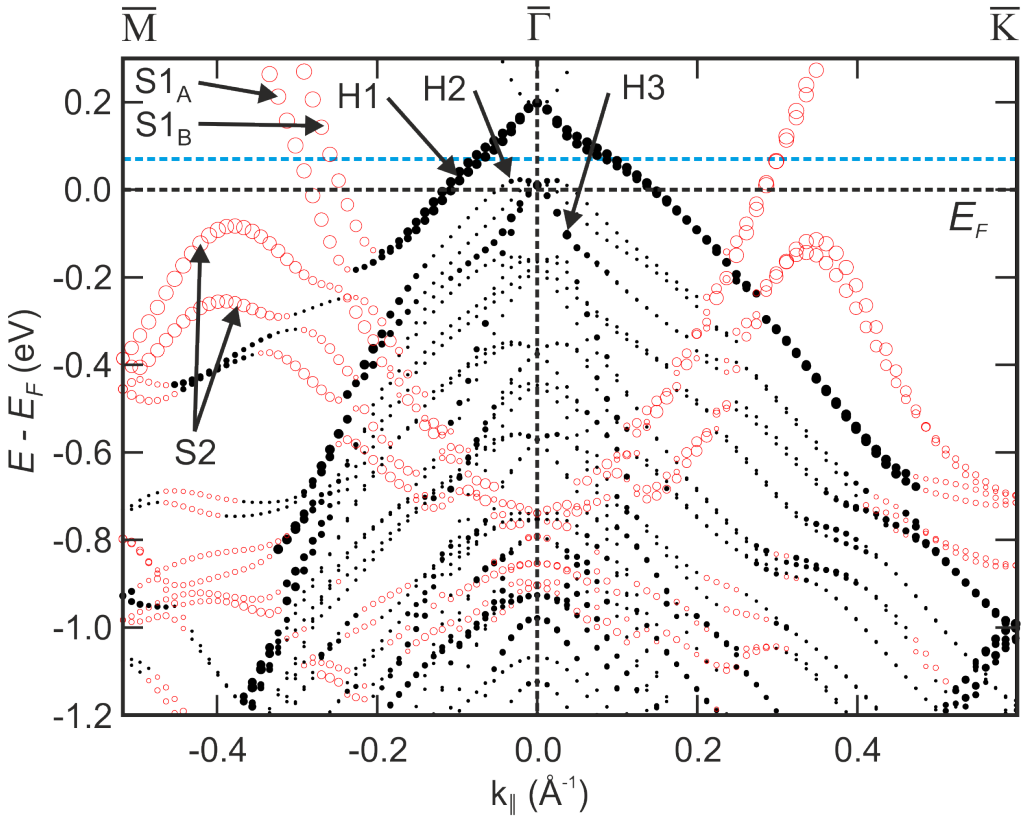

Figure 6.12: *The electronic band structure of Au/Ge(111)-($\sqrt{3} \times \sqrt{3}$) calculated by the LDA-SIC within the DFT. Four metallic surface states $S1_A/S1_B$, H1, H2, and H3 are obtained in good agreement with ARPES. Black color indicates a predominant Ge origin of the respective states, whereas red color signifies a predominant Au origin. Larger symbols correspond to a near surface localization of the state, and small symbols refer to an enhanced bulk character. The Fermi level E_F is shifted by +110 meV with respect to the Fermi energy returned from the calculations in order to enhance the agreement with the experimentally obtained Fermi vectors [H5], Copyright (2011) by the American Physical Society. The blue dashed line corresponds to the Fermi energy chosen in comparison with the spin information obtained from SARPES (shift: +180 meV).*

addition, the classification of bands into electron-like surface states and resonances (S), hole-like surface states and resonances (H), and bulk band features (B) bases on the ratio of surface/bulk localization of the respective wave functions. Accordingly, large symbols in Fig. 6.12 represent states that are localized at the surface, which is the case for S1 and S2, while H2 and H3 are only partly of surface character (smaller symbols). In particular, H2 and H3 exhibit a notable delocalization of their wave functions from the surface into the bulk, that leads to an overlap with the projected bulk band structure. Accordingly, these bands must be assigned to surface resonance states. Another vital information provided by DFT modeling is the orbital origin of the respective bands, which is signified by the symbol color. Red color denotes states that are predominantly derived from Au atoms, whereas for black color Ge orbitals dominate. This classification

is made by inspecting the integrated charge of a specific state with respect to its in-plane momentum and depth in the slab construction. In case that more than 50 % of the charge of the relevant band is, e.g., located within the Au layer, this state must predominantly originate from Au orbitals. In particular, this is true for the quasi-parabolic S1 surface state. Similarly Ge derived states have a charge majority located in a germanium layer.

Spin-orbit coupling effects

Apart from these first and important theoretical details on the band structure, Fig. 6.12 also reveals that SOIs play a crucial role at the Au/Ge(111)-($\sqrt{3} \times \sqrt{3}$) surface. In this regard, the most obvious finding is that the Au derived surface state S1 exhibits a significant spin splitting of $2k_0 = 0.040\,\text{Å}^{-1}$ along the $\overline{\Gamma}$–$\overline{\text{M}}$ direction due to a notable potential gradient at the surface. Such a rather large splitting is eligible to explain the band broadening of $\Delta k_{\parallel} = 0.064\,\text{Å}^{-1}$ seen in ARPES. In particular, the total broadening, which is a convolution of instrumental resolution, scattering at phase-slip domain walls, and the band splitting, must be highly dominated by the latter. The splitting is even predicted to be larger than the one approximately derived by the MDC fitting in Fig. 6.9 ($2k_0 = 0.028\,\text{Å}^{-1}$). With these new insights, the separate notations S1_A and S1_B, earlier suggested in Sec. 6.2.1 based on ARPES only, are now generally introduced. Another essential aspect of the calculated band structure is that the splitting is almost absent along $\overline{\Gamma}$–$\overline{\text{K}}$. This means that the SOI at the surface of Au/Ge(111)-($\sqrt{3} \times \sqrt{3}$) does not act isotropically, but rather shows significant deviations from a conventional Rashba scenario. Here, the DFT calculations also indicate that the potential landscape at the surface must be somewhat complex with clear deviations from a strict homogeneous and perpendicular electric field. At first sight, such an anisotropic band splitting seems to contradict the ARPES finding of a rather constant broadening of the S1 band along its whole FS. However, assuming that we deal with a faint unresolved spin-orbit splitting here, a satisfying agreement is found as follows. According to the DFT calculations, the spin-orbit splitting is of constant magnitude for almost all in-plane momenta along the FS. The only exception exists in a very narrow region close to the $\overline{\Gamma}$–$\overline{\text{K}}$ direction, where the splitting is reduced (see Sec. 6.3). Hence, the vanishing spin splitting predicted by the DFT is highly localized in k-space. In an ARPES experiment a certain amount of averaging over adjacent k-space momenta is inevitable and limits the achievable angular resolution. Consequently, this can lead to the observation of an overall band broadening larger than the one predicted theoretically along the $\overline{\Gamma}$–$\overline{\text{K}}$ axis.

With respect to the other electronic states, S2 also shows a large splitting induced by SOIs, whereas smaller splittings are found for H1, H2, and H3. Notably, the splitting of the H1 surface resonance is almost entirely of the Rashba type, i.e., the spin momentum vector is approximately oriented orthogonal to the momentum and field vectors. However, the following section will restrict the discussion to the prominent Au derived S1 state due to four striking reasons. **i)** S1 has the largest spin splitting, **ii)** it features an intense signal in photoemission, which is relevant for the high statistics needed in

SARPES, **iii)** it has no crossings with other bands in a sufficiently large energy window below E_F, and **iv)** S1 shows metallic behavior, which could be favorable for future spintronic applications.

6.3 The complex spin texture at the surface of Au/Ge(111)-($\sqrt{3} \times \sqrt{3}$)

The theoretical prediction of a strong band splitting due to SOIs in the metallic surface 2DES Au/Ge(111)-($\sqrt{3} \times \sqrt{3}$) is of particular relevance, since its experimental realization would represent a valuable step in view of an electronic manipulation of spins [23]. Recent reports dealing with the spin texture at related surface 2DESs established on semiconductor surfaces have shown that heavy atoms may induce an exceptionally large Rashba splitting. In particular, this applies to the bands formed by Bi and Tl reconstructions on Si(111), which are insulating surfaces [24, 25, 222]. Yet, a mandatory requirement for controllable spin currents in electronic transport applications is the presence of *conducting* spin-split states [H6]. A recent, and so far unique, example of conducting spin-split surface states was presented in 2010 by K. Yaji *et al.* in the dense β-phase of Pb/Ge(111)-($\sqrt{3} \times \sqrt{3}$) [26]. Utilizing SARPES, the authors were able to give evidence of a sizable Rashba type band splitting in the hexagonally warped surface state. Importantly, recent speculations on the interplay of crystalline anisotropies and the corresponding potential gradients at the surface have pointed at the relevance of additional in-plane electric fields [25, 223]. Unfortunately, the experimental setup in the study of K. Yaji *et al.* was limited to the detection of the in-plane spin orientation only, leaving potential out-of-plane components of the spin polarization vector unresolved.

In general, a homogeneous and perpendicular built-in electric field, as at the Au(111) surface, is rather an exceptional case. Typically, out-of-plane and in-plane potential gradients are assumed to intermix, resulting in a variety of complex and anisotropic spin patterns. Thus, a complete 3D determination of the spin polarization at the FS of spin-orbit coupled surface systems is advisable. In this regard, experimental evidence of a symmetry-dependent rotation of the spin polarization vector out of the surface plane has been found for Tl/Si(111)-(1 × 1) and for surface alloys [22, 25]. An example is given in Fig. 6.13(a), where the measured spin polarization along the surface normal (z) of the $l4$ state in Pb/Ag(111) is depicted (graph taken from [22]). Here, it turns out that a Rashba type spin orientation, i.e., planar and orthogonal to the momentum vector, is only maintained along the $\overline{\Gamma}$–$\overline{\mathrm{M}}$ direction, whereas a rotation out of the surface plane is found elsewhere. This modified spin pattern exhibits an undulating character, following the 120 ° rotational symmetry of the surface. Contrary to the spin vector orientation in the original Rashba model, such a modified spin pattern can be described by an effective Hamiltonian, which includes both Rashba- and Dresselhaus-like spin-orbit terms [43, 224, 225]. In this context, complex spin patterns in surface 2DESs should

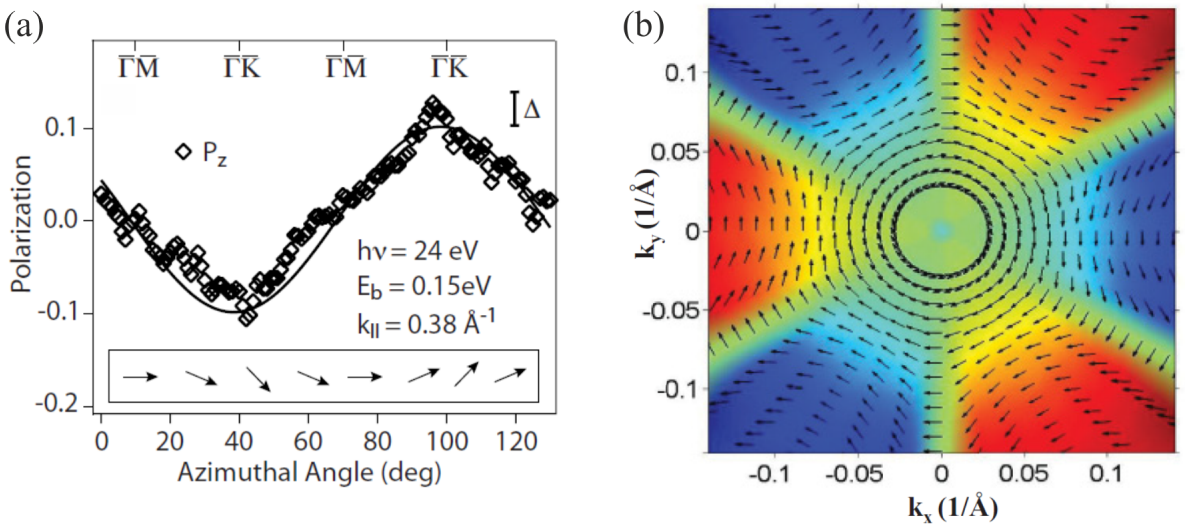

Figure 6.13: *(a) Pb/Ag(111) surface alloy: Measured z component of the spin polarization in SARPES, depending on the azimuthal direction in k-space for the band l4 at 0.15 eV binding energy; graph taken from [22], Copyright (2008) by the American Physical Society. The spin lies in plane along* $\overline{\Gamma}$–$\overline{\mathrm{M}}$ *only, whereas it undulates from downward to upward for directions in between, as is schematically visualized in the inset. (b) Topological insulator* Bi_2Te_3*: Projection of the spin vector in the Dirac fermion band onto the surface plane, as obtained from first principles calculations; graph taken from [27], Copyright (2011) by the American Physical Society. The innermost arrows reflect the spin orientation close the Dirac point, where the band is of circular shape. Arrows away from the center correspond to higher binding energies, with the band curvature altered to hexagonal and finally warped shape. The color coding reflects the spin z orientation, which is out of (into) the surface for red (blue) color, while green represents an in-plane spin alignment.*

generally be discussed.

Importantly, this discussion of topical interest also extends to topological insulators, which currently experience lively interest in solid state physics [226]. It has recently been predicted by first principles calculations that an even more complex spin pattern, involving undulations and an additional in-plane spin rotation, should exist in the warped FS of the 3D topological insulator Bi_2Te_3 [27, 28, 55]. This behavior is visualized in Fig. 6.13(b), where the spin orientation (arrows) in the Dirac fermion state, projected onto the surface plane, is plotted (graph taken from [27]). The spin lies fully in plane (*green* color) and is orthogonal to the in-plane momentum vector close to the Dirac point (innermost arrows), where the constant energy surface is of circular shape. Yet, its orientation is drastically modified at the warped FS, which is located in the region of $k_x, k_y \approx 0.1$ Å. Here, similar as in Pb/Ag(111), the spin alignment remains unchanged only along the mirror symmetric directions (*green*), while in between an out-of-plane spin undulation (*red*: out of the surface; *blue*: into the surface) with threefold rotational symmetry is found. Remarkably, also additional *in-plane rotations* of the spin can be spotted close to the mirror symmetric directions. Although indications of such a spin

pattern have been found in SARPES [227], unambiguous experimental verification is still missing. Quite generally, it is an alluring perspective to scrutinize such complex spin textures not only in the Dirac fermion state of topological insulators, but also in metallic bands of related surface structures.

The spin-polarized Fermi surface in density functional theory

Inspired by the complexity and variety of possible spin textures in surface 2DES, it means a vital task to clarify the spin polarization in Au/Ge(111)-($\sqrt{3} \times \sqrt{3}$) by both DFT and 3D SARPES. Since the relevant physics happen at the FS, it is a good starting point for the spin analysis to extract a plot of the band topology and spin pattern at E_F from the DFT calculations, as shown in Fig. 6.14.[1] First of all, the experimentally observed S1 surface sheet with its six straight segments in hexagonal appearance is well reproduced [H6]. As already known from the DFT band map in Fig. 6.12, the S1 band is significantly spin-split into the subbands $S1_A$ and $S1_B$ by $2k_0 = 0.040\,\text{Å}^{-1}$ along the $\overline{\text{M}}$–$\overline{\Gamma}$–$\overline{\text{M}}$ direction, while the splitting collapses to almost zero along the $\overline{\text{K}}$–$\overline{\Gamma}$–$\overline{\text{K}}'$ direction. In the next step, the orientation of the spin polarization vector $\mathbf{P}$ on each of the two subbands $S1_A$ and $S1_B$ shall be scrutinized. Its orientation in reciprocal space is represented by colored arrows, where red, blue, and green mean that $\mathbf{P}$ points out of the surface, into the surface, or is aligned in the plane, respectively. A coarse inspection of the spin pattern yields that the in-plane circulation of the spin is counter-clockwise for $S1_A$ and clockwise for $S1_B$, which is conform to the situation in Au(111) [20]. The latter surface represents an ideal Rashba spin-orbit splitting, i.e., the spin is always aligned in plane and orthogonal to the momentum vector. However, the present DFT FS unveils that such a strict situation is only valid along the $\overline{\text{K}}$–$\overline{\Gamma}$–$\overline{\text{K}}'$ directions in Au/Ge(111)-($\sqrt{3} \times \sqrt{3}$). In between, the spin polarization vector abruptly turns out of the momentum plane by up to 75 °, with only slight variations in the perpendicular direction along the straight FS segments. Notably, the z orientation is inverted when regarding the adjacent FS segments of the same subband. This leads to an overall undulating behavior of the z component of the spin polarization vector, corresponding to the $C_{3\nu}$ symmetry of the surface. Moreover, the perpendicular spin alignment is also inverted, when comparing the adjacent and rather parallel FS segments of $S1_A$ and $S1_B$. A surprising additional finding is that the in-plane component of the spin is neither orthogonal to $\mathbf{k}_\parallel$ nor tangential to the Fermi sheets in between the two high symmetry directions. In fact, it exhibits a pronounced *in-plane rotation*, that becomes strongest in close vicinity to the $\overline{\text{K}}$–$\overline{\Gamma}$–$\overline{\text{K}}'$ azimuth. Such a complex spin pattern has not been observed experimentally so far for any surface 2DES,

[1] The Fermi level in the DFT is adjusted by +180 meV, which is necessary to account for a remaining inconsistency in the self-interaction error. As a result, theory and experiment are well compatible with regard to the size and shape of the FS, while also the orientation of the spin polarization vector at the FS is in good agreement. The adjustment corresponds to the blue dashed line in Fig. 6.12, which is different from the initial shift by +110 meV, based on a comparison with ARPES only. However, the overall agreement is even better due to the inclusion of the spin information here.

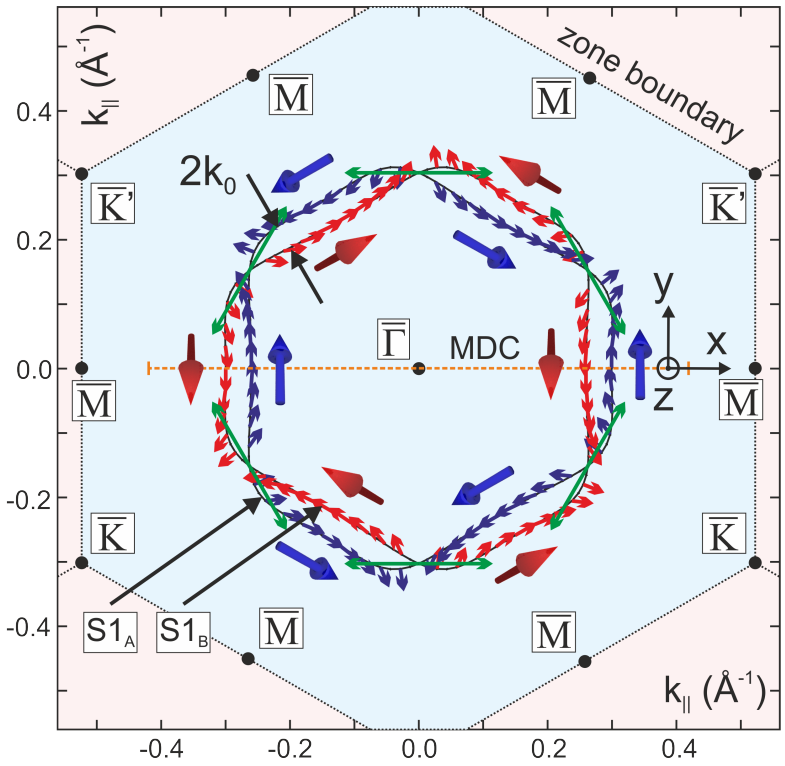

Figure 6.14: *FS of the S1 surface state (black contour line) in Au/Ge(111)-($\sqrt{3} \times \sqrt{3}$) calculated for the first SBZ within the LDA-SIC code. The band exhibits a momentum-dependent splitting $2k_0$ into the subbands $S1_A$ and $S1_B$ due to the SOI. The orientation of the spin polarization vector* **P** *is given by small arrows at 60 distinct locations for each subband. The arrow lengths correspond to the proportion of the in-plane orientation, while color coding signifies an additional orientation of up to 75° out of (red) or into (blue) the momentum plane. The longest arrows (green) represent full in-plane spin alignment, which is only the case along* $\overline{\mathrm{K}}$–$\overline{\Gamma}$–$\overline{\mathrm{K}}'$ *directions. Larger arrows beneath the S1 FS with red/blue color code are used to emphasize the undulating behavior of the out-of-plane component of the spin polarization vector between adjacent straight segments of the FS. For MDC scans, as indicated by the dashed line, a local coordinate system (x, y, z) is used. Contributions of H1 and H2 are omitted for clarity, and the Fermi energy is displaced by +180 meV to improve the agreement with SARPES [H6], Copyright (2012) by the American Physical Society.*

apart from being theoretically proposed for the topological insulator Bi_2Te_3 [27], as presented above. It would thus mean an important contribution to topical fundamental research to provide experimental verification of the scenario predicted here.

The spin-polarized Fermi surface in 3D SARPES

The COPHEE setup, which has been introduced in Sec. 3.3.2, is the ideal experiment to validate the theoretical prediction above, since it provides access to the spin polarization along all quantization axes (3D SARPES). Furthermore, even very little band splittings or overlapping bands with a distinct polarization can be separated therein due to the

high sensitivity of the *two-step fitting routine* (see Sec. A.2) [49, 116]. Nevertheless, the poor statistics in Mott scattering, in spite of the utilization of synchrotron radiation, restrict the applicability to MDC or EDC scans, rather than capturing full spin-resolved band maps or even FSs. Since the S1 surface state is strongly dispersing, MDCs represent the more appropriate approach to resolve the spin structure here. In Fig. 6.14 the dashed line indicates the orientation of such a scan profile along the $\overline{\mathrm{M}}$–$\overline{\Gamma}$–$\overline{\mathrm{M}}$ direction. All MDCs have been captured at 70 meV binding energy to enhance the statistics in comparison with a scan exactly at E_F, since the rather coarse energy resolution (120 meV) in SARPES experiments integrates over a broad energy range. Fortunately, the S1 band is the only one present in the specified energy window near $k_{\parallel,F,S1}$. SARPES measurements were further restricted to the second SBZ, where the S1 photoemission band intensity is strongest and neighboring states are mostly suppressed. Utilization of linearly polarized light ensures that the measured spin polarizations mostly comply to the initial states, whereas additional contributions added during the excitation into the final states are rather low, as has been discussed in Sec. 3.3.1 [51, 107].

The spin-resolved intensities along the specified scan direction, corrected by the instrumental Sherman function $S = 0.068$, are presented in Fig. 6.15(a)–(c). These curves exhibit a clear profile consisting of two peaks with their maxima located at $k_{\parallel,F,S1}$, as already derived by ARPES. While both curves still almost coincide for the x direction (a), a pronounced shift between the profiles is found for the y (b), and even more explicitly for the z direction (c).[1] This corresponds to a splitting between intensities for positive ($\uparrow$, spin up) and negative ($\downarrow$, spin down) spin alignment with regard to the quantization axis of the respective detector. Hence, the present SARPES data exhibit a clearly resolved band splitting [H6]. The splitting is anti-symmetric with respect to the zone center $\overline{\Gamma}$, e.g., the peak maxima along the positive (negative) z quantization axis are shifted to lower (higher) $k_{\parallel}$-values. On the basis of these data, one can easily envisage that the spin on the outer Fermi sheet, i.e., $\mathrm{S1_A}$ to the right side of the $\overline{\Gamma}$ point, is oriented in positive y direction and negative z direction, while it has no component along x. Returning to the calculated spin pattern in Fig. 6.14, it turns out that this result from SARPES is in excellent agreement with the theory. The same conformity is also found to the left of $\overline{\Gamma}$ and for the inner contour $\mathrm{S1_B}$, which evidences the helical circumference and undulating z component of the spin. In conclusion, the spin pattern obeys the $C_{3\nu}$ symmetry, and time-reversal symmetry remains intact in Au/Ge(111)-($\sqrt{3} \times \sqrt{3}$).

In addition to these important results, Fig. 6.15(d) shows the total intensity MDC $I(k_{\parallel})$, which is just the sum of the single spin-resolved intensities in (a)–(c). The spin information is lost in this plot, and it alone does not provide more information than already available by a conventional ARPES MDC like the ones in Fig. 6.9(b). However, in conjunction with the spin-resolved data and under exploitation of the *two-step fitting routine* (see Sec. A.2), fitting with two Voigt line shapes per peak leads to an excellent

[1] The quantization axes always refer to the coordinate system shown in Fig. 6.14, which is fixed to the MDC scan line.

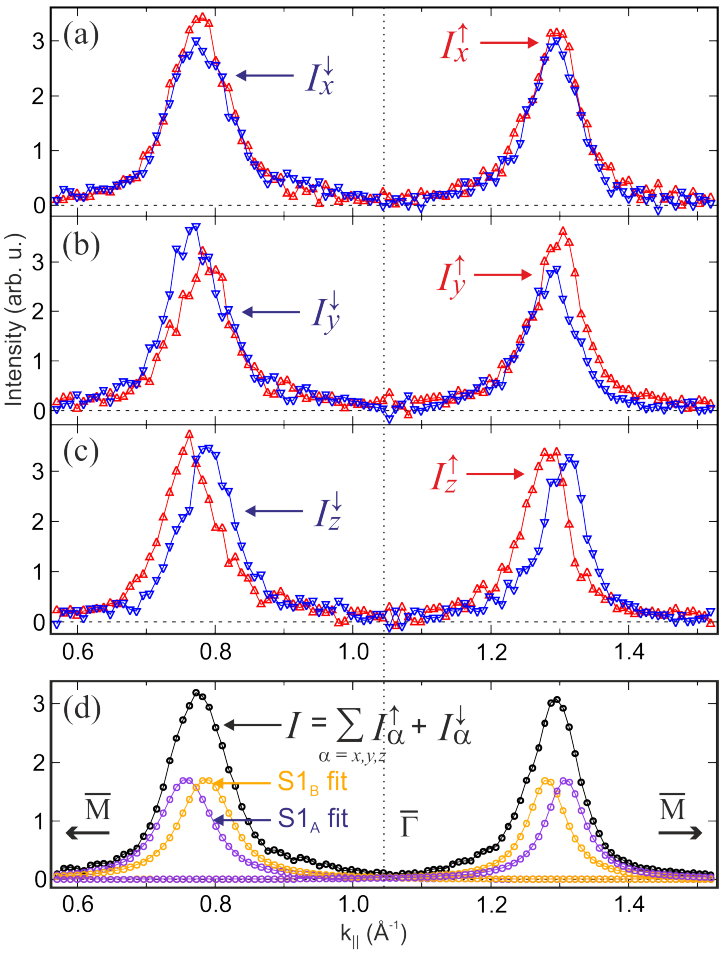

Figure 6.15: *(a) Spin-resolved intensities for the x quantization axis along the $\overline{\mathrm{M}}$–$\overline{\Gamma}$–$\overline{\mathrm{M}}$ direction in the second SBZ of Au/Ge(111)-($\sqrt{3}\times\sqrt{3}$) after correction with the Sherman function $S = 0.068$; $T = 300\,K$, $h\nu = 35\,eV$. Red upward (blue downward) triangles correspond to the electron spin aligned with the positive (negative) quantization axis of the x Mott detector. (b), (c) Spin-resolved intensities for the y and z quantization axes. (d) Total spin-integrated intensity $I(k_{\|})$, i.e., the sum of the curves in (a)–(c). The purple and yellow curves are the best fits to the data within the two-step fitting routine and allow allocation of the two spin-split bands $S1_{\mathrm{A}}$ and $S1_{\mathrm{B}}$ [H6], Copyright (2012) by the American Physical Society.*

overall reproduction of the total intensity. Therefore, the separate profiles $S1_{\mathrm{A}}$ (purple) and $S1_{\mathrm{B}}$ (yellow) do quite reliably reflect the peak shapes hidden in the spin-integrated MDC data. The size of the band splitting is expected to be largest along this scan direction, according to the DFT results, i.e., $2k_0 = 0.040\,\text{Å}^{-1}$. The peak-to-peak separation determined by fits of multiple MDC scans in SARPES along the same direction is $2k_0 = 0.025\,\text{Å}^{-1}$, and thus smaller. Yet, the latter value is close to the one estimated from ARPES MDC fitting before ($2k_0 = 0.028\,\text{Å}^{-1}$). Therefore, one has to conclude that while theory succeeds in the prediction of the spin vector orientation at the FS, a

slight discrepancy remains in the size of the splitting. This is most likely related to the inherent inaccuracies in LDA-based semiconductor band structure modeling in general.

The SARPES data so far have provided striking evidence of the spin-orbit induced band splitting with large out-of-plane spin orientations, that deviates from a conventional Rashba situation. It would furthermore be vital to clarify the spin texture at the $\overline{\mathrm{K}}$–$\overline{\Gamma}$–$\overline{\mathrm{K}}'$ azimuth, where the spin is assumed to be fully in-plane oriented. Moreover, the important prediction of in-plane spin rotations in the regions between the two high symmetry directions calls for experimental inspection. In this regard, the FS has been mapped by seven location sensitive MDC scans (indicated by straight lines, top of Fig. 6.16). The spin-resolved intensities $I_\alpha^\uparrow(k_\parallel)$ and $I_\alpha^\downarrow(k_\parallel)$ ($\alpha = x, y, z$) gained in this way are transformed to the corresponding *measured* spin polarizations $P'_\alpha(k_\parallel)$ by use of Eq. A.6. The resulting values are plotted in Fig. 6.16 for the seven distinct scan positions (SPs) 1–7. A good starting point is to discuss the measured spin polarization of SP 7, which would also be obtained from evaluation of the data to left of $\overline{\Gamma}$ in Fig. 6.15. Here, a strong polarization in the z direction is confirmed, whereas it is found to be much smaller for the y component. This agrees well with the theoretical prediction of a significant out-of-plane spin orientation along $\overline{\Gamma}$–$\overline{\mathrm{M}}$, accompanied by just a small in-plane component orthogonal to $\mathbf{k}_\parallel$, i.e., along the y direction. The finding of a very little, but still finite polarization along the x axis is not reflected by the DFT, but it can most likely be ascribed to an averaging over a specific area in k-space, defined by the detector acceptance angle. Moreover, a limited precision in moving to a specific location in k-space by tilting the goniometer is inevitable. Also, the sample is usually inclined in the sample carrier, which further limits positioning to a finite accuracy. Fortunately, the distance between neighboring SPs is large enough to allow for a complete mapping of the designated region. In progressing along the SPs to SP 1, which intersects the $\overline{\Gamma}$–$\overline{\mathrm{K}}'$ azimuth, the measured z polarization decreases in favor of both the y and x components. Exactly at SP 1 the spin is fully aligned in plane in agreement with the expectation from the calculated spin pattern at the FS.

Determination of the band-specific spin polarization

Although the preceding evaluation and discussion of the SARPES data has already provided a convincing agreement with the theory, it is not possible to compare theory and experiment quantitatively at this point. This deficiency is overcome by further processing the data within the *two-step fitting routine*, which is reviewed in the appendix (Sec. A.2). In short terms, the routine can be described as an incremental step-by-step fitting process of the spin-integrated data $I(k_\parallel)$ by a judicious number of Voigt line shapes (in this case two), followed by fits to the measured spin polarizations $P'_\alpha(k_\parallel)$ (red curves in Fig. 6.16), until an eligible accuracy in both steps is reached. Furthermore, the unpolarized background signal is removed from the SARPES data here. The parameters obtained in the second step of fitting comprise the angular orientation and the length of the *band-specific* spin polarization vector $\mathbf{P} = (P_x, P_y, P_z)$. Therefore, the direction

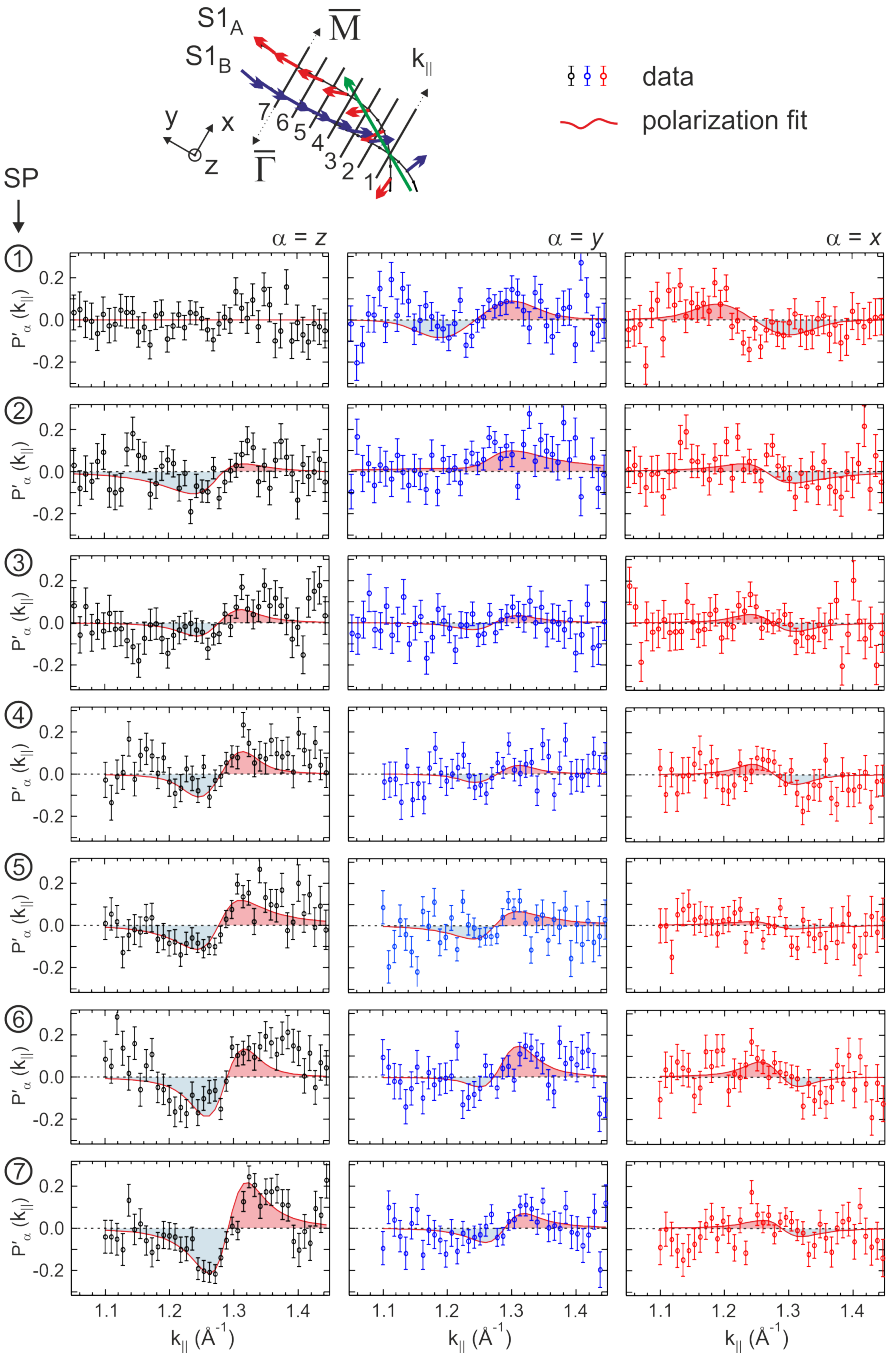

Figure 6.16: *Measured spin polarizations $P'_x(k_\parallel)$ (left panels), $P'_y(k_\parallel)$ (middle panels), and $P'_z(k_\parallel)$ (right panels) along seven site-specific SARPES MDCs at the FS in the second SBZ of Au/Ge(111)-($\sqrt{3} \times \sqrt{3}$) (SPs 1–7); $T = 300\,K$, $h\nu = 35\,eV$. The spin quantization axes correspond to the local coordinate system displayed in the upper part of the figure. The red curves represent fits to the data within the two-step fitting routine (see Sec. A.2). The z spin polarization increases from zero at SP 1 to its largest value at SP 7, while the y and x components are largest for SP 1 [H6], Copyright (2012) by the American Physical Society.*

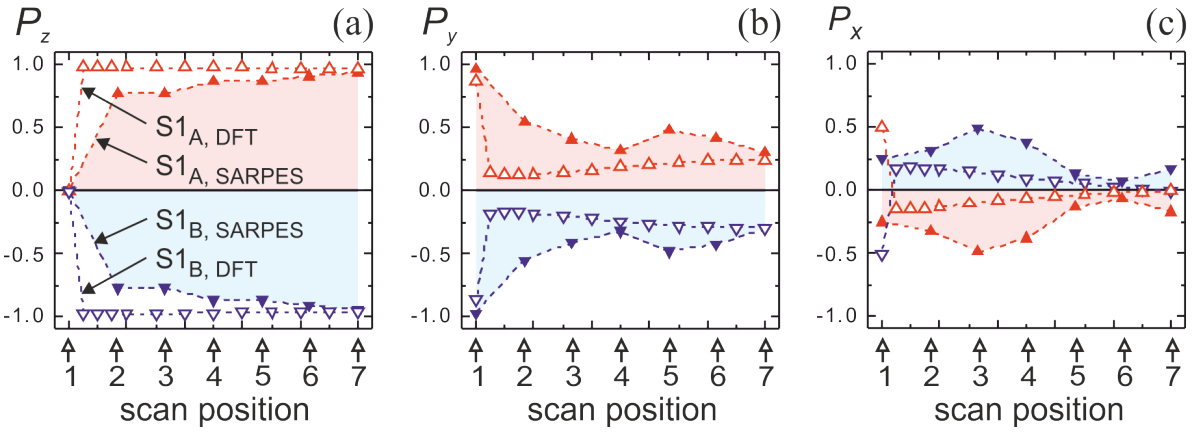

Figure 6.17: *(a) Band-specific z component P_z of the spin polarization vector for the seven distinct SPs obtained from DFT (empty symbols) and SARPES (filled symbols) in Au/Ge(111)-($\sqrt{3} \times \sqrt{3}$). Both theory and experiment exhibit rather high and constant values apart from a collapse to zero at SP 1. (b) Representation of the y and (c) x components P_y and P_x of the band-specific spin polarization vector [H6], Copyright (2012) by the American Physical Society.*

of the spin in k-space can be specified for each subband at the respective SPs. In this way, both experimental and theoretical spin polarization vectors become quantitatively comparable. The components P_x, P_y, and P_z of the spin polarization vector are plotted for both subbands $\mathrm{S1_A}$ and $\mathrm{S1_B}$ in dependency of the seven distinct SPs in Fig. 6.17. Inspecting the z component first (a), one notices that both theory and experiment unveil rather high values from SP 7–SP 2. The SARPES deduced P_z ranges from the maximum 0.94 at $\overline{\Gamma}$–$\overline{\mathrm{M}}$ (SP 7) to 0.77 close to the $\overline{\Gamma}$–$\overline{\mathrm{K}}'$ azimuth. Importantly, exactly at the intersection with the $\overline{\Gamma}$–$\overline{\mathrm{K}}'$ line P_z fully collapses to zero. This breakdown occurs in such a small momentum region that its details remain unresolved in SARPES due to k-space averaging. This abrupt change from out-of-plane to in-plane spin vector orientation is validated by the DFT calculations, that even use a higher data point density close to SP 1 in order to grasp more details of the slope region. On the other hand, the y component (b) remains at lower values but increases from SP 4 to SP 1, where it is close to unity. Theory supports this finding, and P_y remains on a low level apart from SP 1 here. Finally, the x component stays low for all SPs, i.e., $P_x \sim 0$–0.5. Theory again validates this view, except of a sign change at SP 1. Here, the spins exhibit strong in-plane rotations close to SP 1, but snap back to an alignment orthogonal to $\mathbf{k}_\parallel$ directly at SP 1. This relaxation of the in-plane spin rotations at the $\overline{\Gamma}$–$\overline{\mathrm{K}}'$ azimuth remains unresolved in the SARPES data due to the inevitable k-space averaging. Nevertheless, this quantitative comparison has proved the general agreement between the experimental and the theoretical spin pattern once more.

The SARPES spin polarization vectors from Fig. 6.17 are finally merged into a 3D plot along the theoretical FS of $\mathrm{S1_A}$ and $\mathrm{S1_B}$ in Fig. 6.18. This plot features the undulating spin characteristics between neighboring FS arcs. In general, it represents a striking

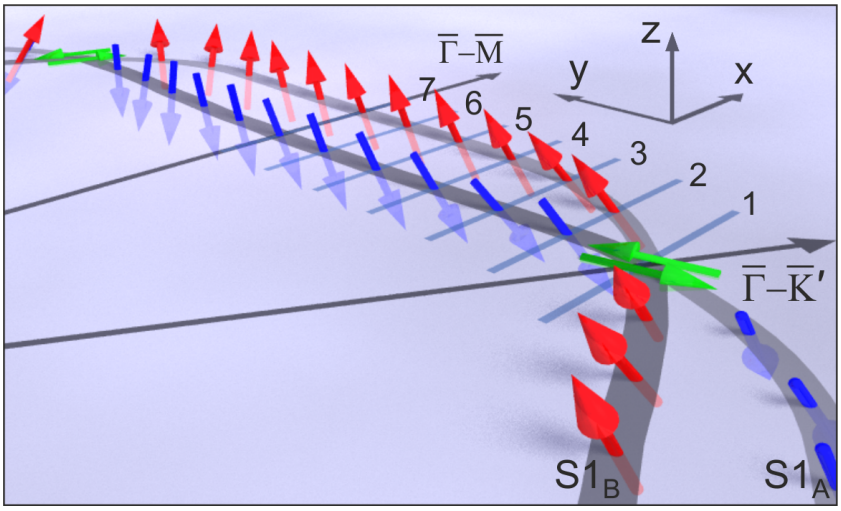

Figure 6.18: *3D plot of the spin pattern derived from the SARPES experiment along the theoretical FS contours $S1_A$ and $S1_B$ in Au/Ge(111)-($\sqrt{3} \times \sqrt{3}$). Orientations of the spin vectors follow the values given in Fig. 6.17 and obey the $C_{3\nu}$ symmetry of the surface. The numbering indicates the SPs [H6], Copyright (2012) by the American Physical Society.*

visualization of the complexity and beauty of the spin texture at the Au/Ge(111)-($\sqrt{3} \times \sqrt{3}$) surface revealed experimentally [H6]. In particular, a radial rotation of the in-plane spin-vector, accompanied by a sizable undulation of the perpendicular spin component, has not been observed before at a semiconductor surface [H6]. Obviously, the specific atomic structure of Au/Ge(111)-($\sqrt{3} \times \sqrt{3}$) must be responsible for such a complex spin pattern. In this regard, it is important to recall that the Au atoms reside at almost the same height as the Ge adatoms, which both form the very edge of the crystal (see Fig. 6.1(b) in Sec. 6.1.1). Thus, one may proceed from the assumption that Au and Ge orbitals will be notably hybridized at the surface. In turn, additional non-perpendicular field gradients intermix with their perpendicular counterpart, and the SOC will depend to some extent on the crystal symmetries of the surface.

As a consequence, the spin orientations of $S1_A$ and $S1_B$ are coupled to the $C_{3\nu}$ symmetry, as has already become visible in the analysis above. In particular, symmetries within the real space structural model are imprinted on the spin landscape in reciprocal space [H6]. As becomes evident from inspection of the surface geometries in Fig. 6.1(a), there exists a mirror symmetric plane along the $\langle \bar{1}\bar{1}2 \rangle$ directions, which are represented by the $\overline{\mathrm{K}}$–$\overline{\Gamma}$–$\overline{\mathrm{K}}'$ azimuth in k-space. However, the $\langle \bar{1}01 \rangle$ directions, which correspond to $\overline{\mathrm{M}}$–$\overline{\Gamma}$–$\overline{\mathrm{M}}$ in reciprocal space, do not feature a mirror symmetry. In a system with non-degenerate states and time-reversal symmetry, the electron spin must be oriented perpendicular to the mirror plane along $\overline{\mathrm{K}}$–$\overline{\Gamma}$–$\overline{\mathrm{K}}'$ [H6]. This requirement is reflected in the spin pattern, where indeed the spin polarization vector lies fully in plane and is orthogonal to the momentum vector along this direction. Combining time-reversal symmetry and the mirror symmetry of the $\overline{\mathrm{K}}$–$\overline{\Gamma}$–$\overline{\mathrm{K}}'$ direction, it follows that the spin of a

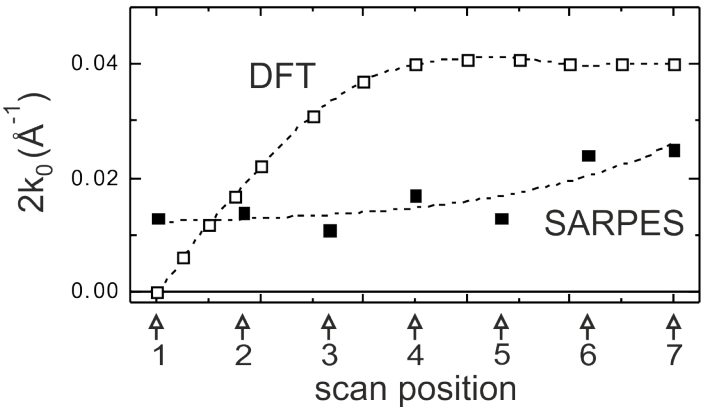

Figure 6.19: *Evolution of the SOI-induced spin splitting $2k_0$ of the S1 state in Au/Ge(111)-($\sqrt{3} \times \sqrt{3}$), derived from DFT and SARPES in dependence of the SP [H6], Copyright (2012) by the American Physical Society.*

non-degenerate state must also be perpendicular to the $\overline{\mathrm{M}}$–$\overline{\Gamma}$–$\overline{\mathrm{M}}$ azimuth. Unlike before, this only concerns the in-plane spin orientation, yet allowing for a non-vanishing z component here, which is in agreement with the results. In addition, it follows from these symmetry requirements that the perpendicular spin component of a particular band, i.e., $\mathrm{S1_A}$ or $\mathrm{S1_B}$, must change its sign between two adjacent FS segments separated by the mirror symmetric $\overline{\mathrm{K}}$–$\overline{\Gamma}$–$\overline{\mathrm{K}}'$ direction. In consequence, the spin topology at the FS is characterized by the undulation of the out-of-plane spin component with threefold symmetry.

An important aspect, which has not been discussed so far, is the strength of the SOI at the Au/Ge(111)-($\sqrt{3} \times \sqrt{3}$) surface. It is usually quantified by the Rashba parameter, which is related to the size of the splitting by Eq. 2.10. Fig. 6.19 compares the splitting in momentum $2k_0$ with respect to the SP at the FS for both theory and experiment. For a large region (SP 7–SP 4) along one straight FS segment the DFT values remain constant at about $0.04\,\mathrm{Å}^{-1}$, and thus overestimate the experimental splitting, which slightly decreases from $0.025\,\mathrm{Å}^{-1}$ at SP 7 to $0.013\,\mathrm{Å}^{-1}$ at SP 1. In approaching the $\overline{\Gamma}$–$\overline{\mathrm{K}}'$ azimuth, the DFT derived splitting gradually decreases to almost zero. The slight discrepancy between experiment and theory found in the region close to $\overline{\Gamma}$–$\overline{\mathrm{K}}'$ can again be attributed to the k-space averaging in experiment, but it also relates to the shortcomings of the DFT. Nevertheless, the deviations remain at an acceptable level and do not contradict the overall good agreement found. On the basis of the largest SARPES derived band splitting at SP 7 and the effective band mass of S1, i.e., $m_e^* = 0.06\,m_e$, the Rashba parameter is calculated as $\alpha_R = 0.10\,\mathrm{eVÅ}$ by use of Eq. 2.10. Obviously, the effect is weaker than at related surfaces (see Tab. 6.1) due to their different atomic structures [202]. As an example, K. Sakamoto *et al.* studied Bi/Si(111)-($\sqrt{3} \times \sqrt{3}$) by SARPES and found a large Rashba splitting of $2k_0 = 0.210\,\mathrm{Å}^{-1}$ [24]. The same authors

also analyzed Tl/Si(111)-(1 × 1) ($2k_0 = 0.4\,\text{Å}^{-1}$) [25]. Both systems involve elements which are heavier than Au and are thus supposed to exhibit a stronger SOC at the surface.

6.3.1 Theoretical modeling of the spin texture

Despite the close analogy between theory and experiment concerning the complex spin texture in Au/Ge(111)-($\sqrt{3} \times \sqrt{3}$), the potential origin of this symmetry related spin configuration remains obscure. A pure Rashba situation, with in-plane spins orthogonal to the momentum vector, can definitely be excluded here. Similarities exist to other systems that exhibit an out-of-plane orientation of the spin polarization vector **P** like the Tl-induced (1 × 1) surface reconstruction on Si(111) [25]. Even an undulation in the z component, that depends on the threefold symmetry at the surface, is found in the surface alloys Bi/Ag(111) and Pb/Ag(111) [22] (see introduction of Sec. 6.3), and in thin film systems composed of multiple MLs of Bi and Pb on top of Si(111) [196, 228]. In close analogy, the insulating system Bi/Si(111)-($\sqrt{3} \times \sqrt{3}$) also exhibits a vertical spin-component which is coupled to the surface symmetries [229]. And finally, it has recently been proposed on the basis of a tight-binding model that the existence of an out-of-plane spin component is a general property in related honeycomb lattices [223]. Yet, up to now there exists no other experimental example of in-plane spin rotations, as observed for Au/Ge(111)-($\sqrt{3} \times \sqrt{3}$) here, and a plausible explanation is still to be delivered.

Assistance in answering this question can be gained by turning to the novel class of 3D topological insulators [226]. Surprising similarities may be found for one of its representatives, i.e., Bi_2Te_3 (see introduction of Sec. 6.3). By means of ARPES it was shown that a single massless Dirac fermion state, centered at the $\overline{\Gamma}$ point, is established in the bulk band gap [230]. By definition its two branches belong to opposite spin directions. Without additional doping the Dirac point is located 0.34 eV below the Fermi level. Yet, the FS topology is highly energy-dependent and turns from warped over hexagonal to round shape upon approaching the Dirac point. The exact location of the Fermi level is controlled by adding Sn atoms as dopants, which then replace the respective amount of Bi atoms in the lattice. Interestingly, the warped and hexagonal FSs of the undoped and slightly doped crystal bear some resemblance to the FS of Au/Ge(111)-($\sqrt{3} \times \sqrt{3}$) [230]. Likewise, the (111) surface of Bi_2Te_3 possesses the $C_{3\nu}$ symmetry, and a recent theoretical study by L. Fu was dedicated to reproduce and understand the FS, the energy dispersions, and the spin texture of Bi_2Te_3 by utilizing the powerful $k \cdot p$ theory [55]. While the general form of the Rashba Hamiltonian in Eq. 2.7 reproduces the isotropic shape of the Dirac fermion state, L. Fu found that it is necessary to introduce a third-order term in k to the $k \cdot p$ Hamiltonian in order to accurately model the FS warping away from the Dirac point. Since this additional term couples to the z spin Pauli matrix, it was concluded that momentum-dependent out-of-plane spin orientations, i.e., those obeying the $C_{3\nu}$ symmetry, must exist along the

FS. This has been validated in a SARPES experiment [28], where it was also shown that the theoretically determined P_z values exceed their experimental counterparts, like it is the case in Au/Ge(111)-($\sqrt{3} \times \sqrt{3}$). In a subsequent *ab initio* study by S. Basak *et al.* in-plane *spin rotations* away from an orthogonal orientation of the spin and momentum vectors were found in between the $\overline{\Gamma}$–$\overline{\mathrm{M}}$ and $\overline{\Gamma}$–$\overline{\mathrm{K}}$ high symmetry directions [see Fig. 6.13(b)] [27]. These could only be reproduced by introducing a fifth-order in k "Dresselhaus" term to their $k \cdot p$ Hamiltonian. That study is thus the first to predict a spin pattern of similar complexity as the one found for Au/Ge(111)-($\sqrt{3} \times \sqrt{3}$) in this thesis. It was even claimed that the necessity for the fifth-order SOC term in k is not restricted to topological insulators alone, but is a *"generic property of surface states in strong spin-orbit coupling materials"* [27], where the electron spin must not be supposed to be orthogonal to the momentum vector as a rule. In addition to these highly relevant results, also other studies have discussed the importance of higher order SOC terms to correctly model such complex spin textures [224, 225, 231].

With these striking similarities at hand, it seems conclusive to adopt the model Hamiltonian

$$\mathcal{H}(k) = E_0(k) + v(k_x\sigma_y - k_y\sigma_x) + \lambda(k_+^3 + k_-^3)\sigma_z + i\zeta(k_+^5\sigma_+ - k_-^5\sigma_-), \qquad (6.1)$$

proposed by L. Fu and extended to fifth-order in k by S. Basak *et al.*, with the intention to reproduce the Au/Ge(111)-($\sqrt{3} \times \sqrt{3}$) FS in Fig. 6.14 [27, 55, H6]. The Hamiltonian is invariant under time-reversal and $C_{3\nu}$ symmetry operations [H6]. $E_0(k)$ describes the degenerate parabolic band dispersion with circular shape at the FS. σ_x, σ_y, and σ_z are the Pauli spin matrices, v, λ, and ζ are k-dependent fit parameters, and $k_\pm = k_x \pm ik_y$, $\sigma_\pm = \sigma_x \pm i\sigma_y$. The second term in Eq. 6.1 is the analog to the Rashba Hamiltonian in Eq. 2.7. It possesses the full $O(2)$ symmetry and leads to a spin splitting which is isotropic in momentum. This is reflected in the spin pattern of the resulting surface of constant energy, i.e., the spins are planar, vortical, and orthogonal to the in-plane momentum vector. Contrary, the third term reduces the rotational symmetry to the $C_{3\nu}$ symmetry. It describes the hexagonal warping of the FS and introduces the out-of-plane undulation of the spin polarization vector. This vertical spin component alternates from downward to upward orientation between the adjacent hexagonal segments of the constant energy surface. Up to this point, the in-plane spin components remain unaffected, and the spin vector is still orthogonal to the momentum vector at each location along the energy contours. This changes by introducing the final term of fifth-order in k, which correctly models the planar rotations of the spin in the Dirac fermion state, predicted to occur in between high symmetry directions by the *ab initio* calculations [27]. While it also contributes to the warping of the energy contours, like already realized by the term of third-order in k, it mainly introduces the rotation of the in-plane spin components to a more radial orientation. Both last two terms in Eq. 6.1 have the lowest possible order in k that still maintains the $C_{3\nu}$ symmetry. This is a prerequisite to adopt this Hamiltonian and apply it to the Au/Ge(111)-($\sqrt{3} \times \sqrt{3}$) system.

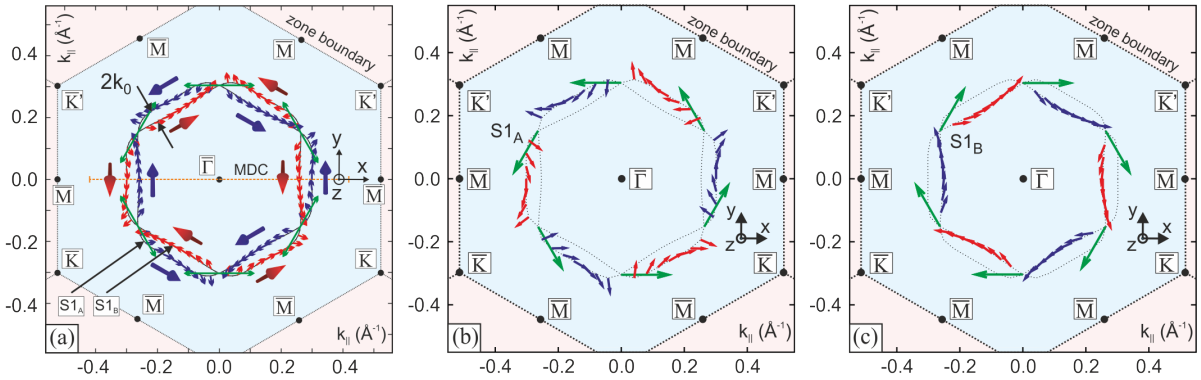

Figure 6.20: *(a) FS of the S1 surface state in Au/Ge(111)-($\sqrt{3}\times\sqrt{3}$) from DFT calculations, replotted from Fig. 6.14. (b) FS of the outer and (c) inner S1 contours $S1_A$ and $S1_B$ obtained from fitting the* ab initio *FS in (a) with Eq. 6.2. The arrows correspond to the length and orientation of the in-plane component of the spin polarization vectors. Red (blue) color signifies an additional perpendicular component directed out of (into) the surface plane. For green arrows no z spin component exists [H6], Copyright (2012) by the American Physical Society.*

Modeling the band shape and the spin pattern in Au/Ge(111)-($\sqrt{3}\times\sqrt{3}$) with neglection of the whole dispersion, i.e., at E_F only, allows to drop the k dependency in the fit parameters v, λ, and ζ. This is a reasonable approximation, since the main interest lies within the spin texture directly at E_F, where the relevant physics take place, and comparability with the *ab initio* calculations and the experiment is given. Fitting the band structure obtained by the DFT calculations, and replotted in Fig. 6.20(a), leads to a quite exact reproduction of both the FS shape and the spin texture. It also turns out that the ratio between v and λ determines the strength of FS deformation from circular to hexagonal or warped form due to the cubic Dresselhaus term. The hexagonal warping itself is introduced by the last two terms in the Hamiltonian in Eq. 6.1, and it is thus coupled to the SOIs. Yet, this is not the case in Au/Ge(111)-($\sqrt{3}\times\sqrt{3}$), where the hexagonal FS contours are primarily induced by the crystal symmetry alone, as evidenced by the DFT calculations. Consequently, the *ab initio* FS is already hexagonally deformed without inclusion of SOIs. Therefore, it is plausible to account for the FS deformation already by a spin-independent term, that needs to be added to the Hamiltonian. This leads to the modified form

$$\begin{aligned}\mathcal{H}(k) &= \left[\tfrac{\hbar k^2}{2m_e^*} - C + c_h(k_+^6 + k_-^6)\right]\sigma_0 \\ &\quad + v(k_x\sigma_y - k_y\sigma_x) + \lambda(k_+^3 + k_-^3)\sigma_z + i\zeta(k_+^5\sigma_+ - k_-^5\sigma_-),\end{aligned} \tag{6.2}$$

which is of lowest order in k and preserves both time-reversal and $C_{3\nu}$ symmetry [H6]. Therein, C and c_h are k-independent constants, and σ_0 is the spin identity matrix. In contrast to Eq. 6.1, the terms in brackets, which act on σ_0, already reproduce the hexagonal shape of the FS accurately for spin degenerate states. The sixth-order term leads to the hexagonal warping here. Contrary, the last three terms are needed to correctly

Table 6.6: *Best parameters obtained from fitting the DFT FS of Au/Ge(111)-($\sqrt{3}\times\sqrt{3}$) in Fig. 6.20(a) with the model Hamiltonian given in Eq. 6.2. For comparison, experimentally derived values are given in brackets.*

m_e^* (m_e)	C (eV)	c_h (eVÅ^6)	ν (eVÅ)	λ (eVÅ^3)	ξ (eVÅ^5)
0.4 [0.06]	0.77 [$E - E_F = -1.0$]	70	-0.1 [$\alpha_R = 0.1$]	-7	5.5

introduce the SOI. The DFT FSs of $S1_A$ and $S1_B$ are then fitted with Eq. 6.2, until a reliable reproduction of both shape and spin pattern is obtained. The fit parameters extracted for the most accurate fit at $E = 0$, which is shown in Fig. 6.20(b) and (c), are listed in Tab. 6.6. In comparing the fitted FSs with the one obtained from DFT (a), an outstanding agreement is found, which demonstrates the applicability of Eq. 6.2 to model the complex spin dependency in the FS of Au/Ge(111)-($\sqrt{3} \times \sqrt{3}$). In this context, it is not surprising that the modulus of the fit parameter $v = -0.1$ eVÅ, which corresponds to the Rashba parameter α_R (see Eq. 2.7), does exactly agree with the value found in SARPES. However, the electron effective mass m_e^* is higher than derived experimentally, which might be related to the fact that the fitting is an approximation to the DFT and not to the experiment. This does also become evident in the S1 band minimum in the DFT, which agrees well with the parameter C in Eq. 6.2.

7 Collinear antiferromagnetic order in a triangular lattice

Triangular lattices have provoked intense research activities in the past, since they suffer from *geometric frustration* and may exhibit strong *electronic correlations* at the same time. In case that a single electron is located at each lattice site, we deal with a spin 1/2 Heisenberg AF on a triangular lattice. Here, *spin frustration* cancels any long-range collinear AFM spin ordering (cf. Fig. 2.4). However, it has been suggested that the ground state of such triangular systems may develop a 120 ° Néel AFM order [70], which further reduces the surface energy. Alternatively, P. W. Anderson proposed that the state of lowest energy should be a resonant valence bond (RVB) state [15]. This is the ground state of a QSL [232], where quantum fluctuations prohibit the development of an ordered phase even at lowest temperatures. Nevertheless, the interplay of spin frustration and correlations is not only a theoretical construct, but is assumed to play a prominent role in experimental systems as, e.g., κ-(BEDT-TTF)$_2$Cu$_2$(CN)$_3$ with a possible QSL ground state [233, 234], κ-(BEDT-TTF)$_2$X as a magnetic Mott insulator relevant for the superconducting behavior found in this system [235], and $Na_xCoO_2 \cdot yH_2O$ a further magnetic Mott insulator with potential topological superconductivity [236].

This chapter addresses the role of electronic correlations and its interplay with geometrical frustration in 2DESs, induced by the deposition of group-IV adatoms onto the (111) oriented semiconductor surfaces of Si and Ge. In particular, the delicate choice of the adatom-substrate composition allows to tune characteristic intrinsic properties, such as the on-site and inter-site Coulomb repulsions, the exchange interaction, and the degree of charge carrier localization. This last-mentioned property is highly influenced by the adatom species and its orbital character. Here, the huge variety of 2DESs must be intersected into the high adatom (dense phases) and the low adatom (dilute phases) coverage regime. The first class of systems is usually less correlated, with a layer thickness equal to or exceeding 1 ML. In consequence, such surfaces will not be discussed in detail here. In contrast, correlations are of significant relevance in the dilute regime, established at 1/3 ML adsorbate coverage, where electron localization is strongly enhanced due to the larger adatom spacing ($\sim$ 6–7 Å). Here, usually a $(\sqrt{3} \times \sqrt{3})$ surface reconstruction is stabilized by reducing the number of DB orbitals compared to the pristine substrate surface. The remaining half-filled orbitals are mostly of p_z type with a strong lateral confinement, which further enhances electronic correlations [14]. In consequence, a narrow half-filled surface state develops, which is sensitive towards instabilities as, e.g., the electron-phonon and the electron-electron interaction [14]. Such

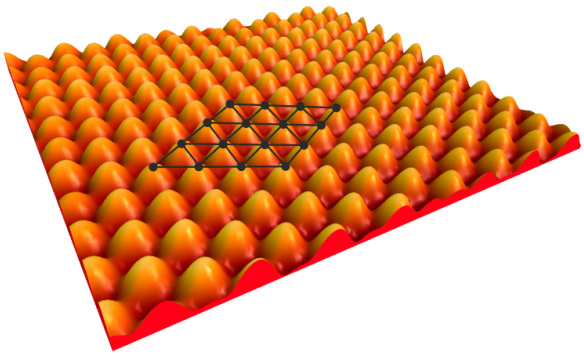

Figure 7.1: *3D plot of the Sn/Si(111)-($\sqrt{3} \times \sqrt{3}$) surface seen in filled states STM data (bias: -1.0 V, 0.5 nA), artificially augmented by auto-correlation of a defect-free ordered area. Maxima correspond to the positions of single Sn atoms at the surface. The overlaid mesh serves to illustrate the* triangular lattice *realized in Sn/Si(111)-($\sqrt{3} \times \sqrt{3}$).*

conditions may represent the basis to stabilize an insulating ground state as described in the *Mott-Hubbard model* (cf. Sec. 2.2). Moreover, the dilute adatom systems do not only serve as a template for the study of strongly correlated phenomena, but also represent an experimental realization of a triangular lattice (see Fig. 7.1).

In order to understand the mechanisms behind the variety of reported phase transitions and ground states, it will be crucial to scrutinize the competition of electronic and structural instabilities. In addition, different symmetries and disorder will be critical here. These key issues will be addressed in the following sections.

7.1 Electronic correlations in two-dimensional electron systems at surfaces

7.1.1 Prototypical two-dimensional Mott-Hubbard insulators at surfaces

Several prototypical surface systems have been studied in order to elucidate their potentially strong electronic correlations. Among these, two prime examples of Mott-Hubbard physics in two dimensions shall be introduced in the following.

K/Si(111)-B-($\sqrt{3} \times \sqrt{3}$)

A well known representative is K/Si(111)-B-($\sqrt{3} \times \sqrt{3}$), being closely related to the adatom systems which are subject of the present thesis. Its atomic structure can be understood as an ideally truncated Si(111) crystal with a complete bilayer on top. In the lower part of the bilayer every third silicon atom is replaced by a boron one. Directly above, i.e., at the T_4 adsorption sites, a potassium atom is found. In all, this gives rise

to a $(\sqrt{3} \times \sqrt{3})$ reconstruction, as shown in Fig. 7.2(a). The electronic properties of this system have first been calculated within the LDA, predicting a half-filled metallic band [237]. Surprisingly, H. H. Weitering *et al.* revealed that this is actually not the case, by combining k-resolved inverse photoelectron spectroscopy (KRIPES) and ARPES [12]. Here, the presence of two weakly dispersing ($\sim 0.2\,\mathrm{eV}$), thus strongly localized surface states S_1 and S_2 was evidenced in unoccupied and occupied states, respectively [see band dispersion in Fig. 7.2(c) along the symmetry direction indicated in (b)]. These bands possess an almost $k_{\|}$-independent spacing of 1.3 eV at RT, which has been interpreted as the effective on-site Coulomb repulsion U_{eff}, with S_1 consequently being the UHB and S_2 the LHB. In other words, a *correlation-induced band gap* is reported here, whose actual size, the conductivity gap, is much smaller ($\sim 0.1\,\mathrm{eV}$ at RT) due to a phonon mediated vibrational band broadening mechanism [12]. Importantly, these findings entail that local magnetic moments exist at the K adsorption sites, which should couple antiferromagnetically. However, as we deal with a triangular lattice here, spin frustration is present. In consequence, the authors proposed K/Si(111)-B-$(\sqrt{3} \times \sqrt{3})$ to represent the first experimental realization of a 2D triangular lattice AFM Heisenberg system [12].

More recently, a novel $(2\sqrt{3} \times 2\sqrt{3})$ ordering at LT has been observed in LEED and STM on the same surface [238]. Its electronic character is explained as a bipolaronic insulating phase [238], contrary to the correlated Mott-Hubbard state. These contradictory findings are most probably related to the difficulty in determining the exact

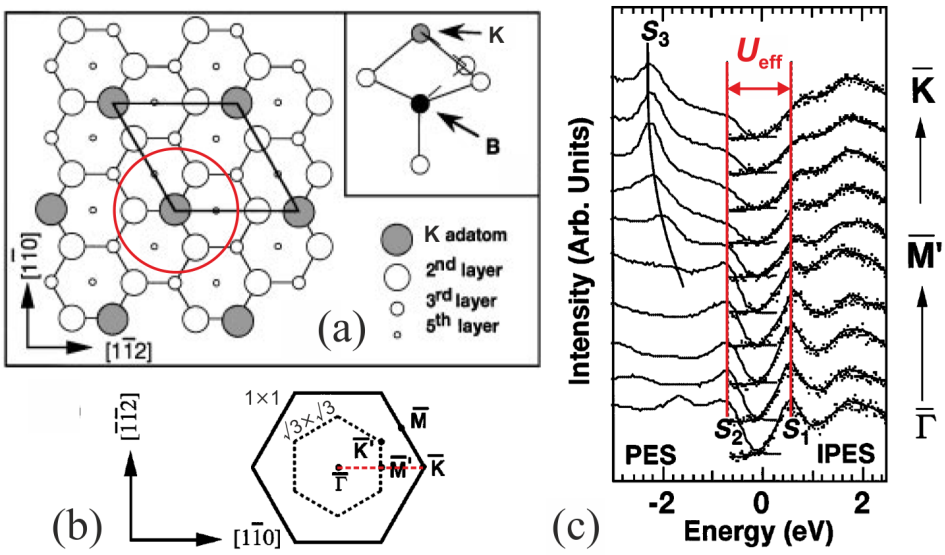

Figure 7.2: *(a) Structural model of K/Si(111)-B-$(\sqrt{3} \times \sqrt{3})$ in top view representation, with the parallelogram indicating the unit cell. The inset (side view) highlights atomic geometries from the first to the fourth layer around one adsorption site (red circle). (b) SBZ scheme indicating the (inverse) photoemission scan direction in (c). (c) ARPES and KRIPES spectra along the dashed line in (b). The spectral features S_1 and S_2 (UHB and LHB) are approximately spaced by U_{eff} for all in-plane momenta. All figures are taken from [12], Copyright (1997) by the American Physical Society.*

potassium coverage at the surface [239]. In this regard, it has recently been observed that a slightly larger amount of K atoms, i.e., 1/2 ML instead of 1/3 ML, induces a $(2\sqrt{3} \times 2\sqrt{3})$ surface reconstruction, which involves a large perpendicular distortion of Si adatoms [240]. The new structural order and the concomitant electronic properties are best compatible with a band insulator, whereas electronic correlations are discarded here [240]. Thus, it turns out that the precise control of the alkali atom coverage is essential to tune the electronic properties in the K/Si(111)-B surface system.

6*H*-SiC(0001)-$(\sqrt{3} \times \sqrt{3})$

A second example is 6*H*-SiC(0001)-$(\sqrt{3} \times \sqrt{3})$, whose geometrical structure is quite similar. For the 6*H* polytype the lattice consists of silicon atoms in fourfold diamond type coordination with carbon atoms, as it is shown in Fig. 7.3(a). The top bilayer is composed of a lower C lattice and an upper Si lattice. On top, silicon adatoms occupy each third T_4 adsorption site, and therefore induce a $(\sqrt{3} \times \sqrt{3})$ surface reconstruction. By applying *ab initio* DFT calculations as a first approach to the electronic band structure of this system, one also derives a half-filled surface state [241], which would imply metallic behavior. However, further scrutiny by ARPES [242] and KRIPES [243] experiments contradicts this first guess, and instead unveils the existence of two distinct spectral features, interpreted as LHB and UHB at $E - E_F = -1.3\,\text{eV}$ and $E - E_F = +1.0\,\text{eV}$, respectively, see Fig. 7.3(b). These peaks in the DOS were also seen in STS at $E - E_F = -1.1\,\text{eV}$ and $E - E_F = +0.9\,\text{eV}$ [13], and in consequence regarded as a further validation of an impressively large Mott insulating band gap ($U \geq 2.0\,\text{eV}$), that already exists at RT.

Together with K/Si(111)-B-$(\sqrt{3}\times\sqrt{3})$, this system belongs to the group of *undistorted and triangular* wide gap Mott insulators, established at an isoelectronic semiconductor

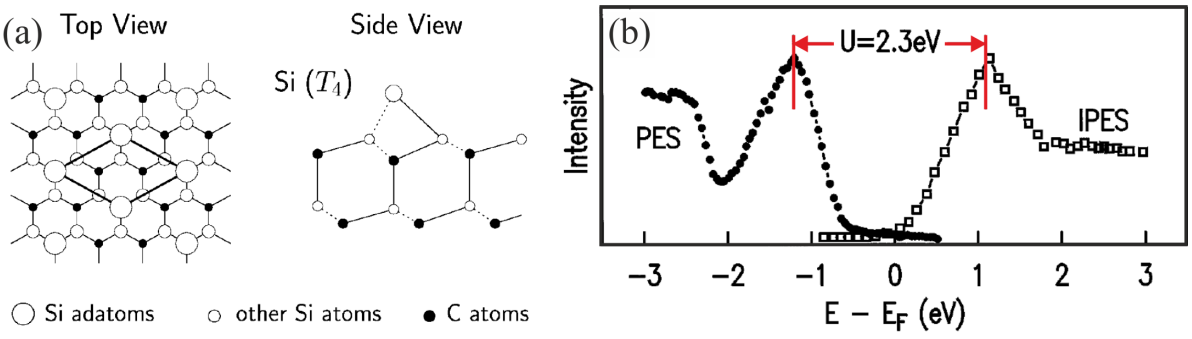

Figure 7.3: *(a) Structural model of 6H-SiC(0001)-$(\sqrt{3} \times \sqrt{3})$ in top view (left) and side view (right) representation. Si adatoms at T_4 adsorption sites generate an overall $(\sqrt{3} \times \sqrt{3})$ surface reconstruction (unit cell indicated by the parallelogram); figure taken from [72], Copyright (1999) by the American Physical Society. (b) Momentum-integrated electronic band structure from both PES and IPES with two prominent spectral features at $E - E_F = -1.3\,\text{eV}$ and $E - E_F = +1.0\,\text{eV}$ divided by U; figure taken from [13], Copyright (1999) by the American Physical Society.*

surface. Here, one deals with a Coulomb repulsion larger than the bandwidth, i.e., $U > W$, in the presence of spin frustration, which ends up in a *non-collinear* AFM spiral SDW insulating ground state [14]. While the charge carriers are uniformly distributed here, the spin ordering induces a magnetic SBZ of (3×3) periodicity. In addition, it would be interesting to study correlations in these surfaces also by novel many-body techniques that include interactions beyond the nearest-neighbor lattice sites, as provided by, e.g., the LDA+DCA, which was also utilized in this thesis (see Secs. 7.2.4 and 7.2.5). This would allow to investigate the details of electronic and magnetic interactions at a more precise level here.

7.1.2 Two-dimensional surface reconstructions of group-IV adatoms on Si(111) and Ge(111)

A further class of 2DESs of significant relevance are Si(111) and Ge(111) surfaces covered by 1/3 ML of lead or tin. The early reports on a transition from a metallic $(\sqrt{3} \times \sqrt{3})$ phase at RT to a LT (3×3) phase in α-Pb/Ge(111), and soon after also in α-Sn/Ge(111),[1] have attracted much attention in the solid state physics community [40, 209]. Despite the manifold of available experimental and theoretical studies, it is not yet understood completely which exact mechanisms stand behind these transitions. Yet, it is clear that the half-filled surface state in the metallic phase must play a dominant role here, while the absence of a pronounced nesting in the FS queries the possibility of an insulating CDW ground state. Instead, it seems plausible that significant electron-electron repulsions will favor a Mott insulating or a SDW phase [14], where a corrugation of the surface is negligible. This would resemble the cases of the 2D Mott insulators K/Si(111)-B-$(\sqrt{3} \times \sqrt{3})$ and 6H-SiC(0001)-$(\sqrt{3} \times \sqrt{3})$, introduced before. In Tab. 7.1 the different phases of the four relevant systems Pb/Ge(111), Pb/Si(111), Sn/Ge(111), and Sn/Si(111) are listed with respect to the corresponding critical temperatures. They all have the $(\sqrt{3} \times \sqrt{3})$ reconstruction as common RT phase which is described by the structural model depicted in Fig. 7.4(a). Adatom adsorption takes place on top of the ideally truncated (111) surface which is completed by a full bilayer. Here, each third T_4 adsorption site is occupied by a tin or lead adatom, thereby saturating three DBs from the substrate. Since all adatoms are located at the same height [see side view representation in Fig. 7.4(b)], no larger unit cell than $(\sqrt{3} \times \sqrt{3})$ is needed to account for the periodic structures at RT. Concerning the electronic band structure, simple electron counting may serve as a starting point to catch a glimpse at the conducting behavior. The single tin or lead atom in the $(\sqrt{3} \times \sqrt{3})$ unit cell provides 4 electrons, and the DB orbitals from the substrate contribute three charge carriers [cf. Fig. 7.4(a)]. Therefore, one gains a total of seven electrons per unit cell, which is followed by the conclusion that the electronic properties

[1] The prefix α denotes the dilute, i.e., 1/3 ML coverage, phase of group-IV adatoms on Si(111) and Ge(111). As most parts of this chapter deal with α-phase 2DESs, the prefix will be omitted for simplicity wherever possible.

Table 7.1: *Different phases of the dilute, i.e., α-phase, Pb- and Sn-induced 2DESs on Ge(111) and Si(111) in dependence of the temperature T. The respective conducting behavior is given in parentheses (met:* metallic, *ins:* insulating*). A backfolding (BF) of the surface state related to a* (3×3) *symmetry, if observed in ARPES, is indicated also.*

T (K)	Pb/Ge(111)	Pb/Si(111)	Sn/Ge(111)	Sn/Si(111)
300	$(\sqrt{3} \times \sqrt{3})$ (met)	$(\sqrt{3} \times \sqrt{3})$ (met)	$(\sqrt{3} \times \sqrt{3})$ (met)	$(\sqrt{3} \times \sqrt{3})$ (met + BF)
< 250	(3×3) (met + BF)			
< 210			(3×3) (met + BF)	
< 86		(3×3) (met)		
< 76	glassy (met)			
< 60				$(\sqrt{3} \times \sqrt{3})$ (ins + BF)

at the surface should be governed by a half-filled metallic band.

C/Si(111)-$(\sqrt{3} \times \sqrt{3})$

Before turning to the lead- and tin-induced reconstructions, the C/Si(111)-$(\sqrt{3} \times \sqrt{3})$ surface should be mentioned first [244]. Its band structure is again predicted to be dominated by a half-filled metallic band, residing in the bulk band gap. This 2DES is suggested to exhibit an electronically induced phase transition to a distorted (3×3) ground state, characterized by two distinct sublattices due to a vertical distortion of the carbon atoms. Moreover, band energy and electron correlations arrange in a favorable way to stabilize a unique kind of ground state in a 2D surface system, i.e., a delicate equilibrium between distortion, magnetic order, and insulating behavior is realized at the same time. In turn, it is proposed that the C/Si(111)-$(\sqrt{3} \times \sqrt{3})$ surface comprises features from both the undistorted magnetic Mott-Hubbard insulators K/Si(111)-B-$(\sqrt{3} \times \sqrt{3})$ and $6H$-SiC(0001)-$(\sqrt{3} \times \sqrt{3})$, as well as from (3×3) distorted metallic phases like those in Pb/Ge(111) and Sn/Ge(111) (see following paragraphs). Finally, it is claimed that this surface would represent the 2D counterpart of the Mott insulator and CDW model system $1T$-TaS_2 [245]. Experimental studies are rare so far, and it remains in intriguing task to uncover these fascinating properties by various techniques.

Pb/Ge(111)

Pb/Ge(111) was the first system of the group-IV quartet which moved into the focus of broad scientific interest. Below $T_{c,1} = 250\,\mathrm{K}$, J. M. Carpinelli *et al.* observed a transition from a plane $(\sqrt{3} \times \sqrt{3})$ order to a distorted (3×3) lattice in STM [40]. The complementary appearance of protrusions in the charge density between filled and empty states was interpreted in terms of a CDW formation at reduced temperatures. In consequence, this was claimed as the first experimental observation of a surface CDW phase transition, triggered by FS nesting. The distorted ground state was suggested

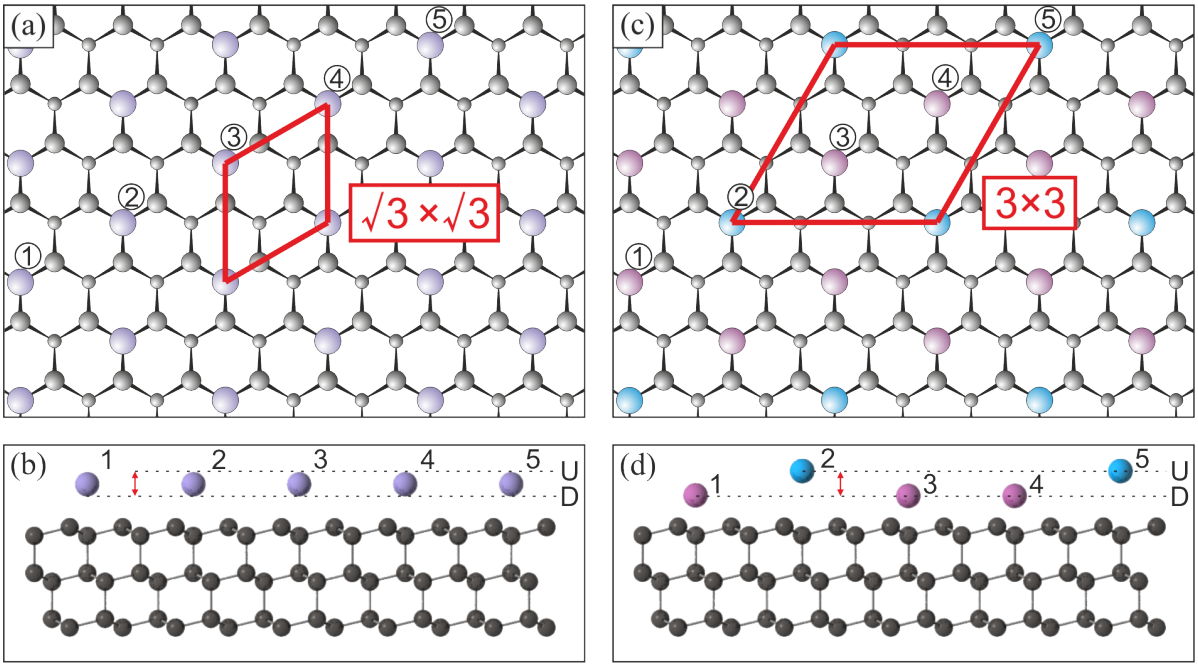

Figure 7.4: *(a) Schematic representation of the atomic geometries in the dilute α-($\sqrt{3} \times \sqrt{3}$) RT configuration of Pb/Ge(111), Pb/Si(111), Sn/Ge(111), and Sn/Si(111) in top view. Purple spheres correspond to Sn (Pb) adatoms, and gray spheres depict substrate atoms in first and second layer. (b) Side view representation along the adatoms labeled 1–5 with the substrate shown down to the sixth layer. All adatoms reside at the same height. (c) Top view of the distorted LT phase with two (pink) out of three adatoms per (3×3) unit cell at a lower height than the third one (blue) (1U2D configuration). (d) Respective side view representation along the adatoms (1–5) with the two stable perpendicular positions "U" and "D". Atom sizes and distances are not to scale in all drawings.*

to be stabilized by electronic correlations, and it has been proposed that even intersite Coulomb repulsions should play a role here [14]. Compatible with such a picture, the opening of an electron correlation energy gap ($E_{\mathrm{gap}} \sim 0.065\,\mathrm{eV}$ at $T = 100\,\mathrm{K}$) was observed in electron energy loss spectroscopy (EELS) [40]. The findings above were substantiated by means of LEED and *ab initio* calculations [40]. In contrast to the CDW system $1T$-TaS_2, correlations were claimed to be a pure consequence of the CDW and not an inherent property of this system.

However, it did not take long until the CDW nature of this transition was doubted. Although FS nesting would agree with a (3×3) lattice reordering, and this is an essential prerequisite for the CDW formation [36], only small sections of the FS are actually well nested, as pointed out by ARPES experiments [246] and susceptibility calculations [14]. Moreover, the electronic band structure in ARPES is not very reminiscent of a highly correlated electron system [246] and was even proved to be metallic in the LT phase against the conclusions drawn by J. M. Carpinelli and coworkers [247]. As a further detail, not resolved before, the p_z type surface state consists of two distinct subbands [246], which are present in the ARPES spectra of both the RT ($\sqrt{3} \times \sqrt{3}$) the LT (3×3)

phase [247]. The only notable differences in the band structure are a more pronounced subband splitting of the surface state at LT and a band backfolding corresponding to the new (3×3) symmetry, yet, the surface remains metallic [246, 247]. The close analogy between the ARPES band structure at RT and LT suggests that both phases should base on the same atomic structures, and the phase transition should be rather a consequence of thermal disordering [247]. Finally, SXRD provided crucial evidence of a buckling of the surface with two out of three Pb atoms located $\sim 0.4\,\text{Å}$ below the third one at LT [248]. This finding argues in favor of a pure structural phase transition to a distorted ground state, being *"stabilized by a gain in electronic energy"* [248]. In conclusion, and contrary to the undistorted magnetic Mott insulators K/Si(111)-B-$(\sqrt{3} \times \sqrt{3})$ and $6H$-SiC(0001)-$(\sqrt{3} \times \sqrt{3})$, Pb/Ge(111) is a less correlated 2DES [14].

Much later (in 2005) a second phase transition in Pb/Ge(111) at $T_{c,2} = 76\,\text{K}$ was reported, which turned the distorted (3×3) phase to a disordered one, described as glassy [249, 250]. This new LT phase was argued to originate from competing interaction forces, relevant at different length scales, that lead to a lack of long-range order [250]. Yet, the nature of this ground state is still under dispute, since it has been proposed that the glassy phase was just a product of hindered surface conductivity at LT [251], which results in a strong bias dependency in STM images, suggestive of disorder.

Sn/Ge(111)

A further closely related representative is the isovalent Sn/Ge(111) surface, which also aggregates in a $(\sqrt{3}\times\sqrt{3})$ reconstruction at RT [252]. Likewise, it features a temperature-induced and fully reversible phase transition to a (3×3) LT phase upon cooling below $T_c = 210\,\text{K}$ [209]. Also in Sn/Ge(111) a complementary appearance of protrusions in the charge density between filled and empty states was found in STM [209]. Therefore, Sn/Ge(111) was proposed as a second example of a CDW, stabilized by correlations in the LT phase [209, 253]. Interestingly, on the basis of EELS, ARPES, and STS it was revealed that both phases are metallic [209, 254, 255], in disagreement with a MIT. The FS is not well nested, since its shape is rather curved, and parallel sections are absent [14, 209]. Moreover, it is also not commensurate with any lattice superstructure. In consequence, FS nesting was no more supposed to play a role in this transition [209]. This makes a CDW rather unlikely for describing the $(\sqrt{3} \times \sqrt{3}) \rightarrow (3 \times 3)$ phase transition in Sn/Ge(111). Instead, a variety of alternative driving mechanisms have been proposed in the literature. Among these, it has been suggested that the phase transition should be due to the softening of a surface phonon [256], a charge disproportionation [257], or defect-controlled density waves [258–260]. Especially the latter scenario has been defended by some authors for a while against the contradictory results presented by others. It was argued that CDW domains are pinned by point defects, with three different domains existing. These should be related to the registry of the respective pinning center (defect). It was further argued that the defect locations are not arbitrarily distributed at LT, but rather display a kind of short-range relation

[258]. At RT, defect hopping occurs, that annihilates the CDW phase. Others discarded such a prominent role of defects [247], and also the relevance of electronic correlations was severely doubted [254, 255].

A possible explanation could be found in the electronic band structure close to the Fermi level in ARPES. Similar to the bands in Pb/Ge(111), two weakly dispersing surface states at an almost constant spacing in energy are observed close to E_F [see Fig. 7.5(a)], while the lower binding energy one even crosses the Fermi level [261]. Moreover, indications of a band backfolding with respect to the (3×3) SBZ symmetries exist at LT in both surface states, yet, metallicity is preserved at all temperatures. Interestingly, this metallic state is split into two separate subbands both in the LT (3×3) and in the RT $(\sqrt{3} \times \sqrt{3})$ phase [261]. A second and even more crucial point in Sn/Ge(111) is the existence of two distinct components (intensity ratio 1:2) in the Sn 4*d* core level line shape [254, 261]. Thus, both valence and core level photoemission data are suggestive of two different bonding environments of the Sn adatoms. On this basis, J. Avila *et al.*, who denied the occurrence of a CDW, introduced a new model, the so-called "dynamical fluctuation model", which agrees with an order-disorder transition and correctly reflects the diverse aspects of the phase transition in Sn/Ge(111) [254]. In this sense, the $(\sqrt{3} \times \sqrt{3})$ structure at RT is the disordered state of the LT (3×3) phase.

The dynamical fluctuation model

The dynamical fluctuation model is similar to what is known for the Si(001) surface, that exhibits a phase transition from a RT (2×1) to a LT $c(4 \times 2)$ phase. The RT configuration originates from asymmetrically buckled surface dimers, that perform a thermally activated *flip-flop* motion [95, 262]. In a "slow" technique, such as STM, which operates at a frequency orders of magnitude below that of the flip-flop oscillation, the imaged height contrast is a time average, with all dimers displayed at a mean height. Thus, the dimers appear to be symmetric, and the buckling remains hidden. However, by recording current traces in STM, the frequency of perpendicular atom oscillations becomes resolvable. In this mode the tunneling tip is positioned directly above an atom, with the feedback loop switched off. This means that the tip remains at a fixed perpendicular position, while the tunneling current is recorded for a given time interval. Hence, any change in the tunneling current must originate from a shift in perpendicular position of the atom. For the Si(001) surface dimers, a reduction of the oscillation frequency upon temperature lowering was indeed observed in this way [262].

In turning back to Sn/Ge(111), the dynamical fluctuation model assumes the Sn adatoms to fluctuate rapidly between two stable vertical positions at RT [up "U" and down "D", see Fig. 7.4(a) and (b)], and in average a $(\sqrt{3} \times \sqrt{3})$ periodicity is seen in STM [254]. For sufficiently reduced temperatures, these motions may freeze out, and the adatoms will be pinned to one of the two stable vertical sites. This ends up with two out of three adatoms at a "D" position and the third one at an "U" position, the so-called "one up two down" (1U2D) configuration [Fig. 7.4(c) and (d)],

which is energetically more stable than the competing 2U1D ordering [257]. It shall be mentioned as a side note here that even the down atoms show a little perpendicular displacement, which is rather hard to resolve [255, 263]. In consequence, with frozen vertical fluctuations, STM reveals a (3×3) reconstruction at LT. Here, the current trace recording technique has been exploited to probe the validity of the dynamical fluctuation model, and indeed, a smaller oscillation frequency at reduced temperatures is observed [264]. Accordingly, the $(\sqrt{3}\times\sqrt{3})$ reconstruction at RT should be interpreted as a mingled phase of fast fluctuating (picosecond timescale), randomly distributed, but local (3×3) configurations which suffer from a lack of long-range order [247]. Thus, the fast method XPS (subfemtosecond timescale) still observes two components in the Sn $4d$ levels at RT, while LEED requires long-range ordered structures and fails to detect a (3×3) superstructure. Also a corresponding band backfolding in ARPES is not expected to be observed at RT for the same reason [247]. Further evidence for the validity of the dynamical fluctuation model is provided by a combined study including STM, STS, and *ab initio* methods [255]. The order-disorder character of this transition is supported by x-ray standing waves (XSW) [265], SXRD [252], and photoelectron diffraction (PED) experiments up to $T = 500\,\mathrm{K}$ [266], which evidence the corrugation in the Sn layer to be present throughout a large temperature range above the transition temperature $T_c = 210\,\mathrm{K}$ [266]. The lateral height difference between up and down Sn atoms is specified as $\sim 0.3\,\text{Å}$ [266], which does well agree with a theoretical estimate of $0.35\,\text{Å}$ [254].

The ground state of Sn/Ge(111)

Despite the manifold of diverse studies on Sn/Ge(111), it was not before 2006 that R. Cortés *et al.* reported a second reversible phase transition at $T_c = 30\,\mathrm{K}$ back to a $(\sqrt{3}\times\sqrt{3})$ reconstruction, by utilizing LEED and STM [267]. The structural change was found to be accompanied by the opening of a band gap ($E_{\mathrm{gap}} \sim 60\,\mathrm{meV}$ at $T = 15\,\mathrm{K}$) seen in ARPES, which is reprinted in Fig. 7.5(a). This turns the system from metallic to insulating. The new LT phase was attributed to a magnetic, undistorted Mott insulating ground state by LDA+U calculations [16]. A CDW type phase transition was excluded due to the higher periodicity of the LT $(\sqrt{3} \times \sqrt{3})$ SBZ and due to the specific shape of the insulating band in ARPES, which does not agree with a CDW related band backfolding picture. Instead, the rather uniform reduction of spectral weight at E_F in momentum space was interpreted as a signature of a Mott-Hubbard insulating ground state. Assuming a symmetric gap around the Fermi level, as suggested by the plot in Fig. 7.5(a), the LHB and the UHB should be spaced by $U_{\mathrm{eff}} \approx 0.5\,\mathrm{eV}$, which is somewhat smaller than in the prototypical 2D Mott systems K/Si(111)-B-$(\sqrt{3} \times \sqrt{3})$ and $6H$-SiC(0001)-$(\sqrt{3} \times \sqrt{3})$.

Nevertheless, speculations on the true nature of the ground state were soon again fueled by two independent reports, arguing that the surface remained metallic and (3×3) ordered down to very low ($4\,\mathrm{K}$ and $2.5\,\mathrm{K}$) temperatures [255, 268]. The LT $(\sqrt{3} \times \sqrt{3})$

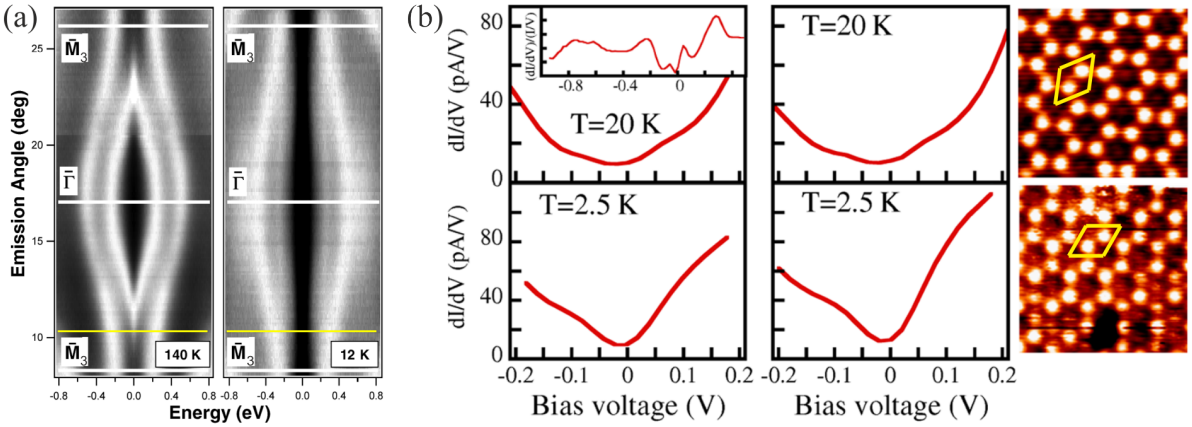

Figure 7.5: *Sn/Ge(111): (a) ARPES band dispersion of the two equidistant surface states in the* (3×3) *LT phase (*$T = 120\,K$*, left panel) and in the postulated Mott insulating* $(\sqrt{3} \times \sqrt{3})$ *LT phase (*$T = 12\,K$*, right panel) along* $\overline{\Gamma}$–$\overline{M}_3$ *in the* (3×3) *SBZ. The spectra are symmetrized with respect to* E_F*, and bright contrast corresponds to high photoemission intensities. The band maps in (a) are taken from [267], Copyright (2006) by the American Physical Society. (b)* $\mathrm{d}I/\mathrm{d}U$ *graphs from STS at two different temperatures in the postulated Mott insulating* $(\sqrt{3} \times \sqrt{3})$ *LT phase. Conductivity at* E_F *is maintained, and empty states STM images (sample bias: +1.0 V, 0.1 nA,* $5 \times 5\,nm^2$*) still exhibit a* (3×3) *surface periodicity (unit cell outlined in yellow) down to* $T = 2.5\,K$*. Spectra to the left (right) are recorded on empty (filled) states STM images; sample bias: +1.0 V (-1.0 V). The inset represents the normalized conductivity spectrum at* $T = 20\,K$ *in a wider bias range. All graphics in (b) are taken from [268], Copyright (2008) by the American Physical Society.*

ordering was shown to be very sensitive to the tunneling conditions, and a *"bias-specific electronic state change"* [255] as well as a *"tip-surface interaction"* [268] mechanism were adduced to explain the earlier observations of R. Cortés and coworkers. Besides doubts concerning the structural change below $T = 30\,K$, also the STS data down to $T = 2.5\,K$ clearly speak against an insulating state of any kind [268]. This becomes obvious in Fig. 7.5(b), where differential conductivity spectra at $T = 20\,K$ and $T = 2.5\,K$ are reprinted from the study of S. Colonna *et al.* [268]. Here it is evident that, although the LDOS at E_F is indeed strongly reduced, it does not fully vanish, thus maintaining the metallic nature of Sn/Ge(111) at LT. Moreover, empty states (sample bias: +1.0 V) STM images [right panels of Fig. 7.5(b)] do not reflect the postulated change to a $(\sqrt{3} \times \sqrt{3})$ periodicity. In addition, the ARPES data of the LT phase [Fig. 7.5(a)] did only cover the $\overline{\Gamma}$–$\overline{M}_3$ direction, which invokes the question, whether there might still be a Fermi level crossing along $\overline{\Gamma}$–$\overline{K}_3$, keeping the surface metallic. Likewise, the LDA+U calculations indicate that an unusually large on-site Coulomb repulsion $U = 4\,eV$ would be necessary to open up a correlation band gap here [16], while the actual gap size is rather small. In this sense, it had earlier been suggested that correlations in Sn/Ge(111)-(3×3) could narrow the conducting surface state, yet leaving the surface metallic [269]. In addition, it might be advisable to raise the question, whether the choice of substrate dopants and the corresponding dopant concentration can influence

the surface conductivity and the characteristics of a phase transition, too. In summary, one must conclude for Sn/Ge(111) that the existence of a Mott insulating ground state is unlikely due to at least four reasons:

- A marginal, but finite conductivity at E_F in STS at LT.
- The observation of a $(\sqrt{3} \times \sqrt{3})$ protrusion arrangement at LT in STM is highly dependent on the tunneling conditions.
- Available gapped ARPES data do not cover the full k-space.
- An extremely large Coulomb repulsion U is necessary to open up the band gap, according to LDA+U calculations.

In the end, the ground state of Sn/Ge(111) rather exhibits the characteristics of a "bad metal" than those of a Mott-Hubbard insulator. Nevertheless, electronic correlations notably govern the spectral features at LT. Further experimental and theoretical efforts will be necessary to unambiguously determine the true nature of the Sn/Ge(111) ground state.

Pb/Si(111)

Compared to Pb/Ge(111) and Sn/Ge(111), the silicon-based representative Pb/Si(111) has been much less studied so far. This is related to the more difficult preparation of Pb/Si(111) and the achievable defect density, which is typically larger than in Pb/Ge(111) [270]. Yet, it is well known that the system also exhibits an intrinsic phase transition from $(\sqrt{3} \times \sqrt{3})$ to a (3×3) distorted 1U2D configuration, as the temperature falls below $T_c = 86\,\mathrm{K}$ [270]. In contrast to Pb/Ge(111), there are no indications of a missing long-range order, and in particular, a glassy phase has not been reported here. Similar as in the Sn/Ge(111) surface system, the Pb $5d$ core levels are split into two components at a ratio of $\approx 1:2$ above the transition temperature [271]. This has been interpreted in terms of a charge fluctuation model in close relation to the dynamical fluctuation model. Also the role of defects in the phase transition has been discussed, yet, apart from local perturbations no further influence on the transition was substantiated [272]. Unfortunately, the role of correlations and magnetic ordering has not been addressed by ARPES so far. Yet, due to the distorted nature of the surface below T_c, a magnetically ordered Mott insulator does not represent a favorable LT phase. Instead, it would not be surprising to observe ground state characteristics closely related to the likewise distorted "bad metals" Pb/Ge(111) and Sn/Ge(111). In conclusion, Pb/Si(111) is the least studied system in the group-IV adatom induced 2DESs and still bears potential for future studies.

Sn/Si(111)

The fourth and last representative in the group-IV adatom induced reconstructions is Sn/Si(111). In view of the three related surfaces introduced above, there is no structural difference for Sn/Si(111) at RT. The validity of the T_4 adsorption model in Fig. 7.4(a) and (b) has been proved by SXRD and XSW [273, 274]. Three out of four Sn directional bonds are saturated by backbonding to the Si(111) substrate, while the remaining perpendicularly oriented p_z-like DBs are located at a rather large in-plane distance. As typical of all these isoelectronic surfaces, simple LDA-based band structure calculations yield a narrow half-filled surface state [275]. Nevertheless, subsequent ARPES [276] and KRIPES [277] experiments point out that the LDA derived band structure is far from being exact, and a more appropriate theoretical approach will be necessary for a convincing description here.

As a first assumption, Sn/Si(111) might behave similarly as Sn/Ge(111). The electronic band structure determined by ARPES is governed by a narrow surface state that crosses the Fermi edge at RT [276, 278, 279]. Also a band backfolding at additional symmetry points, suggestive of a (3×3) order, is found here. Interestingly, no geometric change occurs between RT and $T = 70\,\mathrm{K}$ [279] contrary to Sn/Ge(111), and it seems questionable, whether a structural phase transition also appears in Sn/Si(111). Yet, this possibility is corroborated by a splitting found in the Sn $4d$ core levels, suggestive of two distinct Sn atom coordinations at the surface [279]. This is further supported by an XSW study, which agrees well with a respective lattice distortion [274]. However, and despite the studies speaking in favor of a (3×3) periodic distortion of the tin layer, the Sn/Si(111) system remains the only representative without a change in the $(\sqrt{3} \times \sqrt{3})$ surface periodicity between RT and LT in LEED and STM experiments [17, 279, 280]. This is also supported by means of PED, that reveals only a negligible perpendicular distortion of the Sn atoms ($< 0.06\,\text{Å}$) [17], being five times smaller than in the rippled Sn/Ge(111) system. In conclusion, the splitting in the Sn $4d$ core levels cannot automatically be attributed to a lattice distortion in the tin layer.

The absence of any apparent vertical buckling in the Sn layer might be explainable by the less pronounced hybridization of the Sn atoms with the Si atoms below compared to Sn/Ge(111). It has further been suggested that a LT (3×3) phase is not observed due to a partial softening of a surface phonon [256], in contrast to Sn/Ge(111), where this softening is fully established. Therefore, the (3×3) reconstruction is not a stable option at the Sn/Si(111) surface. The most probable scenario is still a description within the *dynamical fluctuation model* [254, 279], which has been introduced for Sn/Ge(111) before. In contrast to that system, no freeze-out to a (3×3) order, i.e., the 1U2D stable situation, is observed within the temperature range studied, which is down to $T = 2.3\,\mathrm{K}$ [281]. Yet, this does not exclude a freezing at even lower temperatures. In this regard, a potential perpendicular oscillation of the Sn adatoms has also been probed by recording current traces in STM [281]. F. Ronci *et al.* succeeded to resolve a time-dependent oscillatory behavior in the tunneling current, that exhibits a temperature

dependency described by an Arrhenius law down to $T = 15\,\mathrm{K}$. However, a freeze-out of motions is not detected. Interestingly, quantum tunneling of the tin atoms is assumed to govern the signal below $T = 15\,\mathrm{K}$, since the oscillation frequency remains constant below that temperature. Further support for the validity of the dynamical fluctuation model in Sn/Si(111) is given by XSW [274]. Finally, also theoretical calculations indicate that perpendicular atomic fluctuations of local (3×3) order are present over a wide temperature range, while a phase transition does not occur [256]. Hence, it is very likely that the dynamical fluctuation model is also valid for Sn/Si(111)-$(\sqrt{3} \times \sqrt{3})$.

Electronic correlations in Sn/Si(111)

The quite localized nature of the Sn DBs provokes the question, whether correlations would have a significant impact on the electronic properties. In this sense, the undistorted Sn/Si(111)-$(\sqrt{3} \times \sqrt{3})$ surface might represent an experimental realization of a strongly correlated 2D triangular lattice. To clarify this issue, G. Profeta and E. Tosatti performed *ab initio* LDA+U calculations [16], which, in addition to the pure LDA, account for on-site Coulomb repulsions in an approximative way. Indeed, their main finding is a magnetic insulating ground state of the Mott-Hubbard type here. This phase is fully developed at $U = 4\,\mathrm{eV}$, although the correlation band gap already opens at $U = 2\,\mathrm{eV}$. Yet, the actual size of the Hubbard U is still controversial, and constraint LDA calculations have revealed a much smaller estimate of $U_{\mathrm{eff}} = 1.15\,\mathrm{eV}$ [269]. Moreover, as a result of the narrow bandwidth ($W \sim 0.4\,\mathrm{eV}$), a smaller U should already be sufficient to enter the highly correlated regime here [74]. Therefore, a more precise estimate of the on-site Coulomb repulsion in Sn/Si(111)-$(\sqrt{3} \times \sqrt{3})$ still remains an open issue.

From the experimental side, a temperature-induced band gap opening at $T_c \approx 60\,\mathrm{K}$ was reported by S. Modesti *et al.*, who utilized STS and ARPES [17]. This was interpreted as a verification of the theoretically proposed transition to an insulating Mott-Hubbard ground state. The band gap opening in STS is resolved as a dip to zero conductance (estimated gap size $\sim 40\,\mathrm{meV}$) below T_c, see Fig. 7.6(a). Unfortunately, the LT tunneling spectrum lacks clear-cut peaks, that could identify the positions of the LHB and the UHB. Above the transition temperature the conductivity dip evolves into a pseudogap with marginal metallicity, that still remains visible at $T = 290\,\mathrm{K}$. Hence, Sn/Si(111)-$(\sqrt{3} \times \sqrt{3})$ should be interpreted in terms of a "bad metal" at RT. With the absence of any perpendicular buckling in the Sn layer in mind, the elevated temperature phase then represents a sort of undistorted bad metal [17]. Spectra in ARPES likewise show a reduction of spectral weight at E_F when cooling from $T = 290\,\mathrm{K}$ to $T = 30\,\mathrm{K}$, which is in agreement with the opening of a band gap [17]. A further study utilizing micro four-point-probe measurements even claims that the surface remains metallic down to $T_c = 15\,\mathrm{K}$ [282], where the transition to a small gap insulator, probably of the Mott-Hubbard type, occurs. Interestingly, surface doping, by substituting sodium or indium atoms for tin atoms, induces a rigid band shift and significantly enlarges the transition temperature to $T_c = 260\,\mathrm{K}$ for both dopants. Here, the dopant atoms might act as

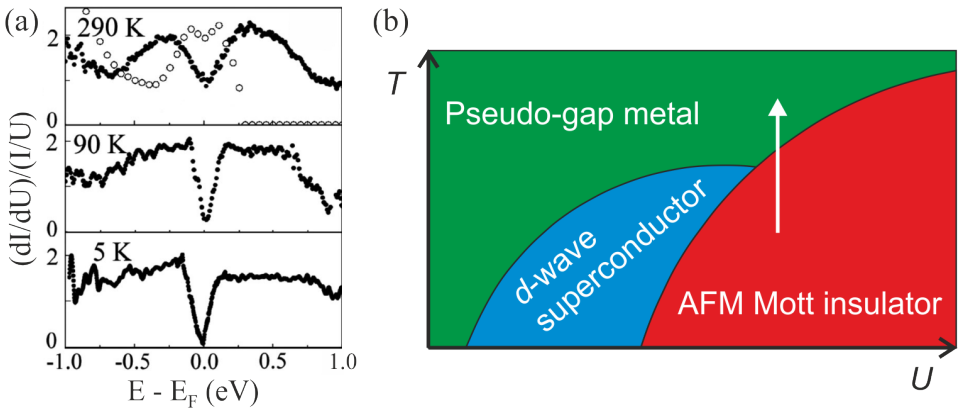

Figure 7.6: *(a) Averaged and normalized* $\mathrm{d}I/\mathrm{d}U$ *spectra of Sn/Si(111)-*$(\sqrt{3} \times \sqrt{3})$ *at three different temperatures, measured apart from defects (full dots); plots are taken from [17], Copyright (2007) by the American Physical Society. Empty dots in the* $T = 290\,K$ *spectrum correspond to the calculated normalized conductance. (b) Illustrative diagram, suggesting the possibility of three different correlation-induced phases at the Sn/Si(111)-*$(\sqrt{3} \times \sqrt{3})$ *surface; according to [16].*

localization centers for the electrons, thereby increasing correlations. Thus, one could interpret this experiment as a demonstration of a band filling controlled MIT. Apart from the disagreement in transition temperature, these results substantiate the findings of S. Modesti *et al.*

Magnetic order in Sn/Si(111)

As a consequence of the Mott insulating ground state in Sn/Si(111)-$(\sqrt{3} \times \sqrt{3})$, G. Profeta and E. Tosatti have also discussed potential magnetic orders [16]. Here, a single electron is located at each Sn atom site, and a 2D triangular grid of local magnetic moments exists. The whole system may then be regarded as a Heisenberg type magnet with inter-site AFM exchange coupling. However, in a triangular lattice, long-range collinear magnetic ordering is prohibited due to the inherent spin frustration (cf. Fig. 2.4). Nevertheless, by profound calculations within the local spin density approximation + U (LSDA+U) scheme it turned out that AFM ordering, most probably the 120 ° Néel type, is dominant in the Mott insulating LT phase [16]. It is further likely that short-range AFM ordering persist up to at least $T = 100\,\mathrm{K}$, although possibly influenced by quantum fluctuations. As the 120 ° AFM coupling includes a larger magnetic unit cell of (3×3) periodicity, band backfolding with respect to this order should be observable experimentally. In this context, one may interpret the spectral intensity seen in ARPES at the $\overline{\Gamma}$ point in two independent studies [17, 276] as a band backfolding purely resulting from a magnetic order, since there exists no intensity in the corresponding single-particle LDA band structure [275]. In contrast to Sn/Ge(111), a structural distortion is not needed then. Unfortunately, no experimental study that directly addresses the magnetic ordering in Sn/Si(111)-$(\sqrt{3} \times \sqrt{3})$ exists until today, although other theoretical studies support the idea of an AFM ordered ground state [18, 74]. In addition,

a competition with a spin liquid has been pointed out [16]. The complex interplay of various phases is visualized in the illustrative phase diagram in Fig. 7.6(b), which is according to Ref. 16. Accordingly, the Sn/Si(111)-($\sqrt{3} \times \sqrt{3}$) surface will stabilize an AFM ordered Mott insulating state in the highly correlated regime (large U), while for elevated temperatures T and for reduced correlations a transition to a pseudogap metal is postulated. Interestingly, also the possibility of d-wave superconductivity is pointed out, achievable by reducing the Coulomb interaction. This could be reached by, e.g., adding dopants to the surface, which will change the band filling away from 1/2, or by heavy substrate doping to control the bandwidth [compare to Fig. 2.3(c)] [16]. A possible origin of the temperature-induced transition from the AFM Mott insulating phase to the pseudogap metallic one could be a lack of spin entropy, which is stabilized by short-range AFM ordering [16]. As a side note, it should also be mentioned that a magnetic undistorted Mott insulator is also a basic ingredient for high-temperature cuprate superconductors [11, 16]. Nevertheless, it will be demonstrated in Sec. 7.2.5 by a combined approach of experiment and theoretical modeling that the surface magnetism in Sn/Si(111)-($\sqrt{3} \times \sqrt{3}$) does not agree with the proposed 120 ° Néel AFM order.

At this point it should finally be stated again that Sn/Si(111)-($\sqrt{3} \times \sqrt{3}$) is the only system that remains undistorted and develops a small, but unambiguous band gap at LT. In combination with the unresolved issues of correlation strengths and the type of magnetic order, Sn/Si(111)-($\sqrt{3} \times \sqrt{3}$) represents the most promising candidate in the circle of isoelectronic group-IV 2DESs to be studied.

7.2 Sn/Si(111)-($\sqrt{3} \times \sqrt{3}$) in view of electronic correlations and competing magnetic orders

7.2.1 Experimental realization

In addition to the requirement of cleanliness, as in any surface preparation process, for Sn/Si(111)-($\sqrt{3} \times \sqrt{3}$) it is mandatory to precisely control the amount of tin deposited onto Si(111)-(7 × 7) in order to obtain exactly the desired phase. This becomes more obvious when regarding the structural phase diagram in Fig. 7.7. It features a pattern of partly overlapping phases in dependence of the temperature T and the tin coverage θ. Accordingly, the ($\sqrt{3} \times \sqrt{3}$) phase formation starts at a nominal coverage $\theta \geq 0.1$ ML. Yet, the first relevant ($\sqrt{3} \times \sqrt{3}$) phase, i.e., the γ-phase, is established not before $\theta = 1/6$ ML. It represents the low coverage limit of the intermediate phase, which is best described as a surface alloy Si_xSn_{1-x}/Si(111)-($\sqrt{3} \times \sqrt{3}$) of Sn and Si atoms ($0.5 \geq x \geq 0$) that occupy T_4 lattice sites, i.e., there exists one Sn or Si adatom per unit cell. The upper limit is formed by the dilute α-phase at 1/3 ML tin coverage, which is most relevant. α-Sn/Si(111)-($\sqrt{3} \times \sqrt{3}$) will be predominantly inspected in the course of this chapter, as it represents the experimental realization of a triangular lattice. Apart

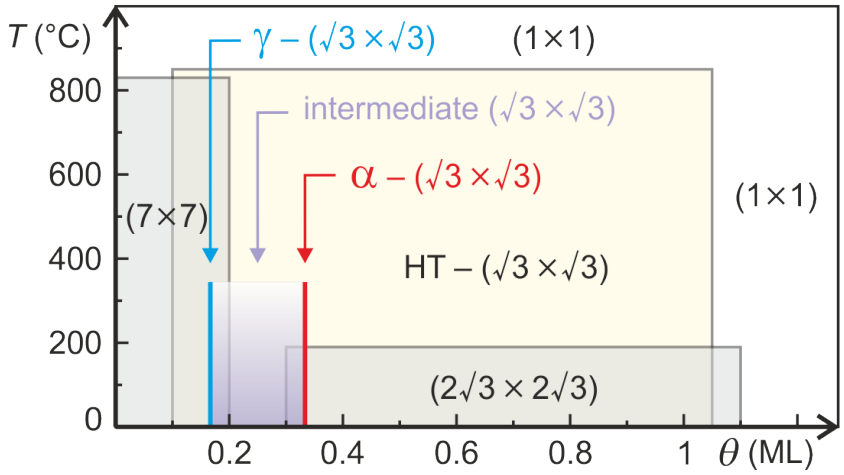

Figure 7.7: *Structural phase diagram for the deposition of Sn in the sub-ML to ML coverage (θ) range onto Si(111)-(7 × 7) substrates in dependence of the temperature T, according to [283]. The most relevant α-phase is reached at exactly $\theta = 1/3$ ML. Overlapping areas indicate coexisting phases.*

from the high-temperature and high-coverage regime, there exists one additional stable RT phase that evolves for $\theta > 0.3$ ML, i.e., a $(2\sqrt{3} \times 2\sqrt{3})$ reconstruction. This higher periodicity superstructure develops in form of islands on top of α-$(\sqrt{3} \times \sqrt{3})$ ordered areas. While its presence is less critical for scanning probe techniques, it has to be strictly avoided in ARPES experiments, where the photon beam inevitably excites electrons from all phases present at the surface. Therefore, precise control of Sn deposition, typically gauged by LEED, is the key parameter in preparation of α-Sn/Si(111)-$(\sqrt{3} \times \sqrt{3})$.

The experimental realization of the α-Sn/Si(111)-$(\sqrt{3} \times \sqrt{3})$ surface 2DES follows the pretreatment of Si(111) substrates, according to the recipe given in Sec. 4.3.1. All experimental data shown in the following sections are derived from Si(111) samples of the wafer "charge 2". Tin (foil, purity 99.99 %) is evaporated from a pyrolytic boron nitride crucible, as part of an electron beam evaporator ("Focus EFM 3"), until the (7 × 7) ordered Si(111) surface is covered by a tin amount of 1/3 ML. During this process the sample is kept at RT. Adatom surface diffusion is then triggered by annealing the sample at $\approx 700\,^\circ$C for 3 min in a direct current heating stage [284]. Moderate cooling down to RT afterwards is ensured, by continuously decreasing the current to zero within 1 min. Annealing at higher temperature should be avoided, since it may lead to enhanced Sn desorption and cluster formation. However, in preparing lower density phases, this is a reasonable approach to continuously decrease the initial Sn coverage by time [277, 285]. In contrast to Pt/Si(111)-$(\sqrt{3} \times \sqrt{3})$ and Au/Ge(111)-$(\sqrt{3} \times \sqrt{3})$, a full adatom removal by flashing at $T = 1250\,^\circ$C is feasible, as verified by the absence of the Sn 4*d* line shape in XPS afterwards. The initial Sn deposition was calibrated by use of a quartz micro balance and by thorough inspection of the LEED diffraction pattern after the anneal. Remaining (7 × 7) reflexes indicate a coverage below 1/6 monolayer, while a streaky or diffuse background in between 1/3-order spots is related to the intermediate phase [285].

Upon development of $(2\sqrt{3} \times 2\sqrt{3})$ islands, corresponding order spots become visible in LEED. Therefore, the α-phase is characterized by a LEED pattern with 1/3-order spots only and the lowest possible background noise. Since excess Sn can be stripped off the surface, one can approach the α-phase by further annealing, if the correct coverage has not been reached in a single step.

The γ- and the intermediate phase

According to the diagram in Fig. 7.7, the γ-$(\sqrt{3} \times \sqrt{3})$ phase is established at a nominal Sn coverage of 1/6 ML [286]. This involves that only half of the T_4 Sn adsorption sites in the model of Fig. 7.4(a) and (b) are occupied by a Sn atom. As the surface tends to minimize its energy, the remaining DB orbitals must be saturated in some way. This is achieved, by placing Si atoms from the substrate at these empty sites instead. Hence, the γ-phase can be regarded as a surface alloy, i.e., Si_xSn_{1-x}/Si(111)-$(\sqrt{3} \times \sqrt{3})$ with $x = 0.5$, where Sn and Si atoms are displaced by 0.75 Å in perpendicular direction from one another [277]. The γ-phase exhibits a streaky (3×3) type diffraction pattern in LEED and a meandering network of bright protrusions in occupied states STM images. The same is true for slightly enhanced Sn coverages in the intermediate phase, see Fig. 7.8 *top panels*. The γ-phase is also known as *mosaic* phase in the literature and has also been reported to exist in Pb/Ge(111) and Pb/Si(111) for lead coverages below 1/3 ML [287]. The meandering network does not show any signature of long-range ordering and is arbitrarily spread at the surface. However, a Fourier transform of such STM images reveals the presence of weak (3×3) besides $(\sqrt{3} \times \sqrt{3})$ spots in agreement with LEED [285]. This reflects the disposition of the system to develop a local (3×3) order due to perturbations. For increasing tin coverages $(0.5 > x > 0)$ the (3×3) streaks in LEED start to become weaker and pass over into a diffuse background noise [285]. In STM the meandering network evolves towards a more homogeneous $(\sqrt{3} \times \sqrt{3})$ protrusion array, which is completely developed in the α-phase only. Interestingly, the electronic band structure at RT is strongly dependent on the Sn coverage and exhibits semiconducting behavior in the γ-phase, with a band gap of 0.3–0.5 eV in size due to charge exchange between Sn and Si atoms [277, 288]. Upon increasing the Sn coverage at the expense of Si atoms in the $(\sqrt{3} \times \sqrt{3})$ unit cell, the surface turns to metallic character, as evidenced by KRIPES for $x \leq 0.05$ [277]. Moreover, also the high-coverage $(2\sqrt{3} \times 2\sqrt{3})$ reconstructed areas exhibit again semiconducting behavior, as revealed by STS [289].

In order to clarify, whether the meandering protrusions reflect the atomic height contrast or rather display the electronic charge density, Fig. 7.8 presents a bias-dependent series of STM images at the very same area in the intermediate phase. In comparison with the results given in Ref. 285, one may estimate the Sn coverage as $\theta \approx 0.2$ ML, which corresponds to $Si_{0.4}Sn_{0.6}$/Si(111)-$(\sqrt{3} \times \sqrt{3})$. In occupied states (top panels) the meandering network is present over a wide bias range (-2.0 to -0.4 V), while close to the Fermi level (-0.2 and -0.1 V) the contrast is significantly weakened. Probably, dark areas in between the protrusions are due to Si substitutional atoms, since the

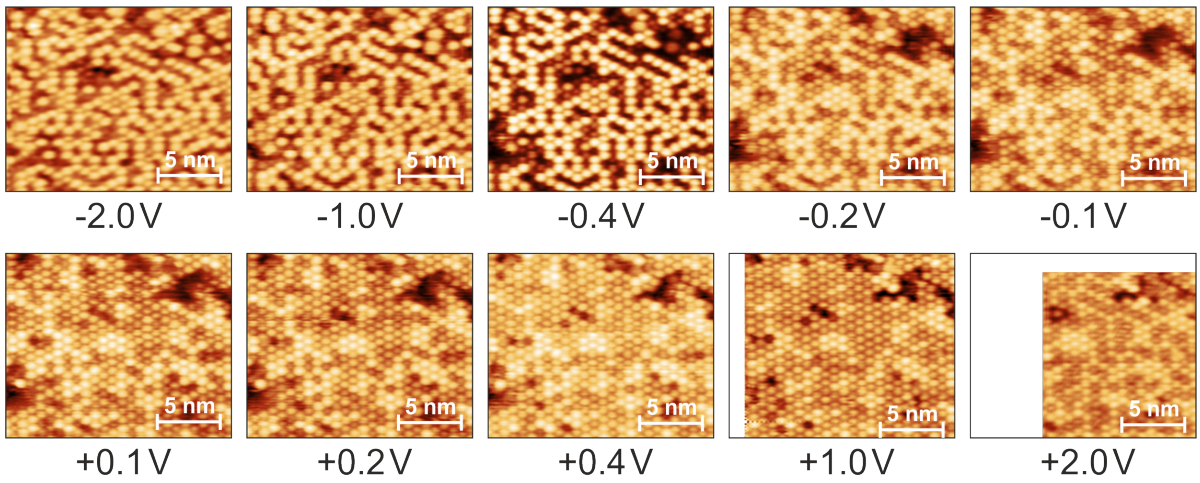

Figure 7.8: *Bias-dependent electronic charge density in STM of the intermediate Si_xSn_{1-x}/Si(111)-($\sqrt{3} \times \sqrt{3}$) phase ($x \approx 0.4$). All images show the same surface area. Filled states (top panels) are characterized by a meandering network of bright protrusions, while empty states (bottom panels) exhibit a patchwork of small equal charge density areas (0.1 nA, 17.9 × 14.6 nm^2).*

bright protrusions cover more than 60 % of the surface area. Moreover, this is in agreement with the dark contrast in occupied states seen for Si substitutional defects in the α-phase (see Sec. 7.2.2). In turning to the unoccupied states (bottom panels), the impression of a meandering network is completely lost. Instead, small patches of ($\sqrt{3} \times \sqrt{3}$) reconstructed areas that differ in intensity exist (+0.1 to +1.0 V). For large positive sample bias (+2.0 V) the electronic charge density does more resemble the occupied states again. From images taken at the same tunneling conditions after a given time interval ($\sim$ 30 min) has passed, it can also be stated that adatom diffusion is negligible at RT. In conclusion, STM imaging of the intermediate phase with $\theta \approx 0.2$ ML reveals a strong bias-dependent electronic contrast, that does not definitely allow to allocate protrusions to either tin or silicon adatoms. It is further likely that charge transfer between silicon and tin atoms plays a crucial role here [277].

The α-phase

In increasing the Sn coverage to $\theta = 1/3$ ML, one ends up with the α-Sn/Si(111)-($\sqrt{3} \times \sqrt{3}$) phase, which represents the high-coverage limit of the intermediate phase. It is characterized by the missing of (3×3) related features in LEED, accompanied by a maximum peak-to-background ratio. An addition, as given by the structural phase diagram in Fig. 7.7, the absence of ($2\sqrt{3} \times 2\sqrt{3}$) superstructure spots has to be checked carefully in order to avoid phase mixing in ARPES. Fig. 7.9(a) presents a LEED image at RT, taken from a Si(111) surface with optimized Sn coverage ($\theta = 1/3$ ML) after annealing. Only ($\sqrt{3} \times \sqrt{3}$) superstructure spots and (1×1) peaks from the substrate are present, while the background noise is barely visible, which is suggestive of a low

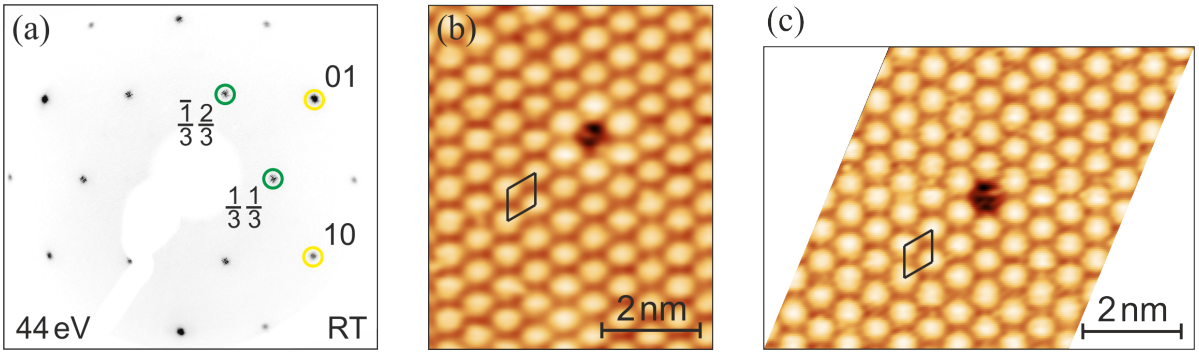

Figure 7.9: *(a) LEED image at RT of α-Sn/Si(111)-($\sqrt{3}\times\sqrt{3}$). Sharp and intense diffraction spots in first-order (Si(111) substrate, yellow) and 1/3-order (surface reconstruction, green) evidence the high quality of preparation. (b) Filled states STM image of the α-phase; bias: -1.0 V, 0.5 nA, 5.8 × 7.0 nm^2. The protrusions in a hexagonal arrangement and the dark hole are related to Sn atoms and to a Si substitutional defect, respectively. The ($\sqrt{3}\times\sqrt{3}$) unit cell is given as black rhomboid. (c) STM image of the empty states with the same assignment of bright protrusions and dark hole as in (b); bias: +1.0 V, 0.5 nA, 8.8 × 6.1 nm^2. Streaks in between protrusions are related to a tip artifact. Both STM images have been Fourier-filtered to enhance the quality of presentation.*

defect density at the surface.

The conclusions drawn above are next confirmed by STM. The occupied states image in Fig. 7.9(b) shows a regular periodic array of bright protrusions in a hexagonal arrangement. The mean distance between adjacent peaks (6.6 ± 0.1 Å) does well coincide with the lattice repetition period $a_{\sqrt{3},\mathrm{Si}}$ of a ($\sqrt{3}\times\sqrt{3}$) reconstructed Si(111) surface (cf. Tab. 4.1). Thus, and in accordance with the literature, the protrusions are attributed to single Sn atoms located at T_4 lattice sites [compare to Fig. 7.4(a)]. The dark hole, surrounded by six even brighter protrusions, must originate from a silicon substitutional defect, following the discussion in Ref. 290. A more detailed investigation of defects is presented in the next section. In turning to the unoccupied states in STM [Fig. 7.9(c)], one finds a rather similar distribution of the electronic charge density apart from the defect, which is no more accompanied by an enhanced contrast of its six neighboring protrusions. This leads to the conclusion that STM images are much less governed by an electronic contrast in the α-phase than in the γ-phase. Therefore, with exception of defects, STM can be regarded as a reliable tool to map the topography of the α-Sn/Si(111)-($\sqrt{3}\times\sqrt{3}$) surface.

Additional STM data acquired at $T = 60\,\mathrm{K}$ (not shown here) do not exhibit any signature of a modified charge density. These results are in good agreement with earlier data by F. Ronci *et al.* [281], H. Morikawa *et al.* [280], and S. Modesti *et al.* [17], who did not observe a change in the electronic charge density even down to $T = 2.3\,\mathrm{K}$. This is consistent with the absence of a structural or electronic phase transition at a certain critical temperature in Sn/Si(111)-($\sqrt{3}\times\sqrt{3}$). Nevertheless, it does not exclude the existence of a phase transition beyond the temperature range covered. In agreement with the dynamical fluctuation model, a freezing of high-frequency perpendicular motions of

the Sn atoms, as reported for Sn/Ge(111)-($\sqrt{3} \times \sqrt{3}$) [264], might still occur at very low temperatures.

7.2.2 The role of defects in surface ordering

In general, and if defects are not the main concern of an experiment, the defect density should be reduced to the lowest level possible, since they may hinder the development of long-range order. Precisely keeping to the recipe given in Sec. 7.2.1 results in long-range ordered ($\sqrt{3} \times \sqrt{3}$) reconstructed surfaces with only few defects. Thorough evaluation of STM images of several different samples allows to safely exclude that the defect densities exceed 4 % of the whole reconstructed area in any case. This order of magnitude is in good agreement with values reported by other groups [280, 291]. The defect density can be tuned by Sn desorption during thermal annealing. Although even lower defect densities have been reached in this way, a completely defect-free Sn/Si(111)-($\sqrt{3} \times \sqrt{3}$) surface has not been reported so far, and it seems questionable, whether this can be realized at all. The experimental setup in ARPES (cf. Sec. 3.3.2) does not include STM to determine the defect concentration simultaneously, thus, a definitive statement about the defect densities of samples used in photoemission is not possible. Moreover, LEED is not sensitive enough to resolve such slight differences. Therefore, the upper limit of 4 % will be taken as the standard defect density in the following.

Defects act as scattering potentials, which can reduce the electron mean free path significantly. For a density of 4 %, each defect is followed by a second in a distance of $\Delta x = 5 \times a_{\sqrt{3},\mathrm{Si}} \approx 33\,\text{Å}$ in average. Since electrons are not scattered at each defect site, this value must be regarded as a minimum for the electron mean free path. The corresponding k-space broadening $\Delta k_{\parallel}$ is estimated by applying Heisenberg's uncertainty relation $\Delta k_{\parallel} = 2\pi/\Delta x = 0.19\,\text{Å}^{-1}$, which represents an upper limit to the total momentum broadening. This is reflected in the broadening of the LEED 1/3-order spots in Fig. 7.9(a), where the FWHM $\Delta k_{\parallel} = 0.064\,\text{Å}^{-1}$ is actually much smaller. In comparison with the LEED 1/3-order spot broadening in Au/Ge(111)-($\sqrt{3} \times \sqrt{3}$) ($\Delta k_{\parallel} = 0.067\,\text{Å}^{-1}$) and Pt/Si(111)-($\sqrt{3} \times \sqrt{3}$) ($\Delta k_{\parallel} = 0.127\,\text{Å}^{-1}$), the corresponding spectral width in ARPES should be of the same size as in Au/Ge(111)-($\sqrt{3} \times \sqrt{3}$). However, the mechanism behind is a different, i.e., while it is most probably defect related here, scattering at domain walls is most relevant in Au/Ge(111)-($\sqrt{3} \times \sqrt{3}$) as also in Pt/Si(111)-($\sqrt{3} \times \sqrt{3}$). For Sn/Si(111)-($\sqrt{3} \times \sqrt{3}$) there is no experimental proof of phase-slip domains, although different adatom registries with respect to the substrate must exist there, too. This implies the presence of only one single domain on a whole atomic terrace. In conclusion, defects will be a main source of spectral broadening in ARPES for Sn/Si(111)-($\sqrt{3} \times \sqrt{3}$), in contrast to the broadening due to small domain sizes in Au/Ge(111)-($\sqrt{3} \times \sqrt{3}$), and in particular, in Pt/Si(111)-($\sqrt{3} \times \sqrt{3}$).

Types of defects

Defects at the Sn/Si(111)-($\sqrt{3} \times \sqrt{3}$) surface do occur in six different variations. In the following these are classified by their respective appearance in occupied states STM images (see Fig. 7.10), their relative frequency of occurrence (given in parentheses), and their probable physical origin [279, 290, 292].

A A hole in the bright ($\sqrt{3} \times \sqrt{3}$) ordered array of elevations surrounded by a ring of six more intense *decorations* (located $\approx 0.2\,\text{Å}$ "higher"). This is the most frequently observed defect ($\approx 38\,\%$). Line profiles indicate a mean "depth" of $\approx 1\,\text{Å}$ with respect to the regularly ordered region. It originates most probably from a silicon substitutional atom located at a T_4 lattice site, thereby replacing a tin atom. Hence, the "depth" must not be interpreted as a topographic feature alone, since electronic effects will be crucial here, i.e., a redistribution of charges is likely to affect the appearence in STM. As a result, the surrounding Sn atoms (decoration atoms) move upwards in order to lower their DB energies [292]. Closer scrutiny of these elevated protrusions unveils a threefold rotational symmetry within the ring. Here, three out of six atoms are positioned $\approx 0.05\,\text{Å}$ "higher" than the rest. Obviously, this slight variation is induced by the symmetry of the substrate.

B A bright protrusion surrounded by six spots of weakened intensity (located $\approx 0.2\,\text{Å}$ "deeper"). This is the second most frequent type of defect ($\approx 28\,\%$). The decorating atoms exhibit the same three-fold rotational symmetry observed for defect type "A", with a perpendicular undulation amplitude of $\approx 0.15\,\text{Å}$. Similarly as for type "A", this decoration should be related to a charge redistribution between

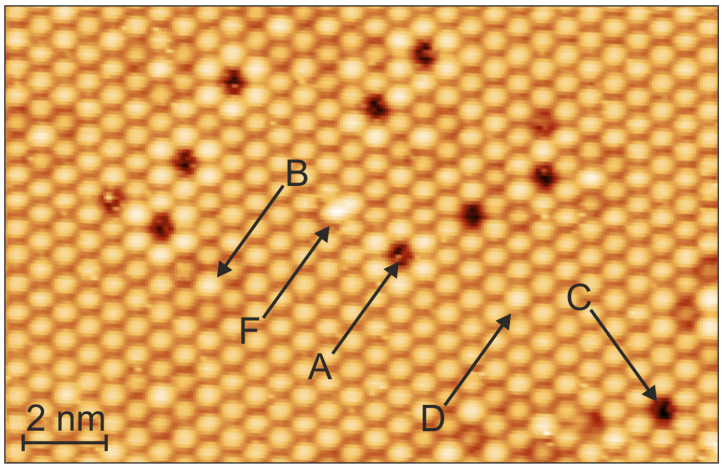

Figure 7.10: *Filled states STM image of Sn/Si(111)-($\sqrt{3} \times \sqrt{3}$), that features five out of six different types of defects (A–D, F); bias: -1.0 V, 0.5 nA, 17.2 × 11.0 nm^2. Small bright spikes are due to tip artifacts. For further details refer to text.*

center and neighboring atoms. In the literature, this defect has been attributed to a Sb substitutional impurity as a consequence of bulk to surface diffusion of the substrate dopants [290]. Its frequency of occurence depends on the duration, the thermal power, and number of cycles of the anneal step, which strongly supports its dopant nature. This defect is found significantly more often than reported in the study of S. T. Jemander *et al.* ($< 1\,\%$) [290], which is consistent with the use of lightly Sb-doped samples in their study in contrast to the high Sb doping level of the Si(111) wafer "charge 2", used here.

C A purely dark hole without any decoration around ($\approx 15\,\%$). This type of defect is attributed to a tin vacancy, and hence, its appearance in STM is rather a representation of the surface topography.

D A bright protrusion without any decoration around ($\approx 8\,\%$).

E Three bright protrusions, agglomerated in a triangular shape. This is the most rarely observed defect ($< 1\,\%$), and it is not present in Fig. 7.10.

F An agglomeration of two bright protrusions that close to one another that a lateral distinction is only possible, by analyzing line profiles along the binding axis ($\approx 10\,\%$).

Defects with decoration, i.e., type "A" and "B", might be interpreted in terms of *Friedel oscillations* [293]. This phenomenon is known from metallic surfaces as an oscillatory modulation of the charge density in the vicinity of step edges. With increasing distance from the step edge the fluctuation is damped and is thus imaged as a decaying plane wave. Transferring this concept to the present case, point defects replace the step edges and may be interpreted as the center of a Friedel oscillation, with the defect decoration as the circularly decaying modulation of the charge density. Damping must be rather strong, so there is no change in the charge density visible in line profiles beyond nearest-neighbor protrusions [290]. The corresponding decay length of the exponentially damped electronic disturbances has been specified as 11 Å at 120 K [294]. This effect has also been associated with a damped CDW in the literature [291, 295].

It should further be noted that there is a significant dependency of the defect appearance in STM on the tunneling conditions, i.e., most strongly depending on the bias. This is already known from the "defect-rich" intermediate phase (cf. Fig. 7.8), where a considerable change in the electronic contrast is observed at different tunneling voltages. Likewise, the bias-dependent appearance of defects in the α-phase is a consequence of a pronounced electronic contrast, and it does only partly represent true geometries. This is particularly the case for defect decorations, where the most prominent change in contrast is observed, when switching from negative to positive sample bias.

Defect-induced local ordering

Interestingly, defects have also been reported to be responsible for faint signatures of (3×3) ordering superimposed on a pure $(\sqrt{3} \times \sqrt{3})$ periodic diffraction pattern in RHEED and LEED experiments [280, 285]. In Fig. 7.11 an occupied states STM image of a defect-free (a) area is compared with surface regions of the same sample, with few defects (b) and multiple defects (c) present. For larger defect densities there exists a higher probability that defects are arranged in a very local (3×3) order, as indicated by the large rhomboid in Fig. 7.11(c), while $(\sqrt{3} \times \sqrt{3})$ ordering still prevails. The corresponding 2D Fourier transforms in (d)–(f) represent a customary approach to resolve superstructure features in the *reciprocal space* representation which are hidden in the original *real space* STM data. For the defect-free area the Fourier transform (d) displays a regular array of $(\sqrt{3} \times \sqrt{3})$ ordered peaks only. However, for few defects (e) smeared intensity features (arrow) develop at reciprocal space locations corresponding to a (3×3) order. This effect becomes even more visible in the Fourier transform of the surface area with multiple agglomerated defects (f). Here, six blurred but distinct intensity maxima at (3×3) reciprocal lattice coordinates indicate the additional periodicity at the surface. In comparison with the corresponding STM images on top, it becomes clear that *local defect ordering* must be the source of the (3×3) spots seen in diffraction experiments.

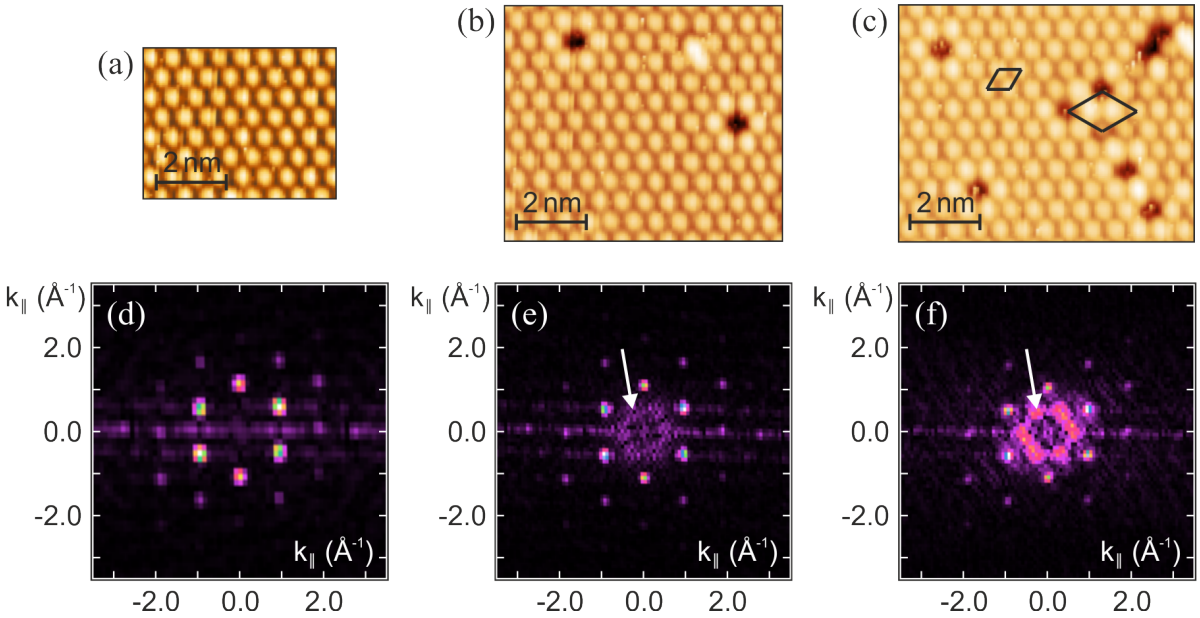

Figure 7.11: *(a) Filled states STM image of a defect-free area on the Sn/Si(111)-$(\sqrt{3} \times \sqrt{3})$ surface; bias: -1.0 V, 0.5 nA, $5.5 \times 4.3\,\mathrm{nm}^2$. (b) Adjacent region of the surface at the same tunneling conditions, with few defects ($8.0 \times 6.7\,\mathrm{nm}^2$), and (c) multiple defects present ($8.5 \times 6.7\,\mathrm{nm}^2$). Black rhomboids indicate the unit cells of $(\sqrt{3} \times \sqrt{3})$ and (3×3) periodicity. (d)–(f) 2D Fourier transforms of the respective STM images in (a)–(c), with reciprocal space intensity maxima corresponding to $(\sqrt{3} \times \sqrt{3})$ order. White arrows point at features related to an additional (3×3) order.*

Importantly, this finding is independent of temperature, which again excludes a phase transition in the range from $T = 120\,\mathrm{K}$ to RT [280].

7.2.3 The electronic band structure

Band structure calculations

As a basic approach to inspect the electronic band structure of Sn/Si(111)-($\sqrt{3} \times \sqrt{3}$), *ab initio* calculations within the LDA represent a valuable tool. Resuming the earlier conjecture of seven electrons per unit cell by simple electron counting in Sec. 7.1.2, one should expect to end up with a half-filled band here. This view is supported by LDA calculations from the literature, which indeed provide evidence of a narrow metallic state at half filling (bandwidth $W \sim 0.3\,\mathrm{eV}$) within the Si bulk band gap [18, 275].

A concrete view on the LDA derived band structure of Sn/Si(111)-($\sqrt{3} \times \sqrt{3}$) is provided in Fig. 7.12(a), where the energy dispersion (Eq. A.2) of the surface state is plotted. Importantly, higher order hopping terms are included here (see Sec. A.1 for further details). The emergence of this narrow surface state is predominantly due to Sn $5p_z$ and, to a small amount, due to Sn $5s$ orbitals [18], although also Si orbitals are assumed to be involved [74]. Prominent features are the minimum in energy at the $\overline{\mathrm{K}}$ point ($E - E_F = -0.31\,\mathrm{eV}$) and the plateau at the $\overline{\mathrm{M}}$ point ($E - E_F = -0.02\,\mathrm{eV}$). The corresponding non-interacting DOS, derived from integration along $\overline{\Gamma}$–$\overline{\mathrm{K}}$–$\overline{\mathrm{M}}$–$\overline{\Gamma}$, is depicted in Fig. 7.12(b). It exhibits an asymmetric shape with respect to the Fermi energy, and it has a pronounced peak close to E_F in the occupied band energy region as well as at the upper band edge in empty states. In the following discourse it will become evident that the inclusion of the higher order hopping terms (Eq. A.2) is also crucial for magnetic ordering.

Finally, it is worth taking a look at the FS, derived from tight-binding model calcula-

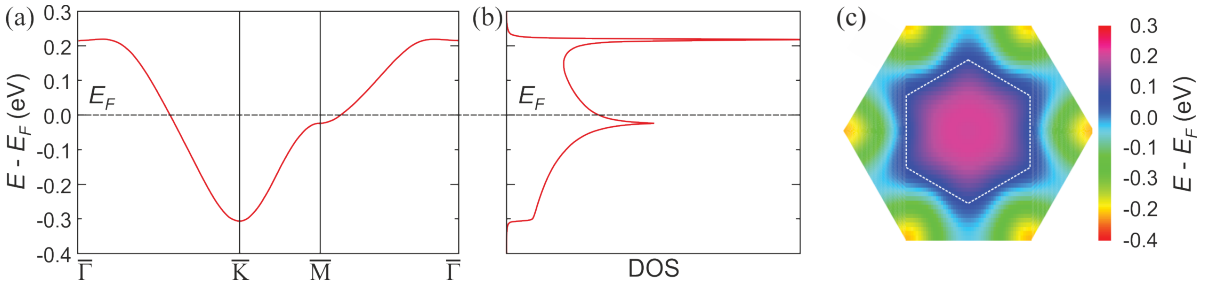

Figure 7.12: *(a) LDA derived band structure of Sn/Si(111)-($\sqrt{3} \times \sqrt{3}$), based on Eq. A.2. (b) Non-interacting DOS, deduced from integration of the band dispersion (Eq. A.2) along $\overline{\Gamma}$–$\overline{\mathrm{K}}$–$\overline{\mathrm{M}}$–$\overline{\Gamma}$. The DOS is asymmetric with respect to E_F and features a pronounced peak in occupied states close to the Fermi level. (c) Location of the single-particle band peak, extracted from a one-band tight-binding model in the ($\sqrt{3} \times \sqrt{3}$) SBZ, in dependence of the binding energy (color code); figure taken from [18], Copyright (2011) by the American Physical Society. The FS exists along the edge of light blue and dark blue colors, and it exhibits a warped contour. The dashed hexagon inside corresponds to a (3×3) SBZ.*

tions [18]. It exists at the warped edge between light blue and dark blue in Fig. 7.12(c). This prominent shape, which is somewhat reminiscent of the Au/Ge(111)-($\sqrt{3}\times\sqrt{3}$) FS (cf. Sec. 6.2.1), is only slightly nested with respect to a (3×3) related lattice distortion as part of a potential CDW transition (the dashed hexagon indicates the respective SBZ). Therefore, and similar to the cases of Sn/Ge(111)-($\sqrt{3}\times\sqrt{3}$) and Pb/Ge(111)-($\sqrt{3}\times\sqrt{3}$) [209, 246], one should not expect an instability in Sn/Si(111)-($\sqrt{3}\times\sqrt{3}$) towards the formation of a CDW.

Fermi level determination in ARPES

In the experiment, the occupied electronic band structure, i.e., the one-electron removal spectral function, is explored by ARPES. The correct determination of the Fermi level E_F is a quite difficult task in Sn/Si(111)-($\sqrt{3}\times\sqrt{3}$). First, the Fermi edge, extracted by use of Eq. 3.52 from UPS spectra of the tantalum clips which are in direct contact to the sample, differs significantly between the left and the right clip. This is most likely due to potential offsets caused by the photo current at the Schottky contacts which exist between the clips and the sample. Hence, in this way allocation of E_F is impossible. A second approach, which has been successfully applied to Au/Ge(111)-($\sqrt{3}\times\sqrt{3}$) in Sec. 6.2.1, is to use angle-integrated EDCs from two band maps captured along both high symmetry directions and to fit these with Eq. 3.52. Yet, this would require an effective thermal broadening $4k_BT_{\text{eff}}$ which is 6–7 times larger than justifiable from the contributing parameters (see Eq. 3.53).[1] Therefore, the electronic band structure is found to be *insulating* with no clear Fermi edge in the spectrum. This is in agreement with the results of S. Modesti *et al.* [17]. Eventually, a notable surface photovoltage effect is reported to complicate this task, too [17]. It is suggested to result from the Schottky contact established at the Sn-Si interface, where one would expect a downward band bending for n-doped substrates due to the generation of electron-hole pairs at the surface. This generation process and the concomitant recombination rate depend on the incident photon current, the photon energy, and the temperature T [296]. Hence, changing the photon flux should shift the electronic states in energy. However, tuning the beamline exit slits from nearly closed to fully open does not lead to a displacement of the bands in energy at all. In conclusion, it remains unclear, whether or not a surface photovoltage effect is of relevance here, and it will not be accounted for in the following.

Due to the difficulties in Fermi edge determination described above, an extrinsic assignment of the Fermi level is impossible. Instead, a third, intrinsic, and reliable approach has been used here. While the Fermi level is located closely below the conduction band edge in the bulk of the n-type Si(111) samples, the surface states lead to a Fermi level pinning at an approximately mid-gap position at the surface. In assuming the general validity of this picture, the location of E_F should not depend on the exact origin or dispersion of the surfaces states, as long as these possess a sufficient DOS in the bulk

[1] This evaluation is based on ARPES spectra recorded at $T = 33\,\text{K}$, but comparable results are obtained at various temperatures from $T = 10\,\text{K}$ to $T = 300\,\text{K}$.

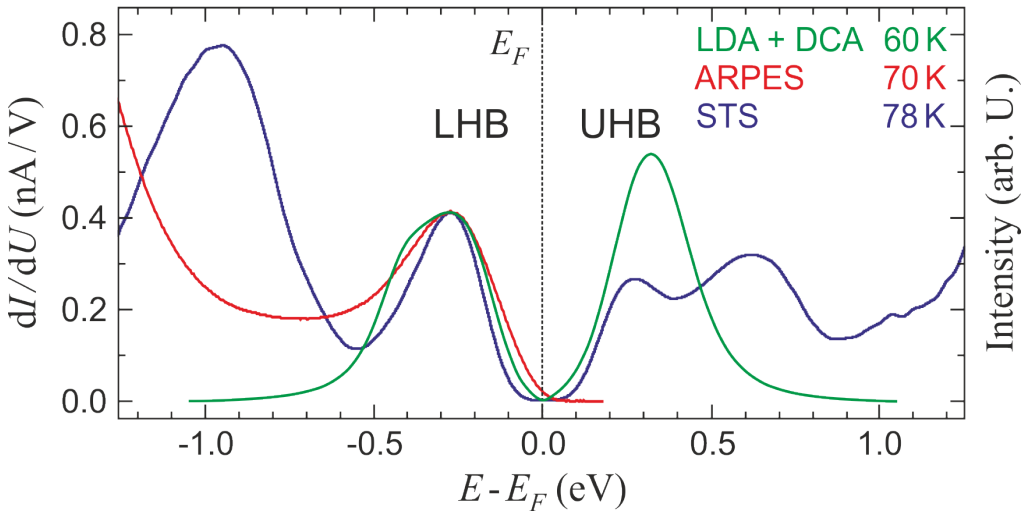

Figure 7.13: *LDOS obtained from ARPES ($T = 70\,K$), STS ($T = 78\,K$), and LDA+DCA ($T = 60\,K$) at the Sn/Si(111)-($\sqrt{3} \times \sqrt{3}$) surface. Tunneling spectra were recorded with a tungsten tip on a $15 \times 15\,nm^2$ sized grid with setpoint values $U_{sp} = -1.5\,V$ and $I_{sp} = 0.5\,nA$. The photoemission LDOS results from an integration of single EDCs between $\pm 0.38\,Å^{-1}$ along $\overline{\Gamma}$–$\overline{M}$ and $\overline{\Gamma}$–$\overline{K}$ in k-space and has been scaled such that the maximum amplitude of the LHB coincides with its STS analog. Both ARPES and STS include a correction to the respective background noise. The LDA+DCA profile stems from integrating the spectral function for $U = 0.66\,eV$ along the full $\overline{\Gamma}$–$\overline{K}$–$\overline{M}$–$\overline{\Gamma}$ path in k-space. The intensity is also scaled to fit to the STS LHB maximum amplitude.*

band gap. Hence, there should also be no difference in the surface Fermi level position between a pure Si(111)-(7 × 7) surface and a metal adatom induced 2DES, such as Sn/Si(111)-($\sqrt{3} \times \sqrt{3}$). For Si(111)-(7 × 7), the distance between the Fermi edge at the surface and the the bulk VBM is known from the literature, i.e., $E_F - E_{VBM} = 0.63\,eV$ [297]. Note that only little volatility in the determination of this value is reported, and results range from 0.58 to 0.65 eV [298]. At this point, one may take advantage of the fact that the VBM can easily be extracted from ARPES band maps in Sn/Si(111)-($\sqrt{3} \times \sqrt{3}$). Thus, the general procedure for Fermi level determination used throughout this chapter is to assign E_F at 0.63 eV above the bulk VBM in each spectrum.

The general applicability of the method is also cross-checked in Fig. 7.13 with the Fermi edge from STS data at a comparable temperature. As an advantage of that technique, E_F is well defined, since it represents the zero voltage limit in I/U scans. STS clearly resolves a prominent feature at $E - E_F = -0.27\,eV$ in the occupied states (LHB). For comparison with ARPES, one needs to consider that STS probes a k-integrated LDOS, which is mainly related to the spectral function at and in vicinity of the $\overline{\Gamma}$ point [299]. Therefore, it is plausible to integrate the k-resolved ARPES band maps only within a certain momentum window around this point to achieve comparability. A common criterion to define the limits of this region is given, by demanding the tunneling current to drop to $1/e$ of its maximum value at $k_{\parallel} = 0\,Å^{-1}$, i.e., $I(k_{limit})/I(0\,Å^{-1}) = e^{-1}$. The momentum dependency of the tunneling current relates to the wave function of the

electron $\Psi(\mathbf{x}, s)$ at the location $\mathbf{x}$ as follows [299]:

$$I(k_\parallel) \propto |\Psi(\mathbf{x}, s)|^2 \propto \left| \sum_{\mathbf{G}} a_{\mathbf{G}} \exp\left[-\left(\kappa^2 + \left| \mathbf{k}_\parallel + \mathbf{G} \right|^2 \right)^{1/2} s \right] \exp\left[i \left(\mathbf{k}_\parallel + \mathbf{G} \right) \cdot \mathbf{x} \right] \right|^2 . \quad (7.1)$$

Apart from the known parameters (see Sec. 3.2), $a_{\mathbf{G}}$ denotes the expansion coefficients of the wave function, and $\mathbf{G}$ is a reciprocal lattice vector. With the silicon work function $\phi_{\mathrm{Si}} = 4.83\,\mathrm{eV}$ [300] and a typical tip-sample distance $s = 8\,\text{Å}$ the $1/e$ criterion is fulfilled for $k_\parallel = 0.38\,\text{Å}^{-1}$. Accordingly, ARPES data along both $\overline{\Gamma}$–$\overline{\mathrm{M}}$ and $\overline{\Gamma}$–$\overline{\mathrm{K}}$ directions are integrated in this momentum range symmetrically around the $\overline{\Gamma}$ point and added up afterwards. In comparison, one finds that a similar spectral feature exists at the same binding energy as in STS, denoted as LHB. Although the spectral width is enhanced in ARPES, the maximum positions do agree well within an error bar of $\pm 0.02\,\mathrm{eV}$, which ascertains the correctness of the intrinsic Fermi edge determination in ARPES, as described above.

The ARPES band structure

Since Sn/Si(111)-($\sqrt{3} \times \sqrt{3}$) is indeed insulating at LT, there is no spectral intensity directly at E_F, and consequently, a FS does not exist. Thus, the overall symmetries of the electronic band structure of Sn/Si(111)-($\sqrt{3} \times \sqrt{3}$) become best visible by a constant energy contour, located at 0.1 eV binding energy, which is shown in Fig. 7.14. A photon energy of $h\nu = 130\,\mathrm{eV}$ has been selected to enhance intensities of the electronic band structure close to E_F, while matrix element effects do not lead to unfavorable extinction at certain momentum vectors here. The sample was cooled to $T = 18\,\mathrm{K}$ to extend the lifetime of the electronic states during the ARPES experiment, with the total energy resolution consistently fixed to $\Delta E_{\mathrm{tot}} = 25\,\mathrm{meV}$ in all measurements.[1] The constant energy map in Fig. 7.14 is dominated by a hexagonal and slightly warped band, that fully lies within the ($\sqrt{3} \times \sqrt{3}$) SBZs. Its corners touch at the $\overline{\mathrm{M}}$ points, where the band is mirrored into neighboring SBZs. Yet, the k-space regions around the $\overline{\Gamma}$ and the $\overline{\mathrm{K}}$ points at 0.1 eV binding energy are basically free from spectral weight. Moreover, a notable momentum broadening governs the electronic band structure. The defect broadening, estimated above as $\Delta k_\parallel = 0.064\,\text{Å}^{-1}$ from LEED, cannot fully account for this alone. Therefore, it probably also relates to an enlarged imaginary part of the self-energy, which is indicative of a reduced QP lifetime due to electron-electron interactions. In comparison with the FSs of Pb/Ge(111)-($\sqrt{3} \times \sqrt{3}$) and Sn/Ge(111)-($\sqrt{3} \times \sqrt{3}$), striking similarities are found. In particular, the roughly hexagonal shape and the reduced spectral weight around the $\overline{\mathrm{K}}$ points are eye-catching features in all three systems [246, 301].

[1] In this section data obtained at different temperatures are shown. This is basically for comparability of STS and theoretical calculations, but also in cases, where spectra are not available at the same quality level for a certain temperature. However, all spectral information remains comparable, since only data within the LT phase are presented, i.e., $T < 100\,\mathrm{K}$ (cf. Sec. 7.2.4).

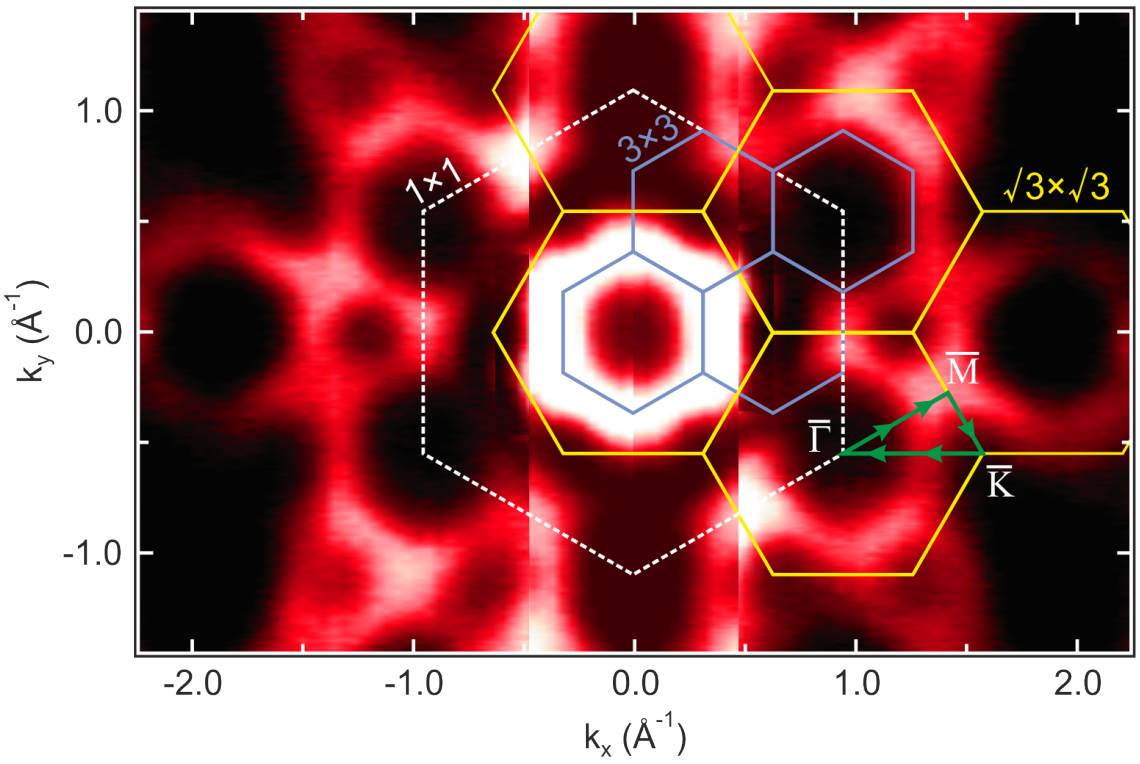

Figure 7.14: *Constant energy surface of Sn/Si(111)-($\sqrt{3} \times \sqrt{3}$) from ARPES FS mapping in an integrated energy window of* $\pm 0.025\,eV$ *around* $E - E_F = -0.1\,eV$*;* $h\nu = 130\,eV$*,* $T = 18\,K$*. Bright contrast corresponds to high intensity in photoemission, and overlaid hexagons indicate different SBZs [*white dashed: *(*1×1*)*, orange: *(*$\sqrt{3} \times \sqrt{3}$*)*, blue: *(*3×3*)]. The green triangle follows the high symmetry directions covered by single band maps in Fig. 7.15. Experimental data were captured in* $k_x < 0\,Å^{-1}$ *regions and have been remapped into the* $k_x > 0\,Å^{-1}$ *area with respect to the mirror symmetry of the* $k_x = 0\,Å^{-1}$ *line.*

More insight to the band dispersion itself is gained, by capturing band maps along the high symmetry directions indicated by the green lines in Fig. 7.14. This has been done in the second SBZ, since matrix elements are convenient there, and the bulk band intensity is significantly reduced compared to the first, but also to the third SBZ. The band dispersion along the whole path is summarized in Fig. 7.15 as the first derivative of the ARPES intensity, i.e., $-\partial I/\partial E$. The most prominent feature is a weakly dispersing state (bandwidth $\sim 170\,meV$), which has a pronounced minimum ($E - E_F = -0.44\,eV \rightarrow \mathbf{A}$) at the $\overline{\mathrm{K}}$ point and a maximum ($E - E_F = -0.27\,eV \rightarrow \mathbf{B}$) between the $\overline{\Gamma}$ and the $\overline{\mathrm{M}}$ point. A second minimum exists at the $\overline{\Gamma}$ point ($E - E_F = -0.34\,eV \rightarrow \mathbf{C}$), and a further maximum between the $\overline{\Gamma}$ and the $\overline{\mathrm{K}}$ point ($E - E_F = -0.31\,eV \rightarrow \mathbf{D}$), while it exhibits a plateau at the $\overline{\mathrm{M}}$ point ($E - E_F = -0.31\,eV \rightarrow \mathbf{E}$). The nature of this band can be clarified by tuning the photon energy. In this way, it is found that there exists no $k_\perp$ dependency, and thus, one must conclude that this band is a pure surface state. Moreover, it follows the periodicity of the ($\sqrt{3} \times \sqrt{3}$) surface reconstruction, and

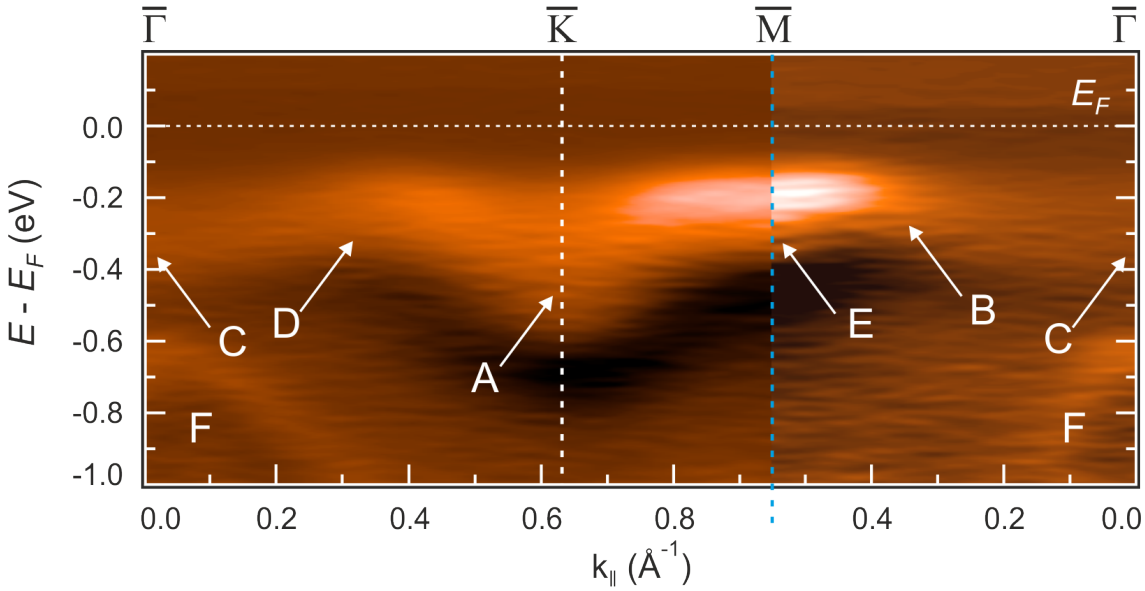

Figure 7.15: *The electronic band structure of the DB-induced surface state in Sn/Si(111)-($\sqrt{3} \times \sqrt{3}$) along both high symmetry directions obtained by ARPES; $h\nu = 130\,eV$, $T = 28\,K$. For better visualization the first derivative of the intensity, i.e., $-\partial I/\partial E$, is shown. Momentum scaling runs from left to right for the band map* left *to the* $\overline{\text{M}}$ *point (blue dashed line), and vice versa to the* right *of* $\overline{\text{M}}$*, since the plot is merged from two distinct scans, each centered at* $\overline{\Gamma}$*. The labels A–F refer to characteristic extremal points in the band structure, which are discussed in the text.*

intensity changes between neighboring SBZs are related to matrix element effects only. Eventually, a second quasi-parabolic, but weaker band exists around the $\overline{\Gamma}$ point (**F**). It relates to the bulk valence band, afore used to determine the Fermi energy.

Contrary to the LDA band structure, the weakly dispersing band is fully occupied, and the surface must be *insulating* in consequence. Moreover, according to these calculations, there should be no intensity at the $\overline{\Gamma}$ point originating from this surface state, in contrast to experimental evidence. Furthermore, the band appears to be backfolded at certain in-plane momenta that do not relate to ($\sqrt{3} \times \sqrt{3}$) symmetry lines, but rather agree with the boundaries of (3×3) SBZs (blue hexagons in Fig. 7.14). In an earlier ARPES study by J. Lobo *et al.* the spectral weight at $\overline{\Gamma}$ has been suggested to originate from a band backfolding as a consequence of an underlying (3×3) structural order [276]. Yet, such an interpretation contradicts the absence of a (3×3) superstructure in LEED. Thus, this order can only be local, and it excludes a possible (3×3) related band backfolding in ARPES. It is more likely that randomly distributed short-ranged (3×3) perturbations, as a building block in the dynamical fluctuation model, exist in Sn/Si(111)-($\sqrt{3} \times \sqrt{3}$), which however, cannot be visible in ARPES. As will be discussed in Sec. 7.2.5, the unexpected intensity at $\overline{\Gamma}$, the occurrence of additional non-($\sqrt{3} \times \sqrt{3}$) related symmetries, and their respective position in k-space relate to a *magnetic ordering* instead.

Electronic correlations in ARPES

As also seen in the constant energy surface, the band is significantly broadened in both energy and momentum, which cannot be explained by a pure defect-related effect only ($\Delta k_{\|} = 0.064\,\text{Å}^{-1}$ from LEED, cf. Sec. 7.2.2). Instead, it is plausible to associate the spectral broadening with correlation-induced contributions to the spectral function. In particular, an enlarged imaginary part of the self-energy indicates a reduced QP lifetime due to the electron-electron interaction. This is corroborated by the enhanced effective electron mass $m_e^* = 1.2\,m_e$, which has been determined by fitting a parabolic band to the dispersion in the vicinity of $\overline{\Gamma}$–$\overline{\text{K}}$. Despite the significant broadening, no spectral weight is found above E_F, and the constant energy surface in Fig. 7.14 does only scratch the trailing edge of the band. Since correlations appear to be strong and due to the weakly dispersing behavior of the band, it is suggestive to argue that we deal with the LHB of a Mott insulator here, which is in agreement with Refs. 16 and 17. Moreover, the ARPES data do not show a signature of the UHB. Hence, the conduction gap size might even surmount the order of 0.3 eV, postulated in LDA+U calculations for $U = 4\,\text{eV}$ [16]. Nevertheless, this extremely large value of U seems to be implausible, and it probably results from an inherent shortcoming of the LDA+U approach, which neglects quantum fluctuations [74]. By means of more appropriate many-body techniques, applied to the problem, it will be shown in Sec. 7.2.4 that a much lower U is sufficient to describe the correlations in this system.

At the end of this section, a brief comparison with STS data and the k-integrated spectral function from LDA+DCA shall be presented in order to support the conclusion of a correlation-induced Mott insulating state in Sn/Si(111)-($\sqrt{3} \times \sqrt{3}$). Details concerning the calculations can be found in Sec. A.1. Here, the reader is again referred to Fig. 7.13. As a common property, the three curves are momentum-independent in this representation and act as some kind of gauge to the DOS. Differences in the temperature should be negligible, since they all belong to the same LT phase (see Sec. 7.2.4). Closer inspection reveals a prominent feature located at $E - E_F \approx -0.27\,\text{eV}$, in all cases. In LDA+DCA, which includes correlations, this is identified as the LHB. Neglecting small deviations in the overall shape and widths of the peak, the good agreement may be seen as a striking proof of a correlation-induced Mott insulating state in Sn/Si(111)-($\sqrt{3} \times \sqrt{3}$). Turning to the unoccupied states, a clear peak, shifted by $\approx 50\,\text{meV}$ between theory and STS, is observed. Despite this somewhat less accurate agreement, assignment of the STS peak to the UHB is strongly motivated by theory. Additional features in both ARPES and STS which are absent in the calculated DOS must arise from bulk band contributions which are not included in the LDA+DCA calculations.

7.2.4 The metal-to-insulator transition in Sn/Si(111)-($\sqrt{3} \times \sqrt{3}$)

This section will address the role of correlations in the MIT, with a particular focus on the size of the Hubbard U. An additional aspect will be the influence of the temperature T.

Control of both parameters allows to explore the phase diagram of Sn/Si(111)-($\sqrt{3}\times\sqrt{3}$) [Fig. 7.6(b)] in more detail.

Access to electronic correlations in theory

From a theoretical point of view, it is necessary to choose an appropriate technique which is capable to include the phenomenon of electronic correlations in a reasonable manner. In this sense, LDA must be seen as an inappropriate approach, which is not that reliable for narrow band systems [14]. Instead, many-body calculations within the LDA+U framework have been utilized in order to address potential correlation phenomena. It turned out in this way that the LT physics present in the Sn/Si(111)-($\sqrt{3}\times\sqrt{3}$) surface are already adequately reproduced [16, 17]. This finding is consistent with recent calculations based on the Hubbard model for a triangular lattice at half-filling [302], where indeed a MIT is proposed to occur for a significantly large U/t ratio. Interestingly, magnetic ordering of the 120° Néel type is found to develop in the insulating phase as a result of nearest-neighbor AFM exchange. This is a quite relevant prediction also for the properties of Sn/Si(111)-($\sqrt{3}\times\sqrt{3}$), as later scrutinized in Sec. 7.2.5.

An even more advanced approach than LDA+U is given by combining classical band structure calculations with dedicated many-body techniques as, e.g., realized by merging LDA and DMFT [74]. While in conventional DFT correlations are only included as an average, the DMFT provides access to all on-site quantum fluctuations [74]. G. Li *et al.* even went beyond this and combined DMFT with two powerful many-body techniques, i.e., the variational cluster approach (VCA) and the dual fermion (DF) approach [303, 304], which both base on the Hubbard model (cf. Sec. 2.2). The aim was to determine a more precise estimate of the critical Coulomb repulsion U_c for the MIT in Sn/Si(111)-($\sqrt{3}\times\sqrt{3}$) [18]. As long as only local fluctuations dominate, the DMFT is usually the technique of choice. But, as soon as non-local correlations gain importance, a sophisticated method such as the DF approach, will give more reliable results, since correlations are included both locally and non-locally here. In turn, the electron proper self-energy (cf. Sec. 3.3.1) will become momentum-dependent, and hence modify the spectral function $A(\mathbf{k},\omega)$, accordingly.

The metal-to-insulator transition as a function of the Hubbard U

The degree of correlation in an electron system is determined by the QP weight $Z_{\mathbf{k}}$ at the Fermi level (see Sec. 3.3.1). Thus, G. Li and coworkers started their recent analysis [18] with a comparison of this quantity within both the DMFT and the DF approach at $T = 61\,\mathrm{K}$ and $T = 300\,\mathrm{K}$. Their results are replotted in Fig. 7.16(a), which is taken from the respective study [18]. Beginning with the lower temperature (green curves), it becomes clear that there is indeed a bandwidth-controlled, i.e., interaction-driven, transition from metal to insulator with increase of U, evidenced by the full loss of QP

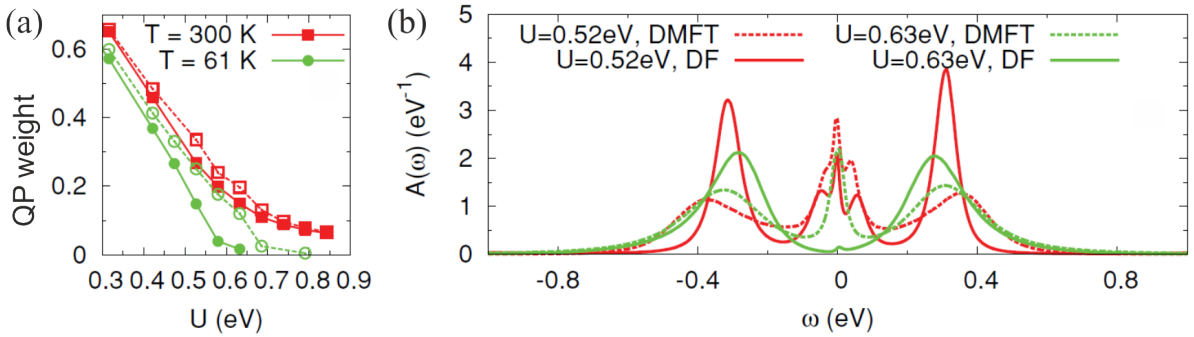

Figure 7.16: *Sn/Si(111)-($\sqrt{3} \times \sqrt{3}$): (a) QP weight in dependence of the on-site Coulomb repulsion U, calculated from DMFT (dashed line) and the DF approach (solid line). (b) Momentum-independent spectral function $A(\omega)$ for two different Coulomb repulsions, i.e., $U = 0.52$ eV and $U = 0.63$ eV. Figures are taken from [18], Copyright (2011) by the American Physical Society.*

weight at the Fermi level. Interestingly, the critical Coulomb repulsion differs between the two methods applied, i.e., $U_{c,\mathrm{DMFT}} = 0.75\,\mathrm{eV}$ (dashed curve) and $U_{c,\mathrm{DF}} = 0.65\,\mathrm{eV}$ (solid curve). In consequence, the relevance of *non-local correlations*, as included in the DF approach, is striking. Moreover, this result, obtained by true many-body techniques, reveals that the earlier reported values for U of up to 4 eV [16] are far from being realistic. The correlation driven transition to an insulating ground state is further elucidated by the k-independent spectral function $A(\omega)$, presented for two distinct values of U in Fig. 7.16(b). For $U = 0.52\,\mathrm{eV}$ the surface is still metallic, and $A(\omega)$ features two incoherent peaks on both sides of the Fermi level, accompanied by a coherent QP peak at E_F ($\omega = 0$). This result is independent of the technique applied, although there are of course differences in the exact spectral function. However, in increasing U to 0.63 eV, which is only slightly below $U_{c,\mathrm{DF}} = 0.65\,\mathrm{eV}$, the spectral weight in the DF approach has almost entirely shifted from E_F to the two incoherent peaks. Such a behavior is the *Hallmark* of a Mott MIT driven by correlations, and the incoherent peaks must be assigned to the LHB and the UHB, respectively. Moreover, this suppression at $U = 0.63\,\mathrm{eV}$ is a pure result of the inclusion of non-local correlations, since the QP weight is only slightly reduced and still present in the DMFT. In addition, it is important to note that despite this non-locality, a comparison of DF and additional VCA calculations indicates that the short-range correlations are still dominating [18].

Similar results with respect to the determination of a more realistic critical U parameter have been reported by S. Schuwalow *et al.* [74]. They utilized combined DFT and many-body DMFT calculations and derived a critical U in the order of $\sim 0.6\,\mathrm{eV}$, accompanied by a weak first-order phase transition. The size of the Mott-Hubbard gap was found to be $E_{\mathrm{gap}} = 0.2\,\mathrm{eV}$ for $U = 0.7\,\mathrm{eV}$, with the Hubbard bands located at approximately 0.3 eV above and below the Fermi level, respectively. These results are in good agreement with the experimentally obtained parameters in this thesis and in the literature, which are based on ARPES and KRIPES [276, 277, 279]. In conclusion, this

also supports the finding by G. Li and coworkers that a smaller U is sufficient to induce a transition from metal to an insulating state in Sn/Si(111)-($\sqrt{3} \times \sqrt{3}$).

Temperature dependence of the metal-to-insulator transition

The second relevant parameter in the Mott MIT, besides U, is the temperature T. Its influence shall first be discussed on the basis of Fig. 7.16(a). On the one hand, at $T = 61\,\mathrm{K}$ the increase of U triggers the transition, but a further decrease of T (not shown) does not influence the critical U parameter anymore [18]. On the other hand, above a certain critical temperature T_c, the QP weight will not drop to zero even for a very large U, but will instead remain at a finite value. This indicates that at elevated temperatures the correlation-induced MIT does not occur. As an example Fig. 7.16(a) displays the DMFT (red dashed line) and the DF (red solid line) QP weights at $T = 300\,\mathrm{K}$. These do not differ significantly and eventually approach a finite value for large U. Thus, no insulating state develops, and rather a pseudogap opening occurs, with the system remaining metallic. Therefore, tuning the temperature is a second possibility to trigger the MIT in Sn/Si(111)-($\sqrt{3} \times \sqrt{3}$), as also evidenced experimentally [17, H7]. This represents an additional proof of the Mott insulating ground state established in this 2DES. With respect to the nature of the phase transition, G. Li *et al.* propose that it is a second-order one at zero temperature, while it is rather a bad first-order transition at finite temperatures [18].

The possibility to trigger the MIT by altering the temperature T shall now be scrutinized by combining ARPES data and theoretical calculations. The latter base on the LDA+DCA (cf. Sec. A.1), which introduces correlation effects to the single-particle calculations within the DFT step-by-step [305, 306]. It represents an alternative to conventional many-body techniques, such as the DMFT, and has in particular prevailed as a unique tool to answer issues of correlation and magnetic ordering in Sn/Si(111)-($\sqrt{3} \times \sqrt{3}$) [H7].

From the experimental side, S. Modesti *et al.* have shown ARPES data that reveal a loss of spectral weight at the Fermi level in agreement with a transition from metallic to insulating behavior upon decreasing temperatures [17]. In Fig. 7.17(a) these results (black curves) are compared with ARPES data on Sn/Si(111)-($\sqrt{3}\times\sqrt{3}$) obtained within this thesis (colored curves). EDCs at three different in-plane momenta along $\overline{\Gamma}$–$\overline{\mathrm{M}}$ in the ($\sqrt{3} \times \sqrt{3}$) SBZ (labeled "1", "2", and "3") are depicted for RT and LT ($T = 30\,\mathrm{K}$), respectively. All LT spectra have a notable reduction of spectral weight at the Fermi level in common, which provides evidence of a MIT upon temperature lowering. The peak positions of the surface state do agree well, while higher binding energy features differ slightly. Moreover, data from this thesis are less broadened in energy, possibly due to a higher surface quality of the sample. In agreement with the full dispersion of the surface state, shown for $T = 28\,\mathrm{K}$ in Fig. 7.15, metallicity is absent in the full k-range of the ($\sqrt{3} \times \sqrt{3}$) SBZ at LT. This is verified by the LDA+DCA derived DOS shown in Fig. 7.17(b). Here, the Coulomb repulsion $U = 0.66\,\mathrm{eV}$ has been determined, by

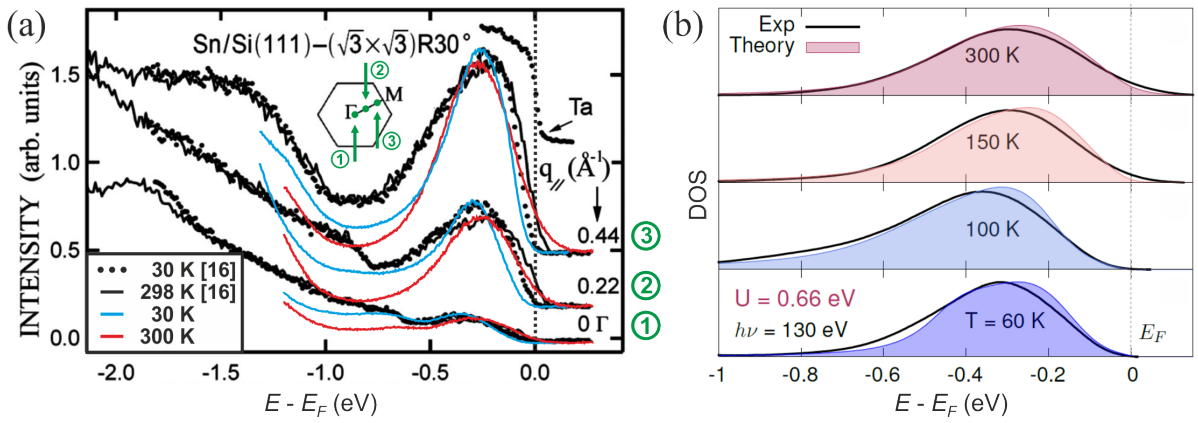

Figure 7.17: *(a) Comparison of ARPES EDCs ($h\nu = 130\,eV$) at RT and LT ($T = 30\,K$) for three distinct in-plane momenta (labeled "1", "2", and "3") along $\overline{\Gamma}$–$\overline{M}$ in the ($\sqrt{3} \times \sqrt{3}$) SBZ of Sn/Si(111). Intensities of the colored curves (data obtained in this thesis) are scaled to agree in their maximum amplitude at the LHB peak with the corresponding maxima of the black curves (data from [17]). At LT a clear reduction of spectral weight at E_F is visible. Original data and the graph layout are taken from [17], Copyright (2007) by the American Physical Society. (b) DOS obtained from the momentum-integrated ARPES dispersion ($h\nu = 130\,eV$) along $\overline{\Gamma}$–$\overline{K}$–$\overline{M}$–$\overline{\Gamma}$ (black lines) in comparison with the LDA+DCA analog ($U = 0.66\,eV$) at four different temperatures. Bulk band contributions have been subtracted from the experimental DOS [H7], Copyright (2013) by Nature Publishing Group.*

requiring the calculated DOS to be the best possible approximation to the experiment. Importantly, this returns a Coulomb repulsion that also fulfills $U > U_c = 0.65\,eV$ [18], which is sufficient to establish a Mott insulating ground state. It turns out that a good overall agreement between the k-integrated spectral function from ARPES (black lines) and theory (color shaded curves) is given at all temperatures investigated. Importantly, spectral weight shifts to lower binding energies, as the temperature increases. This is revealed to be rather a gradual process than an instant one. In particular, it turns out that Sn/Si(111)-($\sqrt{3} \times \sqrt{3}$) is metallic for $T = 150\,K$ and above, but remains insulating for $T = 100\,K$ and below [H7]. Theory is able to specify the critical parameter, i.e., the on-set temperature $T_c = 120\,K$ of the transition. It should be noted that it is larger than the T_c reported by S. Modesti *et al.*, i.e., $T_c = 60\,K$, which in contrary was described as a rather sharp transition. However, due to the presence of quantum fluctuations an abrupt change from metal to insulator seems unlikely, and the gradual transition found in this thesis does much more resemble a MIT of the Mott-Hubbard type. The comparison in Fig. 7.17(a) also shows an even stronger reduction of spectral weight in the ARPES data of this thesis, necessary in the gradual transition to explain the larger T_c. Finally, the marginal gain in spectral weight at the Fermi level at RT suggests that Sn/Si(111)-($\sqrt{3} \times \sqrt{3}$) in its metallic phase must be regarded as a *bad metal* with a pseudo band gap.

Comparison of correlations strengths

In merging the structural and electronic properties of Sn/Si(111)-($\sqrt{3} \times \sqrt{3}$) obtained within this thesis with those from the literature (see Sec. 7.1.2), it is justifiable to add this system to the class of *undistorted* 2D Mott insulators at surfaces. This also means that one has to distinguish between the related surface systems introduced before as follows.

- Undistorted 2D Mott insulators
  - K/Si(111)-B-($\sqrt{3} \times \sqrt{3}$)
  - 6*H*-SiC(0001)-($\sqrt{3} \times \sqrt{3}$)
  - Sn/Si(111)-($\sqrt{3} \times \sqrt{3}$)
- Distorted bad metals
  - Pb/Ge(111)
  - Sn/Ge(111)

This division can further be substantiated, by comparing the Coulomb repulsion U. It is somewhat larger in Sn/Si(111) ($U = 0.66\,\text{eV}$; [H7]) than in Pb/Ge(111) ($U \sim W \approx 0.4\,\text{eV}$; [246]) and in Sn/Ge(111) ($U = 0.55\,\text{eV}$; [254]). Yet, this is far from K/Si(111)-B ($U = 1.3\,\text{eV}$; [12]) and 6*H*-SiC(0001) ($U \geq 2.0\,\text{eV}$; [13]), but obviously just enough to drive Sn/Si(111)-($\sqrt{3} \times \sqrt{3}$) into its Mott insulating ground state. This tendency does also become evident when comparing the relevant ratio of on-site repulsion U and bandwidth W, as presented in Tab. 7.2. Here, Sn/Si(111)-($\sqrt{3} \times \sqrt{3}$) exhibits the largest value ($U/W \approx 3.9$) among the group-IV adatom systems.

Finally, the absence of a perpendicular atomic distortion in the 2D Mott insulators makes them an ideal realization of triangular lattices that exhibit spin frustration. In this regard, the delicate issue of magnetic ordering in Sn/Si(111)-($\sqrt{3} \times \sqrt{3}$) will be addressed in the following section.

Table 7.2: *Magnitudes of the Coulomb repulsion U, the bandwidth W, and the ratio U/W for selected 2DESs. U in Pb/Ge(111) is an estimate from the literature only.*

System	U (eV)	W (eV)	U/W
6*H*-SiC(0001)	2.3 [13]	0.2 [242]	11.5
K-Si(111)-B	1.3 [12]	0.2 [12]	6.5
Sn/Si(111)	0.66 [H7]	0.17 [this study]	3.9
Sn/Ge(111)	0.55 [254]	0.2 [254]	2.8
Pb/Ge(111)	0.4 [14]	0.4 [246]	1.0

7.2.5 Magnetic ordering in the presence of spin frustration

The phenomenon of spin frustration, as inherent to triangular lattices, and the concomitant question on magnetic ordering despite the spin frustration in the Mott insulating state [307], have been reasons for multiple theoretical studies involving the Hubbard model. The main outcome of most many-body calculations is that such a system tends to order in terms of a spiral 120 ° Néel AF for sufficiently large correlations ($U/t \sim 9$) [302]. On the other hand, also the possibility of a spin liquid ground state, i.e., a RVB state, has been proposed [234, 308]. On the basis of experimental data, it is likely that the Mott insulators κ-$(ET)_2Cu_2(CN)_3$ and $Na_4Ir_3O_8$ possess such a RVB state [309, 310]. Theoretically, magnetic ordering in triangular lattices is often effectively described by model Hamiltonians, such as the classical Heisenberg one $\mathcal{H} = -\sum_{i,j} J_{ij}\mathbf{S}_i\mathbf{S}_j$ [69]. Here, J_{ij} introduces the pairwise exchange between the spins at lattice sites i and j. In localized systems it is often sufficient to restrict the exchange to nearest-neighbors, which results in the formation of the non-collinear 120 ° Néel type AF [69]. However, two different major scenarios have been discussed:

- Isotropic AFM exchange, i.e., $J \approx J'$, with J and J' corresponding to nearest-neighbor and next-nearest-neighbor exchange, respectively. In this first scenario, the ground state will be the spiral 120 ° Néel AF, displayed in Fig. 7.18(a).
- In case of anisotropic exchange, i.e., J' is enhanced, magnetic order is prohibited by quantum fluctuations, and a 2D spin liquid ground state is favorable.

In this view, it was an unexpected result that a *collinear* AFM order is established at a small J'/J ratio in a spatially anisotropic AF [311]. This marks a promising result, since it offers a perspective to realize long-range magnetic order other than the usual 120 ° Néel AF, if anisotropy is sufficiently high.

120 ° Néel antiferromagnetic and collinear antiferromagnetic orders

In order to discuss a potential magnetic ordering in Sn/Si(111)-($\sqrt{3} \times \sqrt{3}$), one should start with the possibility of the spiral 120 ° Néel AF, depicted in Fig. 7.18(a), and consider how it would modify the spectral function $A(\mathbf{k}, \omega)$. In the Fermi liquid regime the momentum-dependent QP dispersion $\epsilon_{\mathbf{k}}$ dominates in $A(\mathbf{k}, \omega)$. It basically follows the LDA derived single-particle band (Eq. A.2), which is sketched in Fig. 7.18(c). So far, this is the half-filled band situation, as typical of the class of dilute group-IV adatom induced ($\sqrt{3} \times \sqrt{3}$) reconstructions on (111) semiconductor surfaces. The situation changes drastically, when a SDW, as the spiral one in Fig. 7.18(a), is formed. Then, each in-plane momentum vector $\mathbf{k}$ is intermixed with $\mathbf{k}+\mathbf{Q}$ by exchange Bragg scattering. $\mathbf{Q}$ denotes the magnetic ordering vector related to the (3×3) SBZ, see Fig. 7.18(b). This leads to a SDW-induced band backfolding at (3×3) SBZ boundaries, as depicted in Fig. 7.18(d). Here, the energy eigenstates $|\Psi_{\mathbf{k}}\rangle$ do not possess a sharp momentum any more, i.e., $|\Psi_{\mathbf{k}}\rangle = u_{\mathbf{k}}|\mathbf{k}\rangle + v_{\mathbf{k}}|\mathbf{k}+\mathbf{Q}\rangle$, with the LDA derived eigenstates $|\mathbf{k}\rangle$ and

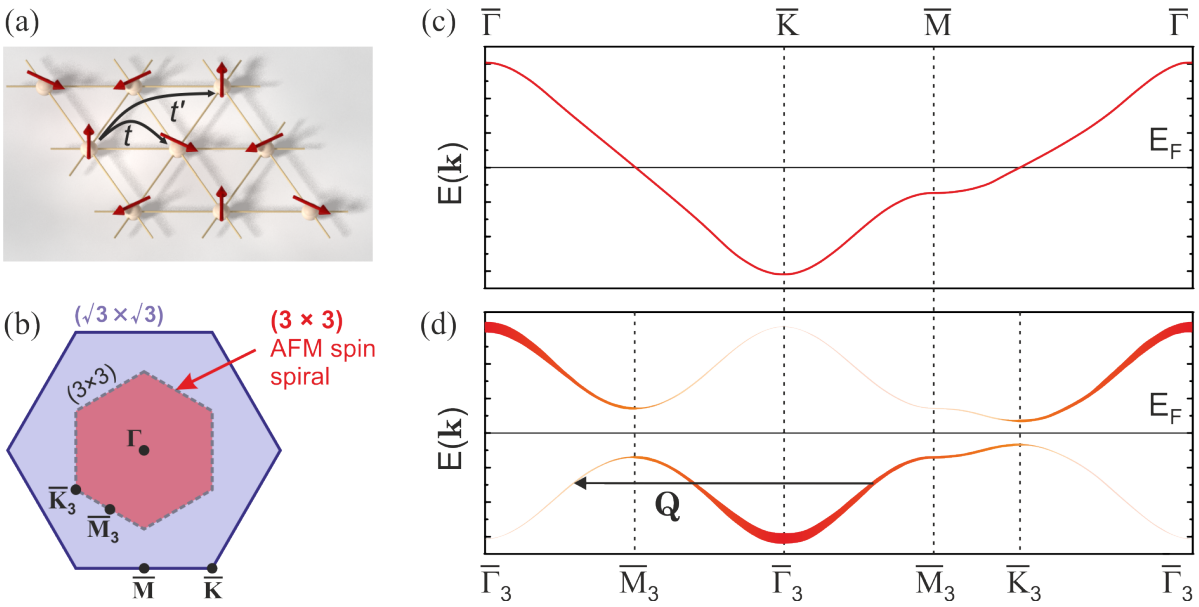

Figure 7.18: *(a) Schematic representation of the spiral 120° Néel AFM spin ordering on a triangular lattice. t and t' are the nearest-neighbor and next-nearest-neighbor hopping parameters, respectively. (b) SBZs of the $(\sqrt{3} \times \sqrt{3})$ reconstruction and a possible (3×3) zone, corresponding to the larger magnetic unit cell of the spiral AF. (c) QP band dispersion in the Fermi liquid regime, akin to the corresponding LDA band dispersion (Eq. A.2). (d) QP (heavy line) and shadow band (light line) dispersion, induced by a SDW band backfolding related to a (3×3) ordered AFM 120° Néel state.* $\mathbf{Q}$ *denotes the magnetic ordering vector here [H7], Copyright (2013) by Nature Publishing Group.*

$|\mathbf{k}+\mathbf{Q}\rangle$. The standard coherence factors within BCS theory $u_\mathbf{k}$ and $v_\mathbf{k}$ fulfill the condition $u_\mathbf{k}^2 + v_\mathbf{k}^2 = 1$. They describe the SDW gap features which are due to the new AFM order [312]. The spectral function now exhibits large spectral weight for $u_\mathbf{k}^2 > 1/2$ (heavy line) and small spectral weight for $v_\mathbf{k}^2 < 1/2$ (light line). In the ARPES experiment a momentum-dependent distribution of spectral weight is the conspicuous consequence, i.e., the probability to detect photoelectrons at $\mathbf{k}$ now relates to $u_\mathbf{k}^2$ and for $\mathbf{k} + \mathbf{Q}$ to $v_\mathbf{k}^2$. In conclusion, a SDW-induced Bragg scattering of electrons leads to *shadow bands* [Fig. 7.18(d)], displaced by the magnetic ordering vector $\mathbf{Q}$ to momentum regions without occupied states in the non-magnetic case [Fig. 7.18(c)]. Such a scenario is reminiscent of the square lattice high-temperature superconducting cuprates [312].

A well approved theoretical tool to investigate magnetic ordering is to calculate the static spin susceptibility $\chi(\mathbf{q}, \omega)$, where $\mathbf{q}$ is a reciprocal lattice vector. The respective locations of maxima in $\chi(\mathbf{q}, \omega)$ in the k-space then relate to the present kind of magnetism. For Sn/Si(111)-$(\sqrt{3} \times \sqrt{3})$ this has been done in a recent study by G. Li *et al.* within the DF frame [18]. Fig. 7.19 gives an overview, on how $\chi(\mathbf{q}, \omega)$ is modulated by the on-site Coulomb repulsion U here. On the basis of the weakly nested tight-binding FS [Fig. 7.12(c)] one would not expect maxima in the spin susceptibility to locate directly at the $\overline{\mathrm{K}}$ points for small values of U. In fact, this can be observed in Fig. 7.19(a) for

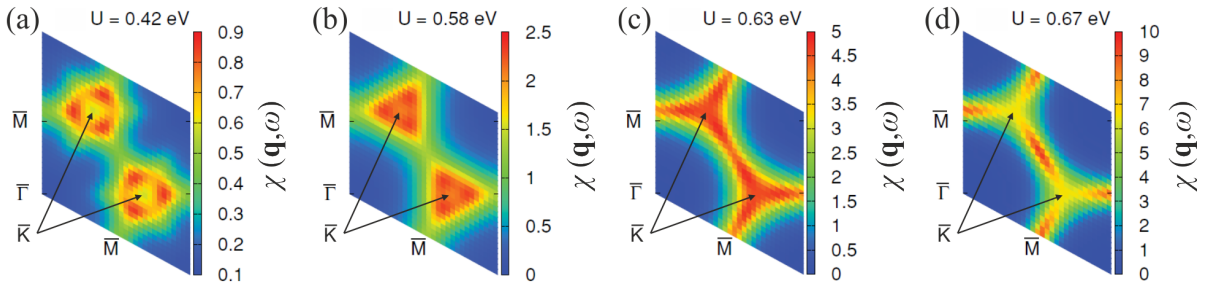

Figure 7.19: *Sn/Si(111)-($\sqrt{3} \times \sqrt{3}$): Color scale plots of the static spin susceptibility $\chi(\mathbf{q}, \omega)$ in k-space, calculated within the DF approach at $T = 61\,K$ as a function of the on-site Coulomb repulsion U, which is increased from (a) to (d). For $U \ll U_{c,\mathrm{DF}} = 0.65\,eV$ (a) $\chi(\mathbf{q}, \omega)$ peaks close to the $\overline{\mathrm{K}}$ points, while for $U \gtrsim U_{c,\mathrm{DF}}$ (d) the maxima are located at the $\overline{\mathrm{M}}$ points. Figures are taken from [18], Copyright (2011) by the American Physical Society.*

$U = 0.42\,\mathrm{eV}$, which is far from the critical $U_{c,\mathrm{DF}} = 0.65\,\mathrm{eV}$. Here, the peak positions (red intensity) do not locate at the $\overline{\mathrm{K}}$ points, but close nearby. This is also in agreement with earlier calculations for the hypothetical triangular surface system Si/Si(111)-($\sqrt{3} \times \sqrt{3}$) [14], where the susceptibility does not peak at high symmetry points. A further increase in U [(b)–(d)] then leads to a general enhancement of the spin susceptibility. In agreement with Ref. 302 and other studies, one should expect $\chi(\mathbf{q}, \omega)$ to peak at $\overline{\mathrm{K}}$ in case of a sufficiently large U, corresponding to the spiral 120° Néel order. Surprisingly, this is not the case, but it unexpectedly occurs at $\overline{\mathrm{M}}$ instead. Importantly, this means that the spins do not align in terms of a spiral 120° Néel AF, but establish a collinear antiferromagnetic (CAF) spin pattern, which has been denoted as "row-wise (RW)-AFM" order in Ref. 18. Nevertheless, the amplitude of $\chi(\mathbf{q}, \omega)$ is still high at the $\overline{\mathrm{K}}$ points, which might be interpreted as an indication of competing magnetic orders at the atomic scale.

Magnetic ordering addressed by combining ARPES and LDA+DCA

In returning to the ARPES band structure in Fig. 7.15, the band dispersion appears to be backfolded at new symmetry lines, that do not agree with the original ($\sqrt{3} \times \sqrt{3}$) lattice order. Moreover, in an earlier ARPES study of the Sn/Si(111)-($\sqrt{3} \times \sqrt{3}$) surface state dispersion a band back folding was also reported and claimed to correspond to a (3×3) *structural* order [276]. However, only recently a connection to a possible SDW [14], i.e., a *magnetic* order instead of a geometric one, has been drawn [16, 17]. Yet, such an interpretation disagrees with the collinear AF suggested by G. Li and coworkers [18]. Therefore, the following comparison of the single-particle spectral function from ARPES and LDA+DCA is the first to scrutinize the possibility of an AFM ordering other than the spiral SDW one. We will see in the subsequent discourse that this comparison represents an ideal tool to investigate the magnetic ordering at the Sn/Si(111)-($\sqrt{3} \times \sqrt{3}$) surface. Importantly, the LDA+DCA calculations base on the undistorted triangular Sn/Si(111)-($\sqrt{3} \times \sqrt{3}$) surface, with all Sn atoms residing in the same lattice plane.

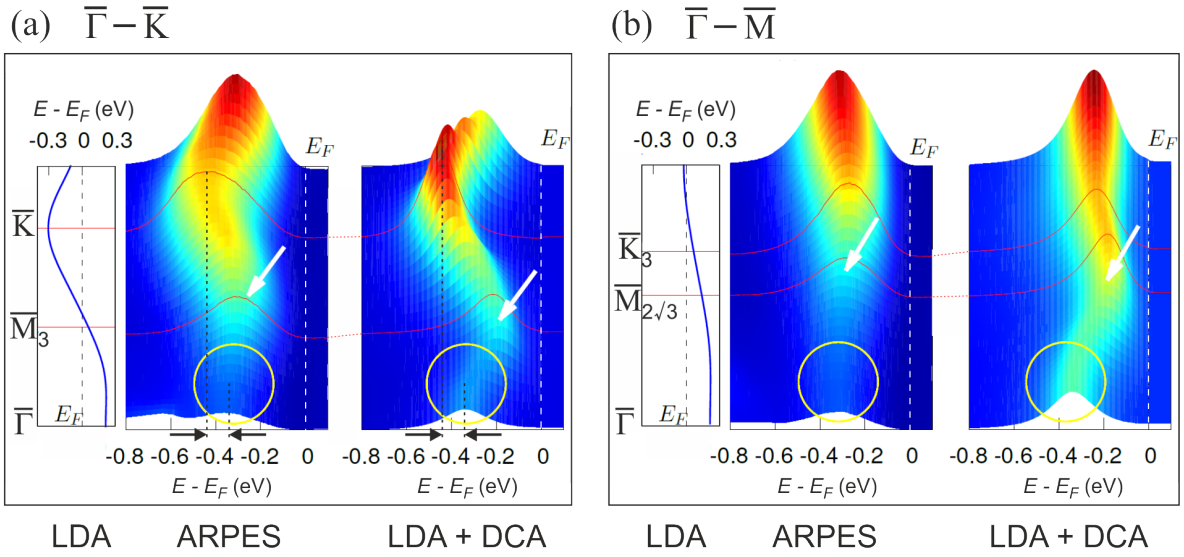

Figure 7.20: *(a) Comparison of the dispersion of the LDA derived single-particle band (left) with the corresponding spectral function $A(\mathbf{k},\omega)$ (color scale plot) in ARPES (middle; $T = 60\,K$, $h\nu = 130\,eV$) and LDA+DCA (right; $T = 60\,K$) along the $\overline{\Gamma}$–$\overline{\mathrm{K}}$ direction of the $(\sqrt{3}\times\sqrt{3})$ SBZ in Sn/Si(111). White arrows mark the in-plane momenta, where a band backfolding takes place, whereas red lines highlight the EDCs at high symmetry points. Circles focus on the* shadow bands *at $\overline{\Gamma}$, and dashed black lines indicate the difference in band minimum energies between $\overline{\mathrm{K}}$ and $\overline{\Gamma}$. (b) The same comparison as in (a), but along the $\overline{\Gamma}$–$\overline{\mathrm{M}}$ high symmetry direction [H7], Copyright (2013) by Nature Publishing Group.*

Thus, any symmetry in the band structure other than $(\sqrt{3}\times\sqrt{3})$ cannot arise from a geometric superstructure.

A detailed comparison of the spectral function at $T = 60\,\mathrm{K}$ from experiment and theory is presented in Fig. 7.20 [H7]. Here, one finds a good overall agreement, in what concerns the dispersion of the surface state along the $\overline{\Gamma}$–$\overline{\mathrm{K}}$ direction (a). Slight deviations in the k-dependent intensity are most likely due to matrix element effects in the ARPES data. Moreover, the experimentally obtained spectral function is notably broadened in energy, a result of defect scattering, as elucidated in Sec. 7.2.2, and electronic correlations. Importantly, there is no Fermi level crossing as in the LDA band (left panel), but a faint spectral feature (yellow circles) is clearly seen at the $\overline{\Gamma}$ point, which is referred to as *shadow band* in the following. Nevertheless, spectral weight is notably smaller here in comparison to the $\overline{\mathrm{K}}$ point. A further observation is the unexpected band backfolding (cf. Fig. 7.15) approximately around the $\overline{\mathrm{M}}_3$ point (white arrows), which is also not present in the LDA band. All these findings, and in particular the appearance of the shadow band around $\overline{\Gamma}$, suggest an electronic dispersion modified from $(\sqrt{3}\times\sqrt{3})$ to (3×3), possibly due to a magnetic order in form of a spiral SDW [cf. Fig. 7.18(a) and (d)] or, alternatively, a geometric surface reconstruction. In turning to the same comparison along the $\overline{\Gamma}$–$\overline{\mathrm{M}}$ direction (b), similar conclusions can be drawn, i.e., an absent Fermi level crossing, a *shadow band* at $\overline{\Gamma}$, and a band backfolding.

Closer scrutiny reveals that the whole situation in Sn/Si(111)-$(\sqrt{3}\times\sqrt{3})$ is much more

complex and exciting. A band backfolding in agreement with the occurrence of a SDW would demand a degeneracy of the *shadow band* at $\overline{\Gamma}$ with the QP band at $\overline{\mathrm{K}}$. However, as indicated by the two dashed black lines in Fig. 7.20(a), the band energies do actually not reside at the same binding energy. Moreover, inspection of Fig. 7.20(b) unveils that the backfolding (white arrows) along $\overline{\Gamma}$–$\overline{\mathrm{M}}$ does not occur at $\overline{\mathrm{K}}_3$, but more closely to a new symmetry line ($\overline{\mathrm{M}}_{2\sqrt{3}}$), corresponding to an enlarged unit cell of $(2\sqrt{3} \times 2\sqrt{3})$ order. In conclusion, the first assumption of a (3×3) band backfolding of the SDW type must be incorrect. Thus, the spiral 120° AFM ordering [Fig. 7.18(a)] does not represent the true ground state in Sn/Si(111)-($\sqrt{3} \times \sqrt{3}$). In addition, also a geometric (3×3) surface reconstruction is not a feasible explanation of the spectral function observed, since only one perpendicular location, i.e., only a single bonding configuration, has been allowed in the LDA+DCA for the tin atoms (see Sec. A.1).

In a second step, it shall now be clarified, whether any other kind of magnetic order is established in Sn/Si(111)-($\sqrt{3} \times \sqrt{3}$) despite the inherent spin frustration, i.e., whether still a magnetic Mott insulator is the ground state. Characteristic features include the emergence of *shadow bands*, and spectral weight, being transferred from the area of minimum band energy around $\overline{\mathrm{K}}$ to the region adjacent to the $\overline{\Gamma}$ point, as visualized schematically in Fig. 7.18(c) and (d). While the first indication has already been evidenced in Fig. 7.20, the latter can be quantified from numerical calculation of the average occupation number

$$n(\mathbf{k}) = \int_{-\infty}^{\infty} \mathrm{d}E A(\mathbf{k}, E) f(E, T) \tag{7.2}$$

in the LDA+DCA. The Fermi-Dirac distribution $f(E, T)$ ensures that only occupied states are accounted for. Accordingly, Eq. 7.2 can be regarded as a measure to the occupied spectral weight at a given momentum $\mathbf{k}$. In order to trace back a transfer of spectral weight between different momentum regions which is caused by electronic correlations, one proceeds as follows in the LDA+DCA. The ($\sqrt{3} \times \sqrt{3}$) SBZ is intersected into nine equal area clusters which describe three different momentum regions "A", "B", and "C", see Fig. A.1. Then $n(\mathbf{k})$ is calculated within each region and plotted in dependence of the Coulomb repulsion U (Fig. 7.21). Here, it becomes evident that $n_{\overline{\mathrm{M}}}$, the spectral weight in sector "B", remains independent of the actual Coulomb repulsion. This region corresponds to the Fermi level crossing of the LDA band. Thus, this finding simply relates to a shift of spectral weight from the QP peak to the incoherent parts of the spectral function on both sides of E_F, i.e., the LHB and UHB, without loosing spectral weight in region "B". This is consistent with the opening of a correlation-induced Mott-Hubbard band gap. Yet, when turning to the region "A", i.e., around the $\overline{\Gamma}$ point, a linear increase of $n_{\overline{\Gamma}}$ upon enlarging the Hubbard U is observed. This is consistent with the appearance of the *shadow band* in this sector. Note that for zero correlations there is no spectral weight present in sector "A" at all. On the contrary, in region "C" a linear decrease of $n_{\overline{\mathrm{K}}}$ is found for increasing U. Thus, and since $n_{\overline{\mathrm{M}}}$ remains constant, the complementary development of curves "A" and "C" must be interpreted as a spectral weight

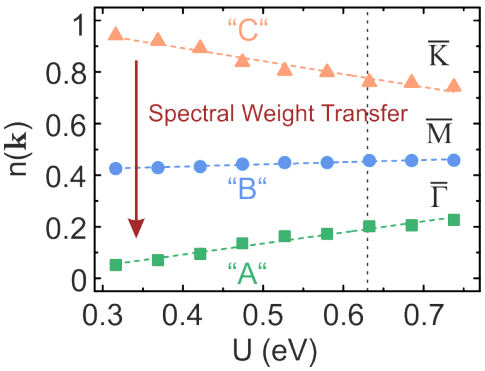

Figure 7.21: *Average occupation number $n(\mathbf{k})$ in dependency of the on-site Coulomb repulsion U in Sn/Si(111)-($\sqrt{3}\times\sqrt{3}$). Colors correspond to the LDA+DCA sectors "A" (green), "B"(blue), and "C" (light orange), defined in Fig. A.1. For increasing U a notable transfer of spectral weight from "C" to "A", i.e., from the region around $\overline{\mathrm{K}}$ to $\overline{\Gamma}$ is found. The dashed perpendicular line corresponds to $U = 0.66\,eV$, as derived in Sec. 7.2.4 [H7], Copyright (2013) by Nature Publishing Group.*

transfer from the region around the $\overline{\mathrm{K}}$ point to the one around $\overline{\Gamma}$ [H7]. In the relevant case of $U = 0.66\,\mathrm{eV}$ (dashed perpendicular line), found by approximating the DOS in LDA+DCA to the ARPES one, about 20 % of the spectral weight has been redistributed between "A" and "C". All these findings are well consistent with the assumption of a correlation driven MIT to a magnetic Mott insulating ground state.

The row-wise-antiferromagnetic order in Sn/Si(111)

The analysis above has clearly ruled out the (3×3) spiral SDW as the magnetic order in the Mott insulating ground state. Instead, one has to raise the question, if the RW-AFM order, suggested to occur in Sn/Si(111)-($\sqrt{3}\times\sqrt{3}$) by G. Li *et al.* [18], is a better candidate here. Therefore, it is necessary to point out which magnetic SBZ is related to this CAF order in a triangular lattice. This shall be explained on the basis of Fig. 7.22. In the real space lattice (a) the spins are oriented collinearly, while alternating rows of up and down spins exist despite the frustration. The pink box indicates the corresponding magnetic unit cell of $(2\sqrt{3}\times\sqrt{3})$ order. With respect to the threefold symmetry of the Si(111) substrate, there must exist three different magnetic domains, rotated against each other by 120 °. Thus, in a reciprocal space experiment as ARPES one will observe a superposition of these three domains [colored rectangles in Fig. 7.22(b)]. This results in a combined magnetic SBZ of $(2\sqrt{3}\times2\sqrt{3})$ periodicity (pink hexagon). Thus, if the RW-AFM order is the true magnetic arrangement in the Sn/Si(111)-($\sqrt{3}\times\sqrt{3}$) system, band backfolding must occur with respect to the $(2\sqrt{3}\times2\sqrt{3})$ zone boundaries instead of the (3×3) ones. A first hint towards answering this question has already been obtained from the spectral function displayed in Fig. 7.20, where it turned out that the surface state is rather backfolded with regard to the $\overline{\mathrm{M}}_{2\sqrt{3}}$ than the $\overline{\mathrm{M}}_3$ symmetry point. This important finding is now further scrutinized in

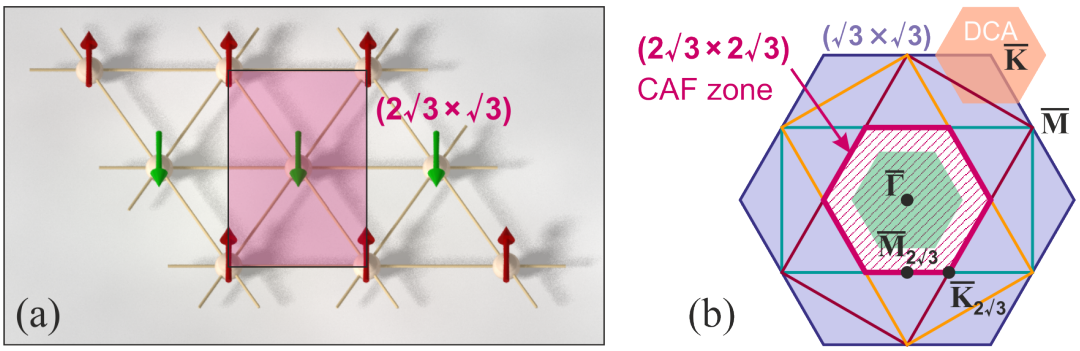

Figure 7.22: *(a) RW-AFM collinear ordering of spins on a triangular lattice despite spin frustration. The magnetic unit cell is indicated by the pink box. (b) Schematics of the ($2\sqrt{3} \times 2\sqrt{3}$) CAF zone (pink) within the geometric ($\sqrt{3} \times \sqrt{3}$) SBZ. The CAF zone stems from a superposition of three rectangular ($2\sqrt{3} \times \sqrt{3}$) zones, being rotated by 120° each (colored rectangles). Green and light red hexagons correspond to clusters within the DCA scheme (see Sec. A.1) [H7], Copyright (2013) by Nature Publishing Group.*

Fig. 7.23(a), which displays the ARPES derived spectral function as a false color plot, overlaid by the band dispersion from the LDA+DCA calculations. While color coding in ARPES is conform with Fig. 7.20, the line width of the calculated dispersion corresponds to the momentum-dependent amplitude of the spectral function. First of all, the general agreement between experiment and theory is obvious. It is also straight forward to see that the shadow band at $\overline{\Gamma}$ (pronounced by the inset with enhanced contrast) is located at a lower binding energy than the QP peak at $\overline{\mathrm{K}}$. Band backfolding corresponding to the (3×3) ordered SDW scenario in Fig. 7.18(d) is assumed to take place at $\overline{\mathrm{M}}_3$. In fact, this is not the case, which becomes clear when regarding the dispersion in both empty and filled states. Instead, a much better agreement is found for a potential backfolding with respect to the $\overline{\mathrm{M}}_{2\sqrt{3}}$ symmetry line [H7]. This is, what one would expect to observe in case of the CAF ordering. Thus, one may conclude from the comparison of ARPES, LDA+DCA, and the spin susceptibility calculations in Ref. 18 that a CAF order is actually established in this isotropic triangular AF, despite the presence of spin frustration.

In consequence, one has to ask, why the surface unexpectedly exhibits RW-AFM order, and why it does not prefer the conventionally assumed 120° Néel order. For answering this question, G. Li and coworkers have calculated the tight-binding non-interacting DOS with nearest-neighbor hopping terms only, as usually done when studying triangular Hubbard models [18]. In a second step, additional next-nearest-neighbor hopping parameters were included. The main result is a strong deviation in the non-interacting DOS between both scenarios. Subsequently, on this basis also the spin susceptibility was calculated. It is found to peak at the $\overline{\mathrm{K}}$ points in the case of nearest-neighbor hopping only. This would then correspond to the spiral 120° Néel magnetic ordering. However, for next-nearest-neighbor hopping terms included, the situation changes dramatically, and $\chi(\mathbf{q}, \omega)$ is found to peak at $\overline{\mathrm{M}}$ now, as indicative of the RW-AFM order. There-

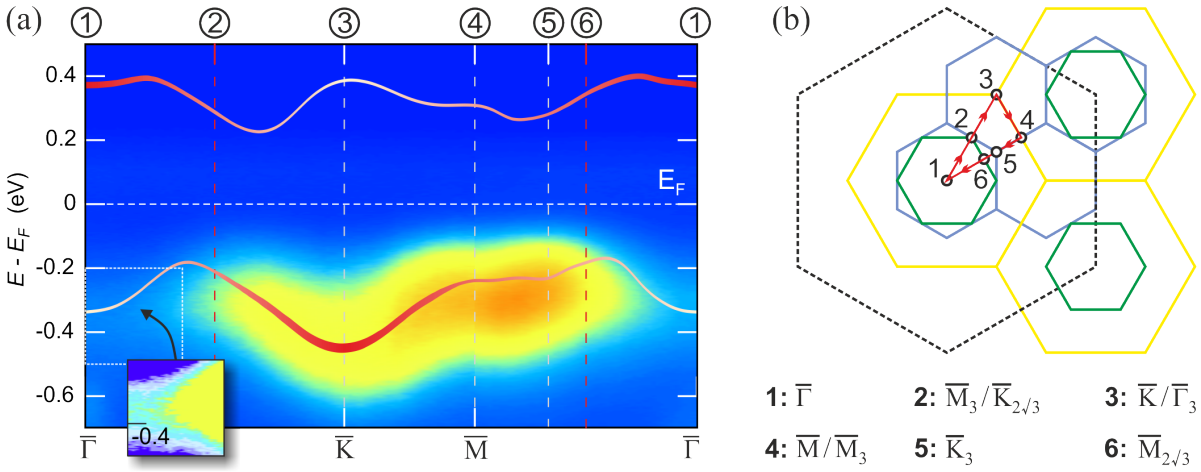

Figure 7.23: *(a) Comparison of the QP dispersion in Sn/Si(111)-($\sqrt{3} \times \sqrt{3}$) from the LDA+DCA (red curve; $T = 60\,K$) with the ARPES spectral function (false color plot; $T = 60\,K$, $h\nu = 130\,eV$) in the original ($\sqrt{3} \times \sqrt{3}$) SBZ (lower labels) and the (3×3) and ($2\sqrt{3} \times 2\sqrt{3}$) SBZs [upper numbering, refer to (b)]. The inset is a replica of the shadow band region close to $\overline{\Gamma}$ (dashed box), modified to display features with enhanced contrast. It evidences the non-degeneracy of the surface state between $\overline{\Gamma}$ and $\overline{\mathrm{K}}$. (b) Drawing of the relevant SBZ geometries in k-space: dashed black hexagon (1×1), yellow hexagons ($\sqrt{3} \times \sqrt{3}$), blue hexagons (3×3), green hexagons ($2\sqrt{3} \times 2\sqrt{3}$). The red path corresponds to the momentum range covered in (a), with numbers indicating the locations of high symmetry points [H7], Copyright (2013) by Nature Publishing Group.*

fore, as a striking result, hopping processes beyond the nearest-neighbor lattice sites are essential in precisely describing the magnetic properties at the Sn/Si(111)-($\sqrt{3} \times \sqrt{3}$) surface.

In conclusion, the discussion in this section has truly revealed that an unexpected and long-range ordered collinear magnetic state, i.e., the RW-AFM order, prevails over the more anticipated spiral 120° Néel AFM order or a disordered spin-liquid ground state. In particular, the important role played by beyond nearest-neighbor interactions, here included by higher order hopping terms, is a surprising, but nonetheless relevant result in respect of future studies on frustrated triangular lattices. As an outlook, one may suggest here that a detailed comparison of ARPES and LDA+DCA should be regarded as a reliable tool to track complex spin patterns in frustrated magnetic 2DESs at surfaces. This should in general be adoptable to other related surfaces, opening up the opportunity to explore a variety of additional frustrated systems. Moreover, such analysis might be suitable to answer the question, whether even a spin liquid might be stabilized in the presence of geometrical frustration.

8 Summary and outlook

The present thesis elucidates low-dimensional physical phenomena and properties occurring in the 2D limit of a metallic adlayer on top of a semiconducting substrate. This encloses the specific characteristics of the atomic arrangement at surfaces and extends to the coupling of spin and orbital degrees of freedom. Moreover, the lateral confinement of charge carriers at surfaces can lead to a strong electron-electron interaction which goes beyond the picture of nearly free electrons. These aspects, among many others, have been studied on the basis of the three different prototypical 2DESs Pt/Si(111)-($\sqrt{3}\times\sqrt{3}$), Au/Ge(111)-($\sqrt{3}\times\sqrt{3}$), and Sn/Si(111)-($\sqrt{3}\times\sqrt{3}$).

Atomic ordering at the surface

Physical quantities in low dimensions, like the electronic band structure and the charge density distribution, are essentially affected by the local atomic structure at the surface. However, for several 2DESs the exact atomic arrangement is not fully understood today. This is essentially true for Pt/Si(111)-($\sqrt{3}\times\sqrt{3}$), whose structure was studied in detail in this thesis.

Experiments by STM reveal the formation of reconstructed domains (size $\sim 10\,\mathrm{nm}^2$), which contain ($\sqrt{3}\times\sqrt{3}$) ordered arrays of protrusions. The domains are surrounded by a meandering network of domain walls. These boundaries possess anti-phase character, i.e., adjacent domains are phase shifted. Such a dense network of domain walls was suggested to arise from an intricate interplay of mechanic strain and surface energy in this thesis. Closer scrutiny of protrusions inside the domains revealed for the first time that these must arise from Pt trimers instead of single atoms. This is consistent with a Pt coverage of 1 ML, which is three times larger than assumed in previous studies. A detailed analysis of the boundary region between domains and their adjacent walls disclosed a Pt trimer rotation of 30 ° with respect to the substrate. This represents an unexpected *symmetry breaking* at the surface of a semiconductor and an exclusive example of the adsorption of a *chiral* structure in the family of ($\sqrt{3}\times\sqrt{3}$) reconstructed surfaces. Based on these results, a refined and novel structural model for Pt/Si(111)-($\sqrt{3}\times\sqrt{3}$) was proposed here, which is capable of describing all geometric properties resolved in STM.

Structural details have also been considered for the related Au/Ge(111)-($\sqrt{3}\times\sqrt{3}$) system. Here, it was previously revealed that the surface is best described within the CHCT model, which is now commonly accepted in the literature. Yet, total energy calculations, which can provide a measure of the energetic stability of the surface, did

not exist so far. Here, theoretical modeling within the LDA was successfully utilized to exclude an instability of the surface towards an alternative atomic configuration. Experimentally, the preparation process could be optimized so that large terraces, covered by $(\sqrt{3} \times \sqrt{3})$ ordered domains with a low defect density ($\sim 2\,\%$), shape the overall image of the surface. Similar to Pt/Si(111)-$(\sqrt{3} \times \sqrt{3})$, the existence of phase-slip domains was evidenced in STM, while periodically ordered domains were shown to be larger here.

Finally, also the atomic structure of Sn/Si(111)-$(\sqrt{3} \times \sqrt{3})$, which is formed at the smaller nominal adsorbate coverage of 1/3 ML, has been studied in this thesis. STM measurements reflect the strongly localized nature of the Sn p_z type orbitals and reveal a high quality of surface preparation, characterized by a point defect density of less than 4 % of the reconstructed surface area. A particular focus has been put on the six different types of defects and on their arrangement at the surface, where in some cases a very local (3×3) order is induced.

Based on the structural information obtained within this thesis, future studies could focus on the **adsorption of molecules** on top of these surfaces. In particular, the chiral structure of the Pt trimers at the Si(111) surface might serve as a basis for enantiomeric adsorption. In addition, the catalytic character of Pt could facilitate reactions at the atomic scale here.

Tunability of interactions

The single-particle spectral function, which is directly accessible in ARPES, represents the key quantity to study interactions of charge, spin, and lattice in low dimensions.

i) *Charge-lattice interactions*: The electronic band structure of Au/Ge(111)-$(\sqrt{3} \times \sqrt{3})$ has been scrutinized for the first time with respect to an instability towards the formation of a CDW. This was motivated by the prominent shape of the FS, which is generated by an intense and hexagonally warped surface state of Au origin, being suggestive of FS *nesting*. However, such a scenario was discarded in the present thesis, since both the band structure and the respective LEED pattern remain unaffected in a wide temperature range from $T = 300\,\mathrm{K}$ to $T = 10\,\mathrm{K}$.

ii) *Electron-electron interactions*: Electronic correlations in surface 2DESs can be tuned by careful selection of the adsorbate-substrate composition. Regarding this, Au/Ge(111)-$(\sqrt{3} \times \sqrt{3})$ is less correlated, as indicated by the rather low effective electron masses near the Fermi level. The situation is different for Sn/Si(111)-$(\sqrt{3} \times \sqrt{3})$, where the adsorbate layer thickness is reduced to 1/3 of a ML. The tetravalent tin atoms introduce directional and strongly localized p_z type orbitals at a large in-plane spacing, which establishes Sn/Si(111)-$(\sqrt{3} \times \sqrt{3})$ as a model system for the study of electronic correlations in a triangular lattice. Pure LDA band structure calculations fail to correctly describe the system and predict a half-filled surface state. On the basis of ARPES experiments at LT, clear evidence of a weakly dispersing and insulating surface state was provided in this thesis. Its effective band mass is significantly enhanced over that in LDA, and the spectral weight is depressed at E_F, which must be regarded as

an indication of the prominent role of correlations at this surface. In agreement with many-body theory, this band has to be interpreted as the LHB of a Mott insulator. These novel insights are consistent with previous reports that predict the surface to transit to a Mott insulating ground state below $T = 60\,\mathrm{K}$ [17]. The details of the phase transition have been reinvestigated here, by comparing the temperature dependence of the spectral function from ARPES with that derived from many-body LDA+DCA calculations. This theoretical method is particularly suitable here, since it accounts for electronic interactions beyond the nearest-neighbor lattice sites, which turned out to be essential in the description of Sn/Si(111)-($\sqrt{3} \times \sqrt{3}$). As a major result of this thesis, the effective on-site repulsion is found to be much smaller than earlier assumed, i.e., $U = 0.66\,\mathrm{eV}$, which is sufficient to drive the system into its insulating ground state at LT. In addition, the phase transition is revealed to be rather a gradual process from a correlated insulator to a bad metal at $T_c \approx 120\,\mathrm{K}$.

Besides the novel insights into interactions in 2DESs provided in this thesis, additional studies can be envisioned here:

- **Tunability of the Mott MIT**: The evolution of the band gap in dependence of the temperature, as successfully explored here by ARPES and many-body theory, should also be addressed by STS. In this way, both the LHB and the UHB could be probed simultaneously. In addition, further extrinsic parameters as, e.g., surface dopants, should be used to scrutinize, whether a band filling controlled MIT could be triggered. This would help to explore the phase diagram in more detail.

- **Degree of correlations**: It would be interesting to investigate, how strongly the degree of correlations can be modified by combining different adatom and substrate atom species. This would allow to fabricate custom-made correlated electron systems involving distinct orbital characters.

- **2D superconductivity**: Surface dopants could also be used in order to drive a correlated 2DES into a superconducting state. In this regard, it has been proposed that an unconventional d-wave superconducting phase should exist in Sn/Si(111)-($\sqrt{3} \times \sqrt{3}$) [16], see phase diagram in Fig. 7.6(b). Also a reduction of the Coulomb repulsion U is suggested as a different route towards unconventional superconductivity and should be realizable by heavy substrate doping [16]. The associated energy gaps should in principle be resolvable in STS and hopefully also in very-high resolution ARPES experiments.

Magnetic order in a triangular lattice

Due to its strongly correlated nature and its triangular lattice structure, Sn/Si(111)-($\sqrt{3} \times \sqrt{3}$) was predestined to scrutinize the delicate interplay of electron-electron interactions and spin frustrations. In particular, this concerns the key issue, whether a magnetic order can be established in the lattice of non-magnetic Sn atoms despite the

spin frustrations. By utilizing a novel approach, combining the complementary strengths of LDA calculations, state-of-the-art ARPES, and many-body LDA+DCA modeling to evaluate the spectral function, this question was successfully addressed in this thesis.

The general idea was that any magnetic superstructure which does not coincide with the lattice periodicity should have its signature imprinted on the spectral function. In fact, ARPES band maps display a band backfolding suggestive of a (3×3) order at LT, accompanied by the formation of a *shadow band* in vicinity of the SBZ center. Such a band backfolding could not be attributed to a higher order lattice periodicity, since all Sn atoms reside in the very same plane, as presumed in the LDA+DCA calculations and evidenced in STM. Moreover, the shadow band is absent in LDA band structure calculations, which do not account for electronic interactions. Instead, its formation must be related to a magnetic coupling of the spins in the Mott insulating ground state, as unveiled by comparing ARPES with many-body LDA+DCA in this thesis. Surprisingly, a closer inspection of the backfolding in experiment and theory revealed that the magnetic superstructure does not relate to a (3×3) spiral AF, but it rather agrees with a $(2\sqrt{3} \times 2\sqrt{3})$ collinear antiferromagnetic (CAF) order, as previously proposed on the basis of spin susceptibility calculations [18]. The formation of this collinearly ordered magnetic ground state despite spin frustrations is basically owed to electronic interactions beyond the nearest-neighbor lattice sites, as included in the many-body LDA+DCA calculations.

These inspiring results certainly call for extended experimental and theoretical studies, which should address the following points:

- **Magnetically resolving STM** would represent the ideal tool to directly probe the orientation and size of the local moments. This would further help to specify the length scale on which the magnetic moments are coupled in phase. However, the persistent dynamical fluctuations of the surface lattice atoms, present even at LT, could complicate such measurements.

- **The fundamental approach** of combining single-particle LDA, ARPES, and many-body LDA+DCA calculations to resolve magnetic orders in triangular lattices still bears a huge potential to scrutinize other related surface systems besides Sn/Si(111)-$(\sqrt{3} \times \sqrt{3})$. In particular, this approach could also help to clarify the mechanisms behind the 2D superconductivity recently reported for 2DESs of atomic layers of In and Pb on Si(111) [39].

Spin-orbit coupling in two dimensions

By utilizing explicitly heavy adatoms with rather delocalized s orbitals, one may quit the regime of strong electronic interactions. Instead, SOC effects gain relevance, and the surface states may lose their spin degeneracy. A key question concerns the spin texture at the FS, which, for most surface systems, turned out to be much more complex than originally described in the Rashba model.

To address SOC effects at surfaces, Au/Ge(111)-($\sqrt{3} \times \sqrt{3}$) has been selected in this thesis. Here, the main quasi-parabolic and Au derived surface state exhibits a significant broadening in energy and momentum, as demonstrated by ARPES. This could not be attributed to scattering at defects or domain walls alone. Yet, on the basis of advanced DFT modeling, including a self-interaction correction, the broadening was assigned to a SOI-induced band splitting into two superimposed, but fully spin-polarized subbands. Particular interest arises from the complex spin topology predicted at the FS. In contrast to a conventional Rashba spin splitting, a significant canting of the spin out of the surface plane, accompanied by a perpendicular undulation with respect to the surface symmetries, was found theoretically here. Utilizing the 3D spin resolution in SARPES, salient consistency with the calculated spin polarization could be obtained. Moreover, additional *in-plane rotations* of the spin were evidenced for the first time in a surface 2DES. Interestingly, this closely resembles the spin texture theoretically proposed for the 3D topological insulator Bi_2Te_3 [27]. Such a spin pattern "beyond Rashba" was ideally modeled in this thesis, by introducing higher order Dresselhaus momentum terms to the original Rashba Hamiltonian.

Future experiments and theoretical approaches are suggested to focus on the following issues:

- **SOI at related surfaces**: With regard to the complexity of the spin pattern, the combined strengths of theoretical and experimental 3D spin determination should be applied to other relevant semiconductor surfaces. A prime candidate would be Au/Si(111)-($\sqrt{3} \times \sqrt{3}$), which has a similar band structure, though implications of the SOI are unknown today.

- **Spin-flip processes**: A further promising experiment has recently been proposed for the related spin pattern at the FS of the dense β-Pb/Ge(111)-($\sqrt{3} \times \sqrt{3}$) system [313]. Accordingly, it should be possible to induce spin-flip excitations between the two spin-polarized subbands by means of optical spectroscopy. Interestingly, these possess a strong momentum-dependent excitation probability, which calls for experimental clarification.

- **Tunability of the spin pattern**: It would be relevant to clarify, whether, and if so, to which extent modifications to the spin pattern at the FS can be induced by depositing additional heavy adatoms, such as Bi and Pb, on top of the reconstructed Au/Ge(111) surface.

- **Combining SOI and electronic correlations**: As a novel and promising approach, one should try to merge the physics of electronic interactions and SOC in a single 2DES. A possible route would be to use heavy adatoms which possess localized orbitals at the same time (e.g., Pb). Particular interest arises from the electronic band structure and the ground state characteristics in such a system.

In conclusion, this thesis has demonstrated that low-dimensional physical properties can be tuned specifically by careful selection of the relevant building blocks from the *atomic toolbox*. The huge variety of options to combine different atom species allows to assemble *custom-made* low-dimensional structures, which can be dominated by, e.g., electronic correlations or the SOC, as demonstrated in this thesis. In particular, the beauty of the spin pattern in Au/Ge(111)-($\sqrt{3} \times \sqrt{3}$), which lies at the interface to the spin physics in 3D topological insulators, represents a direct proof that a SOC far beyond the basic Rashba model prevails in *real-world* systems. Moreover, the conceptional approach of combining explicit many-body calculations with state-of-the-art ARPES, as established here for Sn/Si(111)-($\sqrt{3} \times \sqrt{3}$), should represent a novel route to the local magnetic order in frustrated triangular lattices quite generally. In all, the fundamental aspects revealed in this thesis may help to advance our understanding of the fascinating physics hosted in low dimensions.

A Appendix

A.1 The LDA+DCA approach

In order to theoretically address the complex many-body physics and competing interactions at LT in Sn/Si(111)-($\sqrt{3} \times \sqrt{3}$) (Ch. 7), a combination of band structure determination within the local density approximation (LDA) and the dynamical cluster approximation (DCA) is used. This approach has similarly been described in Ref. H7.

LDA calculations first require to construct an atomic slab of the system under investigation. For Sn/Si(111)-($\sqrt{3} \times \sqrt{3}$) it consists of six silicon layers, complemented by 1/3 ML of tin atoms at T_4 lattice sites on top of the slab, and a layer of hydrogen atoms at the rear side, that saturates the silicon DBs [H7]. This configuration follows the commonly accepted structural model, introduced in Sec. 7.1.2, and does not include any perpendicular displacement of Sn atoms as, e.g., in the 1U2D configuration. The essential Hamiltonian in the problem, i.e.,

$$\mathcal{H}_{\mathrm{LDA}} = \sum_{k,\sigma} \epsilon_k c^{\dagger}_{k\sigma} c_{k\sigma}, \tag{A.1}$$

with the creation and annihilation operators $c^{\dagger}_{k\sigma}$ and $c_{k\sigma}$, is basically the same as the kinetic energy part in Eq. 2.15. The single-particle band ϵ_k has a rather isolated character, being clearly separated from any other band, which is mainly a consequence of the involved Sn $5p_z$ orbitals. It is then projected onto the maximally localized Wannier functions (MLWF) [314, 315], prior to the determination of the single particle hopping parameters t_i, with i indicating hopping among nearest-neighbors ($i = 1$), next-nearest-neighbors ($i = 2$), etc. The t_i's are then derived from the MLWF matrix elements of Eq. A.1, which leads to the dispersion relation

$$\begin{aligned}
\epsilon_k \;=\; & -2t_1[\cos(k_x) + 2\cos(\frac{\sqrt{3}}{2}k_y)\cos(\frac{k_x}{2})] \\
& -2t_2[\cos(\sqrt{3}k_y) + 2\cos(\frac{3}{2}k_x)\cos(\frac{\sqrt{3}}{2}k_y)] \\
& -2t_3[\cos(2k_x) + 2\cos(k_x)\cos(\sqrt{3}k_y)] \\
& -4t_4[\cos(\frac{5}{2}k_x)\cos(\frac{\sqrt{3}}{2}k_y) + \cos(2k_x)\cos(\sqrt{3}k_y) + \cos(\frac{k_x}{2})\cos(\frac{3\sqrt{3}}{2}k_y)] \\
& -2t_5[\cos(2\sqrt{3}k_y) + 2\cos(3k_x)\cos(\sqrt{3}k_y)],
\end{aligned} \tag{A.2}$$

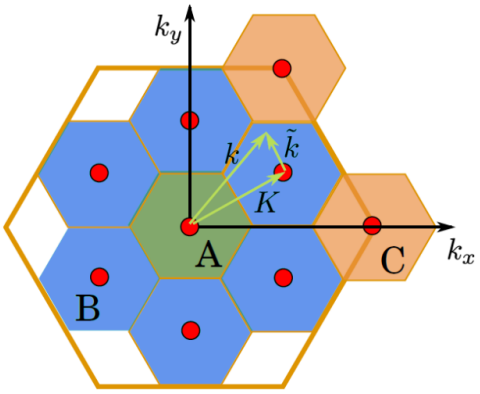

Figure A.1: *The first SBZ of Sn/Si(111)-($\sqrt{3} \times \sqrt{3}$), coarse-grained into nine equal area sectors, containing a basis of three inequivalent sectors, i.e., "A" (green), "B" (blue), and "C" (light orange). Red circles indicate the respective centers of each sector. For further details refer to text [H7], Copyright (2013) by Nature Publishing Group.*

with $t_1 = -52.7\,\text{meV}$ [H7]. The beyond nearest-neighbor hopping parameters scale with t_1 as follows: $t_2/t_1 = -0.3881$, $t_3/t_1 = 0.1444$, $t_4/t_1 = -0.0228$, $t_5/t_1 = -0.0318$. The corresponding dispersion relation is plotted in Fig. 7.12(a) of Sec. 7.2.3.

In a second step, one extends Eq. A.1 to

$$\mathcal{H} = \mathcal{H}_{\text{LDA}} + U \sum_i n_{i\uparrow} n_{i\downarrow} \tag{A.3}$$

in order to account for electronic correlations by the Coulomb term, including the on-site repulsion parameter U and the occupation number operators $n_{i\uparrow}$ and $n_{i\downarrow}$ [H7]. Here, the DCA enters the field, which is utilized to solve this equation. It basically recovers the infinite lattice, by augmenting N_c-site clusters with periodic boundary condition. Translational invariance is conserved in the cluster, by modulating the intercluster hopping amplitudes with the superlattice momentum $\tilde{\mathbf{k}}$ and the intracluster hopping integrals. In Fig. A.1 the first SBZ of Sn/Si(111)-($\sqrt{3} \times \sqrt{3}$) is intersected into $N_c = 9$ equal area hexagons, "A", "B", and "C" as basis of the DCA calculations. This zoning is just a consequence of the underlying lattice symmetry in the 9-site cluster scheme of the DCA. Any momentum $\mathbf{k}$ is then obtained as $\mathbf{k} = \mathbf{K} + \tilde{\mathbf{k}}$, with $\mathbf{K}$ as the cluster momentum. Following the DCA, the Green's function must be coarse-grained [305] over $\tilde{\mathbf{k}}$ by

$$\overline{G}_\sigma(\mathbf{K}, i\omega_n) = \frac{N_c}{N} \sum_{\tilde{\mathbf{k}}} \left(i\omega_n + \mu - \epsilon(\mathbf{K} + \tilde{\mathbf{k}}) - \overline{\Sigma}_\sigma(\mathbf{K}, i\omega_n) \right)^{-1}. \tag{A.4}$$

Then, the DCA self-consistency loop is terminated by the Dyson equation, $\mathcal{G}_\sigma^{-1}(\mathbf{K}, i\omega_n) = \overline{G}_\sigma(\mathbf{K}, i\omega_n)^{-1} + \overline{\Sigma}_\sigma(\mathbf{K}, i\omega_n)$. For calculating the cluster self-energy $\overline{\Sigma}_\sigma(\mathbf{K}, i\omega_n)$ from $\mathcal{G}_\sigma(\mathbf{K}, i\omega_n)$, one needs to solve a N_c-site cluster problem, which is done by utilizing the continuous-time quantum Monte Carlo (QMC) method with the paramagnetic condition, i.e., $\overline{G}_\uparrow(\mathbf{K}, i\omega_n) = \overline{G}_\downarrow(\mathbf{K}, i\omega_n)$. Importantly, despite using only a 9-site cluster in

the calculation, each hopping process in Eq. A.2 is contained in Eq. A.4, after augmenting the 9-site cluster to infinite size. Hence, the LDA single-band model with beyond nearest-neighbor hopping parameters (Eq. A.2) differs significantly from those reported elsewhere, which do only consider nearest-neighbor hopping in the triangular model. The LDA+DCA scheme is concluded, by determining the size of the Coulomb repulsion. This is achieved by adjusting U, until the best agreement in the calculated DOS with the corresponding k-integrated DOS in ARPES is reached. In this way, $U = 0.66\,\mathrm{eV}$ is derived for Sn/Si(111)-($\sqrt{3} \times \sqrt{3}$) (see Sec. 7.2.4).

A.2 SARPES data analysis by the two-step fitting routine

The evaluation of SARPES data basically follows the guidelines in Refs. 22 and 116. In the COPHEE experiment, described in Sec. 3.3.2, six independent spin-resolved intensities $I_\alpha^\uparrow(E_\mathrm{kin}, \mathbf{k})$, and $I_\alpha^\downarrow(E_\mathrm{kin}, \mathbf{k})$ are obtained, with $\alpha = x, y, z$ corresponding to the three quantization axes of the Mott detectors.[1] Accordingly, the spin-integrated intensity along each polarimeter axis is given by

$$I_\alpha(E_\mathrm{kin}, \mathbf{k}) = I_\alpha^\uparrow(E_\mathrm{kin}, \mathbf{k}) + I_\alpha^\downarrow(E_\mathrm{kin}, \mathbf{k}). \tag{A.5}$$

The spin-resolved intensities therein can then be transformed to

$$P'_\alpha(E_\mathrm{kin}, \mathbf{k}) = \frac{I_\alpha^\uparrow(E_\mathrm{kin}, \mathbf{k}) - I_\alpha^\downarrow(E_\mathrm{kin}, \mathbf{k})}{I_\alpha^\uparrow(E_\mathrm{kin}, \mathbf{k}) + I_\alpha^\downarrow(E_\mathrm{kin}, \mathbf{k})}, \tag{A.6}$$

which defines the *measured* spin polarization, since it is directly obtained from measured raw data.[2] As an example, $I_y^\uparrow(k_x)$ and $I_y^\downarrow(k_x)$ in Fig. A.2(b) transform to the measured polarization P'_y shown in Fig. A.2(c) (upward triangles). By a simple conversion one further derives

$$\begin{aligned} I_\alpha^\uparrow(E_\mathrm{kin}, \mathbf{k}) &= \frac{I_\alpha(E_\mathrm{kin}, \mathbf{k})}{2} \cdot (1 + P'_\alpha(E_\mathrm{kin}, \mathbf{k})), \\ I_\alpha^\downarrow(E_\mathrm{kin}, \mathbf{k}) &= \frac{I_\alpha(E_\mathrm{kin}, \mathbf{k})}{2} \cdot (1 - P'_\alpha(E_\mathrm{kin}, \mathbf{k})). \end{aligned} \tag{A.7}$$

Due to the low efficiency in spin detection one is typically restricted to measurements of single MDCs or EDCs instead of a fully spin-resolved band map or FS. As this thesis contains spin-resolved MDCs along the x-coordinate at a defined kinetic energy only, the

[1] In more precise terms, one obtains a total of eight spin-resolved intensities. However, due to the geometrical arrangement of the two Mott stages, $I_z^\uparrow$ and $I_z^\downarrow$ are measured twice in both polarimeters, thus yielding six separate intensities for further evaluation [122].

[2] For non-artificial data as in the experiment, a further correction by the instrument-specific Sherman function is necessary.

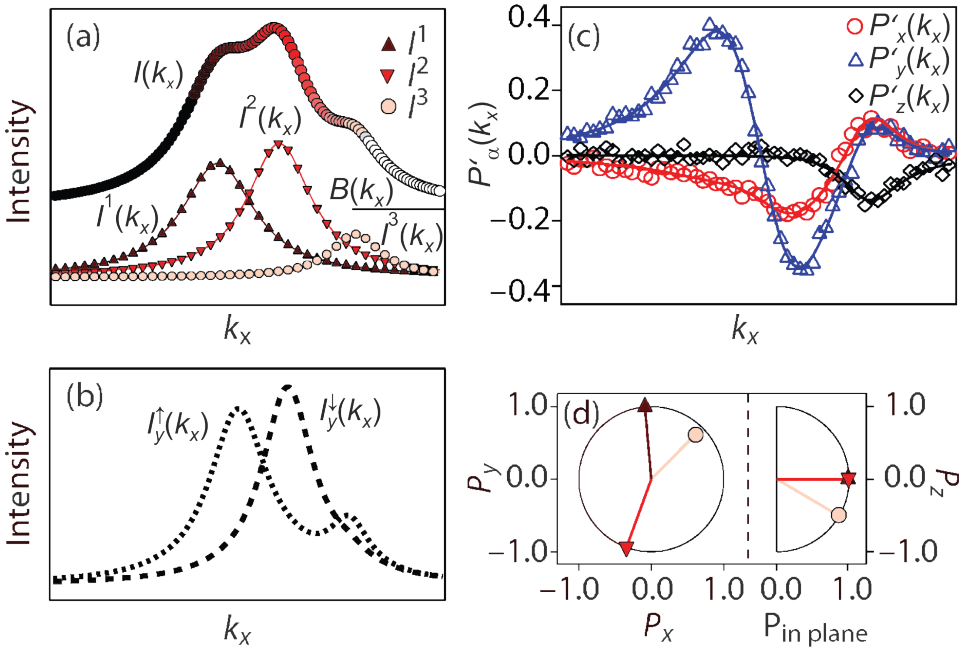

Figure A.2: *(a) Illustration of the two-step fitting routine on the basis of an artificially generated MDC $I(k_x)$. In the first step, the spectrum is deconvolved into the single contributions $I^1(k_x)$, $I^2(k_x)$, $I^3(k_x)$, and the background $B(k_x)$, in sum reproducing the initial line shape. (b) Artificial spin-resolved intensities along the y-detector axis, which represent the raw data in a real experiment. (c) Spin polarizations $P'_x(k_x)$, $P'_y(k_x)$, and $P'_z(k_x)$ derived from spin-resolved intensities by use of Eq. A.6. Solid lines are polarization fits within the second step of the two-step fitting routine. (d) Peak-specific polarization components P_x, P_y, and P_z, extracted as fit parameters. Graphs are taken from [22], Copyright (2008) by the American Physical Society.*

following discussion will be limited to this case. Thus, the quantities above and their dependency on energy and momentum are simplified to $I_\alpha(k_x) = I^\uparrow_\alpha(k_x) + I^\downarrow_\alpha(k_x)$ and $P'_\alpha(k_x)$.

As discussed so far, spin-resolved photoemission does not allow to detect much more than the pure existence of a spin splitting and the corresponding *measured* spin polarizations, while further insight is not given. Nevertheless, it would be essential to determine additional properties, e.g., the exact orientation of the spin polarization vectors. In particular, the material system under investigation does not possess a single spin quantization axis, which could easily be measured by rotating the sample in a way that the quantization axis is aligned with the detector axis. Instead, the present 3D spin configuration requires a more sophisticated vectorial approach to inspect and analyze the data quantitatively. This is achieved within the *two-step fitting routine*, which will be introduced in the following by means of the artificially generated MDC in Fig. A.2(a) [22, 116]. As suggestive of its name, the routine divides the analysis of SARPES data into two steps with a sequential fitting of intensity and polarization spectra.

Step 1
During the first step of SARPES data evaluation, the total spin-integrated intensity

$$I(k_x) = \sum_{\alpha=x,y,z} I_\alpha^\uparrow(k_x) + I_\alpha^\downarrow(k_x) \tag{A.8}$$

from an MDC along k_x must be deconvolved into its single peak contributions $I^i(k_x)$. For non-magnetic samples, as it is the case in this thesis, an unpolarized background $B(k_x)$, which is either a constant or a linear function of k_x, has to be subtracted, i.e., $I(k_x) = \sum_{i=1}^{n} I^i(k_x) + B(k_x)$. The single peaks are usually fitted with a suitable number of Voigt line profiles, each having four fit parameters. All in all, a total of $4n + 2$ parameters has to be adjusted in order to receive a good approximation to the initial MDC (in this example $n = 3$). The fit parameters extracted here are then used in step 2.

Step 2
The second step requires a fit to the *measured* spin polarization $P'_\alpha(k_x)$ (Eq. A.6). To start, a peak-specific spin polarization vector

$$\mathbf{P}^i = \begin{pmatrix} P_x^i \\ P_y^i \\ P_z^i \end{pmatrix} = c_i \begin{pmatrix} \cos\theta_i \cos\phi_i \\ \cos\theta_i \sin\phi_i \\ \sin\theta \end{pmatrix} \tag{A.9}$$

must be allocated to each band contribution $I^i(k_x)$ in the spectrum. Here, the azimuth θ_i and polar ϕ_i angles, as well as the normalization constant c_i sum up to a total of $3n$ fit parameters in step 2.

The peak-specific spin polarization vector $\mathbf{P}^i$ is in turn linked to the corresponding single peak intensity $I^i(k_x)$ obtained from the fit in step 1 by

$$\begin{aligned} I_\alpha^{i,\uparrow}(k_x) &= I^i(k_x)(1 + P_\alpha^i)/2, \\ I_\alpha^{i,\downarrow}(k_x) &= I^i(k_x)(1 - P_\alpha^i)/2. \end{aligned} \tag{A.10}$$

In calculating $\sum_{i=1}^{n} I_\alpha^{i,\uparrow}(k_x) = I_\alpha^\uparrow(k_x)$ and $\sum_{i=1}^{n} I_\alpha^{i,\downarrow}(k_x) = I_\alpha^\downarrow(k_x)$ and utilizing Eq. A.6, a *calculated* spin polarization [solid lines in Fig. A.2(c)] is obtained, which then needs to be fitted to the *measured* spin polarization P'_α. It becomes evident from Eq. A.10 that step 1 and 2 are mutually dependent.

In this way, the parameters from both steps enter into an approximation to the spin-resolved intensities [Fig. A.2(b)], which represent the experimental raw data. In other words, by fitting of the peak-specific line profiles in step 1 and sequentially adjusting the fit parameters in step 2 over several cycles, a satisfying approach to the spin-resolved intensities is reached.

Such a separation into two steps simplifies the determination of suitable fit parameters but also returns reliable results at the same time. It has been demonstrated that the determination of individual peaks which are unresolvable in ARPES is highly accurate [49, 116]. In this sense, small changes in the Voigt line profile parameters in step 1, e.g., the size of the peak splittings, lead to large deviations in the fit curves to $P'_\alpha(k_x)$.

Finally, the fit parameters of step 2 allow to specify the peak-specific spin polarization vector $\mathbf{P}^i$ of each band. This is visualized as a plane representation of the spin polarization vector components in Fig. A.2(d). In this example the spin polarization vectors of the three states are $\mathbf{P}^1 \approx (0, 1, 0)$, $\mathbf{P}^2 \approx (-0.3, -0.95, 0)$, and $\mathbf{P}^3 \approx (0.6, 0.6, -0.5)$.

Bibliography

List of own publications

[H1] C. R. Müller, L. Worschech, P. Höpfner, S. Höfling, and A. Forchel,
Monolithically integrated logic NOR gate based on GaAs/AlGaAs three-terminal junctions,
IEEE Electron Device Letters **28**, 859 (2007).

[H2] A. Hofmann, X. Y. Cui, J. Schäfer, S. Meyer, P. Höpfner, C. Blumenstein, M. Paul, L. Patthey, E. Rotenberg, J. Bünemann, F. Gebhard, T. Ohm, W. Weber, and R. Claessen,
Renormalization of bulk magnetic electron states at high binding energies,
Physical Review Letters **102**, 187204 (2009).

[H3] P. Höpfner, M. Wisniewski, F. Sandrock, J. Schäfer, and R. Claessen,
Structural components of the Pt/Si(111)-($\sqrt{3} \times \sqrt{3}$) surface from scanning tunneling microscopy,
Physical Review B **82**, 075431 (2010).

[H4] S. Meyer, J. Schäfer, C. Blumenstein, P. Höpfner, A. Bostwick, J. L. McChesney, E. Rotenberg, and R. Claessen,
Strictly one-dimensional electron system in Au chains on Ge(001) revealed by photoelectron k-space mapping,
Physical Review B **83**, 121411(R) (2011).

[H5] P. Höpfner, J. Schäfer, A. Fleszar, S. Meyer, C. Blumenstein, T. Schramm, M. Heßmann, X. Cui, L. Patthey, W. Hanke, and R. Claessen,
Electronic band structure of the two-dimensional metallic electron system Au/Ge(111),
Physical Review B **83**, 235435 (2011).

[H6] P. Höpfner, J. Schäfer, A. Fleszar, J. H. Dil, B. Slomski, F. Meier, C. Loho, C. Blumenstein, L. Patthey, W. Hanke, and R. Claessen,
Three-dimensional spin rotations at the Fermi surface of a strongly spin-orbit coupled surface system,
Physical Review Letters **108**, 186801 (2012), *Editors' Suggestion*.

[H7] G. Li, P. Höpfner, J. Schäfer, C. Blumenstein, S. Meyer, A. Bostwick, E. Rotenberg, R. Claessen, and W. Hanke,
Magnetic order in a frustrated two-dimensional atom lattice at a semiconductor surface,
Nature Communications **4**, 1620 (2013).

[H8] S. Meyer, C. Blumenstein, L. Dudy, P. Höpfner, T. Umbach, J. Schäfer, R. Claessen, X. Y. Cui, and L. Patthey,
Photon energy and temperature dependent analysis of the Tomonaga-Luttinger system Au/Ge(001) by high-resolution angle-resolved photoemission,
manuscript (2013).

[H9] J. Settelein, P. Höpfner, J. Schäfer, and R. Claessen,
Novel insights into the 2D Mott insulator Sn/Si(111) by scanning tunneling spectroscopy,
manuscript (2013).

General literature

[10] J. G. Bednorz and K. A. Müller, Zeitschrift für Physik B - Condensed Matter **64**, 189 (1986).

[11] M. Imada, A. Fujimori, and Y. Tokura, Reviews of Modern Physics **70**, 1039 (1998).

[12] H. H. Weitering, X. Shi, P. D. Johnson, J. Chen, N. J. DiNardo, and K. Kempa, Physical Review Letters **78**, 1331 (1997).

[13] V. Ramachandran and R. M. Feenstra, Physical Review Letters **82**, 1000 (1999).

[14] G. Santoro, S. Scandolo, and E. Tosatti, Physical Review B **59**, 1891 (1999).

[15] P. W. Anderson, Science **235**, 1196 (1987).

[16] G. Profeta and E. Tosatti, Physical Review Letters **98**, 086401 (2007).

[17] S. Modesti, L. Petaccia, G. Ceballos, I. Vobornik, G. Panaccione, G. Rossi, L. Ottaviano, R. Larciprete, S. Lizzit, and A. Goldoni, Physical Review Letters **98**, 126401 (2007).

[18] G. Li, M. Laubach, A. Fleszar, and W. Hanke, Physical Review B **83**, 041104 (2011).

[19] Y. A. Bychkov and E. I. Rashba, JETP Letters **39**, 78 (1984).

[20] S. LaShell, B. A. McDougall, and E. Jensen, Physical Review Letters **77**, 3419 (1996).

[21] Y. M. Koroteev, G. Bihlmayer, J. E. Gayone, E. V. Chulkov, S. Blügel, P. M. Echenique, and P. Hofmann, Physical Review Letters **93**, 046403 (2004).

[22] F. Meier, H. Dil, J. Lobo-Checa, L. Patthey, and J. Osterwalder, Physical Review B **77**, 165431 (2008).

[23] J. Sinova, D. Culcer, Q. Niu, N. A. Sinitsyn, T. Jungwirth, and A. H. MacDonald, Physical Review Letters **92**, 126603 (2004).

[24] K. Sakamoto, H. Kakuta, K. Sugawara, K. Miyamoto, A. Kimura, T. Kuzumaki, N. Ueno, E. Annese, J. Fujii, A. Kodama, T. Shishidou, H. Namatame, M. Taniguchi, T. Sato, T. Takahashi, and T. Oguchi, Physical Review Letters **103**, 156801 (2009).

[25] K. Sakamoto, T. Oda, A. Kimura, K. Miyamoto, M. Tsujikawa, A. Imai, N. Ueno, H. Namatame, M. Taniguchi, P. E. J. Eriksson, and R. I. G. Uhrberg, Physical Review Letters **102**, 096805 (2009).

[26] K. Yaji, Y. Ohtsubo, S. Hatta, H. Okuyama, K. Miyamoto, T. Okuda, A. Kimura, H. Namatame, M. Taniguchi, and T. Aruga, Nature Communications **1**, 17 (2010).

[27] S. Basak, H. Lin, L. A. Wray, S. Y. Xu, L. Fu, M. Z. Hasan, and A. Bansil, Physical Review B **84**, 121401 (2011).

[28] S. Souma, K. Kosaka, T. Sato, M. Komatsu, A. Takayama, T. Takahashi, M. Kriener, K. Segawa, and Y. Ando, Physical Review Letters **106**, 216803 (2011).

[29] A. Herdt, L. Plucinski, G. Bihlmayer, G. Mussler, S. Döring, J. Krumrain, D. Grützmacher, S. Blügel, and C. M. Schneider, ArXiv e-prints (2012), arXiv:1210.2241.

[30] E. I. Rashba and A. L. Efros, Physical Review Letters **91**, 126405 (2003).

[31] J. Fabian, A. Matos-Abiague, C. Ertler, P. Stano, and I. Žutić, Acta Physica Slovaca **57**, 565 (2007).

[32] S. Datta and B. Das, Applied Physics Letters **56**, 665 (1990).

[33] T. Koga, J. Nitta, and H. Takayanagi, Physical Review Letters **88**, 126601 (2002).

[34] A. A. Burkov, A. S. Núñez, and A. H. MacDonald, Physical Review B **70**, 155308 (2004).

[35] J. Nitta, T. Akazaki, H. Takayanagi, and T. Enoki, Physical Review Letters **78**, 1335 (1997).

[36] G. Grüner, *Density Waves In Solids* (Addison-Wesley Publishing Company, 1994).

[37] A. K. Geim and K. S. Novoselov, Nature Materials **6**, 183 (2007).

[38] D. Hsieh, D. Qian, L. Wray, Y. Xia, Y. S. Hor, R. J. Cava, and M. Z. Hasan, Nature **452**, 970 (2008).

[39] T. Zhang, P. Cheng, W. J. Li, Y. J. Sun, G. Wang, X. G. Zhu, K. He, L. L. Wang, X. C. Ma, X. Chen, Y. Y. Wang, Y. Liu, H. Q. Lin, J. F. Jia, and Q. K. Xue, Nature Physics **6**, 39 (2010).

[40] J. M. Carpinelli, H. H. Weitering, E. W. Plummer, and R. Stumpf, Nature **381**, 398 (1996).

[41] S. D. Kevan and R. H. Gaylord, Physical Review B **36**, 5809 (1987).

[42] L. Petersen and P. Hedegård, Surface Science **459**, 49 (2000).

[43] G. Dresselhaus, Physical Review **100**, 580 (1955).

[44] E. I. Rashba, Soviet Physics - Solid State **2**, 1109 (1960).

[45] E. Lipparini, *Modern Many-Particle Physics: Atomic Gases, Nanostructures and Quantum Liquids* (World Scientific, 2008).

[46] S. D. Ganichev, V. V. Bel'kov, L. E. Golub, E. L. Ivchenko, P. Schneider, S. Giglberger, J. Eroms, J. De Boeck, G. Borghs, W. Wegscheider, D. Weiss, and W. Prettl, Physical Review Letters **92**, 256601 (2004).

[47] G. Engels, J. Lange, T. Schäpers, and H. Lüth, Physical Review B **55**, R1958 (1997).

[48] J. Schliemann, J. C. Egues, and D. Loss, Physical Review Letters **90**, 146801 (2003).

[49] J. H. Dil, Journal of Physics - Condensed Matter **21**, 403001 (2009).

[50] S. Hatta, T. Aruga, Y. Ohtsubo, and H. Okuyama, Physical Review B **80**, 113309 (2009).

[51] U. Heinzmann and J. H. Dil, Journal of Physics - Condensed Matter **24**, 173001 (2012).

[52] M. Hoesch, M. Muntwiler, V. N. Petrov, M. Hengsberger, L. Patthey, M. Shi, M. Falub, T. Greber, and J. Osterwalder, Physical Review B **69**, 241401 (2004).

[53] M. Hochstrasser, J. G. Tobin, E. Rotenberg, and S. D. Kevan, Physical Review Letters **89**, 216802 (2002).

[54] T. Hirahara, T. Nagao, I. Matsuda, G. Bihlmayer, E. V. Chulkov, Y. M. Koroteev, P. M. Echenique, M. Saito, and S. Hasegawa, Physical Review Letters **97**, 146803 (2006).

[55] L. Fu, Physical Review Letters **103**, 6801 (2009).

[56] L. Landau and E. Lifshitz, *Quantum Mechanics: Non-Relativistic Theory* (Butterworth-Heinemann, 1977).

[57] J. H. de Boer and E. J. W. Verwey, Proceedings of the Physical Society **49**, 59 (1937).

[58] R. W. Lof, M. A. van Veenendaal, B. Koopmans, H. T. Jonkman, and G. A. Sawatzky, Physical Review Letters **68**, 3924 (1992).

[59] N. F. Mott and R. Peierls, Proceedings of the Physical Society **49**, 72 (1937).

[60] N. F. Mott, Proceedings of the Physical Society - Section A **62**, 416 (1949).

[61] N. F. Mott, Philosophical Magazine **6**, 287 (1961).

[62] N. F. Mott, *Metal-Insulator Transitions* (Taylor & Francis, 1990).

[63] J. Hubbard, Proceedings of the Royal Society of London - Series A **276**, 238 (1963).

[64] M. C. Gutzwiller, Physical Review Letters **10**, 159 (1963).

[65] J. Kanamori, Progress of Theoretical Physics **30**, 275 (1963).

[66] P. Fazekas, *Lecture Notes on Electron Correlation and Magnetism* (World Scientific, 1999).

[67] F. Gebhard, *The Mott Metal-Insulator Transition: Models and Methods* (Springer-

Verlag, 1997).

[68] A. Fetter and J. Walecka, *Quantum Theory of Many-Particle Systems* (Dover Publications, 2003).

[69] P. Kurz, G. Bihlmayer, K. Hirai, and S. Blügel, Physical Review Letters **86**, 1106 (2001).

[70] G. H. Wannier, Physical Review **79**, 357 (1950).

[71] W. Tremel, R. Seshadri, and E. W. Finckh, Chemie in unserer Zeit **35**, 42 (2001).

[72] M. Rohlfing and J. Pollmann, Physical Review Letters **84**, 135 (2000).

[73] V. I. Anisimov, J. Zaanen, and O. K. Andersen, Physical Review B **44**, 943 (1991).

[74] S. Schuwalow, D. Grieger, and F. Lechermann, Physical Review B **82**, 035116 (2010).

[75] L. de Broglie, Philosophical Magazine - Series 6 **47**, 446 (1924).

[76] F. Jona, J. A. Strozier, and W. S. Yang, Reports on Progress in Physics **45**, 527 (1982).

[77] S. Hüfner, *Photoelectron Spectroscopy: Principles and Applications* (Springer-Verlag, 2003).

[78] M. P. Seah and W. A. Dench, Surface and Interface Analysis **1**, 2 (1979).

[79] G. Ertl and J. Küppers, *Low Energy Electrons and Surface Chemistry* (Wiley-VCH, 1985).

[80] H. Over, C. P. Wang, and F. Jona, Physical Review B **51**, 4231 (1995).

[81] SPECS Surface Nano Analysis GmbH, *ErLEED 100/150 - Reverse View LEED Optics*, `http://www.specs.de/cms/upload/PDFs/SPECS_Prospekte/2010_11_ErLEED_100_150_brochure_final_web.pdf`, downloaded on 13/01/2012.

[82] G. Binnig, H. Rohrer, C. Gerber, and E. Weibel, Physical Review Letters **49**, 57 (1982).

[83] G. Binnig, H. Rohrer, C. Gerber, and E. Weibel, Applied Physics Letters **40**, 178 (1982).

[84] J. Tersoff and D. R. Hamann, Physical Review B **31**, 805 (1985).

[85] R. Wiesendanger, *Scanning Probe Microscopy and Spectroscopy* (Cambridge University Press, 1994).

[86] C. Bai, *Scanning Tunneling Microscopy and its Applications* (Springer-Verlag, 2000).

[87] D. A. Bonnell, *Scanning Probe Microscopy and Spectroscopy* (Wiley-VCH, 2001).

[88] J. Bardeen, Physical Review Letters **6**, 57 (1961).

[89] J. Tersoff and D. R. Hamann, Physical Review Letters **50**, 1998 (1983).

[90] Omicron NanoTechnology GmbH, *Variable Temperature SPM*, `http://www.omicron.de/mzag/gui/download/17767007734eb155c467931/VT_STM_n.pdf`, downloaded on 02/11/2011.

[91] G. K. White, *Thermal Conductivity at 273 - 300 K*, Landolt-Börnstein - Group III Condensed Matter Numerical Data and Functional Relationships in Science and Technology Vol. 15c (Springer-Verlag, 1991), chap. 2.1, p. 6.

[92] H. Schultz, *Special Remarks*, Landolt-Börnstein - Group III Condensed Matter Numerical Data and Functional Relationships in Science and Technology Vol. 25 (Springer-Verlag, 1991), chap. 2.2.1, p. 115.

[93] C. Blumenstein, *Strukturelle Eigenschaften und Tieftemperaturverhalten von atomaren Nanodrähten aus Gold auf Ge(001)*, Diploma thesis, University of Würzburg, 2008.

[94] Omicron Nanotechnology GmbH, *VT STM Users Guide*, 2000.

[95] J. A. Kubby and J. J. Boland, Surface Science Reports **26**, 61 (1996).

[96] F. Reinert and S. Hüfner, New Journal of Physics **7**, 97 (2005).

[97] A. Damascelli, Physica Scripta **T109**, 61 (2004).

[98] K. Siegbahn, Science **217**, 111 (1982).

[99] A. Einstein, Annalen der Physik **322**, 132 (1905).

[100] H. Hertz, Annalen der Physik **267**, 983 (1887).

[101] C. N. Berglund and W. E. Spicer, Physical Review **136**, A1030 (1964).

[102] C. N. Berglund and W. E. Spicer, Physical Review **136**, A1044 (1964).

[103] P. Hofmann, *Lecture Notes on Surface Science*, `http://philiphofmann.net/surflec3/index.html`, downloaded on 23/02/2012.

[104] C. S. Fadley, Journal of Electron Spectroscopy and Related Phenomena **178**, 2 (2010).

[105] A. Damascelli, Z. Hussain, and Z. X. Shen, Reviews of Modern Physics **75**, 473 (2003).

[106] L. Perfetti, C. Rojas, A. Reginelli, L. Gavioli, H. Berger, G. Margaritondo, M. Grioni, R. Gaál, L. Forró, and F. R. Albenque, Physical Review B **64**, 115102 (2001).

[107] J. Osterwalder, Journal of Physics - Condensed Matter **24**, 171001 (2012).

[108] J. D. Koralek, J. F. Douglas, N. C. Plumb, Z. Sun, A. V. Fedorov, M. M. Murnane, H. C. Kapteyn, S. T. Cundiff, Y. Aiura, K. Oka, H. Eisaki, and D. S. Dessau,

Physical Review Letters **96**, 017005 (2006).

[109] P. Willmott, *An Introduction to Synchrotron Radiation: Techniques and Applications* (John Wiley & Sons, 2011).

[110] Swiss Light Source, *SIS - X09LA: Surface / Interface: Spectroscopy* , `http://www.psi.ch/sls/sis/sis`, downloaded on 13/01/2012.

[111] Advanced Light Source, *Insertion Device and Bend Magnet Parameters: U50 Undulator*, `http://www-als.lbl.gov/index.php/beamlines/photon-source-parameters.html`, downloaded on 22/11/2012.

[112] Advanced Light Source, *Beamline 7.0.1: Surface and Materials Science, Spectromicroscopy*, `http://www-als.lbl.gov/index.php/beamlines/beamlines-directory/111-701.html`, downloaded on 13/01/2012.

[113] SPECS Surface Nano Analysis GmbH, *PHOIBOS Hemispherical Energy Analyzer Series*, 2005.

[114] VG Scienta, *Electron Spectrometer - Scienta R4000*, `http://www.vgscienta.com/_resources/File/R4000%20data%20sheet%20v4.0%20web.pdf`, downloaded on 13/01/2012.

[115] J. Kessler, *Polarized Electrons* (Springer-Verlag, 1985).

[116] F. Meier, J. H. Dil, and J. Osterwalder, New Journal of Physics **11**, 125008 (2009).

[117] N. F. Mott, Proceedings of the Royal Society of London - Series A **124**, 425 (1929).

[118] T. J. Gay and F. B. Dunning, Review of Scientific Instruments **63**, 1635 (1992).

[119] M. Hoesch, T. Greber, V. Petrov, A. Muntwiler, M. Hengsberger, W. Auwärter, and J. Osterwalder, Journal of Electron Spectroscopy and Related Phenomena **124**, 263 (2002).

[120] N. Sherman, Physical Review **103**, 1601 (1956).

[121] A. Gellrich and J. Kessler, Physical Review A **43**, 204 (1991).

[122] M. Hoesch, *Spin-resolved Fermi Surface Mapping*, PhD thesis, University of Zurich, 2002.

[123] WebElements, *WebElements: The Periodic Table on the Web* , `http://www.webelements.com/`, downloaded on 30/03/2012.

[124] H. Stöcker, *Taschenbuch der Physik* (Deutsch-Verlag, 2004).

[125] W. Mönch, *Semiconductor Surfaces and Interfaces* (Springer-Verlag, 2001).

[126] J. E. Northrup and M. L. Cohen, Physical Review Letters **49**, 1349 (1982).

[127] G. X. Qian and D. J. Chadi, Physical Review B **35**, 1288 (1987).

[128] M. A. Olmstead, Surface Science Reports **6**, 159 (1986).

[129] R. E. Schlier and H. E. Farnsworth, Journal of Chemical Physics **30**, 917 (1959).

[130] K. Takayanagi, Y. Tanishiro, S. Takahashi, and M. Takahashi, Surface Science **164**, 367 (1985).

[131] R. J. Hamers, R. M. Tromp, and J. E. Demuth, Physical Review Letters **56**, 1972 (1986).

[132] G. V. Hansson and R. I. G. Uhrberg, Surface Science Reports **9**, 197 (1988).

[133] Y. G. Ding, C. T. Chan, and K. M. Ho, Surface Science **275**, L691 (1992).

[134] J. E. Northrup, Physical Review Letters **53**, 683 (1984).

[135] M. S. Finney, C. Norris, P. B. Howes, R. G. van Silfhout, G. F. Clark, and J. M. C. Thornton, Surface Science **291**, 99 (1993).

[136] V. G. Kotlyar, A. A. Saranin, A. V. Zotov, and T. V. Kasyanova, Surface Science **543**, L663 (2003).

[137] R. H. Miwa, T. M. Schmidt, and G. P. Srivastava, Journal of Physics - Condensed Matter **15**, 2441 (2003).

[138] J. S. Hovis, R. J. Hamers, and C. M. Greenlief, Surface Science **440**, L815 (1999).

[139] C. Blumenstein, S. Meyer, A. Ruff, B. Schmid, J. Schäfer, and R. Claessen, Journal of Chemical Physics **135**, 64201 (2011).

[140] D. J. Chadi and C. Chiang, Physical Review B **23**, 1843 (1981).

[141] T. Ichikawa and S. Ino, Surface Science **85**, 221 (1979).

[142] I. Razado-Colambo, J. P. He, H. M. Zhang, G. V. Hansson, and R. I. G. Uhrberg, Physical Review B **79**, 205410 (2009).

[143] J. Nogami, K. Wan, and J. C. Glueckstein, Japanese Journal of Applied Physics **33**, 3679 (1994).

[144] H. Aizawa, M. Tsukada, N. Sato, and S. Hasegawa, Surface Science **429**, L509 (1999).

[145] T. Nagao, S. Hasegawa, K. Tsuchie, S. Ino, C. Voges, G. Klos, H. Pfnür, and M. Henzler, Physical Review B **57**, 10100 (1998).

[146] J. Falta, A. Hille, D. Novikov, G. Materlik, L. Seehofer, G. Falkenberg, and R. L. Johnson, Surface Science **330**, L673 (1995).

[147] N. Sato, T. Nagao, and S. Hasegawa, Surface Science **442**, 65 (1999).

[148] P. B. Howes, C. Norris, M. S. Finney, E. Vlieg, and R. G. van Silfhout, Physical Review B **48**, 1632 (1993).

[149] H. Huang, H. Over, S. Y. Tong, J. Quinn, and F. Jona, Physical Review B **49**, 13483 (1994).

[150] Y. G. Ding, C. T. Chan, and K. M. Ho, Physical Review Letters **67**, 1454 (1991).

[151] T. Takahashi, S. Nakatani, N. Okamoto, T. Ishikawa, and S. Kikuta, Japanese Journal of Applied Physics **27**, L753 (1988).

[152] L. Seehofer and R. L. Johnson, Surface Science **318**, 21 (1994).

[153] K. J. Wan, X. F. Lin, and J. Nogami, Physical Review B **47**, 13700 (1993).

[154] H. Tajiri, K. Sumitani, S. Nakatani, A. Nojima, T. Takahashi, K. Akimoto, H. Sugiyama, X. Zhang, and H. Kawata, Physical Review B **68**, 035330 (2003).

[155] I. Matsuda, H. Morikawa, C. Liu, S. Ohuchi, S. Hasegawa, T. Okuda, T. Kinoshita, C. Ottaviani, A. Cricenti, M. D'angelo, P. Soukiassian, and G. Le Lay, Physical Review B **68**, 085407 (2003).

[156] H. Kaji and K. Kakitani, Surface Science **601**, 2491 (2007).

[157] P. Morgen, M. Szymonski, J. Onsgaard, B. Jørgensen, and G. Rossi, Surface Science **197**, 347 (1988).

[158] G. Rossi, I. Abbati, L. Braicovich, I. Lindau, and W. E. Spicer, Physical Review B **25**, 3627 (1982).

[159] G. Rossi, D. Chandesris, P. Roubin, and J. Lecante, Physical Review B **34**, 7455 (1986).

[160] P. Morgen, B. Jørgensen, and J. Gordon, Physica Scripta **54**, 278 (1994).

[161] A. Wawro, S. Suto, and A. Kasuya, Physical Review B **72**, 205302 (2005).

[162] A. Wawro, S. Suto, and A. Kasuya, Japanese Journal of Applied Physics **45**, 2166 (2006).

[163] S. Okada, Y. Kishikawa, K. Oura, and T. Hanawa, Surface Science **100**, L457 (1980).

[164] W. S. Yang, S. C. Wu, and F. Jona, Surface Science **169**, 383 (1986).

[165] P. Morgen and B. Jørgensen, Surface Science **208**, 306 (1989).

[166] N. Franco, J. E. Klepeis, C. Bostedt, T. Van Buuren, C. Heske, O. Pankratov, T. A. Callcott, D. L. Ederer, and L. J. Terminello, Physical Review B **68**, 045116 (2003).

[167] J. Y. Tsai, B. Y. Tsui, and M. C. Chen, Journal of Applied Physics **67**, 3530 (1990).

[168] A. Saedi, B. Poelsema, and H. J. W. Zandvliet, Surface Science **605**, 507 (2011).

[169] D. E. P. Vanpoucke and G. Brocks, Physical Review B **81**, 035333 (2010).

[170] F. Sandrock, *Atomare Struktur und elektronische Eigenschaften der Pt/Si(111)-($\sqrt{3} \times \sqrt{3}$)-Oberflächenrekonstruktion*, Diploma thesis, University of Würzburg,

2007.

[171] D. V. Gruznev, I. N. Filippov, D. A. Olyanich, D. N. Chubenko, I. A. Kuyanov, A. A. Saranin, A. V. Zotov, and V. G. Lifshits, Physical Review B **73**, 115335 (2006).

[172] K. N. Altmann, J. N. Crain, A. Kirakosian, J. L. Lin, D. Y. Petrovykh, F. J. Himpsel, and R. Losio, Physical Review B **64**, 035406 (2001).

[173] J. N. Crain, K. N. Altmann, C. Bromberger, and F. J. Himpsel, Physical Review B **66**, 205302 (2002).

[174] J. Schulze, *Konzepte Siliziumbasierter MOS-Bauelemente* (Springer-Verlag, 2005).

[175] R. H. M. Smit, C. Untiedt, A. I. Yanson, and J. M. van Ruitenbeek, Physical Review Letters **87**, 266102 (2001).

[176] F. Kajzar and J. Mizia, Journal of Physics F - Metal Physics **7**, 1115 (1977).

[177] D. Dornisch, W. Moritz, H. Schulz, R. Feidenhans'l, M. Nielsen, F. Grey, R. L. Johnson, and G. Le Lay, Surface Science **274**, 215 (1992).

[178] K. Akiyama, K. Takayanagi, and Y. Tanishiro, Surface Science **205**, 177 (1988).

[179] Y. Yamada, A. Girard, H. Asaoka, H. Yamamoto, and S. Shamoto, Physical Review B **77**, 153305 (2008).

[180] J. H. Byun, J. S. Shin, P. G. Kang, H. Jeong, and H. W. Yeom, Physical Review B **79**, 235319 (2009).

[181] A. Kara and T. S. Rahman, Journal of Physics - Condensed Matter **18**, 8883 (2006).

[182] L. Guillemot and K. Bobrov, Physical Review B **79**, 201406 (2009).

[183] L. B. Zhao, W. B. Mi, E. Y. Jiang, and H. L. Bai, Applied Physics Letters **91**, 052113 (2007).

[184] M. Zölfl, M. Brockmann, M. Köhler, S. Kreuzer, T. Schweinböck, S. Miethaner, F. Bensch, and G. Bayreuther, Journal of Magnetism and Magnetic Materials **175**, 16 (1997).

[185] A. Kimura, E. E. Krasovskii, R. Nishimura, K. Miyamoto, T. Kadono, K. Kanomaru, E. V. Chulkov, G. Bihlmayer, K. Shimada, H. Namatame, and M. Taniguchi, Physical Review Letters **105**, 076804 (2010).

[186] K. Sugawara, T. Sato, S. Souma, T. Takahashi, M. Arai, and T. Sasaki, Physical Review Letters **96**, 046411 (2006).

[187] C. R. Ast, J. Henk, A. Ernst, L. Moreschini, M. C. Falub, D. Pacilé, P. Bruno, K. Kern, and M. Grioni, Physical Review Letters **98**, 186807 (2007).

[188] L. Moreschini, A. Bendounan, I. Gierz, C. R. Ast, H. Mirhosseini, H. Höchst, K. Kern, J. Henk, A. Ernst, S. Ostanin, F. Reinert, and M. Grioni, Physical Review B **79**, 075424 (2009).

[189] C. R. Ast, D. Pacilé, L. Moreschini, M. C. Falub, M. Papagno, K. Kern, M. Grioni, J. Henk, A. Ernst, S. Ostanin, and P. Bruno, Physical Review B **77**, 081407 (2008).

[190] J. H. Dil, F. Meier, J. Lobo-Checa, L. Patthey, G. Bihlmayer, and J. Osterwalder, Physical Review Letters **101**, 266802 (2008).

[191] D. Sánchez-Portal, S. Riikonen, and R. M. Martin, Physical Review Letters **93**, 146803 (2004).

[192] T. Okuda, K. Miyamaoto, Y. Takeichi, H. Miyahara, M. Ogawa, A. Harasawa, A. Kimura, I. Matsuda, A. Kakizaki, T. Shishidou, and T. Oguchi, Physical Review B **82**, 161410 (2010).

[193] J. W. Wells, J. H. Dil, F. Meier, J. Lobo-Checa, V. N. Petrov, J. Osterwalder, M. M. Ugeda, I. Fernandez-Torrente, J. I. Pascual, E. D. L. Rienks, M. F. Jensen, and P. Hofmann, Physical Review Letters **102**, 096802 (2009).

[194] F. Reinert, G. Nicolay, S. Schmidt, D. Ehm, and S. Hüfner, Physical Review B **63**, 115415 (2001).

[195] I. Gierz, B. Stadtmüller, J. Vuorinen, M. Lindroos, F. Meier, J. H. Dil, K. Kern, and C. R. Ast, Physical Review B **81**, 245430 (2010).

[196] A. Takayama, T. Sato, S. Souma, and T. Takahashi, Physical Review Letters **106**, 166401 (2011).

[197] B. J. Knapp, J. C. Hansen, M. K. Wagner, W. D. Clendening, and J. G. Tobin, Physical Review B **40**, 2814 (1989).

[198] G. Le Lay, M. Manneville, and J. J. Métois, Surface Science **123**, 117 (1982).

[199] M. Göthelid, M. Hammar, M. Björkqvist, U. O. Karlsson, S. A. Flodström, C. Wigren, and G. Le Lay, Physical Review B **50**, 4470 (1994).

[200] A. Fleszar and W. Hanke, to be published.

[201] G. Le Lay, Surface Science **132**, 169 (1983).

[202] K. Nakatsuji, R. Niikura, Y. Shibata, M. Yamada, T. Iimori, and F. Komori, Physical Review B **84**, 035436 (2011).

[203] E. J. van Loenen, J. E. Demuth, R. M. Tromp, and R. J. Hamers, Physical Review Letters **58**, 373 (1987).

[204] M. Hammar, M. Göthelid, U. O. Karlsson, and S. A. Flodström, Physical Review B **47**, 15669 (1993).

[205] G. Le Lay, V. Y. Aristov, L. Seehofer, T. Buslaps, R. L. Johnson, M. Göthe-

lid, M. Hammar, U. O. Karlsson, S. A. Flodström, R. Feidenhans'l, M. Nielsen, E. Findeisen, and R. I. G. Uhrberg, Surface Science **307**, 280 (1994).

[206] K. J. Wan, X. F. Lin, and J. Nogami, Physical Review B **45**, 9509 (1992).

[207] D. J. Spence and S. P. Tear, Surface Science **398**, 91 (1998).

[208] S. J. Tang, T. R. Chang, C. C. Huang, C. Y. Lee, C. M. Cheng, K. D. Tsuei, H. T. Jeng, and C. Y. Mou, Physical Review B **81**, 245406 (2010).

[209] J. M. Carpinelli, H. H. Weitering, M. Bartkowiak, R. Stumpf, and E. W. Plummer, Physical Review Letters **79**, 2859 (1997).

[210] G. Grüner, Reviews of Modern Physics **60**, 1129 (1988).

[211] H. Morikawa, I. Matsuda, and S. Hasegawa, Physical Review B **77**, 193310 (2008).

[212] P. Hohenberg and W. Kohn, Physical Review **136**, B864 (1964).

[213] W. Kohn and L. J. Sham, Physical Review **140**, 1133 (1965).

[214] K. Capelle, ArXiv e-prints (2002), arXiv:cond-mat/0211443.

[215] R. van Leeuwen, Density functional approach to the many-body problem: Key concepts and exact functionals Vol. 43, pp. 25–94, Academic Press, 2003.

[216] Wikipedia, *Dichtefunktionaltheorie (Quantenphysik) — Wikipedia, Die freie Enzyklopädie*, `http://de.wikipedia.org/w/index.php?title=Dichtefunktionaltheorie_(Quantenphysik)&oldid=104459074`, downloaded on 14/09/2012.

[217] J. P. Perdew and A. Zunger, Physical Review B **23**, 5048 (1981).

[218] A. Fleszar, M. Potthoff, and W. Hanke, Physica Status Solidi C **4**, 3270 (2007).

[219] A. Fleszar, W. Hanke, W. Weigand, C. Kumpf, C. Heske, E. Umbach, L. Plucinski, and R. L. Johnson, Physica Status Solidi C **4**, 3204 (2007).

[220] A. Fleszar and W. Hanke, Physical Review B **71**, 045207 (2005).

[221] A. Fleszar and W. Hanke, Physical Review B **56**, 12285 (1997).

[222] I. Gierz, T. Suzuki, E. Frantzeskakis, S. Pons, S. Ostanin, A. Ernst, J. Henk, M. Grioni, K. Kern, and C. R. Ast, Physical Review Letters **103**, 046803 (2009).

[223] M. H. Liu and C. R. Chang, Physical Review B **80**, 241304 (2009).

[224] S. Vajna, E. Simon, A. Szilva, K. Palotas, B. Ujfalussy, and L. Szunyogh, Physical Review B **85**, 075404 (2012).

[225] E. Frantzeskakis and M. Grioni, Physical Review B **84**, 155453 (2011).

[226] M. Z. Hasan and C. L. Kane, Reviews of Modern Physics **82**, 3045 (2010).

[227] S.-Y. Xu, L. A. Wray, Y. Xia, F. von Rohr, Y. S. Hor, J. H. Dil, F. Meier,

B. Slomski, J. Osterwalder, M. Neupane, H. Lin, A. Bansil, A. Fedorov, R. J. Cava, and M. Z. Hasan, ArXiv e-prints (2011), arXiv:1101.3985.

[228] B. Slomski, G. Landolt, F. Meier, L. Patthey, G. Bihlmayer, J. Osterwalder, and J. H. Dil, Physical Review B **84**, 193406 (2011).

[229] M. Nagano, A. Kodama, T. Shishidou, and T. Oguchi, Journal of Physics - Condensed Matter **21**, 064239 (2009).

[230] Y. L. Chen, J. G. Analytis, J. H. Chu, Z. K. Liu, S. K. Mo, X. L. Qi, H. J. Zhang, D. H. Lu, X. Dai, Z. Fang, S. C. Zhang, I. R. Fisher, Z. Hussain, and Z. X. Shen, Science **325**, 178 (2009).

[231] C. X. Liu, X. L. Qi, H. J. Zhang, X. Dai, Z. Fang, and S. C. Zhang, Physical Review B **82**, 045122 (2010).

[232] P. W. Anderson, Materials Research Bulletin **8**, 153 (1973).

[233] R. Moessner and S. L. Sondhi, Physical Review Letters **86**, 1881 (2001).

[234] Y. Shimizu, K. Miyagawa, K. Kanoda, M. Maesato, and G. Saito, Physical Review Letters **91**, 107001 (2003).

[235] R. H. McKenzie, Science **278**, 820 (1997).

[236] K. Takada, H. Sakurai, E. Takayama-Muromachi, F. Izumi, R. A. Dilanian, and T. Sasaki, Nature **422**, 53 (2003).

[237] H. H. Weitering, J. Chen, N. J. DiNardo, and E. W. Plummer, Physical Review B **48**, 8119 (1993).

[238] L. Cardenas, Y. Fagot-Révurat, L. Moreau, B. Kierren, and D. Malterre, Physical Review Letters **103**, 046804 (2009).

[239] A. Tejeda, Y. Fagot-Révurat, R. Cortés, D. Malterre, E. G. Michel, and A. Mascaraque, Physica Status Solidi A **209**, 614 (2012).

[240] L. Chaput, C. Tournier-Colletta, L. Cardenas, A. Tejeda, B. Kierren, D. Malterre, Y. Fagot-Révurat, P. Le Fèvre, F. Bertran, A. Taleb-Ibrahimi, D. G. Trabada, J. Ortega, and F. Flores, Physical Review Letters **107**, 187603 (2011).

[241] J. E. Northrup and J. Neugebauer, Physical Review B **52**, 17001 (1995).

[242] L. I. Johansson, F. Owman, and P. Mårtensson, Surface Science **360**, L478 (1996).

[243] J. M. Themlin, I. Forbeaux, V. Langlais, H. Belkhir, and J. M. Debever, Europhysics Letters **39**, 61 (1997).

[244] G. Profeta and E. Tosatti, Physical Review Letters **95**, 206801 (2005).

[245] P. Fazekas and E. Tosatti, Philosophical Magazine B **39**, 229 (1979).

[246] A. Mascaraque, J. Avila, E. G. Michel, and M. C. Asensio, Physical Review B **57**,

14758 (1998).

[247] A. Tejeda, R. Cortés, J. Lobo, E. G. Michel, and A. Mascaraque, Journal of Physics - Condensed Matter **19**, 355008 (2007).

[248] A. Mascaraque, J. Avila, J. Alvarez, M. C. Asensio, S. Ferrer, and E. G. Michel, Physical Review Letters **82**, 2524 (1999).

[249] J. Shi, B. Wu, X. C. Xie, E. W. Plummer, and Z. Zhang, Physical Review Letters **91**, 076103 (2003).

[250] J. D. Guo, J. R. Shi, and E. W. Plummer, Physical Review Letters **94**, 036105 (2005).

[251] I. Brihuega, O. Custance, M. M. Ugeda, N. Oyabu, S. Morita, and J. M. Gómez-Rodríguez, Physical Review Letters **95**, 206102 (2005).

[252] O. Bunk, J. H. Zeysing, G. Falkenberg, R. L. Johnson, M. Nielsen, M. M. Nielsen, and R. Feidenhans'l, Physical Review Letters **83**, 2226 (1999).

[253] A. Goldoni and S. Modesti, Physical Review Letters **79**, 3266 (1997).

[254] J. Avila, A. Mascaraque, E. G. Michel, M. C. Asensio, G. Le Lay, J. Ortega, R. Pérez, and F. Flores, Physical Review Letters **82**, 442 (1999).

[255] H. Morikawa, S. Jeong, and H. W. Yeom, Physical Review B **78**, 245307 (2008).

[256] R. Pérez, J. Ortega, and F. Flores, Physical Review Letters **86**, 4891 (2001).

[257] G. Ballabio, G. Profeta, S. de Gironcoli, S. Scandolo, G. E. Santoro, and E. Tosatti, Physical Review Letters **89**, 126803 (2002).

[258] A. V. Melechko, J. Braun, H. H. Weitering, and E. W. Plummer, Physical Review Letters **83**, 999 (1999).

[259] H. H. Weitering, J. M. Carpinelli, A. P. Melechko, J. D. Zhang, M. Bartkowiak, and E. W. Plummer, Science **285**, 2107 (1999).

[260] T. E. Kidd, T. Miller, M. Y. Chou, and T. C. Chiang, Physical Review Letters **85**, 3684 (2000).

[261] R. I. G. Uhrberg and T. Balasubramanian, Physical Review Letters **81**, 2108 (1998).

[262] T. Mitsui and K. Takayanagi, Physical Review B **62**, R16251 (2000).

[263] A. Tejeda, R. Cortés, J. Lobo-Checa, C. Didiot, B. Kierren, D. Malterre, E. G. Michel, and A. Mascaraque, Physical Review Letters **100**, 026103 (2008).

[264] F. Ronci, S. Colonna, S. D. Thorpe, A. Cricenti, and G. Le Lay, Physical Review Letters **95**, 156101 (2005).

[265] J. S. Okasinski, C. Kim, D. A. Walko, and M. J. Bedzyk, Physical Review B **69**,

041401 (2004).

[266] L. Petaccia, L. Floreano, A. Goldoni, D. Cvetko, A. Morgante, L. Grill, A. Verdini, G. Comelli, G. Paolucci, and S. Modesti, Physical Review B **64**, 193410 (2001).

[267] R. Cortés, A. Tejeda, J. Lobo, C. Didiot, B. Kierren, D. Malterre, E. G. Michel, and A. Mascaraque, Physical Review Letters **96**, 126103 (2006).

[268] S. Colonna, F. Ronci, A. Cricenti, and G. Le Lay, Physical Review Letters **101**, 186102 (2008).

[269] F. Flores, J. Ortega, R. Pérez, A. Charrier, F. Thibaudau, J. M. Debever, and J. M. Themlin, Progress in Surface Science **67**, 299 (2001).

[270] I. Brihuega, O. Custance, R. Pérez, and J. M. Gómez-Rodríguez, Physical Review Letters **94**, 046101 (2005).

[271] V. Dudr, N. Tsud, S. Fabík, M. Vondráček, V. Matolín, V. Cháb, and K. C. Prince, Physical Review B **70**, 155334 (2004).

[272] I. Brihuega, O. Custance, M. M. Ugeda, and J. M. Gómez-Rodríguez, Physical Review B **75**, 155411 (2007).

[273] K. M. Conway, J. E. MacDonald, C. Norris, E. Vlieg, and J. F. van der Veen, Surface Science **215**, 555 (1989).

[274] A. A. Escuadro, D. M. Goodner, J. S. Okasinski, and M. J. Bedzyk, Physical Review B **70**, 235416 (2004).

[275] G. Profeta, A. Continenza, L. Ottaviano, W. Mannstadt, and A. J. Freeman, Physical Review B **62**, 1556 (2000).

[276] J. Lobo, A. Tejeda, A. Mugarza, and E. G. Michel, Physical Review B **68**, 235332 (2003).

[277] A. Charrier, R. Pérez, F. Thibaudau, J. M. Debever, J. Ortega, F. Flores, and J. M. Themlin, Physical Review B **64**, 115407 (2001).

[278] T. Kinoshita, S. Kono, and T. Sagawa, Physical Review B **34**, 3011 (1986).

[279] R. I. G. Uhrberg, H. M. Zhang, T. Balasubramanian, S. T. Jemander, N. Lin, and G. V. Hansson, Physical Review B **62**, 8082 (2000).

[280] H. Morikawa, I. Matsuda, and S. Hasegawa, Physical Review B **65**, 201308 (2002).

[281] F. Ronci, S. Colonna, and A. Cricenti, Physical Review Letters **99**, 166103 (2007).

[282] T. Hirahara, T. Komorida, Y. Gu, F. Nakamura, H. Idzuchi, H. Morikawa, and S. Hasegawa, Physical Review B **80**, 235419 (2009).

[283] T. Ichikawa, Surface Science **140**, 37 (1984).

[284] C. Törnevik, M. Göthelid, M. Hammar, U. O. Karlsson, N. G. Nilsson, S. A.

Flodström, C. Wigren, and M. Östling, Surface Science **314**, 179 (1994).

[285] H. M. Zhang, S. T. Jemander, N. Lin, G. V. Hansson, and R. I. G. Uhrberg, Surface Science **531**, 21 (2003).

[286] B. Ressel, C. Di Teodoro, G. Profeta, L. Ottaviano, V. Cháb, and K. C. Prince, Surface Science **562**, 128 (2004).

[287] L. Seehofer, G. Falkenberg, and R. L. Johnson, Surface Science **290**, 15 (1993).

[288] G. Profeta, L. Ottaviano, S. Santucci, and A. Continenza, Physical Review B **66**, 081303 (2002).

[289] L. Ottaviano, G. Profeta, L. Petaccia, C. B. Nacci, and S. Santucci, Surface Science **554**, 109 (2004).

[290] S. T. Jemander, N. Lin, H. M. Zhang, R. I. G. Uhrberg, and G. V. Hansson, Surface Science **475**, 181 (2001).

[291] L. Ottaviano, A. V. Melechko, S. Santucci, and E. W. Plummer, Physical Review Letters **86**, 1809 (2001).

[292] W. Kaminski, P. Jelinek, R. Pérez, F. Flores, and J. Ortega, Applied Surface Science **234**, 286 (2004).

[293] J. Friedel, Il Nuovo Cimento **7**, 287 (1958).

[294] L. Ottaviano, M. Crivellari, L. Lozzi, and S. Santucci, Surface Science **445**, L41 (2000).

[295] E. Tosatti and P. W. Anderson, Japanese Journal of Applied Physics - Supplement **2**, 381 (1974).

[296] M. Alonso, R. Cimino, and K. Horn, Physical Review Letters **64**, 1947 (1990).

[297] F. J. Himpsel, G. Hollinger, and R. A. Pollak, Physical Review B **28**, 7014 (1983).

[298] H. M. Zhang, K. Sakamoto, G. V. Hansson, and R. I. G. Uhrberg, Physical Review B **78**, 035318 (2008).

[299] J. E. Griffith and G. P. Kochanski, Annual Review of Materials Science **20**, 219 (1990).

[300] F. G. Allen and G. W. Gobeli, Physical Review **127**, 150 (1962).

[301] J. Avila, Y. Huttel, G. Le Lay, and M. C. Asensio, Applied Surface Science **162**, 48 (2000).

[302] T. Yoshioka, A. Koga, and N. Kawakami, Physical Review Letters **103**, 036401 (2009).

[303] A. N. Rubtsov, M. I. Katsnelson, and A. I. Lichtenstein, Physical Review B **77**, 033101 (2008).

[304] A. N. Rubtsov, M. I. Katsnelson, A. I. Lichtenstein, and A. Georges, Physical Review B **79**, 045133 (2009).

[305] T. Maier, M. Jarrell, T. Pruschke, and M. H. Hettler, Reviews of Modern Physics **77**, 1027 (2005).

[306] M. H. Hettler, A. N. Tahvildar-Zadeh, M. Jarrell, T. Pruschke, and H. R. Krishnamurthy, Physical Review B **58**, R7475 (1998).

[307] P. Fazekas and P. W. Anderson, Philosophical Magazine **30**, 423 (1974).

[308] L. F. Tocchio, A. Parola, C. Gros, and F. Becca, Physical Review B **80**, 064419 (2009).

[309] B. Kyung and A. M. S. Tremblay, Physical Review Letters **97**, 046402 (2006).

[310] A. E. Antipov, A. N. Rubtsov, M. I. Katsnelson, and A. I. Lichtenstein, Physical Review B **83**, 115126 (2011).

[311] O. A. Starykh and L. Balents, Physical Review Letters **98**, 077205 (2007).

[312] J. R. Schrieffer, X. G. Wen, and S. C. Zhang, Physical Review B **39**, 11663 (1989).

[313] J. Ibañez-Azpiroz, A. Eiguren, E. Y. Sherman, and A. Bergara, Physical Review Letters **109**, 156401 (2012).

[314] A. A. Mostofi, J. R. Yates, Y. S. Lee, I. Souza, D. Vanderbilt, and N. Marzari, Computer Physics Communications **178**, 685 (2008).

[315] P. Giannozzi, S. Baroni, N. Bonini, M. Calandra, R. Car, C. Cavazzoni, D. Ceresoli, G. L. Chiarotti, M. Cococcioni, I. Dabo, A. Dal Corso, S. de Gironcoli, S. Fabris, G. Fratesi, R. Gebauer, U. Gerstmann, C. Gougoussis, A. Kokalj, M. Lazzeri, L. Martin-Samos, N. Marzari, F. Mauri, R. Mazzarello, S. Paolini, A. Pasquarello, L. Paulatto, C. Sbraccia, S. Scandolo, G. Sclauzero, A. P. Seitsonen, A. Smogunov, P. Umari, and R. M. Wentzcovitch, Journal of Physics - Condensed Matter **21**, 395502 (2009).

Acknowledgment

Last but not least, these pages are reserved to address my thanks to all those who have helped and supported me throughout the past years in accomplishing this thesis.

- First of all, I would like to thank Prof. Ralph Claessen, who gave me the opportunity to work as a PhD student at his chair. His worthwhile comments and suggestions gave me a deeper understanding of the general physical concepts standing behind the pure data alone. Owing to his efforts in the establishment of the DFG research unit FOR1162, we had a quite successful collaboration with the theory group of Prof. Werner Hanke. I am also very thankful to him and Jörg Schäfer for providing the opportunity to work at renowned synchrotron radiation sources around the world, from where I returned with loads of novel scientific results.

- I further acknowledge the good scientific support given by my advisor Jörg Schäfer. His instructions in the very beginning of my thesis have helped me to grow into the field of low-dimensional physics. Moreover, his aid during the experimental sessions and the profound discussions of results afterwards have been the basis to conduct a successful thesis. I would further like to thank him for initiating the collaboration with the theory group, which has helped significantly in interpreting my results.

- Prof. Werner Hanke deserves high appreciation for successfully working together within the scope of our research unit. In this regard, I address special thanks to Andrzej Fleszar and Gang Li from his chair, who have notably contributed to my understanding and scientific progress by their accurate calculations. I would also like to express my appreciation of the nice atmosphere in working together. Additional thanks to Andrzej for contributing the total energy calculations, which represent a valuable ingredient of this thesis.

- I also would like to express my thanks to Jan Hugo Dil, who has provided support in the spin-resolved photoemission experiments at the synchrotron from the very beginning, and thereby enriched my understanding of spin-orbit coupling effects at surfaces.

- Special thanks go to my diploma students Maik Heßmann, Thomas Schramm, and Max Herpich, who significantly helped in the development of preparation recipes and in the characterization of the samples. Also many thanks to Jochen Settelein for providing data from STS for comparison.

- My PhD colleagues in the "nanoteam" Christian Blumenstein and Sebastian Meyer deserve high appreciation for supporting me with the synchrotron experiments. Our extended scientific discussions have improved my knowledge and understanding significantly.

- The scientific staff at the SLS and ALS, namely Xiao-Yu Cui, Bartosz Slomski, Fabian Meier, Jan Hugo Dil, Aaron Bostwick, and Eli Rotenberg shall not be forgotten to mention here. Successful preparation and conduct of the synchrotron experiments, but also the subsequent data analysis was realized with their help.

- I also thank the proofreaders of this thesis, Sebastian Meyer, Christian Blumenstein, Jörg Schäfer, Gang Li, and Andrzej Fleszar, whose corrections have helped me to eliminate errors.

- Thanks to Monika Seifer, who always gave indispensable assistance in any kind of non-scientific matter.

- Here, I would further like address my appreciation to the rest of the EP4 members, former and actual, for the convenient atmosphere.

- Many thanks go to all my friends for the wonderful times and moments I have shared with them during the past years.

- Finally, I would like to express my thanks to my parents and my brothers and sisters for their continual interest in my research. Thank you for your support during the past years.

Erklärung

Hiermit erkläre ich an Eides statt, dass ich die Dissertation eigenhändig, d.h. insbesondere selbstständig und ohne Hilfe einer kommerziellen Promotionsberatung angefertigt und keine anderen als die angegeben Quellen und Hilfsmittel benutzt habe.

Würzburg den 06.12.2012 Philipp Höpfner

Hiermit erkläre ich an Eides statt, dass ich die Gelegenheit zum Promotionsvorhaben nicht kommerziell vermittelt bekommen habe und insbesondere nicht eine Person oder Organisation eingeschaltet habe, die gegen Entgelt Betreuer bzw. Betreuerinnen für die Anfertigung von Dissertationen sucht.

Würzburg den 06.12.2012 Philipp Höpfner

Hiermit erkläre ich, dass ich die Regeln der Universität Würzburg über gute wissenschaftliche Praxis eingehalten habe.

Würzburg den 06.12.2012 Philipp Höpfner

Hiermit erkläre ich, dass die vorliegende Dissertation nicht in gleicher oder anderer Form bereits in einem anderen Prüfungsfach vorgelegt habe.

Würzburg den 06.12.2012 Philipp Höpfner